Doctoral theses at NTNU, 2021:157

Asgeir Bjørgan

Physics-informed and learning-based approaches to biomedical hyperspectral data analysis

Doctoral thesis

NTNU
Norwegian University of Science and Technology
Thesis for the Degree of
Philosophiae Doctor
Faculty of Information Technology and Electrical Engineering
Department of Electronic Systems

NTNU
Norwegian University of
Science and Technology

Asgeir Bjørgan

Physics-informed and learning-based approaches to biomedical hyperspectral data analysis

Thesis for the Degree of Philosophiae Doctor

Trondheim, May 2021

Norwegian University of Science and Technology
Faculty of Information Technology and Electrical Engineering
Department of Electronic Systems

NTNU
Norwegian University of
Science and Technology

NTNU
Norwegian University of Science and Technology

Thesis for the Degree of Philosophiae Doctor

Faculty of Information Technology and Electrical Engineering
Department of Electronic Systems

ISBN 978-82-326-5461-1 (printed ver.)
ISBN 978-82-326-6491-7 (electronic ver.)
ISSN 1503-8181 (printed ver.)
ISSN 2703-8084 (online ver.)

Doctoral theses at NTNU, 2021:157

Printed by NTNU Grafisk senter

Preface

The work constituting this thesis was carried out at the Department of Electronic Systems at the Norwegian University of Science and Technology (NTNU) in Trondheim, Norway, from September 2016 to December 2020. The work was financially supported by the Department of Electronic Systems. Travel expenses to SPIE Photonics West 2019 were covered by a grant from Tandberg radiofabrikkers fond and Norges tekniske høgskoles fond.

First of all I want to thank my supervisor Professor Lise Lyngsnes Randeberg for putting enough trust in me to let me do more or less (within reasonable limits) what I wanted these past 4 years, and for a good collaboration throughout the 7.5 years (technically 8.5) we've been working together. Thanks for all the support and help and good and enlightening discussions, and for answering emails at odd times. I've had lots of opportunities to work on fun and challenging things, and I am truly grateful for that. Thanks for ensuring that I could work on a PhD in the end. I also want to thank for feedback on this thesis beast over these last weeks before submission.

Thanks to Terje for putting up with me and for support when life is hard, for being on the receptive end when the frustrations mount up and needs outlet, and for sharing home office during the Covid-19 times. I don't know how happy "Nordic Semiconductor avdeling Terje" has been about this arrangement during busy times, but "NTNU avdeling Asgeir" has been very happy indeed. I know that this otherwise would have been a very lonely experience and that I probably wouldn't have been able to finish, and I am glad that I have had someone. A huge thanks for the final proof-reading of the thesis, and for all the discussions we've had. Also a small grain of thanks to our surdeig "Ragni" for unlimited supplies of yeast and lactic acid.

Thanks to Ragni Helene (not surdeig) and Øyvind K. for dealing with walls of text, for being good friends and for dining arrangements, and to Ragni for visiting often. Thanks to Jens for being a good friend both within and without IES, and for always having time for lunch breaks and walks in the sunshine to

calibrate our poorly adjusted souls to the darkness of winter. Thanks to Jens and Gara for post-rush Covid-19 lunch breaks during the fall. Thanks to Stine and Perkrifj, Molven, Marita, Knuts, Ryeng, Magne, Ingar, Bjørgor and other current and previous constants, and to Dall'Osso, Anja, Terje Runde, Firing and Astrid.

A thanks to Akademisk Radioklubb and its members, 8/9 of the skills I might have are probably things I've learned at or due to ARK/Samfundet. Also a thanks to Sikringskomiteen at Samfundet for giving me something else to do during the free time of my first 2.5 PhD years, and a thanks to Oda, Øyvind B., Arne Magnus, Stig, Andreas, Bent, Håvard S., Yngvild, Anders, Sveinung, Miriam, Nora-Marie, Ivar, Jørgen, Håvard D. and Julie for a great time.

Thanks to people at the "lunch group" at IES. It was a nice part of the daily life until March 12 2020. Thanks to directly adjacent office colleagues Lukasz and Matija during an earlier post-master, pre-PhD (pre-doc?) life, and Ine Mari and Yi during earlier periods of the current PhD life. Thanks to Dr. Brita Pukstad for collaboration on the in vitro wound model manuscripts, and for all support when we were planning for a new experiment. Thanks to Eirik Svendsen at SINTEF Ocean for giving me some fish data to work on, which made a nice and exciting change. Thanks to Professor Astrid Aksnes for support and being a friendly face in the corridor, and for collaboration in TFE12, and Professor Peter Svensson and Dr. Egil Eide for collaboration in TTT4280. Also a thanks to the student assistants Manar, Asbjørn, Eirik and Christian, and students in TTT4280 for a fun experience, and a thanks to Kristoffer for nice collaboration and follow-up when lab responsibility in TTT4280 was handed over to me.

Last, but not least, thanks to my immediate family: my mother Elsa, and Øyvind, Torstein, Tonje and Johanne.

Asgeir Bjørgan
Stadsbygd, Norway (Christmas working vacation away from Trondheim)
December 2020

Abstract

The high spectral and spatial resolution of hyperspectral imaging makes it a promising imaging technique for a wide range of biomedical applications. A recurring challenge is the handling and processing of the large amounts of data generated by the technique. The work of this thesis has focused on the analysis of an in vitro wound model dataset and a burn wound model dataset, utilizing supervised and unsupervised learning techniques and photon and heat transport modeling to extract information from the data. New insights on the characterizable optical property changes of these applications has been obtained, along with their relation to the tissue composition and underlying mechanisms. This enables development of targeted automated processing algorithms and better understanding of the technique.

List of papers

Work included in the thesis

I: A. Bjorgan, B. Pukstad, and L. L. Randeberg, "Hyperspectral characterization of re-epithelialization in an in vitro wound model," *J. Biophotonics*, vol. 13(10):e202000108, 2020

II: A. Bjorgan and L. L. Randeberg, "Exploiting scale-invariance: A top layer targeted inverse model for hyperspectral images of wounds," *Biomed. Opt. Express*, vol. 11(9):5070–5091, 2020

III: A. Bjorgan, B. S. Pukstad, and L. L. Randeberg, "Identification of wound healing in an in vitro wound model," To be submitted

IV: A. Bjorgan and L. L. Randeberg, "Application of smoothing splines for spectroscopic analysis in hyperspectral images," *Proc. SPIE*, vol. 10873, 2019

V: A. Bjorgan and L. L. Randeberg, "A random forest-based method for selection of regions of interest in hyperspectral images of ex vivo human skin," *Proc. SPIE*, vol. 10889, 2019

VI: A. Bjorgan and L. L. Randeberg, "Combining hyperspectral classification and heat transport modeling: An investigation of experimental burn wound heterogeneity," In submission

Other published work not included in the thesis

1. A. Bjorgan, L. A. Paluchowski, S. T. K. Seljebotn, and L. L. Randeberg, "Combined 3d model acquisition and autofocus tracking system for hyperspectral line-scanning devices," *Proc. SPIE*, vol. 10870, 2019

2. P. Henriquez, B. J. Matuszewski, Y. Andreu-Cabedo, L. Bastiani, S. Colantonio, G. Coppini, M. D'Acunto, R. Favilla, D. Germanese, D. Giorgi, P. Marraccini, M. Martinelli, M.-A. Morales, M. A. Pascali, M. Righi, O. Salvetti, M. Larsson, T. Strömberg, L. L. Randeberg, A. Bjorgan, G. Giannakakis, M. Pediaditis, F. Chiarugi, E. Christinaki, K. Marias, and M. Tsiknakis, "Mirror mirror on the wall... an unobtrusive intelligent multisensory mirror for well-being status self-assessment and visualization," *IEEE Trans. Multimedia*, vol. 9(7):1467–1481, 2017

3. L. A. Paluchowski, H. B. Nordgaard, A. Bjorgan, S. A. Berget, and L. L. Randeberg, "Can spectral-spatial image segmentation be used to discriminate burn wounds?" *J. Biomed Opt.*, vol. 21(10):101413, 2016

4. L. A. Paluchowski, A. Bjorgan, H. B. Nordgaard, and L. L. Randeberg, "Spectral-spatial classification combined with diffusion theory based inverse modeling of hyperspectral images," *Proc. SPIE*, vol. 9689, 2016

5. A. Bjorgan and L. L. Randeberg, "Real-time noise removal for line-scanning hyperspectral devices using a minimum noise fraction-based approach," *Sensors*, vol. 15(2), 2015

6. M. Milanic, A. Bjorgan, M. Larsson, T. Strömberg, and L. L. Randeberg, "Detection of hypercholesterolemia using hyperspectral imaging of human skin," *Proc. SPIE*, vol. 9537, 2015

7. A. Bjorgan and L. L. Randeberg, "Towards real-time medical diagnostics using hyperspectral imaging technology," *Proc. SPIE*, vol. 9537, 2015

8. A. Bjorgan, M. Denstedt, M. Milanic, L. A. Paluchowski, and L. L. Randeberg, "Vessel contrast enhancement in hyperspectral images," *Proc. SPIE*, vol. 9318, 2015

9. M. Milanic, A. Bjorgan, M. Larsson, P. Marraccini, T. Strömberg, and L. L. Randeberg, "Hyperspectral imaging for detection of cholesterol in human skin," *Proc. SPIE*, vol. 9332, 2015

10. M. Denstedt, A. Bjorgan, M. Milanic, and L. L. Randeberg, "Wavelet based feature extraction and visualization in hyperspectral tissue characterization," *Biomed. Opt. Express*, vol. 5(12):4260–4280, 2014

11. A. Bjorgan, M. Milanic, and L. L. Randeberg, "Estimation of skin optical parameters for real-time hyperspectral imaging applications," *J. Biomed. Opt.*, vol. 19(6):066003, 2014

12. A. Bjorgan and L. L. Randeberg, “Estimation of skin optical parameters for real-time hyperspectral imaging applications,” *Proc. SPIE*, vol. 8926, 2014

13. L. A. Paluchowski, M. Milanic, A. Bjorgan, B. Grandaunet, A. Dhainaut, M. Hoff, and L. L. Randeberg, “Identification of inflammation sites in arthritic joints using hyperspectral imaging,” *Proc. SPIE*, vol. 8947, 2014

Contents

Chapter 1

Introduction

Fast, non-invasive decision support systems for clinical diagnostics could be made feasible by optical methods capable of characterizing human tissue properties. This includes techniques like optical coherence tomography [1], photoacoustic tomography [2], reflectance spectroscopy [3], spatial frequency domain imaging (SFDI) [4, 5] and hyperspectral imaging [6]. Hyperspectral imaging was originally developed for remote sensing [7–10], but has over the years found applications in the food industry [11], waste sorting [12] and medical applications like wound imaging [6, 13–20], burn wound imaging [21, 22], skin bruises [23], cancer diagnostics [6, 24, 25] and surgical guidance [6, 26]. Hyperspectral imaging is an imaging technique that provides a "normal" image of a given object, but with full spectral resolution in every pixel rather than just the red, green and blue color channels. This has the potential to differentiate between objects that appear identical to the human eye, and can reveal information on the chemical composition of the material. Hyperspectral imaging generates large amounts of data, and a recurring challenge is the handling of and exploration of the resulting data sets. Not much is able to beat the human brain in pattern recognition, but the high dimensionality of the images makes manual evaluation cumbersome.

The advance of GPU computing has over the last years spurred the successful use of large convolutional neural networks (CNN) in e.g. image processing, which has taken huge leaps ahead of more traditional techniques [27]. This has kindled a general interest in machine learning and artificial intelligence across many fields. The original motivation of the work in this thesis was to investigate and utilize such techniques for hyperspectral image processing. Techniques under this umbrella have previously been used by other groups [19, 22, 28–33] and our own [14, 21, 23, 34].

An underlying and general motivation of the work has been to analyze larger hyperspectral datasets in a more convenient way, to script, automatize and streamline the process by developing tools and utilizing appropriate machine learning techniques and associated paradigms. This underlying goal was partially fulfilled by a move to Python to make use of well-established libraries and possibilities for data manipulation, and the development of a selection of Python modules and command line utilities. In addition to use of statistical techniques, being able to understand the results is important. The statistical models should be explainable. Previously developed physics-informed photon transport models have been utilized in new ways in order to explain the results and couple spectral changes and statistical results to changes in optical properties. In combination, new models and algorithms for hyperspectral data analysis have been developed.

The work in this thesis has focused on analyzing existing datasets. Much data have been acquired by our group over the years, but the main focus has previously been on data collection, with insufficient time for development and in-depth testing of new approaches to data analysis. The direct outcome of the analysis, resulting in the included manuscripts, was not the developed tools, but rather the new insights gained. The major motivation has been to understand the datasets and the underlying physics, both out of curiosity and in order to better understand how automated algorithms could be developed. Finally, the motivation in analyzing existing datasets is to obtain closure, and find out whether taking the application further is feasible.

The two applications that were included are in vitro wound model imaging and burn wound imaging. The main contribution for the in vitro wound model application is a clear characterization of spectral features that can be used to detect re-epithelialization, and the development of a specialized photon transport model to estimate re-epithelialized tissue properties. For burn wounds, explanations for observed artifacts have been obtained, and the feasibility of the technique in characterizing damage more closely investigated.

The rest of the thesis is structured as follows. The hyperspectral imaging technique is explained in chapter 2. The main applications are outlined in chapter 3. The analysis techniques used, statistical learning and physics-informed modeling, are described in chapter 4 and 5. The main findings of the included manuscripts are summarized in chapter 6, and the conclusions and further work in chapter 7.

Chapter 2

Image acquisition

Analysis of hyperspectral images was the main focus throughout the work, and included both fluorescence and reflectance data. The techniques and the rationale for their use in tissue characterization is explained in this chapter.

2.1 Hyperspectral imaging

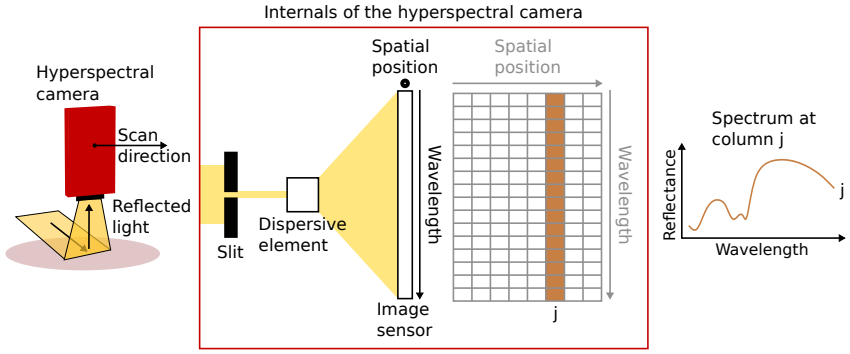

Figure 2.1: Simplified illustration of the working principle of a line-scanning hyperspectral camera measuring reflected light. The camera images one line at a time. A dispersive element disperses the different wavelengths of the incoming light into different directions, and the dispersed light is mapped to a 2D image array. Each pixel j gains a high spectral resolution as a result. A full image is obtained by scanning, through physical movement of the camera or the imaged sample.

A line-scanning hyperspectral camera was used to obtain all images con-

sidered throughout the work. The simplified working principle is illustrated in figure 2.1. A dispersive element (e.g. grating, prism) disperses the different wavelengths of the incoming light into different directions. The dispersed light is captured by an image array sensitive to the desired wavelength range. Different wavelengths are mapped to different rows in the image array, while a column corresponds to the same spatial position. A slit ensures that the camera sees only a single line of the full scene at a time. The full scene is imaged by scanning.

Each image acquired at each line consists of $p \times M$ values. The column vector at column j represents the spectrum from the corresponding spatial position. The final result is a datacube consisting of N lines $\times$ M samples $\times$ p bands/wavelengths.

All included images have been obtained using a HySpex VNIR-1600 hyperspectral camera (Norsk Elektro Optikk, Lillestrøm, Norway), providing a resolution of $p = 160$ bands over the wavelength region 400-1000 nm, and $M = 1600$ pixels across-track. A close-up lens was used for the in vitro wound model data (pixel size $\sim 25 \times 25\,\mu$m), and a 30 cm lens for the burn wound data (pixel size $\sim 60 \times 60\,\mu$m).

2.2 Imaging methods

Different illumination modalities or geometries probe the imaged tissue in different ways. The two methods considered in this work are wide-field reflectance imaging and wide-field autofluorescence imaging.

2.2.1 Reflectance imaging

Working principle and calibration The tissue is illuminated with a spectrally and spatially broad beam of light, and the camera measures the intensity of the reflected light. An acquired spectrum is a combination of the light source spectrum and a tissue spectrum. A reflectance standard is typically included in the scene in order to acquire the light source spectrum. Given a flat scene, the reflectance is obtained from the acquired intensities by

$$R = \frac{I - I_{\text{dark}}}{I_{\text{standard}} - I_{\text{dark}}}, \tag{2.1}$$

where I_{dark} is the dark current of the sensor.

Spectralon reflectance targets (WS-1-SL, Ocean Optics, Duiven, The Netherlands) were used in the images considered in the included work. Two linear

light sources (Model 2900 Tungsten Halogen, Illumination Technologies, New York, USA) were used for illumination, and polarizers were mounted on the camera lens and the light sources in order to avoid specular reflection.

Normalization A challenge in hyperspectral imaging is the wider imaging field. Strictly correct reflectance levels are obtained only when the sensor-object distance to the reflectance standard is equal to the sensor-object distance to the imaged object. Changes in height or curvature leads to level changes that needs to be handled in the processing or interpretation of the data, and makes the spectral behavior more important than the level. This was dealt with by using spectral derivatives in the wound model study, which work as a high-pass filter that eliminates the low/near constant offsets due to illumination variations. The burn wound data had more extensive illumination variations, and normalization was used to reduce shadow artifacts to some extent.

Tissue optics The reflected light consists of light reflected directly at the surface due to mismatch in refraction indices (specular reflectance) and light probing the tissue before being back-scattered out of the tissue (diffuse reflectance). The diffuse part of the reflectance is interesting for tissue characterization since the back-scattered light is influenced by the absorption and scattering properties of the tissue, which are in turn influenced by the tissue properties. The basic working principle is illustrated in figure 2.2.

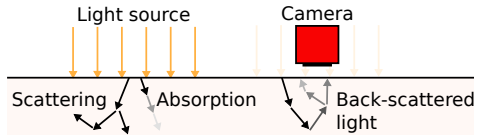

Figure 2.2: Working principle of reflectance imaging: Light emitted from a light source is absorbed and scattered by the tissue, and the back-scattered light is captured by the camera as diffuse reflectance.

Scattering and absorption mechanisms govern the photon transport in turbid media like tissue. Scattering is expressed using the scattering coefficient μ_s, which describes the probability per length unit that a photon is scattered into a different direction [35]. Absorption is correspondingly expressed using the absorption coefficient μ_a, describing the probability per length unit that a photon is absorbed [35].

The physical origin of scattering is inhomogeneities in refraction indices in structures like cells and collagen fibrils [35, 36]. Scattering from particles much

smaller than the wavelength is modeled using Rayleigh theory [35], leading to a wavelength dependence $\mu_s \propto \lambda^{-4}$. Scattering from particles in the order of or larger than the wavelength is modeled using Mie theory [35]. The Mie scattering can roughly be approximated using an exponential dependence $\mu_s \propto \lambda^{-b}$ [37]. In sum, scattering in a tissue layer is described by

$$\mu_s' = \mu_{\text{s,Mie,500}}'(\lambda/500)^{-b_{\text{Mie}}} + \mu_{\text{s,Ray,500}}'(\lambda/500)^{-4}. \tag{2.2}$$

Examples of values for $\mu_{\text{s,Mie,500}}'$, b_{Mie} and $\mu_{\text{s,Ray,500}}'$ in ex vivo human skin are $1800\,\text{m}^{-1}$, 0.22 and $1700\,\text{m}^{-1}$, respectively [38]. Resulting spectra are plotted in figure 2.3.

Light is absorbed by constituents like hemoglobin, melanin, water and lipids [35]. The light induces rotations or vibrations in the molecules which are converted into and dissipated as heat. Oxygenated and deoxygenated hemoglobin and melanin are always present within living tissue and have significant absorption within the visible wavelength range. The absorption spectra are plotted in figure 2.3. Other examples of constituents with significant absorption in the visible wavelength range include methemoglobin, CO-Hb, beta-carotene, bilrubin and lycopene, but appear only under special circumstances. Water and fat have significant absorption properties towards longer wavelengths.

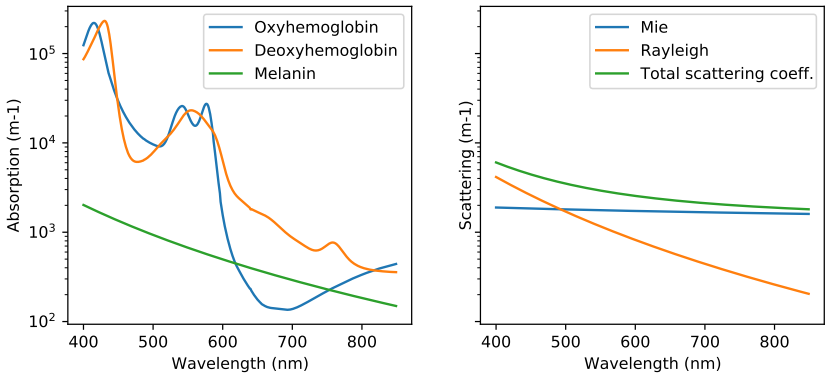

Figure 2.3: Absorption and scattering properties in tissue. The hemoglobin absorption spectra are obtained from Spott [36], while the melanin wavelength dependence is obtained from $\mu_{a,\text{melanin}} = \mu_{a,m,694}(\lambda/694)^{-3.46}$ [39], with $\mu_{a,m,694} = 300\,\text{m}^{-1}$ (fair to moderatedly dark skin [40]).

2.2.2 Fluorescence imaging

Working principle Photons can excite electrons into higher energy states, which on the return to lower states re-emit part of the energy as photons with lower energy, i.e. longer wavelengths [41, 42]. This effect is called fluorescence [41, 42].

In fluorescence imaging, a narrow-banded light source at a short wavelength is used (e.g. ultra-violet), which excites emission in longer wavelength bands that can be acquired by the camera without influence from the excitation wavelength. The basic working principle is illustrated in figure 2.4.

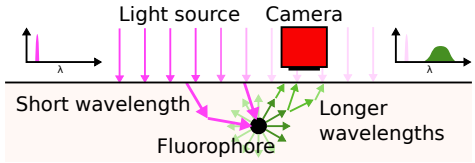

Figure 2.4: Working principle of fluorescence imaging: Short-wave light excites fluorescence in the longer wavelengths, which is captured by the camera.

Fluorophores Fluorescent material are called fluorophores [42]. The fluorophores act as light sources embedded in the tissue. The emitted light undergoes similar transport mechanisms as in the reflectance case [41], but probes the tissue in a different way that adds to the information obtained from the reflectance spectra. Tailoring the excitation wavelength targets specific fluorophores [42]. The existence or amount of fluorophores is valuable for investigating tissue metabolism and tissue composition [42]. Some fluorophores exist only in specific layers of the tissue (e.g. tryptophan in epidermis, collagen in dermis) [43], meaning that different tissue layers can be targeted by changing the excitation wavelength.

Excitation wavelength 355 nm was primarily used in the included studies. Fluorophores at this wavelength include NADH, collagen cross-links, elastin cross-links, lipo-pigments and flavins [43–45]. Examples of fluorescence emission spectra are shown in figure 2.5.

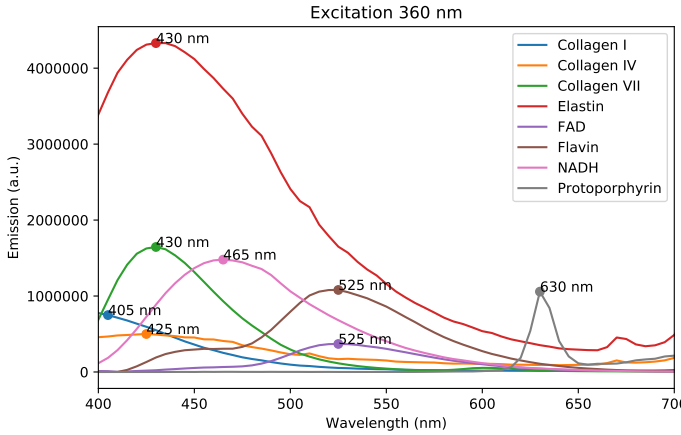

Figure 2.5: Fluorescence emission spectra extracted from data made available by DaCosta et al. [46]. The figure is reused from paper III.

Normalization Light at the excitation and emission wavelengths are influenced by photon transport mechanisms, and appropriate normalization depends on the application at hand. Raw spectra can be treated directly, or the spectra can be e.g. sum- or max-normalized.

Chapter 3

Applications

Two main applications of hyperspectral imaging have been investigated in the included work: Detection of wound healing in an in vitro wound model, and evaluation of burn wound severity in pigs.

3.1 In vitro wound model

Investigation of wound healing in a controlled lab setting is useful for investigating the effects of wound or skin treatments. Wound models mimicking human wound healing are useful for this purpose. Examples include the use of animals, cell models and ex vivo/in vitro skin models [47]. In case of the latter, wounds are prepared on smaller segments of human donor skin that are incubated in a growth medium, providing nutrients to the skin and causing the wound to heal. An example of a partially re-epithelialized sample is shown in figure 3.1. The presence and rate of re-epithelialization is used to evaluate wound healing under different conditions [48–52]. The evaluation normally requires destructive and time-consuming histology analysis, and follow-up over time requires a high number of identical samples. The wounds can end up with different sizes due to the wound preparation method [53], or heal unevenly or be evaluated differently due to the sample processing [54], requiring yet more samples for statistical validity. Optical techniques like hyperspectral imaging are a promising alternative that can make it possible to non-destructively follow the healing of a sample over time.

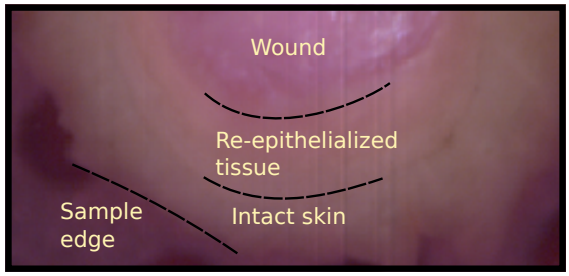

Figure 3.1: Section of an RGB image of a wound model sample with regions corresponding to wound, re-epithelialized tissue and intact tissue marked.

Wound healing in a wound model In general, in vivo wound healing consists of several interconnected, overlapping processes [55, 56]. The processes likely most relevant for optical imaging are re-epithelialization and remodeling of the extracellular matrix, due to expected changes to the layer composition, scattering properties and fluorescence. Wound healing also includes clot formation and an inflammatory response [55], but this is not present in the in vitro wound model due to lack of an intact circulatory system. Roughly, re-epithelialization is initialized a few hours after injury by keratinocytes migrating into the wound from the surrounding tissue [55, 56]. This ultimately leads to reconstruction of an epidermal layer. Remodeling of the extracellular matrix starts with migration of fibroblasts into the wound, and ultimately causes production of collagen I and III which are used to reconstruct the extracellular matrix [55–57]. A simplified illustration is shown in figure 3.2.

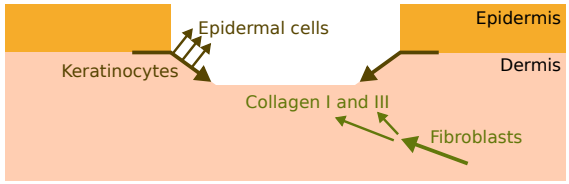

Figure 3.2: Simplified illustration of re-epithelialization and remodeling of the extracellular matrix.

The imaged wound model was based on a wound model developed by Jansson et al. [58] and Kratz [59]. Here, circular 6 mm diameter samples of human breast or abdominal tissue are prepared with 3 mm diameter wounds. Incubating the samples in a cell culture medium consisting of Dulbecco's Modified Eagle Medium (DMEM) with 10% fetal calf serum, 50 U/ml streptomycin

and 50 ug/ml penicillin causes the wounds to re-epithelialize by day 7 [58–60]. Submersion in the medium causes the neoepidermis to consist of a single cell layer [59], while exposure to air ensures multiple cell layers resembling a normal human epidermis [58]. Re-epithelialization is the main reported and investigated event, although some studies also report on some expression of collagenase [61] and production of collagen I and III [57].

Data Reflectance data and fluorescence emission data excited at 355 nm were acquired over the wavelength range 400-1000 nm. The data were acquired by Ingvild Haneberg and Matija Milanic during Ingvild Haneberg's master thesis work in 2014 [62]. The data consisted of images of samples with total size of 8 mm and wounds of size 3 mm and 4 mm. The standard Jansson/Kratz medium was used, and the samples were exposed to air. The samples were followed up over 22 days. The analysis of these data is further described in section 6.1.

3.2 In vivo burn model

Burn wounds can generally be divided in first degree, second degree and third degree burns [63]. First degree burns correspond to superficial damage to the epidermal layer only, while third degree correspond to damage down to subcutis [63]. The former re-epithelialize and heal on their own due to viability of the blood vessels in dermis, while the latter need surgical intervention since the vessels are destroyed or severely impaired [64–66]. Deciding which is which by inspection is feasible for a trained clinician [64–66]. Second degree burns are confined to dermis, but anywhere between superficial and deep dermis [63]. It is challenging for a clinician to determine how deep a second degree burn is during the first 48 hours, which has motivated research into objective optical methods for early evaluation [64–67]. A challenge is the dynamic response of the burn close after time of injury, which interferes with evaluations of the vessel viability [64, 65, 68, 69].

Heat transforms the tissue in various irreversible ways. The collagen structure is destroyed, blood vessel walls are ruptured, and the blood vessels coagulate [70]. The destruction of different tissue structures is expected to co-vary, with progression of collagen destruction happening simultaneously with progression of vascular destruction [64]. Techniques like SFDI can target collagen structure changes specifically by the technique's ability to separate scattering from absorption, which makes it suitable for early evaluation [64–66]. In a previous study by our group, it was investigated if hyperspectral imaging was sensitive to similar changes, leading to a feasibility study using an animal model

in 2014 [21, 71, 72]. The collected data were subjected to further analysis in the included work.

Data The data were collected by Lukasz Paluchowski as a part of his PhD work in 2015 [21, 71, 72]. Burns were induced on two pigs by metal heated to 100 °C, using different contact times to create burns of different severity. Hyperspectral images were acquired every other hour, stopping at 30 hours for pig 1 and 8 hours for pig 2. Images in the visible to near infrared wavelength range (VNIR) and short-wave infrared range (SWIR) were collected, but only the VNIR images were analyzed in this work. The burns had been evaluated by pathologists using histologies according to the method in Papp et al. [73]. Data analysis is further described in section 6.2.

Chapter 4

Statistical learning techniques

Both unsupervised and supervised analysis techniques were used to analyze the data, in addition to photon transport modeling techniques. The modeling techniques are outlined in chapter 5, while the statistical techniques are outlined in the current chapter.

A desired end goal of hyperspectral data analysis is often to use hyperspectral data to estimate variations, detect specific changes in tissue properties, or understand the relation between an underlying variation and the spectral data. Statistical learning techniques are suitable both for building predictive models, and for infering patterns in the data.

4.1 Basic concepts

4.1.1 Input and output

Assuming some feature vector x which describes input variables, and a response variable y which describes some output, many problems can be formulated as finding a function $f(x)$ that best predicts y from x [74, 75]. In case of hyperspectral data, x can be the p-dimensional vector $x = [x_1, x_2, \ldots, x_p]^T$ which describes the reflectance value at each wavelength band i, or another suitable representation.

Working on the spectra directly would be the most convenient, but has some challenges due to the high dimensionality and each dimension being a digitization of an analog signal [74, 75]. Some techniques allow for direct application, while others benefit from e.g. dimensionality reduction techniques.

4.1.2 Regression and classification

The techniques are customarily divided in supervised and unsupervised learning techniques, and further divided into regression and classification techniques [74, 75]. Regression techniques are appropriate for problems where y is a continuous function of x and can take any real value [74, 75], while classification techniques are appropriate where y is a discrete function of x and can only take a limited set of discrete values or classes $g \in g_1, g_2, \ldots, g_K$ [74, 75]. Regression is illustrated in figure 4.1, and classification in figure 4.2. Examples of the former include prediction of tissue properties like blood content or blood oxygenation from hyperspectral data, while examples of the latter include detection of whether a wound is re-epithelialized or not, or whether a region is a second or third degree burn.

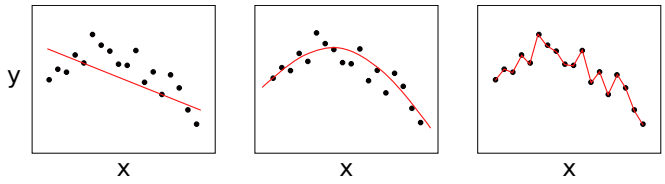

Figure 4.1: Regression of y vs x: Biased linear fit (right), more flexible fit (center) and too flexible fit with low bias but high variance (right).

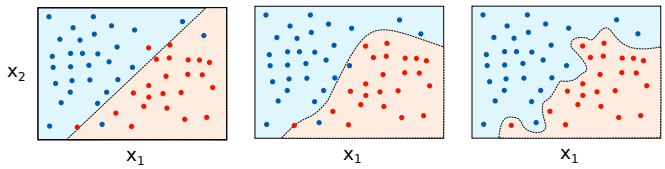

Figure 4.2: Classification of red and blue labels in a two-dimensional input space: Biased linear boundary (left), more flexible decision boundary (center) and too flexible decision boundary with low bias but high variance (right).

Assuming that the data are distributed according to a known probability distribution $P(X, Y)$, it can be shown that the optimal strategy is to find a function

$$f(x) = E(Y|X = x) \tag{4.1}$$

for regression [74], and

$$\hat{G}(x) = \text{argmax}_{g \in G} P(g|X = x) \tag{4.2}$$

for classification [74]. These approaches are interrelated in that the posterior probability $P(Y|X)$ is considered or modeled [74, 76], except that the discrete nature of classification leads to a treatment of the probabilities directly rather than the expectation. Classification problems have been the main focus of this work. Most classification techniques try to model class probabilities according to assumptions on the data distribution (e.g. linear discriminant analysis, logistic regression, Naive Bayes, K nearest neighbours [74]), or try to separate the input space according to some heuristics or decision surface model (e.g. support vector machine, random forest, decision trees [74]).

4.1.3 Supervised and unsupervised learning

Supervised techniques rely on having pairs (x_i, y_i) to model $P(Y|X)$ [74, 76]. Unsupervised techniques have only (x_i) available, and try to extract information on the underlying behavior of x [74, 75]. The goal of an unsupervised technique is not necessarily well-defined, and could for example be to model $P(X)$, try to cluster x into naturally occurring classes, decompose x in terms of a few components, or any other goal not involving corresponding y values [74–76]. Finding spectrally similar regions in a hyperspectral image is an unsupervised classification problem.

4.1.4 Model selection and cross-validation

A given supervised regression or classification model can be selected or tuned to perform arbitrarily well on the training data, in the extreme case fit the data exactly [74, 75]. Such models neither capture the underlying behavior nor predict well on unseen data [74, 75]. A separate test set is customarily used to evaluate the model performance on independent data to infer whether the model has been able to capture the underlying behavior [74, 75].

Bias and variance Assuming that y follows the distribution $Y = f(X) + \epsilon$ with $\mathrm{Var}(\epsilon) = \sigma_\epsilon^2$, the expected squared-error loss at an independent data point x_0 can be decomposed as [74]

$$Err(x_0) = \sigma_\epsilon^2 + [E[\hat{f}(x_0)] - f(x_0)]^2 + \mathrm{Var}(\hat{f}(x_0)), \tag{4.3}$$

$$= \sigma_\epsilon^2 + \mathrm{Bias}^2(\hat{f}(x_0)) + \mathrm{Var}(\hat{f}(x_0)), \tag{4.4}$$

where the expectation and the variance are taken over repeated sampling of new training data sets. A model that follows the datapoints exactly has no bias, but varies with different training sets and has high variance [74, 75]. A

constrained model is expected to have lower variance, but lowered flexibility results in higher bias to the underlying behavior [74, 75]. Model selection balances model bias and model variance to find the lowest combined error [74, 75]. Models with different flexibilities are demonstrated in figure 4.2 and 4.1.

Test and validation sets Keeping a separate collection of datapoints for final evaluation of the test error (test set) is a possible way of evaluating the generalization ability of the model [74]. If data have been used to select, tune or train a model, they are no longer independent. The training set is therefore often also further split into a training and validation set, where the validation set is used to select or tune models, and the test set used for final evaluation [74].

This approach requires that both training, validation and test data capture the full data variation, which is difficult if limited amounts of independent data are available. An alternative approach is cross-validation [74, 75].

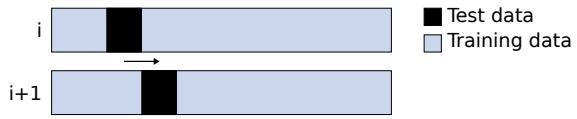

Figure 4.3: Illustration of two subsequent steps i and $i+1$ in cross-validation: The segment corresponding to the test data is systematically changed, and the model re-trained and re-tested.

Cross-validation Cross-validation randomly splits the dataset into a training set and test set, and repeats the split several times [74, 75]. This is illustrated in figure 4.3. The size of each test set is too low for representative estimates, but averaging over multiple splits improves the test error statistics. This also directly estimates the bias and variance by repeatedly changing the training set.

Cross-validation is a suitable replacement for a validation set since it provides a score that can be used to compare models, but the final model is based on performance evaluated on all available data, and further test data are necessary if the generalization error is needed.

4.2 Techniques

Used techniques are briefly explained here.

4.2.1 Regression techniques

Smoothing splines The penalized residual sum of squares (PRSS) of a function $f(x)$ is given as [74]

$$\mathrm{PRSS}(f,\alpha) = \sum_{i=1}^{p}\{y_i - f(x_i)\}^2 + \alpha\int_{-\infty}^{\infty}\left\{\frac{d^2}{dt^2}f(t)\right\}^2 dt. \tag{4.5}$$

The first term evaluates the closeness of the function $f(x_i)$ to y_i, while the second term penalizes curvature in $f(x)$ [74]. The parameter α controls the smoothness of $f(x)$, where $\alpha = 0$ allows $f(x)$ to interpolate y_i exactly and $\alpha > 0$ penalizes high variation in $f(x)$, gradually changing the function to a straight line with $\alpha \to \infty$. The solution for $f(x)$ is the smoothing spline, and is a natural cubic spline with p knots [74].

The method was used to fit fluorescence spectra in paper IV, as α can objectively be selected through cross-validation and the linearity of the method has some satisfying consequences for application to multiple spectra. The access to analytic derivatives makes direct evaluation of peak positions convenient.

4.2.2 Classification techniques

Linear discriminant analysis Linear discriminant analysis (LDA) is an example of a technique that tries to model $P(G|X)$ directly. Assuming $f_k(x) = P(X = x|G = k)$ and $P(G = k) = \pi_k$ [74] and using Bayes' rule [74],

$$P(G = k|X = x) = \frac{P(X = x|G = k)P(G = k)}{P(X = x)} = \frac{f_k(x)\pi_k}{\sum_{l=1}^{K} f_l(x)\pi_l}. \tag{4.6}$$

LDA assumes a Gaussian probability density function with a common covariance matrix Σ among all classes [74],

$$f_k(x) = \frac{1}{(2\pi)^{p/2}|\Sigma|^{1/2}}\exp\left(-\frac{1}{2}(x-\mu_k)^T\,\Sigma^{-1}(x-\mu_k)\right). \tag{4.7}$$

Finding the maximum posterior probability among all classes is equivalent with comparing $\log\left(\frac{P(G=k|X=x)}{P(G=l|X=k)}\right)$ among all class pairs k, l [74]. Due to the Gaussian assumption and assumption of a common Σ in f_k and the common denominator in $P(G = k|X = x)$, this essentially reduces to comparing discriminant functions [74]

$$\delta_k(x) = x^T\Sigma^{-1}\mu_k - \frac{1}{2}\mu_k^T\Sigma^{-1}\mu_k + \log\pi_k. \tag{4.8}$$

This is roughly equivalent with classifying to the closest class centroid [74]. Projecting all datapoints down to the subspace spanned by the centroids yields the same distances and sufficient information for LDA classification [74].

The method was used to demonstrate linear classification in paper III, and as the final burn classification model in paper VI. The method can be suitable in general due to the low variance of the technique, despite high bias from incorrect assumptions, and provides a useful, class-aware dimensionality reduction.

Decision trees Decision trees sequentially split the input space in smaller regions until each region contains a single class, and is visualized as a tree [74]. The technique notoriously overtrains and has high variance [74, 75]. The main strength is the interpretability of the technique [74, 75].

The technique was used to understand relations among the histologies in paper VI.

Random forest The random forest classifier consists of a majority vote among a given number of decision trees [74]. Each decision tree is trained in such a way that each split in the tree considers a random selection of input features rather than all features, which decorrelates the trees and improves the variance reduction obtained by averaging [74, 75, 77].

The method was used to segment background from the tissue of interest throughout the work, and is the main focus of paper V. It was also used to segment wound from intact/re-epithelialized tissue in paper I and III. Lack of tuning necessities, the flexibility and the robustness to a large number of features makes the technique convenient for hyperspectral imaging.

Support vector machine Support vector machine (SVM) classifies the datapoints by finding an optimal separating hyperplane where a given number of points are allowed to be on the wrong side of the decision surface [74, 75]. The problem can be formulated in terms of inner products, which can be replaced by arbitrary kernel functions that turn the linear decision surface into general, non-linear decision surfaces [74, 75].

SVM has not been used much throughout the work, but was compared for burn wound classification in paper VI due to reported good performance for hyperspectral classification [78–80].

4.2.3 Unsupervised techniques

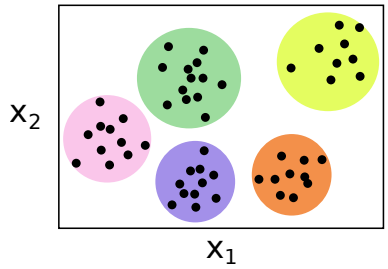

Figure 4.4: Illustration of K-means clustering with $K = 5$ in a two-dimensional input space.

K-means clustering K-means clustering finds K clusters in the data set, where cluster membership is decided from the distance to the cluster centers [74, 75]. By definition, each cluster should optimally be spherical in the image space. K-means is a convenient method wherever this assumption is valid, but generally breaks down for hyperspectral data. The method can be used to reduce the data variation down to a smaller number of clusters, however. K-means clustering has the advantage that it can be applied to unseen data by clustering to the closest centroid. The technique is illustrated in figure 4.4.

The technique was used as a first step in the clustering of the data in paper I.

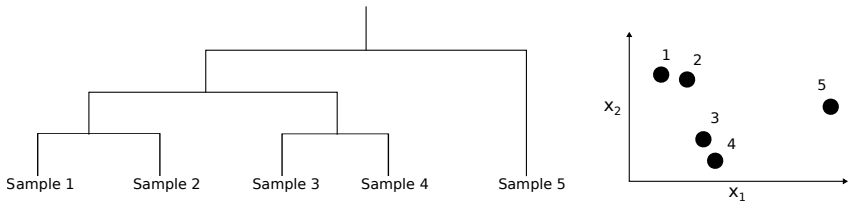

Figure 4.5: Illustration of agglomerative clustering in a two-dimensional input space. The tree to the left illustrates the distance structure for the points to the right, with sample 1 and 2, and 3 and 4 being closest.

Agglomerative analysis Agglomerative analysis is suitable for any kind of image structure, but is memory intensive and does not readily extrapolate to new data. Essentially, agglomerative clustering compares two and two observations or clusters by some distance metric, and merges the closest datapoints first [74, 75]. This yields a tree which shows the distance structure among all observations, which can be used to divide the observations into clusters by

visual inspection [74, 75]. The technique is illustrated in figure 4.5.

The method was used as the second step in the clustering of the data in paper I, combining the too-large number of K-means clusters to a lower number of clusters.

Principal component analysis Principal component analysis (PCA) finds new coordinate axes within the input space along the directions of maximum data variance [75]. The result is p orthonormal components (loadings) which can be used to linearly transform the original data and yield new coordinates (scores) that each describe the position along the variance-maximizing direction [75]. This is illustrated in figure 4.6. All datapoints can be decomposed and expressed as scores and associated loadings. The first few components often summarize the main variation in the data, and the technique is suitable for compression or dimensionality reduction.

The technique can be used for dimensionality reduction and for investigating high-dimensional data in a lower-dimensional space in the cases where variance maximization coincides with the information content. The technique is highly convenient for reducing the redundancy in the hyperspectral imaging bands [81–83].

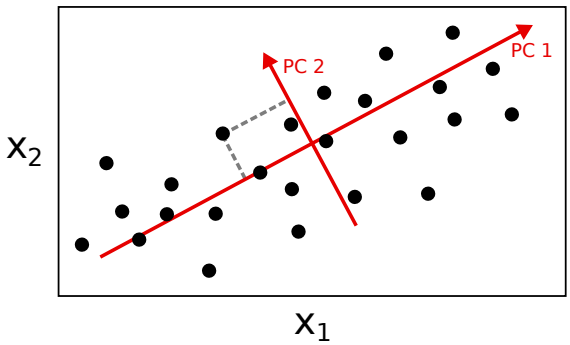

Figure 4.6: Illustration of PCA in a two-dimensional input space. The datapoints have the largest variation along principal component (PC) 1, and next to largest along PC 2. The technique would extract these directions and project each datapoint to the new coordinate directions.

The minimum noise fraction transform (MNF) is a related technique developed for hyperspectral imaging, which sorts the data in terms of signal-to-noise ratio rather than variance [84]. The technique is used for noise removal and dimensionality reduction. This technique was compared to smoothing splines

in paper IV, but was otherwise not used. It was initially tested for dimensionality reduction in the wound model data, but PCA was found to be more suitable and extensible across the entire dataset. The technique was not used for noise removal in any of the presented work, since more degraded spectra got elements from unrelated spectral components mixed in after application of the technique.

Chapter 5

Physics-informed modeling

Physical models can be used to explain the underlying physical rules behind measurements or statistical results. Photon transport modeling and heat transport modeling were used in this work, the former for understanding the relation between optical properties and reflectance results in paper I, II, III and VI, and the latter for understanding heat propagation in the burn wounds in paper VI.

5.1 Photon transport modeling

Photon transport techniques are used to understand the photon propagation through tissue. Tissue is a turbid medium where the light rapidly loses coherence due to high absorption and scattering coefficients.

The photon transport through tissue with a time-independent light source and defined absorption and scattering properties can be described by the radiative transport equation (RTE) [35]

$$\hat{s} \cdot \nabla L(\vec{r},\hat{s}) + \mu_t L(\vec{r},\hat{s}) = \mu_s \int_{4\pi} L(\vec{r},\hat{s}')P(\hat{s}' \cdot \hat{s})d\Omega' + S(\vec{r},\hat{s}). \tag{5.1}$$

$L(\vec{r},\hat{s})$ is the radiance, the energy flowing at position $\vec{r}$ in the direction $\hat{s}$. The transport coefficient $\mu_t = \mu_a + \mu_s'$ describes total loss due to absorption and scattering. $P(\hat{s}',\hat{s})$ is the probability of a photon arriving from direction $\hat{s}'$ being scattered into direction $\hat{s}$. The equation describes light loss and light gain at the position $\vec{r}$ into the direction $\hat{s}$. The left hand side describes losses due to divergence of the beam and absorption/scattering. The right hand side describes contributions from light scattered from other directions, and the light source S.

Common solution approaches include Monte Carlo and the diffusion approximation.

5.1.1 Monte Carlo solution

A direct solution to the photon transport problem is to use Monte Carlo simulations. In this case, individual photon packets are launched into the tissue. The simulation step size and whether the photon is absorbed or scattered are determined by sampling from probability distributions. Statistically correct results are obtained by launching enough photons. Monte Carlo simulations represent an accurate and flexible approach that allows for different tissue and light source geometries to be modeled, but is time-consuming. Software packages include MCML [85] and GPU-MCML [86], the latter an implementation of MCML that uses GPU parallelization to speed up the simulations.

5.1.2 Diffusion approximation

The main approximation step is to write the radiance as a Legendre polynomial expansion with two terms: an isotropic term, and a term with a small deviation from isotropy,

$$L = \frac{\phi}{4\pi} + \frac{3}{4\pi}\vec{j}\cdot\hat{s}, \tag{5.2}$$

where j is the photon flux (net energy flow) and ϕ the fluence rate (integrated radiance, or energy flow regardless of direction). Inserting the expansion into (5.1), integrating over all solid angles and assuming the source function to be isotropic yields [35]

$$\nabla\vec{j}(\vec{r}) = -\mu_a\phi(\vec{r}) + q(\vec{r}), \tag{5.3}$$

with q as the isotropic source function. Inserting (5.2) into (5.1), multiplying by $\hat{s}$ and integrating over all solid angles yields Fick's law [35]

$$\vec{j}(\vec{r}) = -D\nabla\phi(\vec{r}, t), \tag{5.4}$$

where the diffusion constant $D = \frac{1}{3\mu_{tr}}$. This is finally combined with (5.2) and (5.3) to yield

$$-D\nabla^2\phi + \mu_a\phi = q, \tag{5.5}$$

i.e. the time-independent diffusion equation for photon transport. The term $\mu_a\phi$ describes loss due to absorption, and $D\nabla^2\phi$ a diffusion process due to

changes in the energy density. Assuming isotropic source functions, the photon source q in a layered medium can be described by [40, 87]

$$q_i(z) = \mu'_{s,i} \exp(-\mu_{tr,i} z) \prod_{j=1}^{i-1} \exp(-\mu_{tr,j} d_j), \tag{5.6}$$

which describes the unscattered and unabsorbed photons from the light source throughout each layer i. The $\mu'_{s,i} \prod(.)$ accounts for photons in the beam being allowed to scatter further downwards, and $\exp(-\mu_{tr,i} z)$ accounts for photons in the beam lost to absorption and scattering into other directions. The product accounts for photons already being lost throughout the previous layers. Describing the light source in this way rather than directed photons incident on the surface allows for increased validity of the diffusion solution by modeling the light source as a near-isotropic quantity [36]. The solution for the fluence rate in layer i is given by [40, 87]

$$\phi_i(z) = \frac{\delta_i \mu'_{s,i}}{D_i(1-\mu_{tr,i}\delta_i^2)} \exp[-\mu_{tr,i}(z-d_i)] \prod_{j=1}^{i-1} \exp[-\mu_{tr,j}(d_j - d_{j-1})] + \ldots$$
$$A_{i1} \exp(-x/\delta_i) + A_{i2} \exp(x/\delta_i), \tag{5.7}$$

where δ_i is the penetration depth $\delta = \frac{1}{3\mu_a \mu_{tr}}$. Relating the irradiance propagating back into the tissue to the irradiance propagating out of the tissue by an effective reflection coefficient gives the boundary condition [40]

$$j(z=0) = A\phi(z=0). \tag{5.8}$$

Here, $A = 0.17$ for a tissue refractive index $n = 1.4$ [40]. The constants A_{ij} are determined by using continuity in $j(z)$ and $\phi(z)$ between each layer and the boundary condition above [40]. The diffuse reflectance R_d is found by [40]

$$R_d = j(z=0). \tag{5.9}$$

The last expression is obtained by considering the irradiance transmitted into the air. It can also be obtained by integrating (5.5), and observing that $j(z = 0)$ represents the difference between the absorbed energy and the incoming energy, leaving the back-scattered energy. The analytic solution for a two-layer model can be found in Svaasand et al. [40]. The one-layer solution is given as

$$R_d = \frac{\mu'_s \cdot A \cdot \delta^2}{(\frac{\delta}{3D} + 1)(D + \delta \cdot A)}. \tag{5.10}$$

The included studies mainly use the isotropic source function solutions above. An alternative source function is the Delta-Eddington source function, which includes more anisotropy and can give more accurate solutions [88].

5.1.3 Inverse modeling

The goal of inverse photon transport modeling is to infer tissue properties from measured light distributions. Well-defined examples include estimation of absorption and scattering properties based on the light distributions obtained in SFDI, and spatially resolved reflectance measurements with source-detector separation.

This can also technically be achieved in reflectance imaging by setting up an objective function e.g. $o = \sum(R_{\text{modeled}}(\lambda_i) - R_{\text{measured}}(\lambda_i))^2$ and minimize with respect to the modeled input parameters. However, the reflectance is scale-invariant with respect to the optical properties in each layer. The one-layer reflectance can be written as $R(\mu_a, \mu_s') = R(\mu_a/\mu_s)$, and similar relations exist for multi-layered media. This limits the information that can be extracted from the spectra without fixating some of the parameters or doing assumptions on the geometry.

The main inverse model developed in this work is an inverse model that can estimate re-epithelialized tissue properties, which is described further in paper II.

5.2 Heat transport modeling

Heat transport modeling was used to model heat propagation in paper VI.

The Pennes bioheat equation [89] is often used to model heat transport in tissue [90–94],

$$K\frac{d^2T}{dx^2} - \rho c\frac{dT}{dt} = (w_{\text{blood}}c_{\text{blood}})(T_{\text{core}} - T) + Q_{\text{metabolism}}. \tag{5.11}$$

The terms respectively describe the change in heat flux, the heat gained by the medium, the heat lost from the medium due to blood circulation, and heat produced by metabolism. Additional heat sources are added to the right hand side. The modeled heat transfer problems during this work involve heat fluxes so large and damages so rapid and extensive that the two terms on the right hand side could be ignored, yielding

$$\frac{d^2T}{dx^2} - \frac{1}{\kappa}\frac{dT}{dt} = 0. \tag{5.12}$$

The diffusivity κ is given as $\kappa = \frac{K}{\rho c}$.

Heat transport modeling was used to characterize the expected temperature development in the burn injuries considered in paper VI. Burns of different severity were induced using different contact times. The temperature was

simulated throughout the contact periods and beyond using the appropriate boundary conditions, and used to characterize the expected damage through an Arrhenius integral,

$$\Omega = \int_0^t P \exp(-\Delta E/RT) dt. \tag{5.13}$$

The used initial conditions and boundary conditions and their associated solutions and usecases are given below. The boundary conditions are illustrated in figure 5.1.

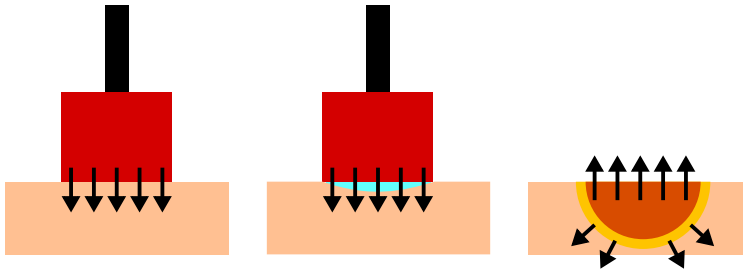

Figure 5.1: The three boundary conditions considered in the heat transport models: Direct contact with metal (left), heat transfer being impeded by an effective surface contact resistance (center) and accumulated heating being propagated throughout the tissue or exchanged with air (right). The figure is reused from paper VI.

Prescribed constant temperature at the surface The initial condition is

$$T(x, t = 0) = T_0 \tag{5.14}$$

and the boundary condition

$$T(x = 0, t) = T_{\text{external}}. \tag{5.15}$$

The solution can be derived using the Laplace transform [95] to yield

$$T(x, t) = (T_{\text{external}} - T_0)\text{erfc}\left(\frac{x}{2\sqrt{\kappa t}}\right) + T_0. \tag{5.16}$$

The solution was used to model direct contact between tissue and metal heated to $T_{\text{external}} = 100\,^{\circ}\text{C}$, as metal is considered to have a high enough conductivity that surface contact resistance can be disregarded [93, 96].

Linear heat transfer at the surface The initial condition is the same as above, but the boundary condition is

$$K\frac{dT}{dx}\bigg|_{x=0} = H(T(x=0,t) - T_{\text{external}}). \tag{5.17}$$

The Laplace transform can again be used to yield [95]

$$T(x,t) = \left[\text{erfc}\left(\frac{x}{2\sqrt{\kappa t}}\right) - \exp(hx + h^2\kappa t)\text{erfc}\left(\frac{x}{2\sqrt{\kappa t}} + h\sqrt{\kappa t}\right)\right](T_e - T_0) + T_0, \tag{5.18}$$

where $h = H/K$. With $H \to \infty$, the solution converges to (5.16). The solution was used to model the temperature evolution when there is a thin interface of steam between the tissue and the metal causing an effective surface contact resistance $R = 1/H > 0$ which impedes heat transfer to the tissue.

Arbitrary start temperature profile, heat exchange with the air at the surface The initial condition is

$$T(x, t=0) = T(x) \tag{5.19}$$

and the boundary condition is the same as (5.17) with $H \to H_{\text{air}}$ and $T_{\text{external}} \to T_{\text{air}}$. Using a Green's function formalism yields the solution [95]

$$T(x,t) = \int_0^\infty u(x', x, t)T(x')dx' + \kappa h \int_0^t u(x'=0, x, t-\tau)T_0 d\tau, \tag{5.20}$$

with

$$u(x', x, t) = \frac{1}{2\sqrt{\pi\kappa t}}\left\{\exp(-(x-x')^2/4\kappa t) + \exp(-(x+x')^2/4\kappa t)\right\} - \ldots$$
$$h\exp(\kappa t h^2 + h(x+x'))\text{erfc}\left\{\frac{x+x'}{2\sqrt{\kappa t}} + h\sqrt{\kappa t}\right\}. \tag{5.21}$$

The solution was used to model the temperature development in the tissue after the metal was lifted.

Chapter 6

Summary and discussion of included work

6.1 Wound model analysis

The main bulk of the thesis work consists of analysis of reflectance and fluorescence hyperspectral images of in vitro wound model samples. The data were acquired by Ingvild Haneberg and Matija Milanic during Haneberg's master thesis work in 2014 [62]. The work here is split in two conference papers (paper IV and V), two journal publications (paper I and II) and one paper draft (paper III). Paper IV and V are supporting work with preprocessing techniques. Paper II concerns the validation of an inverse photon transport model, while the main data analysis is done in paper I and III.

The goal was to detect re-epithelialization and potentially other wound healing processes within the samples using appropriate processing methods on the images. The main motivation was that re-epithelialization should perturb the optical properties and have a recognizable influence on the reflectance spectra. Remodeling of the extracellular matrix might have some influence on the scattering and thus the reflectance, and should have influence on the fluorescence spectra due to changes in the fluorophore distribution. It later became evident that re-epithelialization caused major changes to the fluorescence intensity.

Hyperspectral imaging is a suitable technique for basic research into the relation between the wound healing processes and the reflectance and fluorescence. The full spectral range is available for relation to and understanding of the changes in optical properties, and the spatial resolution gives a context for the spectra. As discussed in paper I and III, it is expected that the work could

result in simpler multispectral systems.

6.1.1 Initial fluorescence analysis

Originally, the focus was on the fluorescence data since they seemed more interesting. The most prominent feature of these data was an apparent fluorescent peak shift from wound to intact tissue. Initially, we thought that the peak shift could be attributed to changes in collagen composition. However, the peak shift was not entirely consistent across the samples and measurement times, and sensor noise combined with wavelength discretization effects made analysis challenging. Further, it was found that noise removal based on MNF led to undesired mixing of the spectra.

Spline methods were tested for extracting the peak positions at a subresolution level in a more objective way. The preliminary analysis here resulted in a conference paper which presented a smoothing splines-based approach with focus on recovery of noise-free spectra (paper IV). Analysis and visualization was hindered by the presence of unwanted background regions, the removal of which is a tedious affair unless automated by e.g. classification methods. Background masking was investigated in paper V, and used as a preprocessing method during fluorescence analysis and the later reflectance analysis.

It became apparent that the shifts in fluorescence could not be explained by changes to the collagen composition alone, and it was suspected that the data were influenced by the optical properties of the tissue. A complete characterization of the reflectance data was therefore necessary in supporting the fluorescence analysis.

6.1.2 Reflectance analysis and final fluorescence analysis

The reflectance characterization showed that the fluorescence results could be related to corresponding changes in the reflectance data rather than intrinsic changes to the collagen composition. The analysis and focus of the work therefore gradually shifted towards analysis of the reflectance data, which resulted in the publication of paper I.

For the conclusions of paper I, and for investigating the correspondence between reflectance and fluorescence, it was necessary to understand the origin of the changes in optical properties from wound to apparent healed and intact skin. This necessitated the development of a specialized photon transport technique. This method was interesting to investigate more fully, and gave rise to a more complete validation and investigation in paper II.

Finally, the results of the fluorescence analysis, in light of the reflectance results, were written up in paper III (draft) along with results on automated wound detection in the reflectance data using both all and a smaller set of wavelengths.

6.1.3 Included manuscripts

Paper I: Characterization of the reflectance data

A. Bjorgan, B. Pukstad, and L. L. Randeberg, "Hyperspectral characterization of re-epithelialization in an in vitro wound model," J. Biophotonics, vol. 13(10):e202000108, 2020

The goal of this paper was to characterize the spectral behavior in the reflectance data. The characterization was used to explain the influence of re-epithelialization on the spectral properties, and understand the feasibility of using hyperspectral imaging to detect re-epithelialization. An overview over the development in optical properties could further be used to understand corresponding changes in the fluorescence.

This paper showed that cluster analysis could discern wounded skin from intact skin and apparent re-epithelialized skin, and used decomposition techniques to show the spectral behavior of either tissue type. Re-epithelialized skin was found to be representable by wound spectral features with a suppression and sloping that could be attributed to an epidermis placed on top of wound-like tissue. Further, a temporal development in the optical properties was found and characterized.

This paper represents basic research into the spectral behavior of the wound model, and is a prerequisite in doing informed development of classification techniques.

Contribution I preprocessed and gained overview over the data, selected analysis methods, did the data analysis and wrote most of the manuscript, with input from and discussion of the results with Lise Lyngsnes Randeberg and Brita Pukstad. Pukstad and Randeberg were involved in the design and planning of the original experiment, and Pukstad prepared the samples. Randeberg and I had discussions on reorganizations of the paper, and we discussed the structure, the presentation and the conclusions.

Paper II: Development of an inverse photon transport model for the upper tissue layer

A. Bjorgan and L. L. Randeberg, "Exploiting scale-invariance: A top layer targeted inverse model for hyperspectral images of wounds," Biomed. Opt. Express, vol. 11(9):5070–5091, 2020

Some of the conclusions in paper I depended on the evaluation of wound reflectance spectra with an epidermal layer added. This evaluation was required for understanding the origin of the changes in the reflectance spectra in the different regions of the images. Such evaluation would normally require modeling of individual constituents and layer compositions in both dermis and epidermis, but this was complicated due to the lack of complete knowledge on the tissue composition and chromophores for the in vitro samples.

Scale-invariance had turned out to be a general obstacle during earlier stages of the thesis work. Faced with the above modeling problem, this led to the realization that the scale-invariance limitation could be used to avoid modeling the wound tissue. By exploiting scale-invariance, the deeper layer of a two-layer model could be set to any absorption/scattering matching the reflectance of the wound tissue, and adding an epidermal layer was simply evaluated by setting epidermal layer properties in the top layer. This was sufficient to understand the spectral properties in paper I, but the technique was interesting by itself, which led to paper II.

The scale-invariance properties and the validity of adding the epidermal layer were investigated by Monte Carlo simulations. It was suspected that also the top layer had a similar scale-invariance, and the uniqueness of the solution was investigated. It was found that some of the parameters had to be fixed, but once fixed, the method represented a useful approach in investigating the property variation of the re-epithelialized tissue layer. We also combined this approach with decomposition of the wound spectra by PCA to more easily represent any wound spectrum by a few number of components, and the final technique ended up as a direct combination of a statistical technique and a physics-based model.

Contribution I came up with the method, set up simulations to test the method and wrote most of the manuscript, with input from Lise Lyngsnes Randeberg. We had discussions on the structure of the manuscript and the presentation and conclusions of the work, and the method and the results.

Paper III: Supervised wound reflectance classification and fluorescence data analysis (manuscript draft)

A. Bjorgan, B. S. Pukstad, and L. L. Randeberg, "Identification of wound healing in an in vitro wound model," To be submitted

Paper I originally included investigation of supervised classification evaluated through cross-validation, in order to demonstrate the utility of the found spectral behavior to separate the tissue types. This quickly fell out of scope, and was combined with the fluorescence analysis in the current paper, focusing solely on identification of wound healing through the use of fluorescence and reflectance hyperspectral imaging.

The hypothesis was that fluorescence could be used to detect changes to the extracellular matrix, and reflectance to detect re-epithelialization, and that the former was detectable by peak shifts. The changes in optical properties identified in paper I co-varied with the peak changes in the fluorescence, however. The inverse model of paper II was used to estimate optical properties in the re-epithelialized parts of the reflectance images, and these were used to show that the peak shift could be attributed to the same change in optical properties. The peak shifts were thus actually a marker of re-epithelialization rather than collagen fluorescence changes. Temporal changes in the fluorescence could further be attributed to corresponding temporal changes identified in paper I.

The fluorescence provided a good visualization of the re-epithelialization, however, and confirms the wound extents found by the reflectance analysis. Further, the fluorescence as a probing tool is interesting since the light sources are effectively placed beneath epidermis, rather than illuminating epidermis and then being back-scattered from dermis.

As for the reflectance analysis, it was found that classification could be performed on a reduced wavelength subset using linear methods like LDA, and that a multispectral system targeting these wavelengths could be feasible.

We decided to wait with submission of this manuscript until the experiment could be repeated with histologies, for testing of the classification algorithms on independent data, and confirmation of the behavior identified in the previous papers. The manuscript is still included in this thesis for completeness.

Contribution I preprocessed and analyzed the fluorescence data, with initial suggestions from Lise Lyngsnes Randeberg on which paths to take. I did the reflectance analysis, and wrote most of the manuscript, with input from and discussion of the results with Lise Lyngsnes Randeberg and Brita Pukstad. Pukstad and Randeberg were involved in the design and planning of the original exper-

iment, and Pukstad prepared the samples. Randeberg and I had discussions on reorganizations of the paper, and we discussed the structure, the presentation and the conclusions.

Paper IV: Smoothing splines for fluorescence spectra

A. Bjorgan and L. L. Randeberg, "Application of smoothing splines for spectroscopic analysis in hyperspectral images," Proc. SPIE, vol. 10873, 2019

Subresolution peak extraction was needed for the initial wound fluorescence analysis in order to remove possible causes for apparent inconsistency in the peak shift estimates. The work resulted in this conference paper. It was presented in a 15 minute talk at SPIE Photonics West 2019.

Any splines method is capable of subresolution peak extraction due to the existence of and possibility for systematization of analytical first and second derivatives. The smoothing splines method is especially suitable due to the objective way it can find a smooth function through noisy data. The paper mainly tested the method for its ability to recover noise-free fluorescence spectra from the data, and compared the results to MNF. Methods were given for how to apply smoothing splines to hyperspectral data and for estimating the tuning parameter for each individual pixel.

We wanted to save the final presentation of the wound fluorescence data for a later journal publication (paper III), and the method was instead applied to autofluorescence data acquired from atherosclerotic plaques. The method was less optimal here since the fluorescence data had coincident absorption peaks in the fluorescence peaks, but the performance was comparable enough.

Paper III found that apparent inconsistencies in the peak estimates could be attributed to corresponding perturbations to the optical properties of the tissue. Applying smoothing splines to extract peak estimates at a sub-resolution level was an important step in verifying that there were systematic changes in the peaks that could not be attributed to noise.

Contribution I identified the method and applied it to the data, and wrote most of the manuscript, with input from Lise Lyngsnes Randeberg. We had discussions of the structure and conclusions of the manuscript and the presentation of the work, and the method and the results.

Paper V: Automatic selection of regions of interest

A. Bjorgan and L. L. Randeberg, "A random forest-based method for selection of regions of interest in hyperspectral images of ex vivo human skin," Proc. SPIE,

vol. 10889, 2019

Building a toolset with modules and tools that could help streamline and automatize data analysis was one of the important parts of the work, and resulted in various Python tools and utilities written in C++. Scripting as much of the data analysis as possible and avoiding manual work was important for speeding up the analysis process.

One of these techniques was to more conveniently remove background from the images and focus on tissue analysis, based on a least-effort procedure. Background removal can be reformulated as a classification problem. Many classification methods are appropriate, but the random forest classifier is particularly interesting since it has few modeling assumptions and is reported to be able to yield good results despite a low number of training data samples, and does not have to be tuned.

In hindsight, more linear/constrained methods like LDA or SVM could have yielded good performance due to the high separation between the background and tissue classes. SVM would require tuning, however, and LDA would fare worse in case of complicated data formations with multiple implicit clusters. Random forest represents something which is easily trained on training samples, and is a least-effort approach to this preprocessing step. The main goal is to quickly segment a few images with similar properties rather than constructing a general method that would work on any future image.

The results were presented as a poster presentation at SPIE Photonics West 2019. The method was also applied to fish data in collaboration with SINTEF Ocean, where fish tissue spectra were extracted across a large dataset containing much background.

Contribution I applied and compared the methods on the data, and wrote most of the manuscript, with input from Lise Lyngsnes Randeberg. We had discussions of the structure, presentation and conclusions of the work, and the methods and the results.

6.2 Burn wound model analysis

Lukasz Paluchowski collected hyperspectral burn wound data as a part of his PhD work in 2014 [21, 71, 72]. Controlled burn wounds were induced in two pigs using heated metal, and hyperspectral images were acquired. The ultimate goal of this experiment was to investigate whether hyperspectral imaging could be used for early separation of superficial and deep partial thickness burns, i.e. different gradings of second degree burns. The hypothesis was that the changes

to collagen and perfusion should have an influence on the reflectance spectra that could be detected, and give a burn severity discrimination performance similar to SFDI. This previously led to a collection of papers which used unsupervised classification to find spectrally similar regions across the images [21] and the development of an inverse photon transport model to estimate scattering and perfusion properties [71].

The results were challenging to interpret, however, in part due to the high heterogeneity of the wounds. We wanted to revisit the data, investigate this more closely by returning to basic principles, and understand the relations in the data rather than attempt to fulfill the original obligation directly. Basic understanding of the data could then be used to understand whether the original goal is feasible. It was desired to make the most of the already collected data rather than subjecting new pigs to the same burn procedure.

Further, understanding the heterogeneity is an interesting application of heat transport modeling. Application of heated metal to the tissue represents a specific boundary condition, and the existence of regions with much lower damage grading within the burn region indicates that the boundary condition is changed. Supervised classification could be used to investigate the full spatial extent of the heterogeneity, which could be related to the burn wound modeling results.

The work here resulted in a single manuscript described below.

6.2.1 Included manuscripts

Paper VI: Analysis of burn data

A. Bjorgan and L. L. Randeberg, "Combining hyperspectral classification and heat transport modeling: An investigation of experimental burn wound heterogeneity," In submission

Only the images collected at the last timepoint were subjected to analysis due to the immediate availability of histology damage gradings. Supervised classification methods were selected based on cross-validation over histology locations. A major result was that classification of the final burn level and vascular damage had low accuracy, whereas collagen damage classification corresponded to natural clusters in the data. Simpler methods like LDA were sufficient for collagen damage classification.

A forward photon transport model along the lines of the model in paper II was used to demonstrate likely changes to the optical properties: Progression of collagen damage could be related to the introduction of a blood-less layer down to a depth. Perfusion properties were thus the main responsible factor

rather than the expected collagen scattering changes. This was in line with a heat transport characterization of the damage types and the literature, where expected damage thresholds for complete destruction to the blood vessels coincides with the collagen destruction.

The final burn level labeled in the histology data was found to be more related to the deepest histological finding for vascular damage than any other of the properties. The hyperspectral data was more related to the collagen damage grading, however. This discrepancy could explain the impaired performance of direct classification on burn level in both the current and previous studies on the same data.

Two alternative boundary conditions to explain the burn heterogeneity were proposed: lowered contact temperature in regions of the metal, and the addition of an impeding steam interface between the metal and the skin. The wound induced at each contact time had both severe and less severe damages present. Arrhenius damage integrals were used to characterize the temperature development necessary to induce the most severe damages, which were then used to estimate necessary changes to the boundary conditions to cause the less severe damages within the same contact time. In light of the extent of the classification maps, the steam interface explanation was found to be more likely. A too-large region with a too-low contact temperature would be required for the lowered contact temperature explanation, which would otherwise be homogenized by the high conductivity of the metal.

Contribution I preprocessed the hyperspectral data and set up classification and cross-validation frameworks, and obtained the hyperspectral analysis results. Lise Lyngsnes Randeberg had the idea for the heat transport model, and suggested boundary conditions, model setup and ideas for how we could associate temperature development with actual damage. I chiseled out the details, did the simulations, gained overview over the histology data and characterized the damage. I wrote most of the manuscript, with contributions from Randeberg. We had discussions on the structure of the manuscript, the results, the conclusions, and how the work should be presented.

Chapter 7

Conclusions and further work

The work in this thesis has been focused around analysis of data collected from two main applications of hyperspectral imaging. One of the major decisions during the work was a move to Python, which enabled use of established machine learning libraries. Use of memory mapping enabled automatic swapping of hyperspectral data in and out of memory and convenient data access. Together with some command line utilities, this enabled fast high-level analysis across full datasets.

The in vitro wound model study found that re-epithelialization caused a suppression and sloping of spectra similar to spectra sampled directly from the wound, in line with the expected re-epithelialization process. The sloping could be used as a feature for classification. An inverse photon transport model was developed specially for characterization of the re-epithelialized layer by exploiting wound spectra and scale-invariance. Fluorescence spectra excited at 355 nm were found to be influenced mainly by optical property changes rather than changes in fluorophores like collagen, confirming that re-epithelialization is the main healing process in this model.

Supervised classification could be applied for collagen damage classification in the burn wound data. These damages were primarily related to what seemed to be perfusion properties higher up in the tissue than the deepest found histological damage. Heat transport modeling was successfully used to characterize the damage, and could support the hyperspectral data analysis and help understand the burn heterogeneity.

The work in this thesis was originally motivated by recent developments and uses of CNNs, but the main focus has been on traditional machine learning techniques. Simpler models are easier to train and understand, and these techniques were found to be sufficient for the tasks at hand. Application to

single pixel spectra further enables attribution to physical processes. CNNs are still a promising path for future studies. Retraining existing networks for image classification to other applications using transfer learning is a viable approach for the available data, which for example could benefit in vitro wound imaging by e.g. training on spatial neighbourhoods at selected wavelengths that enhance contrast of re-epithelialized tissue, but does not enable classification of single pixels by traditional techniques.

The main candidate for future work is the in vitro wound model analysis. The results and the developed techniques are promising, and reduced multispectral systems that can either detect or enhance re-epithelialization could be feasible. The in vitro wound experiment needs repetition with proper collection of histologies, however. Some plans were proposed in paper I, which need follow-up. The developed photon transport model setup is novel, and could further be made usable for in vivo wounds, but this needs more testing.

Appendix A: Software packages

Some of the software developed throughout the work of this thesis has been made available on GitHub (`http://github.com/bjorgan/phd_utils/`). Minor analysis/plotting scripts have not been included here, but can be made available on request. For complete lists and descriptions, see the repository. A general overview is given below.

C++ libraries:

- `libsprectral`: Library for representation of single spectra.
- `libhyperread`: Library for reading hyperspectral data into memory, as memory mapped arrays or to and from stdin/stdout.

Basic C++ command line utilities:

- `hyper_calibrate`: Hyperspectral reflectance calibration, by specified regions or by searching at the start or end of the image for the reflectance standard.
- `hyper_rgb`: Generate RGB images.
- `hyper_cropper`: Crop hyperspectral images.
- `mnf`: Application of the MNF transform.
- `hyview`: Graphical user interface for scrolling through image bands.

The command line utilities were built with support for piping (e.g. `hyper_calibrate image.hyspex | mnf`), and for bulk processing of multiple files (e.g. `hyper_rgb *.hyspex`).

Python modules:

- `hyperread`: Hyperspectral input/output functions. Reads into memory mapped numpy arrays, which enables application of all libraries that support numpy arrays, e.g. scipy, sklearn, ...
- `heat_transfer`: Implementation of heat transport models.
- `mnf`: MNF transform functions.
- `photon_transport`: Functions for obtaining absorption and scattering properties for skin, calculating diffusion model reflectance and some prior work on inverse models.
- `procspec_utils`: Input/output functions for reading OceanOptics ProcSpec files.
- `pymcml`: Python wrapper for MCML and GPU-MCML, compatible with `photon_transport` structures.
- `random_forest`: Wrapper around sklearn's RandomForestClassifier for convenient separation of tissue from background, and a command line utility for bulk separation.
- `region_selector`: Tool for selecting smaller regions from multiple hyperspectral files and collecting the region information in a single file.

Acronyms

CNN Convolutional neural network. 1, 39, 40

DMEM Dulbecco's modified eagle medium. 10

GPU Graphics processing unit. 1, 24

LDA Linear discriminant analysis. 17, 18, 33, 35, 36

MNF Minimum noise fraction. 20, 30, 34, 41, 42

PC Principal component. 20

PCA Principal component analysis. 20, 21, 32

PRSS Penalized residual sum of squares. 17

RGB Red, green, blue. 10, 41

RTE Radiative transport equation. 23

SFDI Spatial frequency domain imaging. 1, 11, 26, 36

SVM Support vector machine. 18, 35

SWIR Short-wave infrared. 12

VNIR Visible to near-infrared. 12

Bibliography

[1] J. M. Schmitt, "Optical coherence tomography (oct): A review," *IEEE J. Sel. Top. Quantum Electron.*, vol. 5(4):1205–1215, 1999.

[2] J. Xia, J. Yao, and L. V. Wang, "Photoacoustic tomography: Principles and advances," *Electromagn. Waves*, vol. 147:1–22, 2014.

[3] T. M. Bydlon, R. Nachabé, N. Ramanujam, H. J. C. M. Sterenborg, and B. H. W. Hendriks, "Chromophore based analyses of steady-state diffuse reflectance spectroscopy: Current status and perspectives for clinical adoption," *J. Biophotonics*, vol. 8(1-2):9–24, 2014.

[4] D. J. Cuccia, F. P. Bevilacqua, A. J. Durkin, F. R. Ayers, and B. J. Tromberg, "Quantitation and mapping of tissue optical properties using modulated imaging," *J. Biomed. Opt.*, vol. 14(2):024012, 2009.

[5] J. P. Angelo, S. Chen, M. Ochoa, U. Sunar, S. Gioux, and X. Intes, "Review of structured light in diffuse optical imaging," *J. Biomed. Opt.*, vol. 24(7):071602, 2018.

[6] G. Lu and B. Fei, "Medical hyperspectral imaging: A review," *J. Biomed. Opt.*, vol. 19(1):010901, 2014.

[7] A. F. H. Goetz, G. Vane, J. E. Solomon, and B. N. Rock, "Imaging spectrometry for earth remote sensing," *Science*, vol. 228(4704):1147–1153, 1985.

[8] A. Plaza, J. A. Benediktsson, J. W. Boardman, J. Brazile, L. Bruzzone, G. Camps-Valls, J. Chanussot, M. Fauvel, P. Gamba, A. Gualtieri, M. Marconcini, J. C. Tilton, and G. Trianni, "Recent advances in techniques for hyperspectral image processing," *Remote Sens. Environ.*, vol. 113(1):S110–S122, 2009.

[9] J. M. Bioucas-Dias, A. Plaza, G. Camps-Valls, P. Scheunders, N. Nasrabadi, and J. Chanussot, "Hyperspectral remote sensing data analysis and future challenges," *IEEE Geosc. Rem. Sen. M.*, vol. 1(2):6–36, 2013.

[10] N. Keshava and J. Mustard, "Spectral unmixing," *IEEE Signal Proc. Mag.*, vol. 19(1):44–57, 2002.

[11] A. A. Gowen, C. P. O'Donnell, P. J. Cullen, G. Downey, and J. M. Frias, "Hyperspectral imaging - an emerging process analytical tool for food quality and safety control," *Trends Food Sci. Tech.*, vol. 18(12):590–598, 2007.

[12] P. Tatzer, M. Wolf, and T. Panner, "Industrial application for inline material sorting using hyperspectral imaging in the nir range," *Real-time Imaging*, vol. 11(2):99–107, 2005.

[13] L. Khaodhiar, T. Dinh, K. T. Schomacker, S. V. Panasyuk, J. E. Freeman, R. Lew, T. Vo, A. A. Panasyuk, C. Lima, J. M. Giurini, T. E. Lyons, and A. Veves, "The use of medical hyperspectral technology to evaluate microcirculatory changes in diabetic foot ulcers and to predict clinical outcomes," *Diabetes Care*, vol. 30(4):903–910, 2007.

[14] M. Denstedt, B. S. Pukstad, L. A. Paluchowski, J. E. Hernandez-Palacios, and L. L. Randeberg, "Hyperspectral imaging as a diagnostic tool for chronic skin ulcers," *Proc. SPIE*, vol. 8565, 2013.

[15] A. Nouvong, B. Hoogwerf, E. Mohler, B. Davis, A. Tajaddini, and E. Medenilla, "Evaluation of diabetic foot ulcer healing with hyperspectral imaging of oxyhemoglobin and deoxyhemoglobin," *Diabetes Care*, vol. 32(11):2056–2061, 2009.

[16] D. Yudovsky, A. Nouvong, and L. Pilon, "Hyperspectral imaging in diabetic foot wound care," *J. Diabetes Sci. Technol.*, vol. 4(5):1099–1113, 2010.

[17] A. Holmer, J. Marotz, P. Wahl, M. Dau, and P. W. Kämmerer, "Hyperspectral imaging in perfusion and wound diagnostic - methods and algorithms for the determination of tissue parameters," *BIOMED ENG-BIOMED TE*, vol. 63(5):547–556, 2018.

[18] M. A. Calin, T. Coman, S. V. Parasca, N. Bercaru, S. R. S., and D. Manea, "Hyperspectral imaging-based wound analysis using mixture-tuned matched filtering classification method," *J. Biomed. Opt.*, vol. 20(4):046004, 2015.

[19] M. A. Calin, S. V. Parascal, D. Manea, and R. Savastru, "Hyperspectral imaging combined with machine learning classifiers for diabetic leg ulcer assessment - a case study," in *MIUA 2019: Medical Image Understanding and Analysis*, vol. 1065, 2019. Pp. 74–85.

[20] G. Daeschlein, I. Langner, T. Wild, S. von Podewils, C. Sicher, T. Kiefer, and M. Jünger, "Hyperspectral imaging as a novel diagnostic tool in microcirculation of wounds.," *Clin. Hemorheol. Microcirc.*, vol. 67(3-4):467–474, 2017.

[21] L. A. Paluchowski, H. B. Nordgaard, A. Bjorgan, S. A. Berget, and L. L. Randeberg, "Can spectral-spatial image segmentation be used to discriminate burn wounds?" *J. Biomed Opt.*, vol. 21(10):101413, 2016.

[22] M. A. Calin, S. V. Parasca, R. Savastru, and D. Manea, "Characterization of burns using hyperspectral imaging technique – a preliminary study," *Burns*, vol. 41(1):118–124, 2015.

[23] L. L. Randeberg, E. L. P. Larsen, and L. O. Svaasand, "Characterization of vascular structures and skin bruises using hyperspectral imaging, image analysis and diffusion theory," *J. Biophotonics*, vol. 3(1-2):53–65, 2010.

[24] M. Halicek, G. Lu, J. V. Little, X. Wang, M. Patel, C. C. Griffith, M. W. El-Deiry, A. Y. Chen, and B. Fei, "Deep convolutional neural networks for classifying head and neck cancer using hyperspectral imaging," *J. Biomed. Opt.*, vol. 22(6):060503, 2017.

[25] H. Akbari, L. Halig, D. M. Schuster, B. Fei, A. Osunkoya, V. Master, P. Nieh, and G. Chen, "Hyperspectral imaging and quantitative analysis for prostate cancer detection," *J. Biomed. Opt.*, vol. 17(7):076005, 2012.

[26] J. Shapey, Y. Xie, E. Nabavi, R. Bradford, S. R. Saeed, S. Ourselin, and T. Vercauteren, "Intraoperative multispectral and hyperspectral label-free imaging: A systematic review of in vivo clinical studies," *J. Biophotonics*, vol. 12(9):e201800455, 2019.

[27] Y. LeCun, Y. Bengio, and G. Hinton, "Deep learning," *Nature*, vol. 521(7553):436–444, 2015.

[28] A. O. H. Gerstner, W. Laffers, F. Bootz, D. L. Farkas, R. Martin, J. Bendix, and B. Thies, "Hyperspectral imaging of mucosal surfaces in patients," *J. Biophotonics*, vol. 5(3):255–262, 2012.

[29] M. Wahabzada, M. Besser, M. Khosravani, M. T. Kuska, K. Kersting, A.-K. Mahlein, and E. Stürm|er, "Monitoring wound healing in a 3d wound model by hyperspectral imaging and efficient clustering," *PLoS One*, vol. 12(12):e0186425, 2017.

[30] Y. Khouj, J. Dawson, J. Coad, and L. Vona-Davis, "Hyperspectral imaging and k-means classification for histologic evaluation of ductal carcinoma in situ," *Front. Oncol.*, vol. 8:17, 2018.

[31] E. J. M. Baltussen, E. N. D. Kok, S. G. B. de Koning, J. Sanders, A. G. J. Aalbers, N. F. M. Kok, G. L. Beets, C. C. Flohil, S. C. Bruin, K. F. D. Kulhmann, H. J. C. M. Sterenborg, and T. J. M. Ruers, "Hyperspectral imaging for tissue classification, a way toward smart laparoscopic colorectal surgery," *J. Biomed. Opt.*, vol. 24(1):016002, 2019.

[32] B. Regeling, W. Laffers, A. O. H. Gerstner, S. Westermann, N. A. Müller, K. Schmidt, J. Bendix, and B. Thies, "Development of an image preprocessor for operational hyperspectral laryngeal cancer detection," *J. Biophotonics*, vol. 9(3):235–245, 2015.

[33] A. Grigoroiu, J. Yoon, and S. E. Bohndiek, "Deep learning applied to hyperspectral endoscopy for online spectral classification," *Sci. Rep.*, vol. 10:3947, 2020.

[34] E. L. Larsen, L. L. Randeberg, E. Olstad, O. A. Haugen, A. Aksnes, and L. O. Svaasand, "Hyperspectral imaging of atherosclerotic plaques in vitro," *J. Biomed. Opt.*, vol. 16(2):026011, 2011.

[35] L. V. Wang and H. Wu, *Biomedical Optics, Principles and Imaging*, 1st edition. John Wiley & Sons, 2007.

[36] T. Spott, "Characterization of layered tissue structures with diffusively propagating photon-density waves," Ph.D. dissertation, NTNU, 1999.

[37] S. L. Jacques, "Optical properties of biological tissues: A review," *Phys. Med. Biol.*, vol. 58(11):R37–R59, 2013.

[38] A. N. Bashkatov, E. A. Genina, and V. V. Tuchin, "Optical properties of skin, subcutaneous, and muscle tissues: A review," *J. Innov. Opt. Health Sci.*, vol. 4(1):9–38, 2011.

[39] T. Spott, L. O. Svaasand, R. E. Anderson, and P. F. Schmedling, "Application of optical diffusion theory to transcutaneous bilirubinometry," *Proc. SPIE*, vol. 3195:234–245, 1998.

[40] L. Svaasand, L. Norvang, E. Fiskerstrand, E. Stopps, M. Berns, and J. Nelson, "Tissue parameters determining the visual appearance of normal skin and port-wine stains," *Laser Med. Sci.*, vol. 10(1):55–65, 1995.

[41] R. Richards-Kortum, "Fluorescence spectroscopy of turbid media," in *Optical-thermal response of laser-irradiated tissue*, A. J. Welch and M. J. C. van Gemert, Eds., 1st edition, Springer, 1995, ch. 20. 667–707.

[42] R. Richards-Kortum and E. Sevick-Muraca, "Quantitative optical spectroscopy for tissue diagnosis," *Annu. Rev. Phys. Chem.*, vol. 47:555–606, 1996.

[43] R. Gillies, G. Zonios, R. R. Anderson, and N. Kollias, "Fluorescence excitation spectroscopy provides information about human skin in vivo," *J. Invest. Dermatol.*, vol. 115(4):704–707, 2000.

[44] R. Na, I.-M. Stender, L. Ma, and H. C. Wulf, "Autofluorescence spectrum of skin: Component bands and body site variations," *Skin Res. Technol.*, vol. 6:112–117, 2000.

[45] G. A. Wagnieres, W. M. Star, and B. C. Wilson, "In vivo fluorescence spectroscopy and imaging for oncological applications," *Photochem. Photobiol.*, vol. 68(5):603–632, 1998.

[46] R. S. DaCosta, H. Andersson, and B. C. Wilson, "Molecular fluorescence excitation-emission matrices relevant to tissue spectroscopy," *Photochem. Photobiol.*, vol. 78(4):384–392, 2003.

[47] F. Gottrup, M. S. Ågren, and T. Karlsmark, "Models for use in wound healing research: A survey focusing on in vitro and in vivo adult soft tissue," *Wound Repair Regen.*, vol. 8(2):83–96, 2000.

[48] T. A. Eikebrokk, B. S. Vassmyr, K. Ausen, C. Gravastrand, and B. Pukstad, "Cytotoxicity and effect on wound re-epithelialization after topical administration of tranexamic acid," *BJS Open*, vol. 3(6):840–851, 2019.

[49] S. Lönnqvist, P. Emanuelsson, and G. Kratz, "Influence of acidic ph on keratinocyte function and re-epithelialisation of human in vitro wounds," *J. Plast. Surg. Hand Surg.*, vol. 49(6):346–352, 2015.

[50] S. Lönnqvist, J. Rakar, K. Briheim, and G. Kratz, "Biodegradable gelatin microcarriers facilitate re-epithelialization of human cutaneous wounds - an in vitro study in human skin," *PLoS ONE*, vol. 10(6):e0128093, 2015.

[51] G. Kratz and C. C. Compton, "Tissue expression of transforming growth factor-β1 and transforming growth factor-αduring wound healing in human skin explants," *Wound Rep. Reg.*, vol. 5(3):222–228, 1997.

[52] E. Nyman, F. Huss, T. Nyman, J. Junker, and G. Kratz, "Hyaluronic acid, an important factor in the wound healing properties of amniotic fluid: In vitro studies of re-epithelialisation in human skin wounds," *J. Plast. Surg. Hand Surg.*, vol. 47(2):89–92, 2013.

[53] A. E. Rizzo, L. A. Beckett, B. S. Baier, and R. R. Isseroff, "The linear excisional wound: An improved model for human ex vivo wound epithelialization studies," *Skin Res. Technol.*, vol. 18(1):125–132, 2012.

[54] G. D. Glinos, S. H. Verne, A. S. Aldahan, L. Liang, K. Nouri, S. Elliot, M. Glassberg, D. C. DeBuc, T. Koru-Sengul, M. Tomic-Canic, and I. Pastar, "Optical coherence tomography for assessment of epithelialization in a human ex vivo wound model," *Wound Rep. Reg.*, vol. 25(6):1017–1026, 2017.

[55] V. Arnoux, C. Come, D. F. Kusewitt, L. G. Hudson, and P. Savagner, "Cutaneous wound reepithelialization: A partial and reversible emt," in *Rise and fall of epithelial phenotype: Concepts of Epithelial-Mesenchymal Transition*, P. Savagner, Ed., 1st edition, Plenum Publishers, 2005, ch. 8.

[56] A. J. Singer and R. A. F. Clark, "Cutaneous wound healing," *N. Engl. J. Med.*, vol. 341(10):738–746, 1999.

[57] J. Cheret, N. Lebonvallet, J. L. Carre, L. Misery, and C. Le Gall-lanotto, "Influence of sensory neuropeptides on human cutaneous wound healing process," *J. Dermatol. Sci.*, vol. 74:193–203, 2014.

[58] K. Jansson, G. Kratz, and A. Haegerstrand, "Characterization of a new in vitro model for studies of reepithelialization in human partial thickness wounds," *In Vitro Cell. Dev. Biol.*, vol. 32(9):534–540, 1996.

[59] G. Kratz, "Modeling of wound healing processes in human skin using tissue culture," *Microsc. Res. Tech.*, vol. 42(1):345–350, 1998.

[60] G. Kratz, M. Lake, and M. Gidlund, "Insulin like growth factor-1 and -2 and their role in the re-epithelialisation of wounds; interactions with insulin like growth factor binding protein type 1," *Scand. J. Plast. Reconstr. Hand Surg.*, vol. 28(2):107–112, 1994.

[61] M. Inoue, G. Kratz, A. Haegerstrand, and M. Ståhle-Bäckdahl, "Collagenase expression is rapidly induced in wound-edge keratinocyte after acute injury in human skin, persists during healing, and stops at reepithelialization," *J. Investig. Dermatol*, vol. 104(4):479–483, 1995.

[62] I. J. A. Haneberg, "Hyperspectral imaging of in vitro wound models from human skin," M.S. thesis, Norwegian University of Science and Technology, 2014.

[63] R. R. Seeley, T. D. Stephens, and P. Tate, *Essentials of Anatomy and Physiology*, 6th edition. McGraw-Hill Publishing Co., 2006.

[64] A. Ponticorvo, D. M. Burmeister, B. Yang, B. Choi, R. J. Christy, and A. J. Durkin, "Quantitative assessment of graded burn wounds in a porcine model using spatial frequency domain imaging (sfdi) and laser speckle imaging (lsi)," *Biomed. Opt. Express*, vol. 5(10):3467–3481, 2014.

[65] A. Mazhar, S. Saggese, A. C. Pollins, N. L. Cardwell, L. Nanney, and D. J. Cuccia, "Noncontact imaging of burn depth and extent in a porcine model using spatial frequency domain imaging," *J. Biomed. Opt.*, vol. 19(8):086019, 2014.

[66] D. M. Burmeister, A. Ponticorvo, B. Yang, S. C. Becerra, B. Choi, A. J. Durkin, and Chri, "Utility of spatial frequency domain imaging (sfdi) and laser speckle imaging (lsi) to non-invasively diagnose burn depth in a porcine model," *Burns*, vol. 41(6):1242–1252, 2015.

[67] M. Kaiser, A. Yafi, M. Cinat, B. Choi, and A. J. Durkin, "Noninvasive assessment of burn wound severity using optical technology: A review of current and future modalities," *Burns*, vol. 37(3):377–386, 2011.

[68] H. Hoeksema, K. Van de Sijpe, T. Tondu, M. Hamdi, K. Van Landuyt, P. Blondeel, and S. Monstrey, "Accuracy of early burn depth assessment by laser doppler imaging on different days post burn," *Burns*, vol. 35(1):36–45, 2009.

[69] A. D. Jaskille, J. C. Ramella-Roman, J. W. Shupp, M. H. Jordan, and J. C. Jeng, "Critical review of burn depth assessment techniques: Part ii. review of laser doppler technology," *J. Burn Care Res.*, vol. 31(1), 151-157, 2010.

[70] S. Thomsen and J. A. Pearce, "Thermal damage and rate processes in biologic tissues," in *Optical-Thermal Response of Laser-Irradiated Tissue*, A. J. Welch and M. J. C. van Gemert, Eds., 2nd edition, Springer, 2011, ch. 13.

[71] L. A. Paluchowski, A. Bjorgan, H. B. Nordgaard, and L. L. Randeberg, "Spectral-spatial classification combined with diffusion theory based inverse modeling of hyperspectral images," *Proc. SPIE*, vol. 9689, 2016.

[72] L. A. Paluchowski, "Characterization of biological tissue using statistical and physics-based hyperspectral image processing methods," Ph.D. dissertation, NTNU, 2018.

[73] A. Papp, K. Kiraly, M. Harma, T. Lahtinen, A. Uusaro, and E. Alhava, "The progression of burn depth in experimental burns: A histological and methodological study," *Burns*, vol. 30(7):684–690, 2004.

[74] T. Hastie, R. Tibshirani, and J. Friedman, *The elements of statistical learning*, 2nd edition. Springer, 2009.

[75] G. James, D. Witten, T. Hastie, and R. Tibshirani, *An introduction to statistical learning*, 1st edition. Springer, 2013.

[76] I. Goodfellow, Y. Bengio, and A. Courville, *Deep learning*. MIT Press, 2016.

[77] L. Breiman, "Random forests," *Machine Learning*, vol. 45:5–32, 2001.

[78] F. Melgani and L. Bruzzone, "Classification of hyperspectral remote sensing images with support vector machines," *IEEE Trans. Geosci. Remote Sens.*, vol. 42(8):1778–1790, 2004.

[79] Y. Tarabalka, M. Fauvel, J. Chanussot, and J. A. Benediktsson, "Svm- and mrf-based method for accurate classification of hyperspectral images," *IEEE Geosci. Remote. Sens. Lett.*, vol. 7(4):736–740, 2010.

[80] G. Camps-Valls and L. Bruzzone, "Kernel-based methods for hyperspectral image classification," *IEEE Trans. Geosci. Remote Sens.*, vol. 43(6):1351–1362, 2005.

[81] G. Shaw and D. Manolakis, "Signal processing for hyperspectral image exploitation," *IEEE Signal Process. Mag.*, vol. 19(1):12–16, 2002.

[82] J. Khodr and R. Younes, "Dimensionality reduction on hyperspectral images: A comparative review based on artificial datas," in *2011 4th International Congress on Image and Signal Processing*, IEEE, 2011. Pp. 1875–1883.

[83] M. D. Farrell and R. M. Mersereau, "On the impact of pca dimension reduction for hyperspectral detection of difficult targets," *IEEE Geosci. Remote Sens. Lett.*, vol. 2(2):192–195, 2005.

[84] A. A. Green, M. Berman, P. Switzer, and M. D. Craig, "A transform for ordering multispectral data in terms of image quality with implications for noise removal," *IEEE Trans. Geosci. Remote Sensing*, vol. 26(1):65–74, 1988.

[85] L. Wang, S. L. Jacques, and L. Zheng, "Mcml monte carlo modeling of light transport in multi-layered tissues," *Comput. Meth. Prog. Bio.*, vol. 47(2):131–146, 1995.

[86] E. Alerstam, W. C. Y. Lo, T. D. Han, J. Rose, S. Andersson-Engels, and L. Lilge, "Next-generation acceleration and code optimization for light transport in turbid media using gpus," *Biomed. Opt. Express*, vol. 1(2):658–675, 2010.

[87] A. Bjorgan and L. L. Randeberg, "Exploiting scale-invariance: A top layer targeted inverse model for hyperspectral images of wounds," *Biomed. Opt. Express*, vol. 11(9):5070–5091, 2020.

[88] T. Spott and L. O. Svaasand, "Collimated light sources in the diffusion approximation," *Appl. Opt.*, vol. 39(34):6453–6465, 2000.

[89] H. H. Pennes, "Analysis of tissue and arterial blood temperature in the resting human forearm," *J. Appl. Physiol.*, vol. 1(2):93–122, 1948.

[90] T. Log, "Modeling skin injury from hot spills on clothing," *Int. J. Environ. Res. Public Health*, vol. 14(11):1374, 2017.

[91] E. Y.-K. Ng and L. T. Chua, "Prediction of skin burn injury. part 1: Numerical modelling," *Proc. Inst. Mech. Eng. H.*, vol. 216(3):157–170, 2002.

[92] K. R. Diller and L. J. Hayes, "A finite element model of burn injury in blood-perfused skin," *J. Biomed. Eng.*, vol. 105(5):300–307, 1983.

[93] N. N. Johnson, J. P. Abraham, Z. I. Helgeson, W. J. Minkowycz, and E. M. Sparrow, "An archive of skin-layer thicknesses and properties and calculations of scald burns with comparisons to experimental observations," *J. Thermal Sci. Eng. Appl*, vol. 3(1):011003, 2011.

[94] M. Fu, W. Weng, and H. Yuan, "Numerical simulation of the effects of blood perfusion, water diffusion, and vaporization on the skin temperature and burn injuries," *Numer. Heat Tr. A-Appl.*, vol. 65(12):1187–1203, 2014.

[95] H. S. Carslaw and J. C. Jaeger, *Conduction of heat in solids*, 2nd edition. Oxford science publications, 1959.

[96] K. Buettner, "Effects of extreme heat and cold on human skin. i. analysis of temperature changes caused by different kinds of heat application," *J. Appl. Physiol.*, vol. 3(12):691–702, 1951.

Paper I

A. Bjorgan, B. Pukstad, and L. L. Randeberg, "Hyperspectral characterization of re-epithelialization in an in vitro wound model," *J. Biophotonics*, vol. 13(10):e202000108, 2020. DOI: `https://doi.org/10.1002/jbio.202000108`

Received: 24 March 2020 | Revised: 27 May 2020 | Accepted: 11 June 2020
DOI: 10.1002/jbio.202000108

FULL ARTICLE

JOURNAL OF BIOPHOTONICS

Hyperspectral characterization of re-epithelialization in an in vitro wound model

Asgeir Bjorgan[1*] | **Brita S. Pukstad**[2,3] | **Lise L. Randeberg**[1]

[1]Department of Electronic Systems, NTNU Norwegian University of Science and Technology, Trondheim, Norway

[2]Department of Clinical and Molecular Medicine, NTNU Norwegian University of Science and Technology, Trondheim, Norway

[3]Department of Dermatology, St. Olavs Hospital, Trondheim University Hospital, Trondheim, Norway

***Correspondence**
Asgeir Bjorgan, Department of Electronic Systems, NTNU, NO-7491 Trondheim, Norway.
Email: asgeir.bjorgan@ntnu.no

Abstract

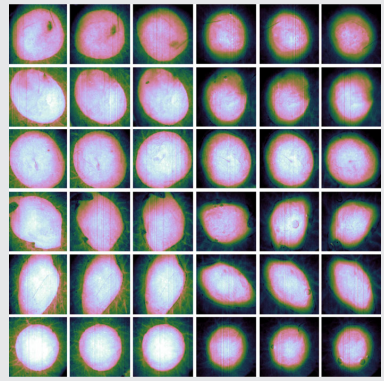

In vitro wound models are useful for research on wound re-epithelialization. Hyperspectral imaging represents a non-destructive alternative to histology analysis for detection of re-epithelialization. This study aims to characterize the main optical behavior of a wound model in order to enable development of detection algorithms. *K*-Means clustering and agglomerative analysis were used to group spatial regions based on the spectral behavior, and an inverse photon transport model was used to explain differences in optical properties. Six samples of the wound model were prepared from human tissue and followed over 22 days. Re-epithelialization occurred at a mean rate of 0.24 mm^2/day after day 8 to 10. Suppression of wound spectral features was the main feature characterizing re-epithelialized and intact tissue. Modeling the photon transport through a diffuse layer placed on top of wound tissue properties reproduced the spectral behavior. The missing top layer represented by wounds is thus optically detectable using hyperspectral imaging.

KEYWORDS

exploratory data analysis, hyperspectral imaging, image processing, photon transport modeling, re-epithelialization, tissue optics, wound healing

1 | INTRODUCTION

Standardized in vitro wound models are useful for controlled investigation of re-epithelialization [1, 2], as systematic research on in vivo wounds is otherwise ethically challenging to carry out. Samples are typically subjected to destructive histology analysis in order to evaluate re-epithelialization, which makes it difficult to follow the same sample over time. Optical techniques like hyperspectral imaging could provide a non-destructive and non-contact alternative.

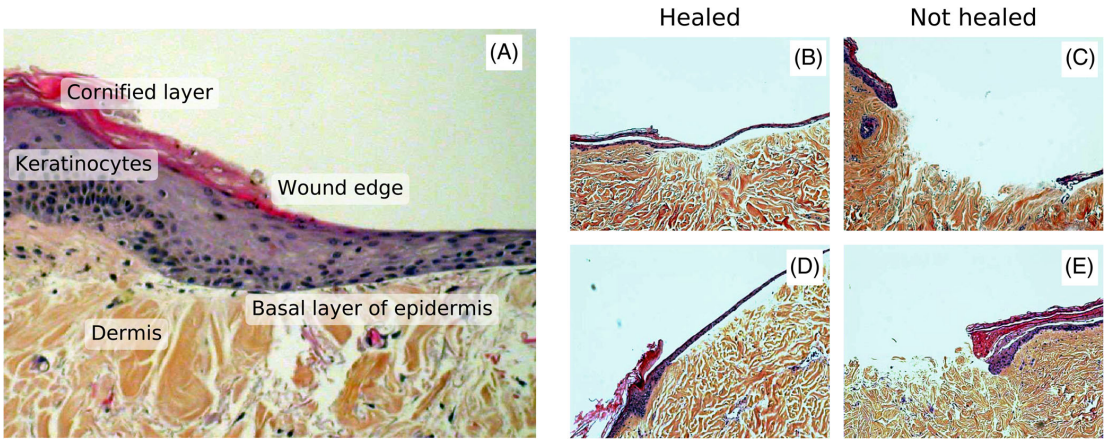

FIGURE 1 Histologies from an unpublished study on a wound model similar to the wound model used in this paper: Day 7 of a re-epithelialized sample (A, ×20 magnification), day 8 from re-epithelialized samples (B, D, ×10 magnification) and day 8 from non-healing samples (C, E, ×10 magnification). The samples here were cut using 6 mm punch biopsy, wounds prepared using 3 mm punch biopsy. The medium consisted of 1 mL DMEM with 10% FCS and penicillin and streptomycin added. Non-healing samples were treated with 10 μM CpG B

A spectral dimension that enables spectroscopy, combined with a high spatial resolution suitable for imaging of heterogeneous structures makes hyperspectral imaging relevant for a wide range of biomedical applications [3]. Examples include wound imaging [3–11], burn wound imaging [9, 12], skin bruises [13], cancer diagnostics and surgical guidance [3, 14]. The large amounts of data generated by the technique require methods for extracting relevant information. These methods should avoid subjective evaluation and be automatic in order to alleviate the effort in handling the data. The overall aim of this study is thus the development of automated analysis methods to enable use of hyperspectral imaging for in vitro wound applications. Histologies were not available for the current study, which somewhat limits the conclusions that may be drawn. The focus of the current paper is therefore on observations of the optical behavior in the available hyperspectral dataset.

Wound healing is a complex multistep process, which involves triggers and biological mechanisms that are fully outlined in Singer et al. [15] and Arnoux et al. [16]. Keratinocytes migrate into the wound from the surrounding tissue a few hours after the injury [15, 16]. The keratinocytes start generating new epidermal cells after 1 to 2 days [15]. The re-epithelialization happens simultaneously with a remodeling of the collagen matrix due to the migration of fibroblasts into the wound [15, 16].

The wound model used in this study is based on an in vitro model setup developed by Jansson et al. [17] and Kratz [2]. Their standardized model consists of circular 6 mm diameter samples of human breast tissue or abdominal tissue that are prepared with 3 mm diameter wounds using punch biopsy. These consistently re-epithelialize by day 7 when embedded in Dulbecco's Modified Eagle Medium (DMEM) containing 10% fetal calf serum (FCS) with streptomycin (50 U/mL) and penicillin (50 μg/mL) added [2, 17–22]. Both partial thickness wounds (epidermis + superficial dermis) [17, 18] and full thickness wounds (1-mm depth) [2, 19] re-epithelialize by day 7 under these conditions. Samples completely submerged in medium were found to be covered by a single cell layer of keratinocytes over the 7 days, which then started to stratify into a thicker epidermis [2]. Jansson et al. [17] showed that submerged wounds and samples with the wounds exposed to air had similar time-course of the re-epithelialization. Exposed wounds had migration of more than one cell layer and a neoepidermis more resembling a normal human epidermis by day 7 [17]. Samples of a submerged model are shown in Figure 1 for illustrational purposes. Here, the healing wounds are covered by keratinocytes after 7 days. Variations over this wound model in similar media have been studied, for example, 4 mm wounds in 12 mm skin samples (48% closure by day 4, 66% closure by day 16) [23] and 4 mm wounds in 6 mm skin samples (52% closure by day 7, above 80% closure by day 12) [24].

Some prior work on optical characterization of in vitro wound models exist. A similar wound model was characterized using fluorescence imaging by Wang et al. [23, 25] This study considered intrinsic fluorescence emission at excitation/emission wavelengths 335/390 nm (collagen) and 295/340 nm (tryptophan). This was done in order to investigate re-epithelialization by epidermal extinction of fluorescent collagen emission from dermis, and

proliferation activity in the newly formed epidermis by tryptophan emission. The current study does not consider fluorescence, but reflectance from a normal light source in the visible range. However, mechanisms influencing the reflectance would be similar to the mechanisms influencing the lack of collagen fluorescence emission in the re-epithelialized regions. Randeberg et al. [26] did initial characterization of hyperspectral images of a previous iteration of the wound model used in this study. This initial analysis was limited to considerations using the cosine distance and sample spectra. The current study seeks to do more in-depth analysis using other statistical techniques and extend the analysis by inverse photon transport modeling. Finally, a 3D wound model constructed using collagen and keratinocytes was characterized using hyperspectral imaging by Wahabzada et al. [27]. This represents a different type of wound model, and mainly the fibroblast migration activity rather than re-epithelialization was correlated with the hyperspectral data. The current study uses similar cluster analysis to analyze the data.

A hyperspectral imaging setup typically acquires reflectance spectra, that is, the amount of light reflected and back-scattered off the imaged samples at different wavelengths. The ability of the hyperspectral system to sense changes in the wounds is dependent on the ability of these changes to influence the reflectance. The reflectance is determined by the optical properties of the tissue, which is typically modeled as a multilayer structure with absorption and scattering coefficients $\mu_a(\lambda)$ and $\mu_s(\lambda)$ in each layer [28–31].

The high spatial and spectral resolution of hyperspectral datasets requires special techniques to handle the large amounts of information. Common processing techniques for biomedical hyperspectral imaging in the literature include clustering analysis [5, 12, 27, 32–34], use of decomposition or dimensionality reduction methods [9, 32, 33] and supervised classification [10, 35–37]. Unsupervised cluster analysis is a first choice to group similar reflectance spectra. Such analysis serves to break apart the dataset and infer properties about wound, re-epithelialized and intact tissue over time, and discern the measurable optical differences of these tissues. Decomposition methods like Principal component analysis (PCA) can be used to investigate the spectral properties in a low-dimensional space. Supervised classification techniques are useful for building classification models to identify samples as wound or intact tissue based on training samples. Such methods yield classification rules that can be investigated and compared against the similarity-based unsupervised analysis results.

In this paper, all these techniques are in combination used to infer the properties of the different types of tissue over time. This is valuable as a part of exploratory data analysis. However, understanding the clustering or classification is important for understanding their general applicability. Explanations are not readily offered up by these statistical methods alone. Photon transport modeling serves as a tool to understand the physics and relate the statistical results and measurable responses in reflectance back to changes in scattering and absorption, and finally changes in skin constitution. The main feature separating wound from re-epithelialized or intact tissue is missing upper layers. These layers are therefore of special interest for characterization of re-epithelialization.

For a semi-infinite, one-layered model, it can be argued that the reflectance can be written as a function of μ_a/μ_s [38]. The same is valid for the semi-infinite layer of an N-layer model. This means that such a model is uniquely defined only down to ratios between the absorption and scattering coefficients of the semi-infinite layer. It is desired to see whether re-epithelialized tissue can be explained by some absorbing and scattering layer added on top of a model representing the optical properties of wound. This can be done without having to completely inverse-model the wound, by exploiting the scale-invariance of the reflectance model.

The combination of statistical methods and photon transport modeling serves to make hyperspectral imaging a promising non-destructive technique for characterization of in vitro wound models. In Section 2, sample preparation and the image acquisition procedure are outlined. The PCA method, proposed clustering method and supervised classification methods used for exploration of the dataset, and the inverse modeling method, are given in Section 3. Results of the clustering and the investigation using PCA and inverse photon transport modeling are then given in Section 4.

2 | MODEL PREPARATION AND DATA ACQUISITION

Reflectance data were acquired using a push-broom Hyspex VNIR-1600 hyperspectral camera (Norsk Elektro Optikk, Lillestrom, Norway). The images were acquired over the wavelength range 400 to 1000 nm, with a spectral resolution of 3.7 nm. The pixel size on the sample surface was approximately 24×24 μm. The camera system acquires one line of the image at a time with an acquisition time of 7.5 ms per line. A full image was acquired by moving the samples under the camera on a translation stage. Raw images containing three wells and a reflectance standard consisted of 6300 image lines, resulting in a total acquisition time of approximately 47 seconds. A tissue sample with diameter 8 mm

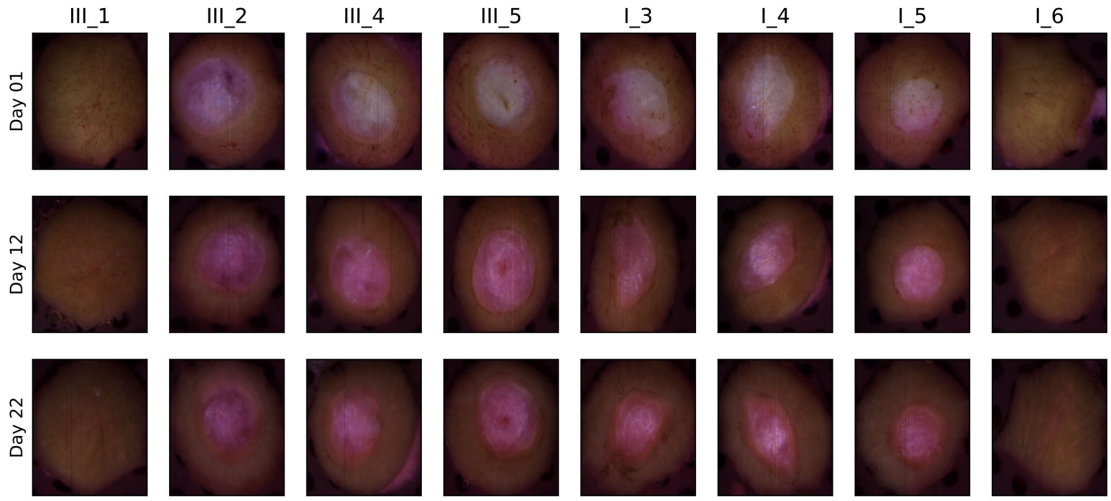

FIGURE 2 RGB images of all samples at day 1, 12 and 22, constructed using the 615, 564 and 459 nm wavelength bands of the hyperspectral images. Models with label III_* consist of one intact sample (III_1) and the samples prepared with 4 mm wounds, while samples with label I_* consist of one intact sample (I_6) and the samples prepared with 3 mm wounds

would have an individual acquisition time of 2.5 seconds.

The reflectance data were acquired with illumination from two linear light sources (Model 2900 Tungsten Halogen, Illumination Technologies, New York). Polarizers (VLR-100 NIR, 450-1100 nm, Meadowlark Optics, Frederick, Colorado) were mounted on the camera lens and the light sources in order to avoid specular reflection. A Spectralon reflectance target (WS-1-SL, Ocean Optics, Duiven, Netherlands) was included within each image.

The samples were prepared from human abdominal skin collected from a single donor during plastic surgery. The project was approved by the regional ethical committee (REK-Midt-Norge), and informed consent was obtained from the donor.

Six samples of the wound model and two tissue samples without wounds were prepared, all with total sample diameter of 8 mm. Wounds were cut into the tissue using 3 mm punch biopsy on three of the samples, and 4 mm punch biopsy on the other three samples. Wounded tissue was lifted using suction for the former three samples, and a cannula for the latter three samples, and cut using scissors. Final samples were cut out from the donor tissue using 8 mm punch biopsy. Due to heterogeneity resulting from the sample preparation, the 3 mm wounds are not circular and do not strictly have 3 mm diameter. For simplicity, these are still referred to as 3 mm wounds.

The samples were placed in separate wells, on metallic grids in order to avoid submersion of the samples. The wells were filled with Dulbecco's Modified Eagle Medium (Gibco), with fetal calf serum (10%), penicillin (50 μg/mL), streptomycin (50 U/mL) and glutamine added. The medium was changed after each imaging session. For more details on the wound preparation, see Haneberg [39].

The samples were followed up over a period of 22 days. Images were acquired at day 1, 2 and then every other day, yielding a total of 12 measurements for every sample. RGB images over all samples are shown in Figure 2, along with labels used in this paper. RGB images are shown at the start, mid and end of the measurement period in order to give an overview over the available data. The samples were sorted in two trays (tray I and III) and inherited the same labeling as the trays for convenience. The samples with label III_* correspond to 4 mm biopsy wounds, while samples with label I_* correspond to 3 mm biopsy wounds. One each of the samples without wounds were sorted along with the 4 mm and 3 mm wounds, respectively. The intact samples were included in order to evaluate shrinking. These are not considered throughout the rest of this paper.

The raw spectra were converted to reflectance, and the images were subset to regions with size 600×600 pixels centered on each sample. The tissue samples were segmented from the background using a random forest classifier, which has been tested for this purpose in a previous study [40]. The classifier was trained on manually labeled regions from sample I_5 at days 1, 16 and 22. Manually selected regions containing both wound and intact tissue were labeled as 'tissue', and non-tissue regions as 'background'.

3 | PROCESSING METHODS

3.1 | Principal component analysis

PCA decomposes a dataset of size N observations $\times$ p features in terms of p orthonormal components (loadings), which transform each mean-subtracted observation into new variance-maximizing coordinates (scores) by a linear combination between the components and the original features [41].

This method is used for dimensionality reduction before clustering and for inference of important spectral features in the wound model. In total, three main PCA models will be constructed throughout this paper:

- As a pre-processing method in order to reduce the dataset before clustering, one PCA model for each trained clustering model.
- For investigation of spectral features of the samples and corroboration of the clustering results. This model was trained on wound and intact tissue at days 1, 2, 6, 12 and 22 across all samples.
- For summarizing the temporal-spatial developments within the wounds. This model was trained on wound spectra only, across all measurement times and samples.

3.2 | Unsupervised clustering analysis

K-means clustering was used to cluster the pre-processed data using a high number of clusters ($K = 25$). The single linkage distance was found between each possible pair of clusters, that is, the distance between the two closest points of each pair. The distances between cluster i and all possible clusters j were organized in a 25×25 distance matrix and subjected to agglomerative analysis, in order to combine the 25 clusters down to two spectrally distinct clusters.

A clustering model was trained for each single sample across all measurement time points, as illustrated in Figure 3. The use of K-Means as the core method enables classification of unseen data. Each trained clustering model could therefore be used to classify all other samples according to its cluster definitions. This was done in order to reduce computational requirements, investigate the stability of the approach by varying the subjected dataset, and finally increase the robustness by combining the assigned clusters through a majority vote.

The images were found to have level variations in the obtained spectra due to changes in illumination. The clustering was found to yield clusters corresponding to different illumination conditions rather than spectral changes unless the level changes were properly suppressed. Spectral derivatives have earlier been used in spectroscopy [42] and hyperspectral imaging [43–47] as a preprocessing technique to better target interesting spectral features rather than level or illumination variations. The first order spectral derivative of a reflectance spectrum $y(\lambda)$ is given as $y'(\lambda) = \frac{dy(\lambda)}{d\lambda}$. For simplicity, the derivatives throughout the paper are taken with respect to the band index rather than the wavelength λ.

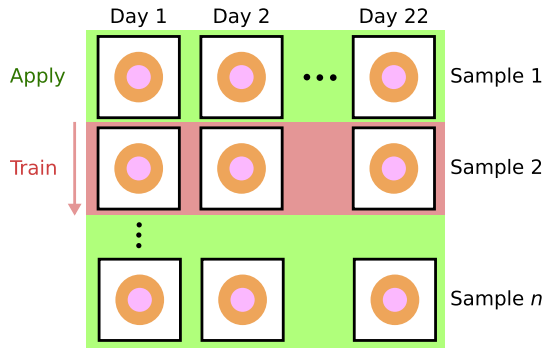

FIGURE 3 Clustering setup: the clustering method is trained on all measurements of a sample and applied to the rest of the samples, producing a variation in the final clustered regions

Smooth numerical estimates of the derivatives can be obtained by Savitzky-Golay filtering [48]. The filter essentially fits polynomial functions to the data in a sliding-window fashion, which can be efficiently implemented as a convolution operation. Third degree polynomials and a window length of 21 were used in the filter. These parameters were by visual inspection found to yield smooth enough spectra (low variance) without smoothing over important spectral features (low bias). The derivative filter was followed by a PCA transform in order to reduce the dimensionality of the data, before clustering finally was applied.

3.3 | Supervised classification

A random forest classifier [49, 50] is used as a standard classification method, as it is simple and sufficiently robust without needing special pre-processing treatments, parameter tuning or many assumptions on the data [49–53]. The classification method can in addition compute feature importances, and show which wavelengths are used the most during classification, which is valuable for further exploration of the data.

The classification model was trained on examples of wound and intact skin from a single wound model sample across all measurement times, and its wound boundaries were compared against the boundaries obtained from the clustering analysis. The method was trained and

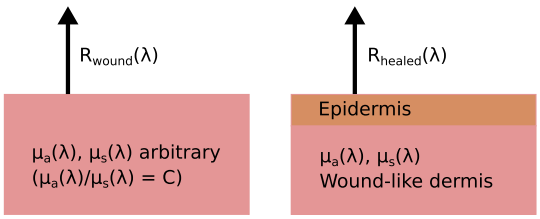

FIGURE 4 Inverse modeling procedure. A one-layered model is first fitted to the wound reflectance. Due to scale-invariance considerations, the effect of adding an epidermis on top of the wound tissue is evaluated by reusing these optical parameters in a two-layer model

compared on the reflectance spectra and the first and second derivatives of the spectra.

3.4 | Inverse photon transport modeling

It is desired to investigate whether the optical properties of apparently re-epithelialized tissue can be explained by the optical properties of wound with some extra layer on top that represents epithelium. This is done in order to strengthen the findings of the statistical analysis.

The scale-invariance of the one-layer model enables the wound to be represented by any μ_a and μ_s which obey the given ratio that reproduces the wound reflectance. Inserting these properties into the semi-infinite layer of a two-layer model lets the boundary conditions of the upper layer be the same as they would be against some arbitrary multilayer model representing wound. This then enables investigation of an upper layer without having knowledge of the constituent layers of the wound tissue.

In practice, the following algorithm is used:

1 Pick a wound reflectance spectrum.
2 Use a semi-infinite, one-layer model to estimate μ_a/μ_s.
3 Assume some μ_s, reuse μ_a, μ_s in a two-layer model to reproduce the correct boundary conditions between the first and second layers of the two-layer model.
4 Find the properties of the first layer by minimization of $\sum \left(\frac{R-R_{meas}}{R_{meas}}\right)^2$.

The properties of the first layer will not be unique. The approach is mainly used to show that some diffuse layer with the correct ratios can be added on top of the wound tissue properties to yield the reflectance from re-epithelialized tissue. The basic geometry of the approach is shown in Figure 4.

4 | RESULTS AND DISCUSSION

The clustering model is first presented and established in Section 4.1 by use of RGB images, principal component analysis and supervised analysis. The apparent clustering rules are investigated in Section 4.2 using an inverse photon transport model to characterize optical properties. The temporal development in optical properties of the samples is characterized in Section 4.3. The main results are finally summarized and discussed in Sections 4.4 and 4.5.

4.1 | Establishing a spectral clustering model

4.1.1 | Comparison of clustering results and RGB images

In lieu of histologies and until a spectral behavior has been established, visual indicators of re-epithelialization must first be established. Close-ups of the RGB images for days 2 and 22 for sample III_5 are shown in Figure 5, with the original wound boundary indicated with arrows in both figures. The general behavior was visually similar for the other samples.

For day 2, the outline of the wound is indicated by a transition from a brown to a pink area. The same outline can be observed in day 22, but now as a darker brown line which divides two similarly brown areas. This brown area gradually transitions to a pink area. Clear pink areas are assumed to correspond to non-healed wound tissue, brown areas within the darker outline are assumed to be tissue which has undergone re-epithelialization, while skin outside the darker outline is intact tissue. This establishes: (1) the sample has likely partially re-epithelialized, with a new apparent wound boundary well within the original wound boundary, and (2) some basic markers for verifying, for example, a clustering model by visual inspection. It can be seen here that the old wound boundary at day 22 has similar extent as the original wound boundary, indicating that there has been no or minimal wound contraction.

Boundaries obtained from each clustering model as applied to sample III_5 are shown in Figure 6. Most of the clustering models agree on a given boundary across the various samples. The disagreement is somewhat larger at day 1. Mean distance between the majority vote boundary and the boundaries of the respective clusters is 3.94 pixels at day 1 (standard deviation (SD) 9.97 pixels), and 1.62 pixels at day 2 to 22 (SD 2.46 pixels) across all wound model samples. Corresponding statistics for the shown sample (III_5) are 2.34 pixels (SD 3.51 pixels) for day 1 and 1.22 pixels (SD 1.52 pixels) for day 2 to 22.

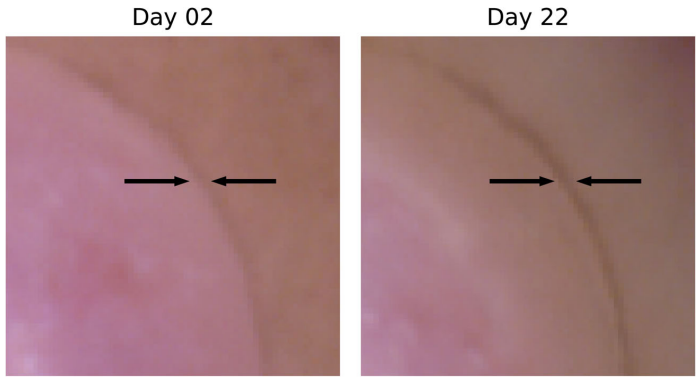

FIGURE 5 Positions of the original wound boundary as determined by RGB images constructed from the hyperspectral images at the 615, 564 and 459 nm wavelength bands, at day 2 and 22 for sample III_5. The new wound boundary at day 22 is somewhere along the unclear, fuzzy region to the left of the original boundary. The image values were raised to the power of 0.4 in order to brighten the darker details

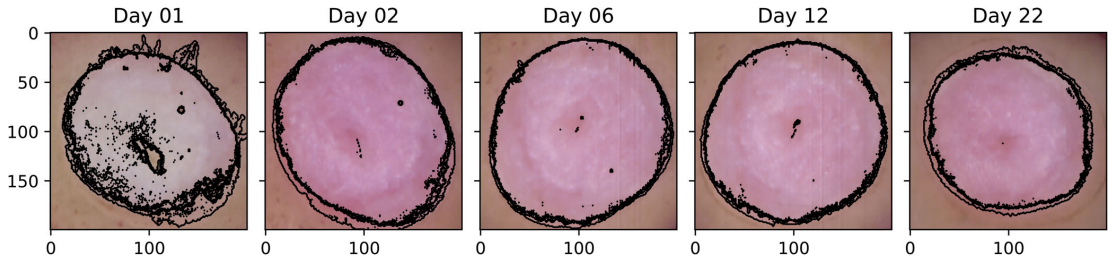

FIGURE 6 The six cluster boundaries for sample III_5 across day 1, 2, 6, 12 and 22. All boundaries are plotted in black in order to enhance contrast, and the variation in the borders is mainly shown through the thickness of the combined boundaries

Increases in both mean and SD at day 1 demonstrate a higher uncertainty in the boundary. There are indications of somewhat lower boundary deviations at day 8 to 14 (mean 1.36 pixels, SD 1.93 pixels) which increase back to day 2 to 6 levels towards day 22. This is visually consistent with the behavior illustrated for sample III_5 in Figure 6, where a single cluster model boundary encompasses a larger area than the rest of the boundaries at day 22 but stays consistent with the rest of the boundaries at day 6 and 12.

Across all samples, all models generally agree on a cluster boundary well within the marks indicating the original wound boundary, except for the first day, and most of the boundaries encompass regions that can be established by visual inspection to be the wound. The regions within boundaries represented by this cluster are therefore likely to correspond to non-reepithelialized wound tissue.

For the shown sample (III_5), the region encompassed by the boundary is smaller than the expected size of the wound at day 1. The region size increases towards day 8. This it at odds with the expected wound development. Inspection of the left-out regions reveals brown spots present only in the intact skin regions, and a separate clustering run on day 1 gave only minor differences to the cluster boundary. The left-out regions are probably thus an artifact from the wound preparation, where there has been removal of dermal tissue with some epidermal tissue remaining.

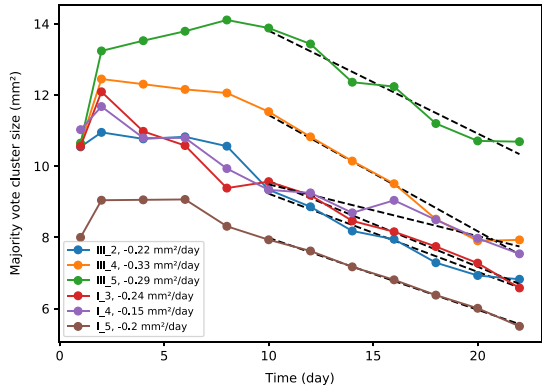

FIGURE 7 Majority vote cluster size as a function of day. Linear fits from day 10 and on are marked with dotted lines, and slopes/re-epithelialization rates are written in the figure legend

The majority vote cluster size as a function of day is shown in Figure 7 for all samples. All samples have an increase in the apparent wound region from day 1 to day

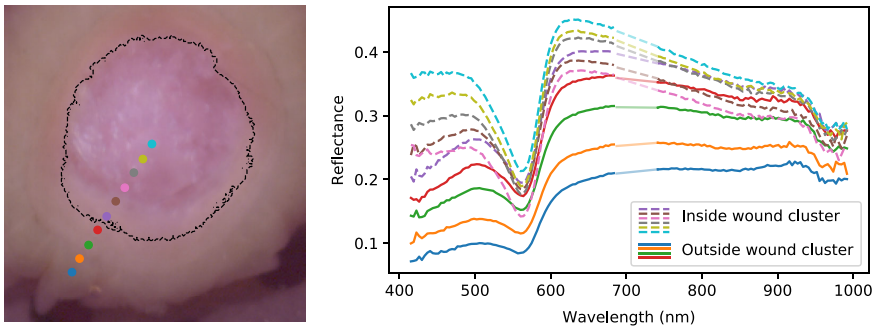

FIGURE 8 Positions across the wound boundary at day 22 (left), and corresponding reflectance spectra (right). A single wound model sample (III_2) is shown. The color used to mark a coordinate to the left is also used for the corresponding reflectance spectrum to the right. Dotted lines are within the boundary of the wound cluster. The artifact described in Figure 9 has been removed by linear interpolation (marked with brighter line color). The general spectral trends over the wound boundary (suppression, increased sloping) was found to be similar for the other samples

2. One sample (III_5) has a clear increase in wound size over the first 8 days, while two (I_3 and I_4) decrease in size from day 2 and on. The remaining samples (I_5, III_4 and III_2) have a stabilization or slight decrease in wound size until day 6 (I_5) or 8 (III_4 and III_2). Mean surface coverage among all samples, with respect to the maximum size of each combined wound cluster region, is 22% (SD 6%) at day 14, and 36% (SD 6%) at day 22. Mean surface coverage rate is 0.24 mm^2/day (SD 0.06).

4.1.2 | Spectral behavior over the cluster boundary at day 22

In Figure 8, reflectance spectra are plotted across the cluster boundary. The trends were found to be the same for all samples, and only sample III_2 is shown for brevity. The main trend which can be observed here is that the spectra are skewed as the pixels transition from wound into intact skin. The reflectance spectra at 600 nm and up have slopes that descend within the wound, while re-epithelialized and intact tissue spectra ascend. Similarly, the reflectance below 500 nm is higher for the wound and lowered for re-epithelialized and intact skin. The cluster boundary seems to set a threshold for when such suppression leads to a pixel being clustered with intact skin rather than wound tissue.

Mean increase at day 22 in the spectral derivative at 650 nm from within each wound cluster to a 25 pixel wide ring outside the wound cluster was found to be 0.0016 (SD 0.0002) across the various samples, and 0.0014 for the shown sample (III_2). Mean over spectral derivatives at the same wavelength inside all wound clusters at day 22 was 0.0001 (SD 0.0008), and 0.0018 (SD 0.0008) in the 25 pixel wide ring outside.

4.1.3 | Comparison of clustering results and PCA

PCA was run in order to generalize the correspondence between clustered regions and the spectral features noted above.

The loading plots are shown in Figure 9, while scores of sample III_5 at days 1, 2, 6, 12 and 22 are shown in Figure 10. All samples showed similar temporal development. Scores for all samples at day 22 are shown in Figure 11. The derivative PCA model showed the best separation between the spatial features of its two components, and for brevity, scores from only this model are shown. The reflectance scores of component 1 showed a mixture of the behavior of component 1 and 2 of the derivatives, while the reflectance scores of component 2 mainly corresponded to component 2 of the derivative model.

The second component of the reflectance PCA model has an overall steep, negative sloping across the entire spectral range, some of which is correspondingly reflected in the second component of the derivative PCA model above 600 nm. Scores of the second component represent these spectral features. Derivative component 1 has a large amplitude from around 540 to 600 nm, with a zero-crossing at around 560 nm corresponding to the minimum at the reflectance loadings at the same wavelength. This component therefore summarizes mainly the behavior responsible for this minimum.

According to the spatial features of component 1, the clustering boundary does not match what could seem to be the real wound boundary at day 1 and 2 for the shown sample in Figure 10 (sample III_5). However, component 2 shows a tight fit around within-wound textures and characteristic values that are not present outside the cluster boundary. The cluster boundary would therefore seem

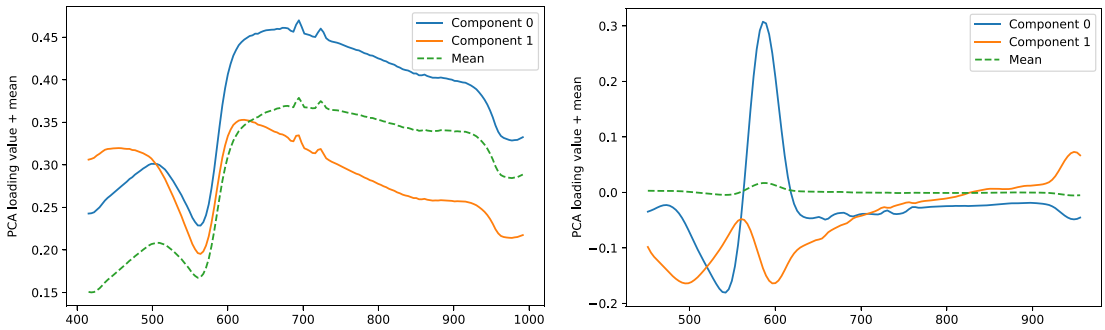

FIGURE 9 PCA loading plots for reflectance (left) and derivatives (right). The peaks between 700 and 750 nm in the reflectance loading plot are artifacts due to mismatch of the order sorting filter in the hyperspectral camera

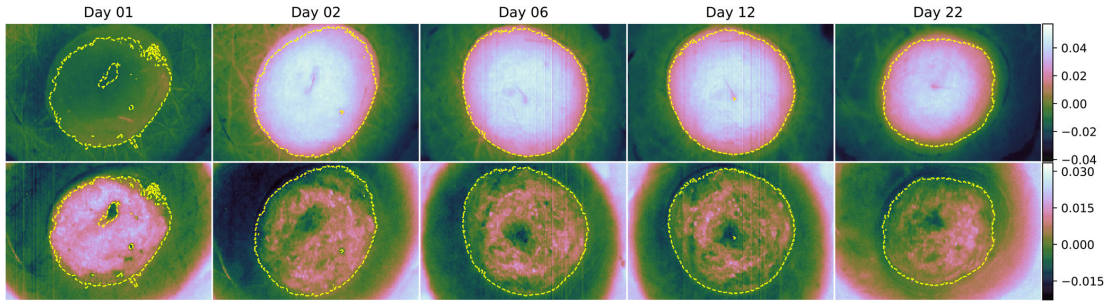

FIGURE 10 Sample III_5 scores from the PCA model trained on derivative spectra, along with boundaries (yellow) obtained from clustering analysis. First and second PCA component scores are shown in the first and second rows, respectively. The development was similar for the other samples. Day 22 scores are shown for the rest of the samples in Figure 11

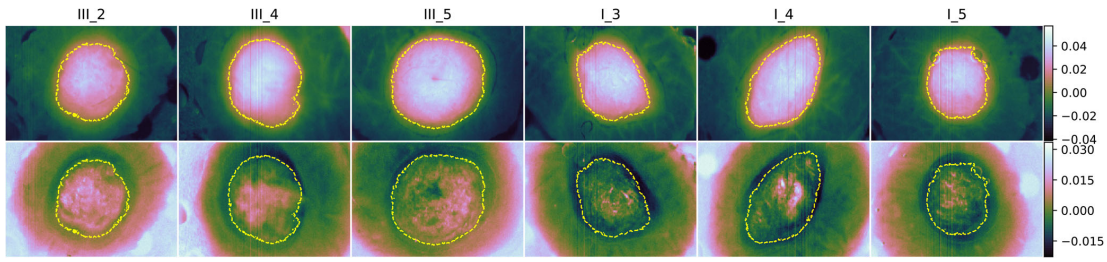

FIGURE 11 Day 22 scores for all samples from the PCA model trained on derivative spectra, along with boundaries (yellow) obtained from clustering analysis. First and second PCA component scores are shown in the first and second rows, respectively

to have separated two distinct spectral behaviors, where the inner region is represented by the right combination of component 1 and component 2. This was visually consistent for the other samples as demonstrated at day 22 in Figure 11.

Thus, the clustering represents a collection of the spectra that have steep, negative slopes, combined with a significant presence of an absorption maximum at 560 nm, in line with the spectra plotted over the boundary in the previous section. Single-pixel spectra (not shown) confirm the trend indicated by the PCA model.

The use of PCA as a data exploratory technique is usually subject to whether its maximization of the variance can reveal useful information. This seems to be the case for this dataset, though changes to illumination conditions or changes to the dataset selection could change the resulting PCA loadings and their order. The PCA decomposition will not represent a perfect decomposition

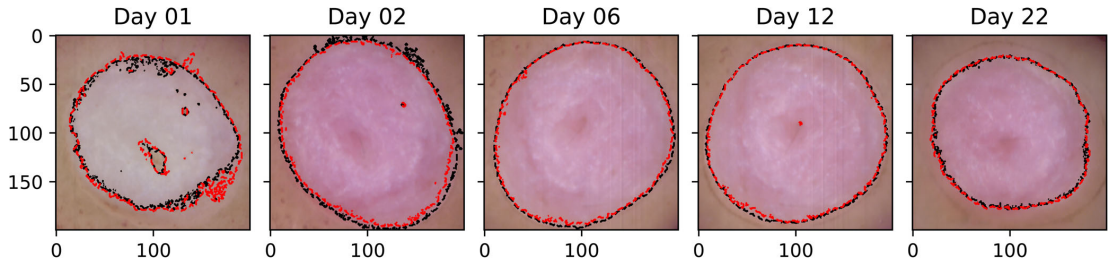

FIGURE 12 Wound boundary obtained from a random forest classifier trained on derivative spectra (black), compared against the majority vote clustering results (red) for sample III_5. Boundary correspondence was similar for the rest of the samples

of the data. There will be discrepancies due to the optical features not being linearly separable. However, the general spectral behavior can be inferred.

4.1.4 | Comparison between clustering results and a supervised classification model

A random forest classifier was trained on the derivative spectra from manually labeled pixels well within and outside the wounds, as per a visual inspection of the RGB images. The wound boundary results are shown for sample III_5 in Figure 12. The mean accuracy of the classification results with respect to the clustering boundary was 98% (SD 1%) for sample III_5, and 97% (SD 2%) for all samples. The boundaries obtained here are similar to the boundaries obtained from the clustering. Thus, the unsupervised clustering results are reproduced when training a supervised model on examples of wound and intact skin, partially confirming the soundness of the unsupervised approach for these data.

The applied classification method, random forest, has the possibility to reveal what features are used for decision making by investigating the feature importances. These are shown in Figure 13. For raw reflectance, the behavior between 400 and 500 nm is used the most, while derivatives result in utilization of the slopes at 520 and 650 nm. For second derivatives, the turning points of the reflectance at 500, 560 and 600 nm are used.

4.2 | Investigation of the re-epithelialization influence by inverse modeling

An intact epidermis has absorption and scattering spectra that can be described by exponentially decaying models. The properties of such an epidermal layer were fitted to a region representing re-epithelialized tissue after using a

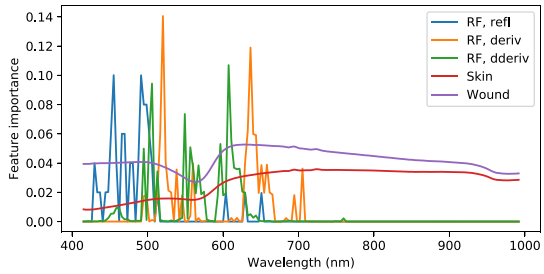

FIGURE 13 Feature importances as obtained from the random forest classifier trained on reflectance, derivative and second derivative spectra, respectively, compared against rescaled reflectance spectra from wound and intact tissue

wound spectrum as a basis, in order to check whether it could fully explain the transition from wound to apparently re-epithelialized regions. The result is shown in Figure 14 for sample III_5 at day 22.

The simulated spectrum shows a remarkably good fit against the measured spectrum between 400 and 700 nm. Some discrepancies are evident above 700 nm, indicating that some minor changes to the scattering in dermis would be needed for a perfect fit across the entire spectral range. Due to coupling between the epidermal parameters, the fitted properties are not unique. Regardless, they demonstrate that the region between wound and intact tissue has a reflectance spectrum which can be explained by the addition of some diffuse layer on top of a dermal layer with properties obtained from the wound tissue.

This then shows that this region likely has re-epithelialized, and that there are no other chromophores involved in dermis other than those already seen in the wound. The apparent absorption minimum towards 400 nm for re-epithelialized tissue, for example, is only due to epidermal suppression. The dermal composition of chromophores seems to be the same. The absorption peak at 561 nm is just as strongly present in the wound spectrum as in the re-epithelialized spectrum, but suppressed by the added epidermis. Gradually altering

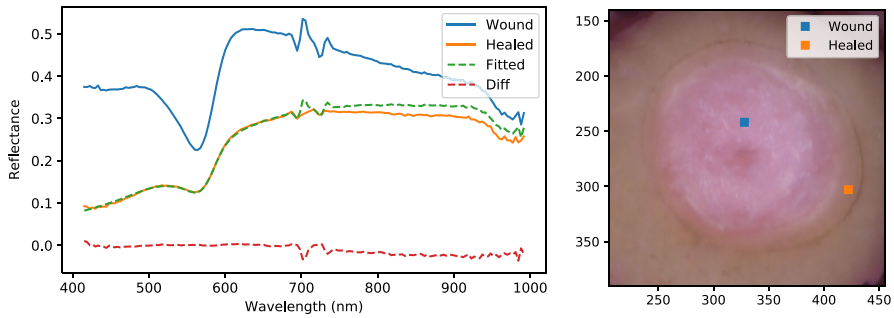

FIGURE 14 Inverse modeling of re-epithelialized tissue using a wound spectrum as the basis for the dermal properties (left) and an RGB image showing the corresponding spatial positions (right). Sample III_5 at day 22 is shown

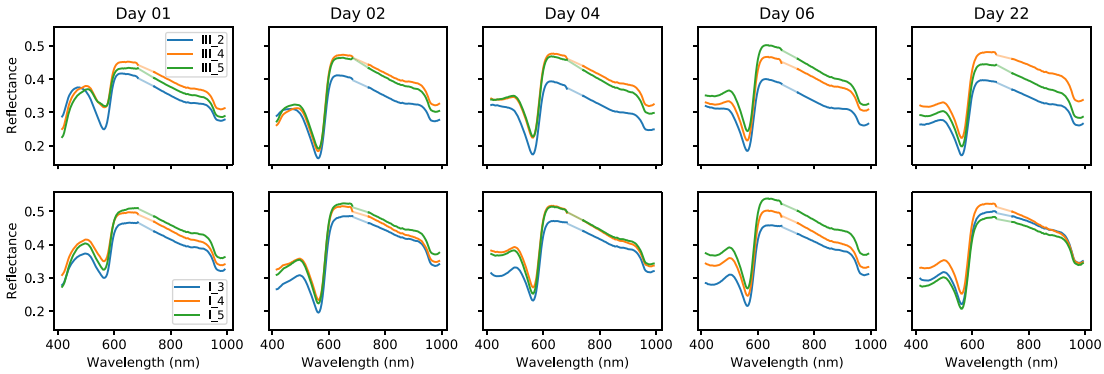

FIGURE 15 Mean spectra from within all wounds during the first and last days. There is a systematic change in the spectra at the 400 to 500 nm wavelength region at day 1 to 4, which then stays the same until day 22. The artifact described in Figure 9 has been removed by linear interpolation (marked with brighter line color). Spectra from 3 mm (I_*) and 4 mm (III_*) wounds have been split in separate rows for increased clarity

the thickness of the layer or the absorption and scattering magnitudes would thus transition the spectrum representing wound into something more or less indistinguishable from intact skin. The increased positive sloping and suppression of spectral features observed earlier is then fully explained by the addition of this diffuse layer.

The strong, unsuppressed presence of the minimum at 561 nm thus serves as a wound marker favored by the random forest as applied to second derivative spectra. Slopes between 600 and 700 nm likely are more robust, however, due to the changes the tissues undergo during the first days below 600 nm, as will be shown during the next sections. This is reflected in the PCA components shown in Section 4.1.3. Component 1 corresponds to the unsuppressed minimum at 561 nm, but the sloping between 600 and 700 nm partially represented by component 2 decides the tightening of the cluster boundary. The latter is likely more sensitive to the epidermal presence than just the suppression of the minimum at 561 nm. A thin epidermis would suppress the minimum some, but has a larger influence on the slope between 600 and 700 nm. Likely due to illumination differences leading to level changes in reflectance, reflectance classification favors the level at 400 to 500 nm which is significantly suppressed by epidermis due to the high absorption and scattering here.

4.3 | Characterization of the temporal development in optical properties

4.3.1 | Mean wound spectra across all times

In Figure 15, mean reflectance spectra from the wounds are plotted. These have different overall heights, but the same spectral characteristics at a given day are clearly evident across samples.

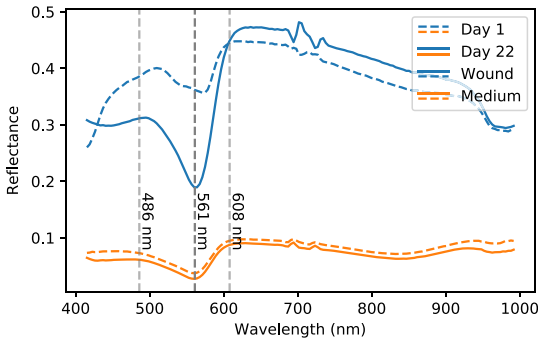

FIGURE 16 Comparison between wound spectra at day 1 and 22 for sample III_5 and corresponding reflectance spectra obtained from the medium. Important features of the medium reflectance spectrum are marked by vertical lines

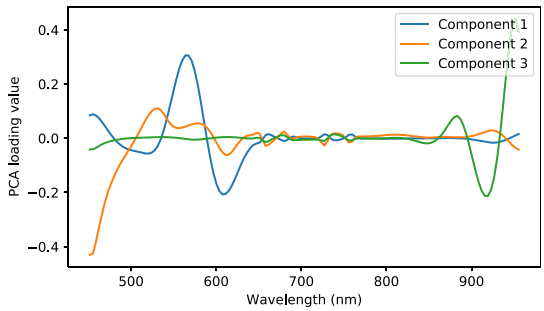

FIGURE 17 Loading vectors for the PCA model trained on the second derivative of all wound samples

The spectral shapes change systematically from day to day. On day 1, all spectra slope upwards from 400 to 500 nm. This slope changes gradually until day 4, where it stabilizes to a flat, slightly curved appearance. All samples seem to have the same absorption peak at 561 nm after the stabilization. Most of the samples have the same absorption peak at the first day, while others show a flatter spectrum at 500 to 600 nm.

Comparing against a reflectance spectrum obtained from the medium, see Figure 16, it can be seen that the absorption peak at 561 nm corresponds well with the main absorption peak in the medium spectrum. The medium spectrum also has slopes in the reflectance which seem to correspond with the slopes of the wound reflectance, except that they are wavelength-shifted with respect to each other. However, since these are slopes and not actual absorption peaks, they could easily be shifted by changes in absorption and scattering spectra. The wounds would seem to obtain the same spectral characteristics as the medium over time. The medium feeds the skin tissue, enabling re-epithelialization, which means that the medium necessarily infuses the tissue. It stands to reason that the skin should obtain similar spectral features as the medium. This is likely difficult to verify, however. Intact skin undergoes similar changes as wound, but not as strongly pronounced. An early theory was that the changes could be due to changes in cytochromes, but no specific evidence has been found for this.

4.3.2 | Wound decomposition by PCA across all times

The wound spectra were decomposed using PCA in order to infer spatial variations that are averaged away by taking the mean. Taking PCA of the wound reflectance was found to mainly show spatial variations within the wound, while taking PCA of higher order derivatives yielded components apparently corresponding to the noted developments above. Only PCA of the second derivatives is shown. Loading vectors are shown in Figure 17, while scores of the two first components are shown in Figure 18.

The first loading vector has a large amplitude at 561 nm, corresponding to the high and positive curvature of the reflectance here. The first component therefore describes the influence of the minimum here. The mean second derivative spectrum already had contributions from the minimum, and negative PCA scores thus express suppression of this, while scores close to zero and above express presence. The corresponding component 1 scores in Figure 18 show an inhomogeneous distribution across the first day (two-peaked distribution with peaks at −0.0050 and −0.0023, mean PCA score −0.0034, SD 0.0014), which changes to a largely homogeneous distribution over the entire wound at day 2 (single-peaked distribution with peak at 0.0016, mean PCA score 0.0011, SD 0.0011). This partially explains the behavior seen in the mean spectra in Figure 15, where some samples (sample III_2, I_3, I_4 and I_5, mean PCA score −0.0030, SD 0.0013) apparently had more contributions from the minimum at 561 nm than others (sample III_4 and III_5, mean PCA score −0.0043, SD 0.0010) at the first day. This contribution homogenizes and becomes stronger from day 1 to day 2 (mean PCA score and SD 0.0011, 0.0011 for sample III_2, I_2, I_3, I_4 and I_5, 0.0010, 0.0009 for III_4 and III_5) in Figure 15.

Some of the wound spectra have demonstrated a "flatness" around 540 to 580 nm at day 1, illustrated in Figure 16. This behavior, and the further decrease in absorption close to 400 nm, likely correspond to component 2 of the PCA model. The positions of the maxima and minima and corresponding curvature in the day 1 wound reflectance spectrum in Figure 16 indicate this.

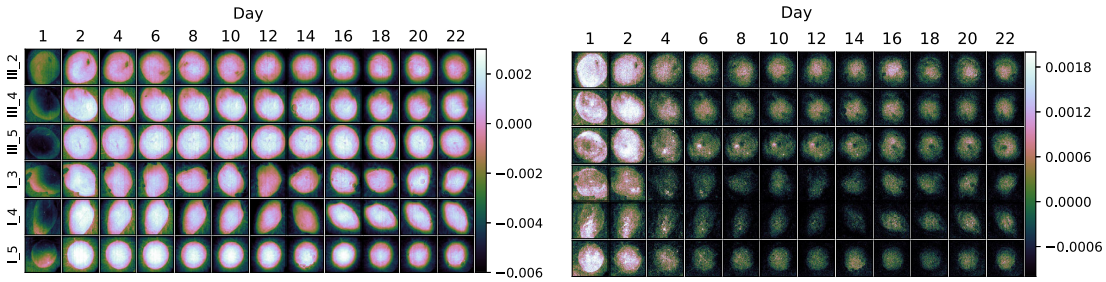

FIGURE 18 Scores of component 1 (left) and component 2 (right) from the PCA model trained on second derivative of the wound spectra, centered on and zoomed in on the wounds. All wound model samples (rows) across all measurement time points (columns) are shown in order to illustrate the temporal change

PCA component 2 has a drop from day 2 (mean PCA score 0.0009, SD 0.0007) to day 4 (mean PCA score 0.0000, SD 0.0006). There are indications in the score images for component 2 in Figure 18 that the scores are further reduced for some samples until day 8.

Thus, there is a temporal development of the optical properties which continues until day 8 for some of the samples. With respect to this, day 1 is a spectral outlier.

4.4 | Summary and discussion of the main clustering results

A clustering of the data helps in separating important spectrally distinct regions from each other and simplifies further analysis. Inspection of spectra from selected regions and a PCA decomposition demonstrates that the clustering is consistent in separating two main spectral behaviors from each other. The results were compared against wound boundaries obtained from supervised analysis and visual inspection of RGB images, which demonstrate that the two clusters correspond to wound and regions with some epidermis intact. Inverse photon transport modeling further confirms the found spectral trends.

A combination of *K*-Means and agglomerative clustering was used as the main technique. Cluster membership in *K*-Means is determined by closest distance to the cluster centers. The technique is therefore naturally extendable to classification of unseen data. This enables training on different samples and subsequent combination of the clustering results. However, the same property means that the clusters optimally should be spherical in the image space. Investigation in a lower-dimensional PCA space would reveal that the structures to be clustered are elongated and twist throughout the image space. *K*-Means is therefore unlikely to reflect the inherent structure of the data by a number of clusters corresponding to the actual, few clusters. Agglomerative clustering is more suitable for such cases, but difficult to apply to large datasets and does not readily extrapolate to new data. As the best of two worlds, agglomerative analysis was therefore successfully used as a technique to combine the too-high number of clusters obtained from the *K*-Means analysis.

Clustering methods are in general difficult to verify. They are highly subject to preprocessing treatments, choice of distance metrics and subjective evaluations [41]. It is still possible to check the stability of such approaches by varying the data subjected to clustering [41]. Separate clustering models were therefore trained on each wound model sample. Splitting across samples was found to be the most natural way to split the data. Training across all measurement times enables the method to generalize across changes in the reflectance of the samples during the first 4 to 8 days. Finally, application to a single sample avoids merging of characteristics of several wounds into the same cluster. Merging of wound clusters instead happens more robustly with the majority vote. The data variation yielded apparently stable and consistent clusters across all samples and days.

The *K*-Means clusters were merged down to two clusters that overall seem to represent wound and re-epithelialized/intact tissue. Including a third cluster was found to be challenging, as it was difficult to retain consistency across all samples and measurement times. This is to be expected in light of the inverse modeling results. Different locations of and stages along the wound re-epithelialization process yield different re-epithelialized layer thicknesses. The layer gradually transforms the reflectance from wound to intact tissue reflectance. The main bulk is therefore best summarized by two clusters with some implicit threshold in spectral behavior.

Spatial features in the RGB images were used for verification of the hyperspectral clustering results. This means that the RGB bands technically are sufficient to identify

similar degrees of re-epithelialization as in the hyperspectral results. The study on fluorescence emission by Wang et al. [23] also seems to indicate, judging from the figures, that there is a similar correspondence between the RGB images of their study, and the re-epithelialization indicated by their collagen fluorescence emission. The hyperspectral system used in the current study acquires images within the visible range. Band redundancy is expected, which is the reason why techniques like PCA are successful in compressing the information down to a few component bands. The RGB bands sample information at spaced intervals throughout most of the imaged wavelength range. Redundancy will cause features in the various bands to be present to a stronger or lesser degree in the RGB bands. Further, the identified photon transport mechanisms affecting the re-epithelialized tissue reflectance will have impact on the RGB bands. The contrast offered by the RGB images alone is weak, however, and re-epithelialized tissue is identifiable mainly when coupled with the hyperspectral analysis results. The spectral dimension is needed when investigating whether visually similar tissue parts should be included or not. There is also a possibility for detection of subtler changes, though the implicit threshold in the cluster analysis mainly corresponded with the visually observable features.

The end goal, a tool for identifying healing in in vitro wound models, does not necessarily require the full spectral dimension offered by hyperspectral imaging. There are indications that a multispectral system with fewer bands is feasible. These might not necessarily be the RGB bands, but other bands that offer better contrast between wound and re-epithelialized tissue. Initial studies using hyperspectral imaging are necessary for understanding the mechanisms affecting such bands, and for establishing a baseline for comparing such reduced systems. Further, classification models can be built based on single pixel spectra. This significantly eases the analysis for larger bulks of data. Classification based on RGB or other bands would require incorporation of spatial information and less intuitive approaches like convolutional neural networks. Hyperspectral imaging is then suitable as an initial research tool to be replaced by less expensive and tailored multispectral systems in the long run.

4.5 | Summary and discussion of the physical interpretation of the results

A challenge with any hyperspectral dataset is the high amounts of data, and automatized and objective methods are required to extract the relevant information. This data exploratory study has gained an overview of the optical properties of the investigated in vitro wound model and showed possible ways detection algorithms could be built for automatic classification of unhealed wound tissue. The missing top layer of unhealed wounds is an important component of this.

Apparent re-epithelialized tissue regions have optical behavior that through inverse photon transport modeling has been shown to be consistent with the addition of a diffuse layer on top of the optical properties represented by wound tissue regions. The influence from the epidermal layer can be characterized by a skewing of reflectance slopes and suppression of the spectral features of the wound. Derivative spectra can thus provide illumination-insensitive and possibly donor-invariant features for classification. Re-epithelialization seems to be the main optically detectable feature, and other changes like migration of fibroblasts or remodeling of the collagen matrix are more subtle, undetectable or absent. Most studies on this type of wound model have focused mainly on re-epithelialization, and complete remodeling might not be expected outside some expression of collagenase [22].

The modeling approach is promising. The properties of re-epithelialized tissue can be probed without having to consider full photon transport modeling of the dermal tissue layers, by utilizing scale-invariance properties. Properties like thickness could be inferred, but this has to be investigated and verified further. However, knowing that *some* diffuse layer with finite thickness can explain the spectral differences of different tissue regions is sufficient for the conclusions in this paper.

The change in reflectance over time indicates a change in the optical properties of the tissues. The change has been established to be related to the spectra attaining the same spectral properties as the medium. This leads to a confusion in the analysis. Spectra representing wound for the later days are not necessarily similar to spectra representing wound for the first day, and the behavior results in some noise and discrepancy in the day 1 clustering. Despite this, the still-present sloping behavior due to epidermis has made the clustering rather consistent.

It has been established that the samples converge towards the same spectral behavior as the medium. What they start out with is not as clear. Possible explanations are absorption due to cytochromes, which in the absence of blood would have a pronounced effect on the reflectance, or absorption due to a residual blood content which is gradually replaced with medium.

The analysis shows that the wound is re-epithelialized from the edge and towards the center of the wound. Multiple cell layers are expected to migrate in this fashion and quickly develop into a mature epidermis when the samples are exposed to air [17], as opposed to the initial single layer of keratinocytes expected from submerged

samples [2, 17]. Glinos et al. [54] (8 mm samples, 3 mm wound, DMEM, 10% FCS, air exposure) used optical coherence tomography to study re-epithelialization in a similar wound model, with a spatial resolution corresponding to the current hyperspectral study. More mature epithelium is shown to migrate over the wound with a small tip of non-cornified epidermis extending on the wound side of the epithelium. Wang et al. [23] (12 mm samples, 4 mm wound, DMEM, 10% FCS, air exposure) shows a correspondence between reduction of dermal collagen fluorescence at 390 nm and wound closure. Extinction here would require the newly formed epithelium to have similar absorption and scattering mechanisms as the intact epidermis. Thus, it is likely that the detected epithelium in the current study represents a more mature epidermis with multiple cell layers. Immature epidermis might be expected at the very edge of this. For example, Figure 5 indicates a more white-ish line extending on the wound side of the newly formed epithelium. This would be consistent in size with the findings of Glinos et al. [54], but has to be investigated further.

The found time development of the re-epithelialization is inconsistent with the expected development of the model. Epithelium is detected at the very edges of the wounds after day 8 to 10 for the 4 mm wounds, and day 3 to 8 for the 3 mm wounds. Mean surface coverage at day 22 is 36%. The 3 mm wounds should be fully covered (100% surface coverage) by epithelium already at day 7 [17]. The prepared wounds are heterogeneous in size, and two of the intended 3 mm sized wounds are closer to 4 mm in size. Available data on 4 mm wounds in the same type of medium indicates somewhat delayed wound coverage (48% closure by day 4 and 66% closure by day 16 [23], or around 50% closure by day 7 and around 80% closure by day 12 [24]), but still earlier and more complete epidermal coverage than what is observed in the current study.

The development in optical properties indicates that medium is diffused throughout the tissue. Delay in access to nutrients due to the need for diffusion of nutrients through the bottom layer could have delayed the re-epithelialization. However, submerged wounds and wounds exposed to air are expected to have similar time development [17]. Full exposure to air over the entire tissue surface [23, 55] or increased tissue sample size [23, 54, 55] does not seem to cause similar delays in other studies. The large number of consistent studies on 3 mm wounds in 6 mm tissue samples [2, 17–22] shows that there is little variation in re-epithelialization rate due to donor variability or donor tissue location. The tissue samples rested on a metallic grid, but it is unlikely that this should have any effect.

Histologies were not available for this particular dataset. Wound tissue is transformed into tissue reminiscent of intact tissue, and photon transport modeling shows that the spectral behavior is consistent with an epidermal layer placed on top of wound tissue. However, histological verification is necessary for final confirmation of these results. The fact that the time kinetics of the investigated samples seem far slower than expected makes comparison to existing studies challenging.

The experiment has to be repeated, preferably with histologies sampled at multiple time points during the course of the experiment. This calls for a high number of samples. Representativeness can be challenging due to heterogeneity from the wound preparation method. Eikebrokk et al. [1] developed a method for creating more reproduceable wounds. These were superficial wounds with the basal layer intact, which re-epithelialize and stratify into a mature epidermis more quickly. In addition to being more reproduceable, this could also be useful for investigating the optical influence of the various stages of layer stratification. This can be corroborated back to the results of the current study. These wounds behave somewhat differently, however, and wounds more similar to the the wounds in the current study should be included for verifying the mechanisms of the epidermal migration. For simplification, only a single wound size should be included.

A major difficulty identified in this study is the general change in optical properties over the period where re-epithelialization normally would be expected. Separating these from the re-epithelialization processes could be important when the experiment is repeated, especially if the normal time course of re-epithelialization is observed. Incubating some of the models in 2% FCS rather than 10% FCS leads to viable tissue with no re-epithelialization [2]. Such modifications could be used to evaluate optical changes without interference from re-epithelialization.

5 | CONCLUSION AND FURTHER WORK

Optical techniques like hyperspectral imaging could provide an objective, non-destructive and non-contact alternative to histology analysis for evaluating re-epithelization in in vitro wound models. Appropriate analysis methods are required for extracting information about the wound coverage.

The different tissue types in the samples have been separated and investigated using clustering analysis. This analysis, along with corroborating techniques like supervised classification and PCA, significantly helped identifying and generalizing important spectral features. Intact tissue and apparently healing regions are characterized by a suppression of and increased sloping in spectral

features that are present in the wound reflectance spectra. The use of a specially developed photon transport model has shown that this behavior can be explained by a diffuse layer of finite thickness placed on top of optical properties representing wounds, which is consistent with the expected re-epithelialization process.

The full characterization of the spatial and temporal behavior enables further development of classification and photon transport techniques that can be used to detect and characterize wound re-epithelialization processes. There is further a possibility that a multispectral system with fewer bands can be feasible for detection of re-epithelialization, which will be investigated in future work. Histologies were not available for this study, however, and the experiment has to be repeated for final confirmation of the found behavior.

ACKNOWLEDGMENTS

Thanks to Ingvild Haneberg and Matija Milanic for acquisition of the data. Thanks to Terje Schjelderup for help with the proofreading.

CONFLICT OF INTEREST

The authors have no conflicts of interest to disclose.

ORCID

Asgeir Bjorgan https://orcid.org/0000-0003-4200-3827

REFERENCES

[1] T. A. Eikebrokk, B. S. Vassmyr, K. Ausen, C. Gravastrand, B. Pukstad, *BJS Open* **2019**, *3*(6), 840.
[2] G. Kratz, *Microsc. Res. Tech.* **1998**, *42*(1), 345.
[3] G. Lu, B. Fei, *J. Biomed. Opt.* **2014**, *19*(1), 010901.
[4] L. Khaodhiar, T. Dinh, K. T. Schomacker, S. V. Panasyuk, J. E. Freeman, R. Lew, T. Vo, A. A. Panasyuk, C. Lima, J. M. Giurini, T. E. Lyons, A. Veves, *Diabetes Care* **2007**, *30* (4), 903.
[5] M. Denstedt, B. S. Pukstad, L. A. Paluchowski, J. E. Hernandez-Palacios, L. L. Randeberg, *Proc. SPIE* **2013**, *8565*, 85650N.
[6] A. Nouvong, B. Hoogwerf, E. Mohler, B. Davis, A. Tajaddini, E. Medenilla, *Diabetes Care* **2009**, *32*(11), 2056.
[7] D. Yudovsky, A. Nouvong, L. Pilon, *J. Diabetes Sci. Technol.* **2010**, *4*(5), 1099.
[8] A. Holmer, J. Marotz, P. Wahl, M. Dau, P. W. Kämmerer, *BIOMED ENG-BIOMED TE* **2018**, *63*(5), 547.
[9] M.-A. Calin, T. Coman, S. V. Parasca, N. Bercaru, R. S. Savastru, D. Manea, *J. Biomed. Opt.* **2015**, *20*(4), 046004.
[10] M. A. Calin, S. V. Parascal, D. Manea, R. Savastru, *MIUA 2019: Medical Image Understanding and Analysis*, Springer, Cham, **2019**, p. 74.
[11] G. Daeschlein, I. Langner, T. Wild, S. von Podewils, C. Sicher, T. Kiefer, M. Jünger, *Clin. Hemorheol. Microcirc.* **2017**, *67* (3–4), 467.
[12] L. A. Paluchowski, H. B. Nordgaard, A. Bjorgan, S. A. Berget, L. L. Randeberg, *J. Biomed. Opt.* **2016**, *21*(10), 101413.
[13] L. L. Randeberg, E. L. P. Larsen, L. O. Svaasand, *J. Biophotonics* **2010**, *3*(1–2), 53.
[14] J. Shapey, Y. Xie, E. Nabavi, R. Bradford, S. R. Saeed, S. Ourselin, T. Vercauteren, *J. Biophotonics* **2019**, *12*(9), e201800455.
[15] A. J. Singer, R. A. F. Clark, *N. Engl. J. Med.* **1999**, *341*(10), 738.
[16] V. Arnoux, C. Come, D. F. Kusewitt, L. G. Hudson, P. Savagner, in *Rise and Fall of Epithelial Phenotype: Concepts of Epithelial-Mesenchymal Transition* (Ed: P. Savagner), Plenum Publishers, New York, **2005** Chapter 8.
[17] K. Jansson, G. Kratz, A. Haegerstrand, *In Vitro Cell. Dev. Biol.* **1996**, *32*(9), 534.
[18] G. Kratz, M. Lake, M. Gidlund, *Scand. J. Plast. Reconstr. Hand Surg.* **1994**, *28*(2), 107.
[19] S. Lönnqvist, P. Emanuelsson, G. Kratz, *J. Plast. Surg. Hand Surg.* **2015**, *49*(6), 346.
[20] G. Kratz, B. Palmer, A. Haegerstrand, *Eur. J. Plast. Surg.* **1995**, *18*, 209.
[21] G. Kratz, C. C. Compton, *Wound Rep. Reg.* **1997**, *5*(3), 222.
[22] M. Inoue, G. Kratz, A. Haegerstrand, M. Ståhle-Bäckdahl, *J. Investig. Dermatol.* **1995**, *104*(4), 479.
[23] Y. Wang, E. Gutierrez-Herrera, A. Ortega-Martinez, R. R. Anderson, W. Franco, *Laser Surg. Med.* **2016**, *48*(7), 678.
[24] E. Nyman, F. Huss, T. Nyman, J. Junker, G. Kratz, *J. Plast. Surg. Hand Surg.* **2013**, *47*(2), 89.
[25] Y. Wang, A. Ortega-Martinez, B. Farinelli, R. R. Anderson, W. Franco, *Proc. SPIE* **2016**, *9689*, 96890G.
[26] L. L. Randeberg, J. L. Hegstad, L. A. Paluchowski, B. S. Pukstad, *Proc. SPIE* **2014**, *8926*, 892607.
[27] M. Wahabzada, M. Besser, M. Khosravani, M. Thomas Kuska, K. Kersting, A.-K. Mahlein, E. Stürmer, *PLoS One* **2017**, *12* (12), e0186425.
[28] N. Verdel, A. Marin, M. Milanic, B. Majaron, *Biomed. Opt. Express* **2019**, *10*(2), 944.
[29] L. L. Randeberg, O. A. Haugen, R. Haaverstad, L. O. Svaasand, *Laser Surg. Med.* **2006**, *38*(4), 277.
[30] C. Mignon, D. J. Tobin, M. Zeitouny, N. E. Uzunbajakava, *Biomed. Opt. Express* **2018**, *9*(2), 852.
[31] T. M. Bydlon, R. Nachabé, N. Ramanujam, H. J. C. M. Sterenborg, B. H. W. Hendriks, *J. Biophotonics* **2014**, *8* (1–2), 9.
[32] E. L. Larsen, L. L. Randeberg, E. Olstad, O. A. Haugen, A. Aksnes, L. O. Svaasand, *J. Biomed. Opt.* **2011**, *16*(2), 026011.
[33] A. O. H. Gerstner, W. Laffers, F. Bootz, D. L. Farkas, R. Martin, J. Bendix, B. Thies, *J. Biophotonics* **2012**, *5*(3), 255.
[34] Y. Khouj, J. Dawson, J. Coad, L. Vona-Davis, *Front. Oncol.* **2018**, *8*, 17.
[35] E. J. M. Baltussen, E. N. D. Kok, S. G. B. de Koning, J. Sanders, A. G. J. Aalbers, N. F. M. Kok, G. L. Beets, C. C. Flohil, S. C. Bruin, K. F. D. Kulhmann, H. J. C. M. Sterenborg, T. J. M. Ruers, *J. Biomed. Opt.* **2019**, *24*(1), 016002.
[36] B. Regeling, W. Laffers, A. O. H. Gerstner, S. Westermann, N. A. Müller, K. Schmidt, J. Bendix, B. Thies, *J. Biophotonics* **2015**, *9*(3), 235.
[37] A. Grigoroiu, J. Yoon, S. E. Bohndiek, *Sci. Rep.* **2020**, *10*, 3947.
[38] G. Zonios, A. Dimou, *Opt. Express* **2006**, *14*(19), 8661.

[39] I. J. A. Haneberg, Master's thesis, Norwegian University of Science and Technology **2014**.
[40] A. Bjorgan, L. L. Randeberg, *Proc. SPIE* **2019**, *10889*, 108891K.
[41] G. James, D. Witten, T. Hastie, R. Tibshirani, *An Introduction to Statistical Learning*, 1st ed., Springer, New York, **2013**.
[42] A. F. Fell, *Trends Anal. Chem.* **1983**, *2*(3), 63.
[43] J. Bao, M. Chi, J. A. Benediktsson, *IEEE J. Sel. Top. Appl. Earth Obs. Remote Sens.* **2013**, *6*(2), 594.
[44] F. Tsai, W. Philpot, *Remote Sens. Environ.* **1998**, *66*, 41.
[45] W. Zheng, C. Wang, S. Chang, S. Zhang, R. X. Xu, *J. Biomed. Opt.* **2015**, *20*(12), 121303.
[46] W. D. Philpot, *IEEE Trans. Geosci. Remote* **1991**, *29*(3), 350.
[47] F. Tsai, W. Philpot, in IGARSS'97. *1997 IEEE International Geoscience and Remote Sensing Symposium Proceedings. Remote Sensing—A Scientific Vision for Sustainable Development* **1997**, pp. 1234–1245.
[48] A. Savitzky, M. J. E. Golay, *Anal. Chem.* **1964**, *36*(8), 1627.
[49] L. Breiman, *Mach. Learn.* **2001**, *45*, 5.
[50] T. Hastie, R. Tibshirani, J. Friedman, *The Elements of Statistical Learning*, 2nd ed., Springer, New York, **2008**.
[51] M. Belgiu, L. Dragut, *ISPRS J. Photogramm. Remote Sens.* **2016**, *114*, 24.
[52] J. C.-W. Chan, P. Bechers, T. Spanhove, J. V. Borre, *Int. J. Appl. Earth Obs.* **2012**, *18*, 13.
[53] J. Ham, Y. Chen, M. M. Crawford, J. Gosh, *IEEE Trans. Geosci. Remote Sens.* **2005**, *43*(3), 492.
[54] G. D. Glinos, S. H. Verne, A. S. Aldahan, L. Liang, K. Nouri, S. Elliot, M. Glassberg, D. C. DeBuc, T. Koru-Sengul, M. Tomic-Canic, I. Pastar, *Wound Rep. Reg.* **2017**, *25*(6), 1017.
[55] J. Mendoza-Garcia, A. Sebastian, T. Alonso-Rasgado, A. Bayat, *Wound Rep. Reg.* **2015**, *23*(5), 685.

How to cite this article: Bjorgan A, Pukstad BS, Randeberg LL. Hyperspectral characterization of re-epithelialization in an in vitro wound model. *J. Biophotonics*. 2020;13:e202000108. https://doi.org/10.1002/jbio.202000108

Paper II

A. Bjorgan and L. L. Randeberg, "Exploiting scale-invariance: A top layer targeted inverse model for hyperspectral images of wounds," *Biomed. Opt. Express*, vol. 11(9):5070–5091, 2020. DOI: `http://dx.doi.org/10.1364/BOE.399636`

Research Article | Vol. 11, No. 9 / 1 September 2020 / Biomedical Optics Express 5070
Biomedical Optics EXPRESS

Exploiting scale-invariance: a top layer targeted inverse model for hyperspectral images of wounds

ASGEIR BJORGAN* AND LISE LYNGSNES RANDEBERG

Department of Electronic Systems, NTNU Norwegian University of Science and Technology, Trondheim, Norway
*asgeir.bjorgan@ntnu.no

Abstract: Detection of re-epithelialization in wound healing is important, but challenging. Hyperspectral imaging can be used for non-destructive characterization, but efficient techniques are needed to extract and interpret the information. An inverse photon transport model suitable for characterization of re-epithelialization is validated and explored in this study. It exploits scale-invariance to enable fitting of the epidermal skin layer only. Monte Carlo simulations indicate that the fitted layer transmittance and reflectance spectra are unique, and that there exists an infinite number of coupled parameter solutions. The method is used to explain the optical behavior of and detect re-epithelialization in an in vitro wound model.

1. Introduction

In vitro wound models are useful for investigation of wound healing in a controlled laboratory setting [1–5]. However, it is challenging to monitor the actual healing in such models without destructive histology analysis. Hyperspectral imaging is a technique providing a non-destructive, objective method for characterizing such tissues optically.

Hyperspectral imaging has a spectral and spatial resolution that has been shown to be useful for biomedical applications like wound imaging [6–14], burn wound imaging [12,15], cancer diagnostics [6,16,17] and surgical guidance [6,18]. Statistical processing techniques are often used to handle the large amounts of data [8,12,13,15,19–25]. The rich spectral content further enables use of inverse photon transport modeling [26–32]. Such modeling techniques can be used to interpret the data and relate spectral changes to changes in skin properties like blood content and blood oxygenation through constrained fitting of optical properties. This indirect way of estimating optical properties is considered to be ill-defined [6,33] since different media can have similar reflectance spectra [33,34]. Further, absorption and scattering properties are fitted to a single reflectance measurement [35]. A priori knowledge of the expected shapes of the absorption and scattering restrains the problem somewhat [35], but there is still a basic ambiguity resulting from a scale-invariance of the reflectance with respect to the absorption and scattering spectra [33,34]. Other possibilities to restrain such models can be a valuable road of study in order to obtain unique and robust estimates.

The tissue model used in this study was based on an in vitro wound model setup developed by Jansson et al. [36] and Kratz [37]. Here, samples with wounds are prepared from ex vivo human tissue and placed in a growth medium, which causes the wounds to re-epithelialize. Characterization of the re-epithelialized layer is of special interest, e.g. the presence, maturity and thickness of the layer. Photon transport modeling techniques could be used to extract this information from the reflectance spectra.

Photon transport modeling of in vitro wounds can be challenging. The spectral characteristics of the dermal part of the wound models are less defined than in normally circulated tissue due to the lack of blood absorption, and the spectra are significantly influenced by the spectral properties

#399636 https://doi.org/10.1364/BOE.399636
Journal © 2020 Received 11 Jun 2020; revised 15 Jul 2020; accepted 28 Jul 2020; published 17 Aug 2020

Biomedical Optics EXPRESS

of the growth medium [38]. However, in wounds, both regions with and without the upper tissue layer are present. The spatial resolution of hyperspectral imaging makes multiple reflectance spectra of each tissue type available as every pixel contains data with high spectral resolution. This could potentially be used to restrain the model and target the epidermal layer specifically.

The main idea of the inverse modeling technique to be presented in this paper is that the basic scale-invariant limitations of the reflectance modeling can be exploited to enable consideration of the upper layers without having to completely model the lower layers. The availability of reflectance spectra from both wound and re-epithelialized tissue then enables quantification of skin properties in re-epithelialized layers, without the need to consider the dermal layers.

The basic method requires knowledge of an appropriate wound spectrum. The high number of available wound spectra in a hyperspectral image makes selection of one unique spectrum somewhat prohibitive. However, the same availability of multiple spectra with a high spectral resolution makes it possible to use dimensionality reduction methods to remove redundant information and represent the spectral information in a low-dimensional space [38]. Principal component analysis (PCA) is such a method, which can decompose a dataset in terms of orthonormal components (loadings) that can linearly transform each observation into new variance-maximizing coordinates (scores) [39]. This technique has been used as a pre-processing technique [40–42] and for investigation of spectra in a low-dimensional space [6,19,38]. The method is used in the current paper to reduce a discrete wound spectrum choice to a continuous choice of PCA scores that can be back-transformed to a wound-like spectrum using the inverse transform. This enables the wound spectrum selection to be an efficiently evaluated part of the model optimization. The main goal of this study is to validate a proof of concept of the presented basic inverse modeling technique including the suggested PCA extension, and explore the limitations and possibilities of this approach.

A simulation study is carried out using Monte Carlo simulations in MCML [43], which represents a gold standard for photon transport simulations. The simulation study is used to investigate and verify the assumptions that enable use of the inverse modeling method. The uniqueness and accuracy of the fitted skin parameters are explored. With the findings of the simulation study on uniqueness and parameter accuracy in place, the method is finally applied to experimental data. Hyperspectral images of an in vitro wound model sample are used as an example for the application of the technique.

The inverse modeling method and its basic assumptions are given in section 2.1, along with the PCA-based modification appropriate for wound imaging. The simulation study used to verify these assumptions and investigate the accuracy and uniqueness of the inverse modeled parameters is outlined in section 2.2. Information on the hyperspectral wound dataset used to demonstrate an application of the method is given in section 2.3. Finally, results and discussion are given in section 3.

The method represents a partial modeling approach which combines data-driven results with photon transport modeling. Model fitting is mainly constrained to the upper layer, alleviating some of the inherent undetermined nature of the inverse photon transport modeling approach. The example given here is wound healing, but the method is generic, and can be used to investigate any top layer given that reflectance spectra are available with and without modifications to or removal of the top layers. Examples include characterization of burn wounds and estimation of epidermal skin thickness in pre-term newborns.

2. Materials and methods

2.1. Inverse modeling setup

2.1.1. Fundamental assumptions

Two main assumptions form the basis of the method:

Biomedical Optics EXPRESS

1. The reflectance of a one-layer model can be written as a function of μ_a/μ_s' (scale-invariance).
2. A multi-layer model and a one-layer representation yield identical reflectance values when a top layer is added.

The method considers cases where reflectance spectra are available from two regions, with and without a top layer. Given the first assumption, the reflectance from the region without the top layer is represented using a one-layer model by estimating its corresponding μ_a/μ_s' ratio without having to consider their actual forms. From the second assumption, using these properties in the deeper layer of a two-layer model can be used to represent the reflectance from the region with the top layer. The skin properties of the top layer can then be fitted without considering the deeper layers if the optical properties of the top layer are known. Insertion of one-layer properties from the region without the top layer into the two-layer model ensures that the boundary conditions towards the top layer are correct. The basic model steps are shown in Fig. 1.

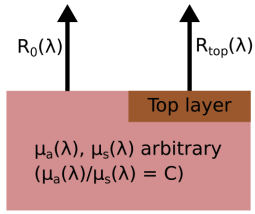

Fig. 1. Basic inverse model geometry. A one-layer model is fitted to the reflectance $R_0(\lambda)$ from a region with the top layer missing. Due to scale-invariance, any absorption coefficient μ_a and scattering coefficient μ_s obeying the required ratio are viable solutions. A top layer can then be fitted to the model by reusing the optical properties in the deeper layer of a two-layer model.

2.1.2. Photon transport model

A diffusion model with an isotropic source function [44] is used as photon transport model. The main advantage of this model is its simple, analytic expression for the reflectance, enabling fast evaluation during optimization. In addition, it can yield μ_a/μ_s' directly from the reflectance without iteration.

Theory Photon transport in biological tissue can be modeled by the radiative transfer equation (RTE) [45]. Assuming an almost isotropic light distribution and isotropic source functions, the time-independent RTE in a one-dimensional geometry is simplified to [44,45]

$$\mu_a\phi(z) - D\frac{d^2}{dz^2}\phi(z) = q(z), \tag{1}$$

where the diffusion constant is $D = \frac{1}{3(\mu_s'+\mu_a)}$ and ϕ is the fluence rate. A multi-layer medium is assumed, with d_i describing the depth of layer interface i. With the source function in a layer i given as [44]

$$q_i(z) = \mu_{s,i}'\exp(-\mu_{tr,i}z)\prod_{j=1}^{i-1}\exp(-\mu_{tr,j}d_j), \tag{2}$$

Biomedical Optics EXPRESS

the solution for the fluence rate in the layer i is given as [44]

$$\phi_i(z) = \frac{\delta_i \mu'_{s,i}}{D_i(1-\mu_{tr,i}\delta_i^2)} \exp[-\mu_{tr,i}(z-d_i)] \prod_{j=1}^{i-1} \exp[-\mu_{tr,j}(d_j - d_{j-1})] \tag{3}$$

$$+ A_{i1} \exp(-x/\delta_i) + A_{i2} \exp(x/\delta_i). \tag{4}$$

The boundary condition at the air-tissue interface is taken as $j(z=0) = A\phi(z=0)$. The property j is the photon flux. The boundary condition essentially relates the irradiance propagating back into the tissue to the irradiance propagating out of the tissue by an effective reflection coefficient [44]. A refraction index of $n = 1.4$ yields $A = 0.17$ [44]. It is required that $\lim_{z\to\infty} \phi(z) = 0$. All constants A_{ij} can then be determined by using continuity in $j(z)$ and $\phi(z)$ between each layer and the boundary conditions above [44]. The diffuse reflectance R_d is found by [44]

$$R_d = j(z=0). \tag{5}$$

The last expression is obtained by considering the irradiance transmitted into the air. Analytic solution for a two-layer model can be found in Svaasand et al. [44]. The one-layer solution is trivial to obtain.

Offset correction A correction constant is applied to the diffusion model reflectance. Comparing the diffusion model with the same boundary conditions and optical properties as a Monte Carlo simulation shows that the output reflectance from the diffusion model has an offset [46,47]. The assumption of an almost isotropic light distribution in the diffusion model leads to a less forward-directed photon flux close to the surface, as compared to other source functions such as the Delta-Eddington source function [47], and this yields a higher output reflectance contributing to the observed offset. The isotropic source function is chosen for simplicity and convenience, and it is considered as out of scope of this proof of principle to minimize this well known and systematic offset. It is however acknowledged that it introduces systematic errors in the estimated parameters.

The diffusion model and two-layer Monte Carlo spectra from model A and model C1 to be described in section 2.2.1 were compared with equal input parameters. An offset correction of 0.036 was found to minimize the average root mean squared error (RMSE) among all spectra. The offset correction is demonstrated in Fig. 2. On average, the RMSE between the model C1 Monte Carlo spectra in section 2.2.1 and corresponding diffusion model spectra were 0.037 (standard deviation 0.003) and 0.005 (standard deviation 0.001) before and after offset correction, respectively.

2.1.3. Inverse modeling method for skin

The main application of the method considers human skin with and without epidermis present, such as in wounds. Construction of a two-layer model from a basis reflectance was outlined in section 2.1.1. The properties of epidermis are then fitted to the reflectance from the region with the top layer. Python was used for development of the technique.

Melanin is assumed to be the main absorber in epidermis in the visible range [45,48,49]. Minor absorbers include carotene, lipids, cell nuclei and filamentous proteins [50], and are often modeled using a bulk background absorption [31,44,51,52]. A small amount of blood is sometimes included in the epidermis to account for the non-planar geometry of the papillary dermis [44,51,52]. For simplicity, neither of these are included in the current model. The epidermis is assumed to consist of a single layer with melanin as the absorber as shown in Eq. (6) and a scattering corresponding to Eq. (8), along with a defined layer thickness.

Biomedical Optics EXPRESS

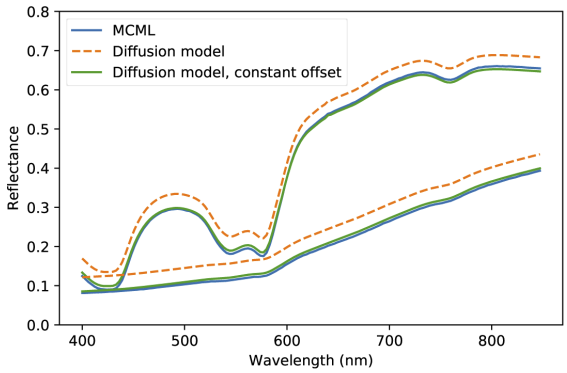

Fig. 2. Demonstration of empirical offset correction of the diffusion model reflectance. Model C1 in section 2.2.1 was used for the demonstrated examples, with the lowest possible parameter choices used for the upper reflectance spectrum, and the highest possible parameter choices for the lower reflectance spectrum. The RMSE between Monte Carlo and diffusion model spectrum was reduced from 0.036 to 0.006 for the upper spectrum, and from 0.043 to 0.007 for the lower spectrum. The Monte Carlo simulations were run with 1000 000 photons per wavelength.

The objective function to be minimized was chosen to be the RMSE between measured reflectance and simulated reflectance, relative to the simulated reflectance. The function `minimize` from the Python package `scipy.optimize` was used to minimize the objective function, using L-BFGS-B (Limited-memory Broyden-Fletcher-Goldfarb-Shanno algorithm with box constraints) as the optimization method. The parameters were bounded, and they were rescaled to values between 0 and 1 in order to make them comparable. The fitted epidermal skin parameters are listed in Table 1.

Table 1. Parameters to be fitted during optimization, along with their lower and upper bounds and the scaling factor applied before they are input into the optimization method.

Property	Lower bound	Upper bound	Scaling	Unit
Layer thickness, d_1	0	500	500	μm
Melanin absorption, $\mu_{a,m,694}$	0	2000	1000	m^{-1}
Scattering, $\mu'_{s,Ray,500}$	0	5000	5000	m^{-1}
Scattering, $\mu'_{s,Mie,500}$	1	5000	5000	m^{-1}
Scattering, b_{Mie}	0	4	4	-

2.1.4. Modifications to the technique for application to wounds

A modification of the inverse model was used for hyperspectral images of wounds, as the appropriate basis spectrum for a given re-epithelialized tissue sample is not known a priori. It was desired to let selection of the wound spectrum be something which could be fitted during optimization rather than iterating through the possible choices.

A PCA transform with three components is applied to spectra from the wound region. This reduces all possible wound spectra down to a combination of three score parameters and corresponding PCA loading vectors. Three additional parameters were input during the optimization. These were used as PCA scores and inverse transformed to construct an artificial

Biomedical Optics EXPRESS

wound basis spectrum onto which an epidermis was placed. This allowed the inverse model to represent a wound spectrum that could be fitted during optimization.

The PCA scores were then fitted along with the rest of the parameters. The fitted scores were bounded within the min/max range of the scores as transformed from the original wound spectra. Reconstructed wound basis spectra were constrained to non-negative values, effectively changing the optimization method to SLSQP (Sequential least squares programming).

2.2. Simulation study

2.2.1. Simulation setup

GPU-MCML [53,54] was used to simulate reflectance spectra from a skin-like geometry. NVIDIA GeForce GTX 670 was used for GPU parallelization. Wavelengths from λ = 400 to 850 nm were modeled with 3 nm discretization. 1 000 000 photons were used in each simulation. The total run time for a full spectrum was between 12 and 22 seconds. All simulations were run with pencil beams incident on the skin model, and the tissue was assumed to have a refraction index of 1.4. The homogeneity of the model makes the total integrated reflectance equivalent with the reflectance from the same model illuminated with an infinitely broad beam. A layer thickness of 1 meter was used in order to emulate a semi-infinite layer.

Absorption properties The absorption in the top layer was modeled using an absorption model for melanin [55]

$$\mu_{\mathrm{a,e}} = \mu_{\mathrm{a,m,694}}(\lambda/694)^{-3.46}, \tag{6}$$

where $\mu_{\mathrm{a,m,694}}$ is a parameter associated with the mean melanin content of the layer. Moderately dark skin corresponds to an absorption in the range 500-900 m^{-1}, while fair skin corresponds to an absorption in the range 200-300 m^{-1} [44]. Assumed low and high values for melanin absorption and epidermal thickness are listed in Table 2. For the dermal layers, the absorption is modeled as

$$\mu_{\mathrm{a,d}} = \mu_{\mathrm{oxy}}(\lambda)c_{\mathrm{oxy}} + \mu_{\mathrm{deoxy}}(\lambda)c_{\mathrm{deoxy}}, \tag{7}$$

where $\mu_{\{\mathrm{oxy,\ deoxy}\}}(\lambda)$ are the absorption spectra for oxygenated and deoxygenated blood, respectively. Assumed low and high values are listed in Table 2. These cover blood volume fractions from 2% to 10%, and oxygenations from approx. 20% to 80%. The inverse model avoids consideration of this layer, and the main goal is to model a layer with absorption and scattering magnitudes representing human skin.

Table 2. Low and high values for parameters varied in the Monte Carlo simulations.

Layer	Property	Low value	High value	Unit
Upper	Layer thickness, d_1	50	500	μm
Upper	Melanin absorption, $\mu_{\mathrm{a,m,694}}$	150	700	m^{-1}
Upper/Deeper	Scattering, $\mu'_{\mathrm{s,Ray,500}}$	1500	3000	m^{-1}
Upper/Deeper	Scattering, $\mu'_{\mathrm{s,Mie,500}}$	1500	3000	m^{-1}
Deeper	Oxy. blood fr., C_{oxy}	0.01	0.05	-
Deeper	Deoxy. blood fr., C_{deoxy}	0.01	0.05	-

Scattering properties For scattering, the following model is used:

$$\mu'_s = \mu'_{\mathrm{s,Mie,500}}(\lambda/500)^{-b_{\mathrm{Mie}}} + \mu'_{\mathrm{s,Ray,500}}(\lambda/500)^{-4}. \tag{8}$$

The parameters $\mu'_{\mathrm{s,Mie,500}}$ and b_{Mie} describe Mie scattering. Examples of values for ex vivo human skin are 1800 m^{-1} and 0.22, respectively [56]. The parameter $\mu'_{\mathrm{s,Ray,500}}$ describes Rayleigh

Biomedical Optics EXPRESS

scattering. Example of an ex vivo value is 1700 m^{-1} [56]. Low and high values are listed in Table 2, and are assumed to represent the expected magnitudes in human skin. The parameter b_{Mie} is kept constant at 0.22 [56] across all simulations. This parameter is expected to vary [57], however, changes in the coefficients were thought to represent a similar change in the wavelength-dependency that could test recovery of b_{Mie}. Further, the reflectance was found to be less sensitive to changes in scattering in the epidermal layer, and full parameter recovery of b_{Mie} was not expected. For simplicity, the parameter was not varied in the simulations.

Model geometries Geometries used in this paper are shown in Fig. 3: One-layer geometry, multi-layer geometry and two-layer geometry. The following simulations were run:

- Model A (one-layer model): All combinations of deeper layer parameters in Table 2 were used, yielding in total 16 varieties.
- Model B (multi-layer model): Deeper layer parameters in Table 2 were randomly picked in each of the layers in a three-layer model. Layer thicknesses were set to 150 µm. The simulation was run with and without an additional top layer with thickness 100 µm, melanin content 300 m^{-1} and the low scattering parameters in Table 2.
- Model C1 (systematic two-layer model): Lowest deeper layer parameters in Table 2 were used for the deeper layer. The thickness of the top layer was varied between 100, 150, 200, 250 and 300 µm, the melanin content between 150, 300 and 700 m^{-1}, and all combinations of the scattering values listed in Table 2 were used. This yielded in total 60 varieties, or 12 spectra per layer thickness step.
- Model C2 (random two-layer model): The properties of the deeper layer were randomly selected among the deeper layer parameters listed in Table 2. Parameters corresponding to the lowest scattering values were selected for the top layer, while melanin in (6) and thickness were randomly selected from a uniform probability distribution bounded by the lower and upper values in Table 2. 50 model varieties were sampled.

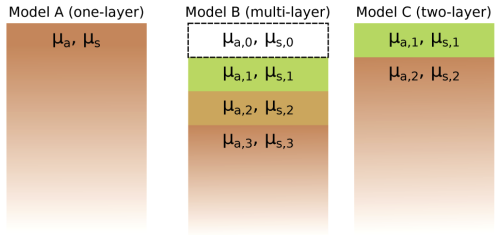

Fig. 3. Model geometries used in the Monte Carlo simulations.

2.2.2. Verification of modeling assumptions

Two main assumptions for the technique to be applicable were given in section 2.1.1.

The model A simulations (one-layer models) above yield, over the various wavelengths, a large range of possible combinations of μ_a (65 to 6714 m^{-1}) and μ_s' (1517 to 5237 m^{-1}). The assumption that the reflectance can be written as a function of μ_a/μ_s' is checked by plotting the output reflectance values as a function of μ_a/μ_s' across all simulations.

Biomedical Optics EXPRESS

The model B simulations (multi-layer models) yield the reflectance from a complex multi-layer model with and without a top layer. An empirical Monte Carlo model was constructed for looking up μ_a/μ_s' given a reflectance value through the use of a Savitzky-Golay fit and an interpolating natural cubic spline. This model was used to find the μ_a/μ_s' ratio for a one-layer model from the complex multi-layer reflectance. A μ_s' was assumed ($\mu_s' = 1000\text{m}^{-1}$), and a μ_a was calculated from the ratio. The assumption that a multi-layer model with an extra top layer is indistinguishable from a fitted one-layer model with the same top layer is then checked by comparing the latter model with an extra top layer to the original model with the same top layer.

2.2.3. Uniqueness of the inverse model solution

Diffusion model simulations were run in order to investigate whether multiple optical parameters could yield the same R, and find the shape of the relation among the optical properties, if any. A reflectance ($R = 0.6$) was picked, and a μ_a/μ_s' ratio (1/200) was set in the deeper layer of a two-layer model. Top layer thicknesses ranging from 10 to 500 µm and scattering coefficients ranging from 10 to 100 000 m^{-1} were put into the top layer. The absorption coefficient necessary to yield the assumed reflectance were derived for each parameter combination.

The uniqueness of the obtained skin parameter solution was then investigated. The inverse model was run repeatedly on the same simulated spectrum from model C1 with randomly generated start parameters in order to see whether it was possible to reach the same global solution.

2.2.4. Accuracy of the inverse modeled parameters

In addition to investigation of the uniqueness of the solution, it is desired to determine the accuracy of the inverse modeled parameters as compared to the input parameters in the Monte Carlo model. Three variations of the inverse model were run on the model C1 simulations:

1. Fit a single parameter, with all parameters except for one fixed. This estimates a baseline accuracy of the inverse model for each parameter.
2. Fit all parameters simultaneously.
3. Fit only thickness and melanin content, with scattering parameters fixed.

Model C2 picks epidermal and dermal parameters randomly across a continuous range, and is suitable for evaluating the parameter resolving performance, evaluating at multiple basis spectra and evaluating the case where the basis spectrum is not known. The same epidermal scattering parameters are used, representing a case where the epidermal scattering is known to be homogeneous. Here, three new cases of the inverse model were run:

1. Set the scattering parameter to the true parameter, estimate melanin content and thickness. Evaluates the inverse model error when the scattering is known.
2. Set the scattering parameter to the results from multi-parameter optimization on the first spectrum, estimate only melanin content and thickness for the rest. This outlines the estimated parameter behavior when the scattering is unknown but known to be homogeneous.
3. Set the scattering parameter to the true parameter and use the PCA inverse model in section 2.1.4 to fit the rest of the parameters. Here, all spectra without epidermis were used to fit a PCA transform, and the PCA transform is used to find a best basis spectrum for the spectrum at hand during optimization.

These tests should then elucidate the accuracy of the inverse model under various conditions, from which conclusions may be drawn about its application to real measurement data.

Biomedical Optics EXPRESS

2.3. Experimental tests

Hyperspectral acquisition Reflectance data were acquired using a push-broom Hyspex VNIR-1600 hyperspectral camera (Norsk Elektro Optikk, Lillestrom, Norway). The images were acquired over the wavelength range 400-1000 nm, with a spectral resolution of 3.7 nm and an integration time of 7.5 ms per line of data. The camera has been radiometrically and spectrally calibrated using light sources with known characteristics. The radiometric calibration was used to apply correction factors to the images.

The reflectance data were acquired with illumination from two linear light sources (Model 2900 Tungsten Halogen, Illumination Technologies, New York). Polarizers (VLR-100 NIR, 450-1100 nm, Meadowlark Optics, Frederick, Colorado) were mounted on the camera lens and the light sources in order to avoid specular reflection. A Spectralon reflectance target (WS-1-SL, Ocean Optics, Duiven, Netherlands) was included within each image and used to convert the raw data to reflectance spectra.

Wound model Samples of the in vitro wound model were prepared from human abdominal skin. The project was approved by the regional ethical committee (REK-Midt-Norge), and informed consent was obtained from the donor. The sample used for demonstration in this study was prepared with a 4 mm wound using punch biopsy, and the full tissue sample was cut using 8 mm punch biopsy. The sample was incubated for 22 days in Dulbecco's Modified Eagle Medium (Gibco, USA), with fetal calf serum (10%), penicillin (50 ug/ml), streptomycin (50 U/ml) and glutamine added. Hyperspectral images were acquired at day 1, 2 and then every other day, and the medium was changed every imaging session. The wound was exposed to air by resting the sample on a metallic grid, in order to ensure development and migration of multiple cell layers [36].

Re-epithelialization visible by visual inspection of the RGB images occurred during the last ten days. The sample was therefore investigated at day 12, 18 and 22.

A larger image subset over the wound boundary was selected at approximately the same region across these three days. PCA transforms were fitted to a subset of wound spectra at each day that by visual inspection and comparison of the spectra had no obvious re-epithelialization present. Each wound subset consisted of 7400 spectra, and 3 PCA components were used (explaining 87.9% of the variance, on average 0.012 RMSE between raw and reconstructed reflectance spectrum when running forward and inverse transforms). The modified PCA-based inverse model in section 2.1.4 was then run on each pixel in the larger subsets in order to yield skin parameters for the top layer.

3. Results and discussion

Simulations are presented in section 3.1. The modeling assumptions that form the basis of the inverse modeling technique are investigated using Monte Carlo simulations in section 3.1.1. The uniqueness and accuracy of inverse modeled parameters as compared to Monte Carlo simulations are given in 3.1.2 and 3.1.3. The simulation results are then summarized and discussed in section 3.1.4. The technique is used to estimate re-epithelialized layer thickness from hyperspectral images of wounds in section 3.1.5, and the performance of the technique is discussed in light of the findings from the simulation study.

3.1. Simulation study

3.1.1. Verification of modeling assumptions

Two assumptions were given in section 2.1.1. These were that the reflectance of a one-layer model can be written as a function of μ_a/μ_s', and that a multi-layer geometry with a top layer has a reflectance indistinguishable from a one-layer representation with the same top layer.

Biomedical Optics EXPRESS

The validity of the first assumption is confirmed in Fig. 4. The figure shows reflectance spectra acquired across a wide range of one-layer models, and a corresponding plot over the same reflectance values as a function of μ_a/μ_s'. The latter clearly demonstrates that there is a one-to-one correspondence between the μ_a/μ_s' ratio and the reflectance. Other studies also confirm this fact [34].

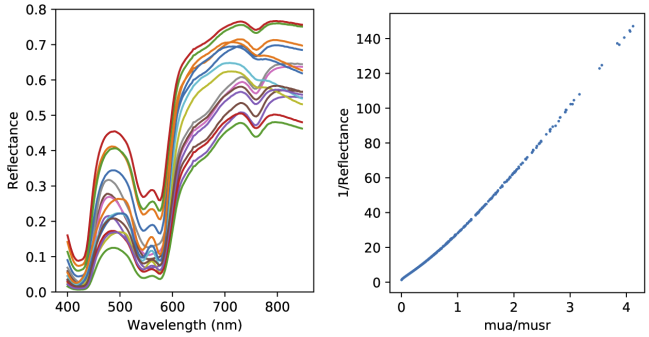

Fig. 4. Simulated Monte Carlo reflectance spectra as a function of wavelength (left), and as a function of μ_a/μ_s' (right). The reflectance is uniquely defined only down to the ratio μ_a/μ_s'. The simulations were run with 1000 000 photons per wavelength.

The second assumption was that a one-layer representation of a multi-layer model yields identical reflectance to the multi-layer model when a top layer is added to either. This is demonstrated in Fig. 5. Here, the reflectance from one-layer models constructed from each layer of the multi-layer model are used to verify that none of the upper layers completely shield the deeper layers. Further, the reflectance from the multilayer model with an epidermis on top is compared to a one-layer representation with the same epidermis on top. As they are indistinguishable, the second assumption is verified. The various optical properties at the different wavelengths represent a wide range of layer combinations that all demonstrate the validity of the second assumption. This is also mostly given by the fact that placing a layer on top of some existing model will not modify the existing parts of the model. Here, the RMSE between the two example spectra was 0.0010. Further testing the same assumption on 20 randomly generated multi-layer skin models yielded an RMSE of 0.0015.

The consequence of the two assumptions is that a top layer can be investigated without having to fully model the deeper layers, if measurements with and without the top layer are available.

3.1.2. Uniqueness of the inverse modeled solution

The combined results above means that the properties of the deeper layer are scale-invariant. This is a consequence of the output reflectance having no units [34]. A top layer is independent from the deeper layers, and a similar scale-invariant relation must exist between μ_a, μ_s' and d_1 in order to produce a unit-less reflectance at the output. The epidermal skin parameters will therefore likely be coupled.

Parameter couplings between d and μ_a for several μ_s' that yield the exact same reflectance are shown in Fig. 6. This demonstrates that there exists an infinite number of parameter sets that all yield the exact same reflectance, and sketches out the hyperplane on which the valid optical parameters reside.

To check potential skin parameter coupling, the model was fitted at random start parameters in Fig. 7. A clear relation between the estimated d_1 and the melanin content is evident. Fixing

Biomedical Optics EXPRESS

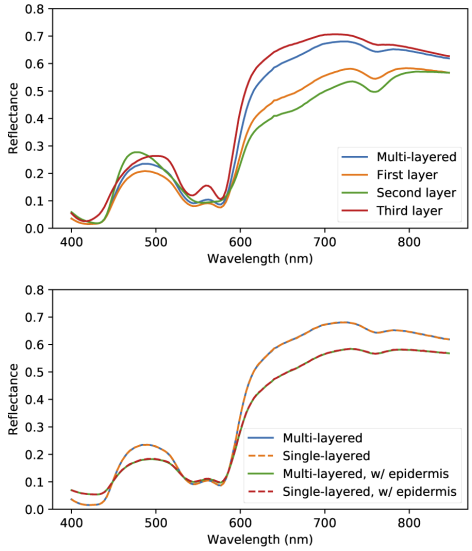

Fig. 5. Demonstration using Monte Carlo simulations that a multi-layer model and its one-layer fit have identical reflectance spectra when adding additional top layers: Comparison of the reflectance spectrum from a multi-layered model and the reflectance spectra from a one-layer model constructed from each layer (top), and the reflectance from the multi-layered model with an epidermis on top compared to a single-layer approximation with the same epidermis on top (bottom). The consequence is that a one-layer model is appropriate for representing a wound spectrum when evaluating the effect of adding an epidermis to the wound spectrum. The simulations were run with 1000 000 photons per wavelength.

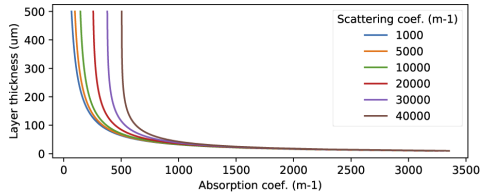

Fig. 6. Demonstration of the coupling between d, μ_a and μ_s' in the top layer in the two-layer diffusion model, for a single reflectance value. All these parameter combinations produce the same output reflectance ($R = 0.6$).

Biomedical Optics EXPRESS

the scattering to the true parameters yields the same solution regardless of the start parameters. The relation is less clear between the estimated d_1 and the scattering parameters, but there are indications of a noisy quadratic relation similar to the melanin content relation. The scattering parameters were not found to influence the reflectance as much as the other parameters within the varied range, which can explain the noisiness of the relation. The lack of influence can be observed in Fig. 6, by the relations here being significantly changed only for larger scattering coefficients.

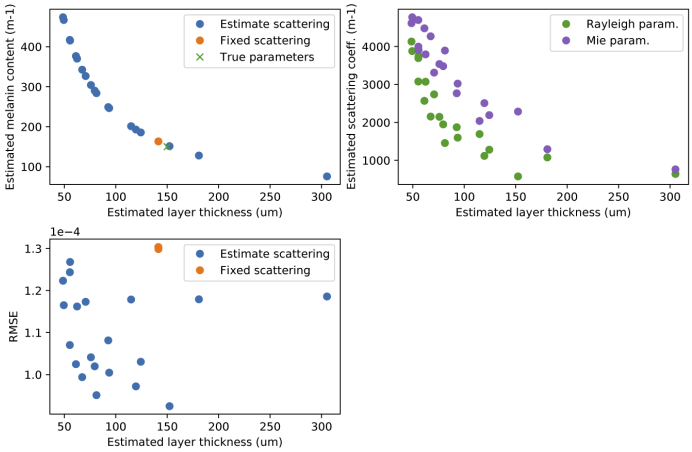

Fig. 7. Results from fitted inverse model at random start parameters, demonstrating the coupling of the fitted parameters. All parameter combinations produce the same reflectance spectra. Top left: Estimated layer thickness versus estimated melanin concentration. Top right: Estimated layer thickness versus scattering parameters. Bottom: Estimated layer thickness versus fit RMSE. Fitted parameters at random start parameters for thickness and melanin, with the scattering parameters fixed to the true scattering parameters, are marked as "Fixed scattering" in the plots.

The RMSE shows that each of these solutions are identical with respect to the simulated reflectance. Fitting all unknown parameters at the same time is therefore not expected to yield a unique solution.

The found parameter non-uniqueness can be argued from the scale-invariance between μ_a, μ_s' and d_1. The absorption coefficient μ_a is here modeled as a varying parameter multiplied by a fixed wavelength-dependency. Since the wavelength-dependency is fixed, it can be argued that the scale-invariance is translated into the parameter, and that this has a scale-invariant relation with d_1 and μ_s'. The scattering model can be re-written to $\mu_s = A\left[f(\lambda/500)^{-b_{\text{Mie}}} + (1-f)(\lambda/500)^{-4}\right]$, where $A = \mu'_{\text{s,Mie,500}} + \mu'_{\text{s,Ray,500}}$ and $f = \frac{\mu'_{\text{s,Mie,500}}}{A}$. Since f is a dimensionless number and the wavelength-dependencies are fixed, the scale-invariant relation can be translated into A and to the scattering parameters $\mu'_{\text{s,Mie,500}}$ and $\mu'_{\text{s,Ray,500}}$. A coupling between the skin parameters is therefore expected.

All of these solutions are valid with respect to the stated problem, as all yield the same fitted reflectance. It can be observed that they all apparently characterize a unique diffuse layer despite the large variation in skin parameters. Each of the valid parameter sets in Fig. 7 were used to model a single-layer model with finite thickness, and Monte Carlo simulations were used to obtain reflectance and transmittance spectra. The spectra are plotted in Fig. 8. These are more

Biomedical Optics EXPRESS

or less identical. Deviations can be attributed to albedo-dependent inaccuracies in identical diffusion model simulations that would lead to variations in a Monte Carlo simulation.

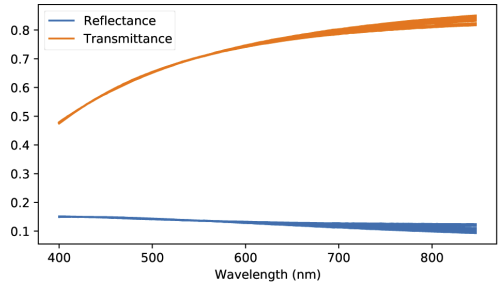

Fig. 8. Monte Carlo simulations of reflectance and transmittance through epidermises fitted at random start parameters, 50 spectra in total. Multiple spectra overlap in the plot. The simulations were run with 1000 000 photons per wavelength.

3.1.3. Accuracy of inverse modeled parameters

Systematic variation in input parameters (model C1) The error deviation results across the different parameters are shown in Fig. 9 for three cases: Fit of the particular parameter only, fit of all parameters simultaneously, and fit of melanin content and layer thickness only. Averages over the corresponding reflectance errors between fitted and original spectra are shown in Fig. 10.

The case where all parameters are fitted simultaneously is first considered. Each fitted parameter deviates over a large range (highest relative error, low/high input parameter: thickness 69%/35%, melanin content 61%/40%, Mie scattering 116%/38%, Rayleigh scattering 93%/45%). This is to be expected due to the non-uniqueness of the solution. The variation in simulated reflectance likely trigger various local minima along the scale-invariance.

Fitting a single parameter is more interesting. The deviation range for thickness and melanin content is more limited for this case, due to the uniqueness of the solution (highest relative error, low/high input parameter: thickness 17%/14%, melanin content 14%/15%). The deviation of the scattering still matches the order of magnitude of the input, however (Mie scattering 122%/46%, Rayleigh scattering 61%/29%). Changing the epidermal scattering parameters do not change the reflectance as much as the absorption and layer thickness. The scattering can therefore not be reliably estimated, even if it is the only fitted parameter. The mismatch between the diffusion model and the Monte Carlo spectra at the true parameter leads to a bias in all parameters. Varying the particular parameter only does not bridge the mismatch entirely, as seen in Fig. 10 by the higher reflectance errors as compared to the cases where multiple parameters are fitted.

The parameter b_{Mie} was not varied in the simulations. Recovered values (input 0.22) ranged from 0 to 3 in full parameter fit, and from 0 to 2 when it was the only parameter fitted.

Last, fixing scattering and fitting the rest of the parameters is considered. Fitting the thickness and melanin at the same time apparently yields a less biased estimate than when considering them apart. Further, the error is at most $80\,\mathrm{m}^{-1}$ for larger melanin contents (highest relative error, low/high input: 12%/12%), while the thickness can be estimated down to an error below 14 µm (11%/5%).

Random selection of input parameters (model C2) Parameter estimation results over random skin models are shown in Fig. 11. Using the true scattering yields a reasonable estimate of thickness and melanin content. The RMSEs are 17 µm (relative RMSE: 7%) and $57\,\mathrm{m}^{-1}$ (8%)

Biomedical Optics EXPRESS

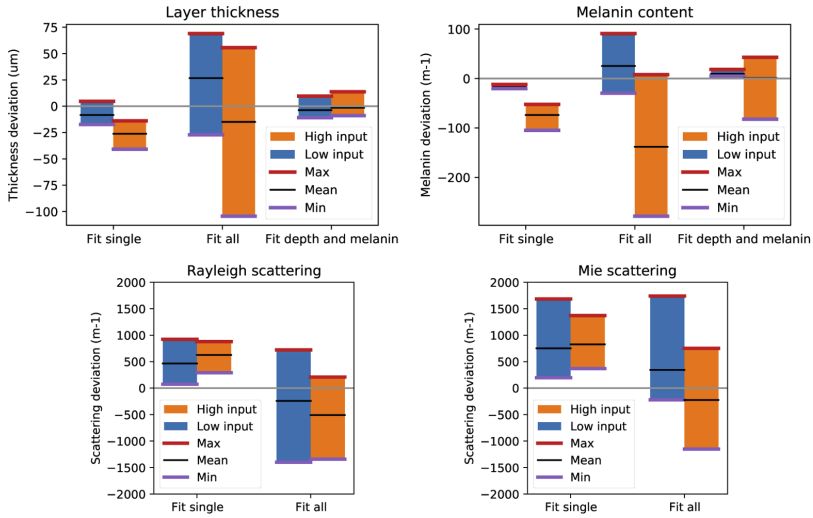

Fig. 9. Inverse model deviations from the original modeled parameters, at lowest and highest input value for each parameter: Layer thickness (top left), melanin content (top right) and scattering (bottom). The range from minimum to maximum deviation illustrates the expected error, while the offset of the mean deviation from the zero-line expresses bias. The different cases are, respectively, a fit of the parameter at hand with all other parameters fixed to the original parameters, a fit of all parameters simultaneously and a fit of layer thickness and melanin content simultaneously with scattering fixed.

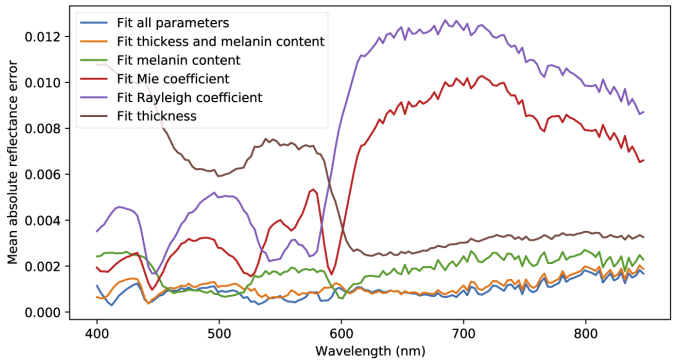

Fig. 10. Average absolute error as a function of wavelength between fitted and original MCML reflectance spectra for the various cases in Fig. 9.

Biomedical Optics EXPRESS

for the thickness and melanin contents, respectively. This is in line with the deviations found for thickness (below 14 µm) and melanin contents (below 80 m^{-1}) when fitting these simultaneously on the systematic variation earlier.

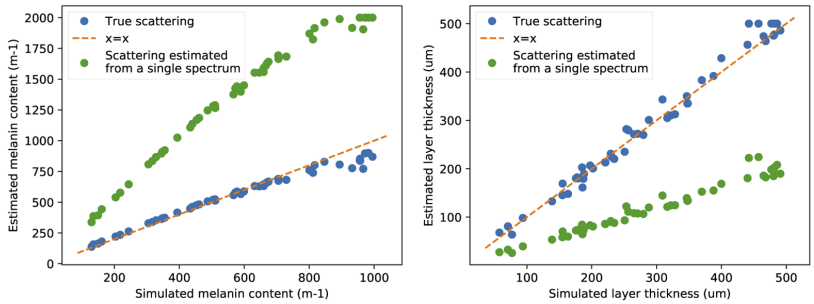

Fig. 11. Modeled parameters versus estimated parameters across Monte Carlo simulations with random input parameters, fixed scattering. Two cases are shown: Scattering parameters fixed to the true scattering (blue), and scattering parameters fixed to the parameters estimated from a single reflectance spectrum (green). The former leads to reasonable estimates of thickness and melanin content, while the latter leads to estimates that are only correlated with the true parameters.

Exact knowledge of the correct scattering is challenging. It is expected that it must be guessed in the application at hand. A case where the scattering is estimated from a single reflectance spectrum and fixed for the rest of the spectra is shown in the same figure above. Both melanin content and thickness estimates become biased, but they remain correlated with the true parameters and retain variations that are similar to the case where the true scattering is used. Although the scattering is not known and the thickness estimates are incorrect, this can then still be used to detect relative thickness changes.

The method is to be applied to hyperspectral images of wounds, where the basis spectrum is not known a priori. The modification of the technique, as outlined in section 2.1.4, was used to fit basis spectra along with the rest of the epidermal skin parameters. The resulting RMSEs were 16 µm (relative RMSE: 6%) and 50 m^{-1} (13%) for the thickness and melanin parameters, respectively, similar to RMSEs in the case where the basis spectra are known exactly.

3.1.4. Summary and general discussion of the simulation results

The inverse modeling method presented in this paper could be a valuable tool for characterizing hyperspectral images of re-epithelialized tissues in wounds.

The main inverse modeling assumptions have been verified. The reflectance of a one-layer model can be written as a function of μ_a/μ_s'. This means that any combination of μ_a and μ_s' yields the same reflectance as long as they obey the given ratio. Further, an arbitrary multi-layer model can be represented by a one-layer model. Adding a top layer to either of these models yields indistinguishable reflectance spectra. Thus, the top layer can be fitted and investigated without considering the deeper layers.

It has been shown that no unique solutions exist for the top layer. The solutions are coupled, however, and yield unique $R(\lambda)$ and $T(\lambda)$ through the upper layer that are common for all parameter sets. The fitted, diffuse layer is therefore unique, though the lack of a known thickness means that the optical properties are undeterminable. The wavelength dependency in R and T can be valuable for drawing conclusions about the nature of the layer.

Biomedical Optics EXPRESS

The solutions for some of the skin parameters were found to be robust to changes in the start parameters during fitting when at least one parameter was fixated. This indicates that unique solutions may be possible to find in such cases. The reflectance was not found to be very sensitive to changes in the scattering parameter within the expected range. The scattering parameter is therefore a first choice for fixation. Fair estimates of the absorption parameter and layer thickness can be found when given the correct scattering, and the main expected levels can be discriminated. The method has been shown to yield reasonable relative estimates when the scattering is homogeneous, but unknown. The parameter value will then vary around a mean level within a small deviation, and be correlated with the true value. Such estimates are useful for determining whether a given location has a top layer thickness greater or less than the thickness of some other location. In practice, the scattering parameters can be fixed to e.g. the low parameter values outlined in section 2.2.1. Another possibility is to let all parameters be fitted simultaneously for a single spectrum in order to estimate a best fit for the wavelength-dependency, and then fixate the scattering parameters to these parameters for the rest of the spectra.

The method is thus useful for in vitro wounds in two ways. First by demonstrating whether the optical properties of various tissue regions can be explained by wound optical properties with an epidermal layer on top. Second by evaluating relative layer thicknesses at different positions, and further use these to explain spatial variations by layer thickness differences.

Melanin and thickness parameter fits have been found to have relative errors from 5 to 12%. Inverse methods in other studies that estimate epidermal thickness and melanin content are reported to have errors in the range of 9% for epidermal thickness and 8-15% for melanin content [58], or 6-8%, 16-20% for epidermal thickness and below 0.5% for melanin content [31], subject to modeling details. Relative errors of the current model are thus in the same range as methods reported in the literature.

A weakness of the method is that the basis spectrum representing the deeper layers must be known. While known exactly for the simulations, wounds have inhomogeneities that result in no clear basis candidate. Taking a mean spectrum over the wound was not found to yield correct wavelength-dependencies. Iterating over all possible wound spectra and selecting the best candidate was found to yield better wavelength-dependencies and lower RMSEs, but this is problematic for a larger number of pixels. Using a PCA transform to represent the possible wound spectra was found to be a viable alternative that could be fitted during optimization. This alternative has been shown to yield similar parameter RMSEs to the case where the basis spectrum is known exactly. This thus represents a suitable modification to the technique for hyperspectral images of wounds.

The layer uniqueness results show that a more direct approach technically could be taken in obtaining the reflectance and transmittance of the diffuse top layer, using a similar approach as the adding-doubling technique [59]. Such a technique would obtain reflectance and transmittance directly. A separate characterization using a one-layer model with finite thickness would be necessary for parameter estimation. The method in the current study obtains the parameters directly as a part of the procedure. Obtaining reflectance and transmittance would have to be done as a second step. Which method would be better to use would then depend on the application and the desired end result of the technique. A variant of adding-doubling would more clearly show that no unique parameters exist. It would not assume anything on the form of the optical properties of the top layer during fitting, which could be valuable as a more independent result. On the other hand, the form assumptions are necessary for enabling application of the PCA modification of the technique.

For this study, an inverse diffusion model with an offset correction obtained from Monte Carlo simulations was used. Its performance would thus be similar to an inverse Monte Carlo model with some minor inaccuracies. This allows the technique to be evaluated in terms of the basic idea rather than being overshadowed by systematic errors, while making the model suitable for

Biomedical Optics EXPRESS

hyperspectral applications. Similar corrections include a background absorption included by Svaasand et al. [44] and blood volume fraction scaling done by Randeberg et al. [46]. The offset correction is not expected to work outside the parameter range for which it was fitted, and is thus not appropriate for any unknown spectrum. More elaborate correction schemes or better model approximations are required. The model could be replaced by an empirical Monte Carlo model, or a diffusion approximation more appropriate for the absorption/scattering ratios in human tissue. Examples include the δ-Eddington/δ-P1 approximation [47,60]. The latter will not eliminate the offset between the model and the Monte Carlo spectra entirely [47]. In addition, it should be noted that correction factors developed for simulated reflectance spectra in an integrating sphere geometry will not directly apply to reflectance spectra from hyperspectral images. Model replacement is out of scope for the current study, where the main aim is to present and demonstrate a proof of concept. Refining the core model will be a part of future studies.

The simulations have thus verified the applicability of the technique, identified limitations and indicated what it can be used for. The technique can then be applied to experimental data. Thickness estimation of re-epithelialized areas in hyperspectral images of wounds is used as an example application.

3.1.5. Experimental results

In the following, hyperspectral images of an in vitro wound model sample were used to demonstrate the inverse modeling technique. The PCA-based modification in section 2.1.4 was used to represent the wound spectra using PCA during fitting. Layer thickness results over a hyperspectral image subset at days 12, 18 and 22 during the wound healing process are shown in Fig. 12. Model fits for selected spectra from day 18 are shown in Fig. 13.

The first main conclusion to be drawn from these results is that the spectral properties of the edge of the wound are explained by a gradually increasing re-epithelialization. This is modeled as a diffuse, epidermal-like layer placed on top of reflectance representing wound tissue. The layer has been shown in the simulation study to be unique. The fitted model then works as an explanatory model. The model shows that these regions have re-epithelialized, and that the optical properties here are no more than the optical properties of the wound with a typical epidermis on top. The main strength of the technique is that this can be shown without having to consider the optical properties of the dermal layers. This is a major advantage of the method as the optical properties of in vitro wound models are largely unknown. Minor changes that are challenging to identify in the RGB images can be found by the technique, as demonstrated by a thin epidermis apparently being present at the wound edge of day 12 in Fig. 12.

Depth profiles along lines placed at the approximately same position across days are shown in Fig. 14. The estimated layer thicknesses here provide a relative estimate of the re-epithelialization thickness, given that the scattering properties are homogeneous, as shown by the simulation study. In vitro wounds which are exposed to air and incubated in the medium used in this study are expected to have migration of multiple epidermal cell layers which quickly stratify into more mature epithelium [36]. This migration occurs from the edge of the wound and towards the center of the wound, with a tip of non-cornified epidermis extending on the wound side of a more mature neo-epidermis [61]. Such behavior is consistent with the migration and increases in thickness represented by the depth profiles. An epidermal thickness of magnitude 50 um is expected [3], however, indicating that higher absorption or scattering magnitudes than the ones currently used in the model are in order. Histologies were not available for the wound model samples in this study, and repetition of the experiment is necessary for proper attribution of the reflectance changes to corresponding changes in epidermal layer composition. However, the epidermal layer presence indicated by the inverse model results is in agreement with statistical characterization of these data [38].

Biomedical Optics EXPRESS

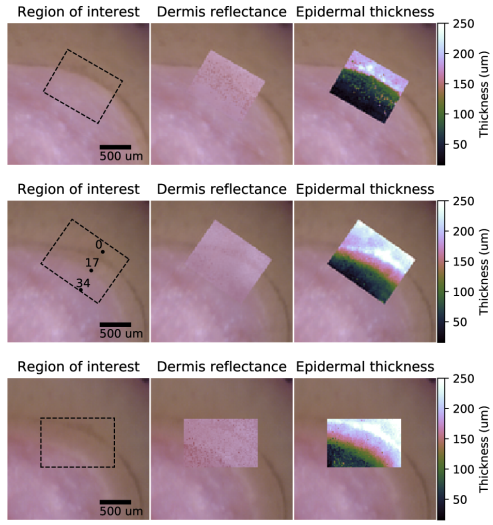

Fig. 12. Results from application of the inverse model to hyperspectral images of an in vitro wound model sample. Three measurements are shown: day 12 (top row), day 18 (center row) and day 22 (bottom row). For each measurement, three images are shown: the RGB image with a dotted square indicating the image subset considered in the inverse model, the RGB values of the reflectance from the one-layer dermis reconstruction within the subset, and the estimated thickness of the epidermis within the subset. RGB images were constructed from the hyperspectral images at 615, 564 and 459 nm wavelength bands, and were gamma-corrected for increased contrast. The white-pink region corresponds to wound, while the brown region is intact tissue. Coordinates of the spectra plotted in Fig. 13 are marked in the day 18 image.

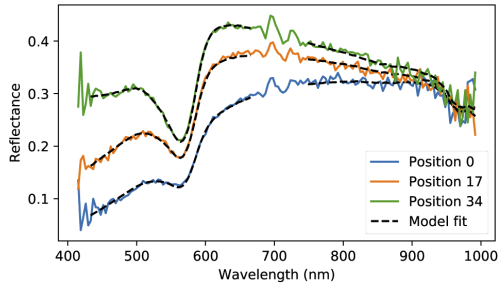

Fig. 13. Model fits at selected spectra from day 18. The labeled positions refer to the positions used in Fig. 14, and are marked in Fig. 12. The peaks between 690 and 750 nm are artifacts due to mismatch of the order sorting filter in the hyperspectral camera, and were not fitted by the model. Fitted parameters were the melanin content, layer thickness and scattering parameters in epidermis, and the three PCA coefficients for the wound basis in dermis.

Biomedical Optics EXPRESS

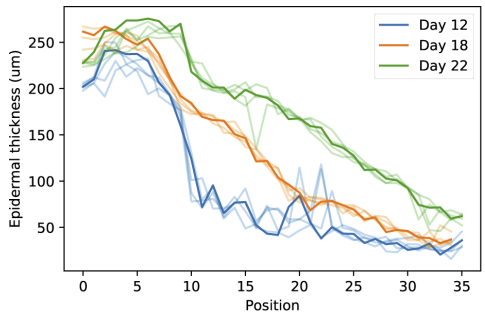

Fig. 14. Estimated depth profile along lines placed at approximately the same region at days 12, 18 and 22. The strongest colored plotted line is along the chosen line in the image, while weaker lines of the same color are profiles offset 1 and 2 pixels from the main line.

Variations in absorption properties are not expected to be decouplable from thickness variations for real measurements. The fitted inverse model is able to match the reality in the simulations, which gives a clear minimum of the RMSE during optimization. More complex geometries or changes to the assumed optical properties broadens the minimum for real measurements, due to existence of multiple slightly sub-optimal solutions to the problem. Here, a melanin content range from $150\,\mathrm{m}^{-1}$ to above $700\,\mathrm{m}^{-1}$ and corresponding layer thicknesses yielded identical solutions. A clear minimum could only be found for high scattering levels, but in this case, this led to compensation by unrealistically high melanin contents.

The only absorber included in epidermis was melanin. Inclusion of a background absorption is expected to perturb the fitted parameter results, and could reduce the required melanin absorption and make the minimum mentioned above more clear. This was not investigated further, however, and tuning of such modeling details should wait until confirmation of the epidermal composition by histology. This will therefore be investigated in future work.

The simulation study indicates that at least one parameter should be fixed. All parameters were fitted simultaneously here, however, and no parameters were fixed, since the optimization seemed to produce stable estimates of both absorption and scattering properties. Only minor instabilities are evident in the day 12 profile in Fig. 14. This then shows that fitting a multi-parameter model to some reflectance might apparently give stable, unique results - but only by accident. Care must be taken, since the end result is dependent on the start parameters. Fixing at least one of the parameters is necessary for trustworthy results, as shown by the simulation study. Yet, as the parameters were stable in current case, these are the same results that would be obtained if e.g. the scattering parameters were fixed. Estimated parameters are then expected to correlate with the true parameters, as shown by the simulation study.

An infinitely wide beam illuminating a spatially invariant slab is effectively assumed in the simulations. The width of the beam is sufficiently broad with respect to the extent of the wound model sample, but the illuminated geometry is not homogeneous. Edge effects will be present in sharp transitions of tissue types, and lead to escaped photons from one type of tissue into the other. This will lead to an under- or over-estimation of thickness or absorption properties in some parts [32], but this is unlikely to have a significant effect within the slowly varying parts of the tissue. More investigation could be made in future studies into adjusting the model to the measurement geometry.

PCA was used to find a low-dimensional representation of the wound spectra that could be fitted during optimization. The PCA inverse transform with the selected number of components

Biomedical Optics EXPRESS

was found to be able to appropriately reproduce a given spectrum, and fitting the PCA scores during optimization gave reasonable results in the epidermal parameters. The simulation results indicate no significant decrease in estimation accuracy for the simulations. However, correctness for measurements should be investigated further in future studies, as the method might need tuning in e.g. number of components, or a different decomposition method than PCA might be more appropriate. The method is promising, however, and combines a data-driven, statistical approach to information extraction with physics-based photon transport modeling.

The method was tailored towards wounds, as the basis spectrum is available and can be used to fit spectra with a top layer. With adaption it might be possible to use the technique to estimate relative variations in the epidermal skin thickness of pre-term newborns and characterize burn wounds. Further, the technique is suitable for characterizing strongly absorptive inclusions in scattering media.

A spectrum from a single pixel was on average fitted in 0.66 seconds on a single CPU core, and 0.14 seconds when naively parallelizing the fitting of different pixels across 8 CPU cores (Intel Core i7-3840 QM, 2.80 GHz, 8 cores). The small subset of 50 x 40 pixels considered here would take 4 minutes and 40 seconds to fit using naive multiprocessing. The method currently runs a full, separate optimization of every pixel, which might not be needed. Future work will include adaption of GPU parallelization to reduce the running times. The current method, albeit slow, represents a proof of concept against which optimized solutions may be compared for correctness, and represents a first step towards a more scalable algorithm.

4. Conclusion

A technique for estimating the skin parameters of the re-epithelialized layer in wounds has been developed. The method has been found to characterize a unique diffuse layer defined by a unique reflectance and transmittance spectrum. There exists an infinite number of valid skin parameters that might characterize this layer. Fixing e.g. scattering parameters, however, can yield good relative estimates of layer thickness. The method has been used to characterize a larger area over the boundary of an in vitro wound model sample, showing the usefulness of the approach in characterizing the re-epithelialized layer. Here, a PCA modification to find the optimal wound basis spectrum has also been demonstrated, and represents a successful combination of data-driven techniques with physical photon transport modeling.

Acknowledgments

Thanks to Ingvild Haneberg and Matija Milanic for acquisition of in vitro skin model data. Thanks to Brita Pukstad for collaboration in the in vitro wound model experiment. Thanks to Terje Schjelderup for help with the proofreading.

Disclosures

The authors declare no conflicts of interest.

References

1. T. A. Eikebrokk, B. S. Vassmyr, K. Ausen, C. Gravastrand, and B. Pukstad, "Cytotoxicity and effect on wound re-epithelialization after topical administration of tranexamic acid," BJS Open **3**(6), 840–851 (2019).
2. S. Lönnqvist, P. Emanuelsson, and G. Kratz, "Influence of acidic ph on keratinocyte function and re-epithelialisation of human in vitro wounds," J. Plast. Surg. Hand Surg. **49**(6), 346–352 (2015).
3. S. Lönnqvist, J. Rakar, K. Briheim, and G. Kratz, "Biodegradable gelatin microcarriers facilitate re-epithelialization of human cutaneous wounds - an in vitro study in human skin," PLoS One **10**(6), e0128093 (2015).
4. G. Kratz and C. C. Compton, "Tissue expression of transforming growth factor-β1 and transforming growth factor-αduring wound healing in human skin explants," Wound Rep. Reg. **5**(3), 222–228 (1997).

Biomedical Optics EXPRESS

5. E. Nyman, F. Huss, T. Nyman, J. Junker, and G. Kratz, "Hyaluronic acid, an important factor in the wound healing properties of amniotic fluid: In vitro studies of re-epithelialisation in human skin wounds," J. Plast. Surg. Hand Surg. **47**(2), 89–92 (2013).
6. G. Lu and B. Fei, "Medical hyperspectral imaging: a review," J. Biomed. Opt. **19**(1), 010901 (2014).
7. L. Khaodhiar, T. Dinh, K. T. Schomacker, S. V. Panasyuk, J. E. Freeman, R. Lew, T. Vo, A. A. Panasyuk, C. Lima, J. M. Giurini, T. E. Lyons, and A. Veves, "The use of medical hyperspectral technology to evaluate microcirculatory changes in diabetic foot ulcers and to predict clinical outcomes," Diabetes Care **30**(4), 903–910 (2007).
8. M. Denstedt, B. S. Pukstad, L. A. Paluchowski, J. E. Hernandez-Palacios, and L. L. Randeberg, "Hyperspectral imaging as a diagnostic tool for chronic skin ulcers," Proc. SPIE **8565**, 85650N (2013).
9. A. Nouvong, B. Hoogwerf, E. Mohler, B. Davis, A. Tajaddini, and E. Medenilla, "Evaluation of diabetic foot ulcer healing with hyperspectral imaging of oxyhemoglobin and deoxyhemoglobin," Diabetes Care **32**(11), 2056–2061 (2009).
10. D. Yudovsky, A. Nouvong, and L. Pilon, "Hyperspectral imaging in diabetic foot wound care," J. Diabetes Sci. Technol. **4**(5), 1099–1113 (2010).
11. A. Holmer, J. Marotz, P. Wahl, M. Dau, and P. W. Kämmerer, "Hyperspectral imaging in perfusion and wound diagnostic - methods and algorithms for the determination of tissue parameters," Biomed. Tech. **63**(5), 547–556 (2018).
12. M. A. Calin, T. Coman, S. V. Parasca, N. Bercaru, and S. R. S. D. Manea, "Hyperspectral imaging-based wound analysis using mixture-tuned matched filtering classification method," J. Biomed. Opt. **20**(4), 046004 (2015).
13. M. A. Calin, S. V. Parascal, D. Manea, and R. Savastru, "Hyperspectral imaging combined with machine learning classifiers for diabetic leg ulcer assessment - a case study," in *MIUA 2019: Medical Image Understanding and Analysis*, vol. 1065, (2019), pp. 74–85.
14. G. Daeschlein, I. Langner, T. Wild, S. von Podewils, C. Sicher, T. Kiefer, and M. Jünger, "Hyperspectral imaging as a novel diagnostic tool in microcirculation of wounds," Clin. Hemorheol. Microcirc. **67**(3-4), 467–474 (2017).
15. L. A. Paluchowski, H. B. Nordgaard, A. Bjorgan, S. A. Berget, and L. L. Randeberg, "Can spectral-spatial image segmentation be used to discriminate burn wounds?" J. Biomed. Opt. **21**(10), 101413 (2016).
16. M. Halicek, G. Lu, J. V. Little, X. Wang, M. Patel, C. C. Griffith, M. W. El-Deiry, A. Y. Chen, and B. Fei, "Deep convolutional neural networks for classifying head and neck cancer using hyperspectral imaging," J. Biomed. Opt. **22**(6), 060503 (2017).
17. H. Akbari, L. Halig, D. M. Schuster, B. Fei, A. Osunkoya, V. Master, P. Nieh, and G. Chen, "Hyperspectral imaging and quantitative analysis for prostate cancer detection," J. Biomed. Opt. **17**(7), 0760051 (2012).
18. J. Shapey, Y. Xie, E. Nabavi, R. Bradford, S. R. Saeed, S. Ourselin, and T. Vercauteren, "Intraoperative multispectral and hyperspectral label-free imaging: A systematic review of in vivo clinical studies," J. Biophotonics **12**(9), e201800455 (2019).
19. E. L. Larsen, L. L. Randeberg, E. Olstad, O. A. Haugen, A. Aksnes, and L. O. Svaasand, "Hyperspectral imaging of atherosclerotic plaques in vitro," J. Biomed. Opt. **16**(2), 026011 (2011).
20. A. O. H. Gerstner, W. Laffers, F. Bootz, D. L. Farkas, R. Martin, J. Bendix, and B. Thies, "Hyperspectral imaging of mucosal surfaces in patients," J. Biophotonics **5**(3), 255–262 (2012).
21. M. Wahabzada, M. Besser, M. Khosravani, M. T. Kuska, K. Kersting, A.-K. Mahlein, and E. Stürmer, "Monitoring wound healing in a 3d wound model by hyperspectral imaging and efficient clustering," PLoS One **12**(12), e0186425 (2017).
22. Y. Khouj, J. Dawson, J. Coad, and L. Vona-Davis, "Hyperspectral imaging and k-means classification for histologic evaluation of ductal carcinoma in situ," Front. Oncol. **8**, 17 (2018).
23. E. J. M. Baltussen, E. N. D. Kok, S. G. B. de Koning, J. Sanders, A. G. J. Aalbers, N. F. M. Kok, G. L. Beets, C. C. Flohil, S. C. Bruin, K. F. D. Kulhmann, H. J. C. M. Sterenborg, and T. J. M. Ruers, "Hyperspectral imaging for tissue classification, a way toward smart laparoscopic colorectal surgery," J. Biomed. Opt. **24**(01), 1 (2019).
24. B. Regeling, W. Laffers, A. O. H. Gerstner, S. Westermann, N. A. Müller, K. Schmidt, J. Bendix, and B. Thies, "Development of an image pre-processor for operational hyperspectral laryngeal cancer detection," J. Biophotonics **9**(3), 235–245 (2016).
25. A. Grigoroiu, J. Yoon, and S. E. Bohndiek, "Deep learning applied to hyperspectral endoscopy for online spectral classification," Sci. Rep. **10**(1), 3947 (2020).
26. D. Yudovsky, A. Nouvong, K. Schomacker, and L. Pilon, "Monitoring temporal development and healing of diabetic foot ulceration using hyperspectral imaging," J. Biophotonics **4**(7-8), 565–576 (2011).
27. S. Vyas, A. Banerjee, and P. Burlina, "Estimating physiological skin parameters from hyperspectral signatures," J. Biomed. Opt. **18**(5), 057008 (2013).
28. W. Feng, R. Shi, C. Zhang, T. Yu, and D. Zhu, "Lookup-table-based inverse model for mapping oxygen concentration of cutaneous microvessels using hyperspectral imaging," Opt. Express **25**(4), 3481–3495 (2017).
29. E. Zherebtsov, V. Dremin, A. Popov, A. Doronin, D. Kurakina, M. Kirillin, I. Meglinski, and A. Bykov, "Hyperspectral imaging of human skin aided by artificial neural networks," Biomed. Opt. Express **10**(7), 3545–3559 (2019).
30. M. Kewin, A. Rajaram, D. Milej, A. Abdalmalak, L. Morrison, M. Diop, and K. S. Lawrence, "Evaluation of hyperspectral nirs for quantitative measurements of tissue oxygen saturation by comparison to time-resolved nirs," Biomed. Opt. Express **10**(9), 4789–4802 (2019).

Biomedical Optics EXPRESS

31. D. Yudovsky and L. Pilon, "Rapid and accurate estimation of blood saturation, melanin content, and epidermis thickness from spectral diffuse reflectance," Appl. Opt. **49**(10), 1707–1719 (2010).
32. A. Bjorgan, M. Milanic, and L. L. Randeberg, "Estimation of skin optical parameters for real-time hyperspectral imaging applications," J. Biomed. Opt. **19**(6), 066003 (2014).
33. M. S. Patterson, B. C. Wilson, and D. R. Wyman, "The propagation of optical radiation in tissue. ii: Optical properties of tissues and resulting fluence distributions," Lasers Med. Sci. **6**(4), 379–390 (1991).
34. G. Zonios and A. Dimou, "Modeling diffuse reflectance from semi-infinite turbid media: application to the study of skin optical properties," Opt. Express **14**(19), 8661–8674 (2006).
35. A. Kim and B. C. Wilson, *Optical-Thermal Response of Laser-Irradiated Tissue* (Springer, 2011), chap. Measurement of ex vivo and in vivo tissue optical properties: Methods and theories, pp. 267–319, 2nd ed.
36. K. Jansson, G. Kratz, and A. Haegerstrand, "Characterization of a new in vitro model for studies of reepithelialization in human partial thickness wounds," In Vitro Cell. Dev. Biol.: Anim. **32**(9), 534–540 (1996).
37. G. Kratz, "Modeling of wound healing processes in human skin using tissue culture," Microsc. Res. Tech. **42**(5), 345–350 (1998).
38. A. Bjorgan, B. Pukstad, and L. L. Randeberg, "Hyperspectral characterization of re-epithelialization in an in vitro wound model," J. Biophotonics (2020).
39. G. James, D. Witten, T. Hastie, and R. Tibshirani, *An introduction to statistical learning* (Springer, 2013), 1st ed.
40. G. Shaw and D. Manolakis, "Signal processing for hyperspectral image exploitation," IEEE Signal Process. Mag. **19**(1), 12–16 (2002).
41. J. Khodr and R. Younes, "Dimensionality reduction on hyperspectral images: A comparative review based on artificial datas," in *2011 4th International Congress on Image and Signal Processing* (IEEE, 2011), pp. 1875–1883.
42. M. D. Farrell and R. M. Mersereau, "On the impact of pca dimension reduction for hyperspectral detection of difficult targets," IEEE Geosci. Remote Sens. Lett. **2**(2), 192–195 (2005).
43. L. Wang, S. L. Jacques, and L. Zheng, "Mcml monte carlo modeling of light transport in multi-layered tissues," Comput. Meth. Prog. Bio. **47**(2), 131–146 (1995).
44. L. Svaasand, L. Norvang, E. Fiskerstrand, E. Stopps, M. Berns, and J. Nelson, "Tissue parameters determining the visual appearance of normal skin and port-wine stains," Laser. Med. Sci. **10**(1), 55–65 (1995).
45. L. V. Wang and H. Wu, *Biomedical Optics, Principles and Imaging* (John Wiley & Sons, 2007).
46. L. L. Randeberg, A. Winnem, R. Haaverstad, O. A. Haugen, and L. O. Svaasand, "Performance of diffusion theory vs. monte carlo methods," Proc. SPIE **5862**, 586200 (2005).
47. T. Spott and L. O. Svaasand, "Collimated light sources in the diffusion approximation," Appl. Opt. **39**(34), 6453–6465 (2000).
48. R. R. Anderson and J. A. Parrish, "The optics of human skin," J. Invest. Dermatol. **77**(1), 13–19 (1981).
49. I. Fredriksson, O. Burdakov, M. Larsson, and T. Strömberg, "Inverse monte carlo in a multilayered tissue model: merging diffuse reflectance spectroscopy and laser doppler flowmetry," J. Biomed. Opt. **18**(12), 127004 (2013).
50. T. Lister, P. A. Wright, and P. H. Chappell, "Optical properties of human skin," J. Biomed. Opt. **17**(9), 0909011 (2012).
51. N. Verdel, A. Marin, M. Milanic, and B. Majaron, "Physiological and structural characterization of human skin in vivo using combined photothermal radiometry and diffuse reflectance spectroscopy," Biomed. Opt. Express **10**(2), 944–960 (2019).
52. L. Vidovic, M. Milanic, and B. Majaron, "Objective characterization of bruise evolution using photothermal depth profiling and monte carlo modeling," J. Biomed. Opt. **20**(1), 017001 (2015).
53. E. Alerstam, W. C. Y. Lo, T. D. Han, J. Rose, S. Andersson-Engels, and L. Lilge, "Next-generation acceleration and code optimization for light transport in turbid media using gpus," Biomed. Opt. Express **1**(2), 658–675 (2010).
54. E. Alerstam, T. Svensson, and S. Andersson-Engels, "Parallel computing with graphics processing units for high-speed monte carlo simulation of photon migration," J. Biomed. Opt. **13**(6), 060504 (2008).
55. T. Spott, L. O. Svaasand, R. E. Anderson, and P. F. Schmedling, "Application of optical diffusion theory to transcutaneous bilirubinometry," Proc. SPIE **3195**, 234–245 (1998).
56. A. N. Bashkatov, E. A. Genina, and V. V. Tuchin, "Optical properties of skin, subcutaneous, and muscle tissues: A review," J. Innov. Opt. Health Sci. **04**(01), 9–38 (2011).
57. S. L. Jacques, "Optical properties of biological tissues: a review," Phys. Med. Biol. **58**(11), R37–R61 (2013).
58. P. Naglic, L. Vidovic, M. Milanic, L. L. Randeberg, and B. Majaron, "Suitability of diffusion approximation for an inverse analysis of diffuse reflectance spectra from human skin in vivo," OSA Continuum **2**(3), 905–922 (2019).
59. S. A. Prahl, *Optical-Thermal Response of Laser Irradiated Tissue* (1995), chap. 5, The adding-doubling method, pp. 101–129.
60. S. A. Carp, S. A. Prahl, and V. Venugopalan, "Radiative transport in the delta-p1 approximation: accuracy of fluence rate and optical penetration depth predictions in turbid semi-infinite media," J. Biomed. Opt. **9**(3), 632–647 (2004).
61. G. D. Glinos, S. H. Verne, A. S. Aldahan, L. Liang, K. Nouri, S. Elliot, M. Glassberg, D. C. DeBuc, T. Koru-Sengul, M. Tomic-Canic, and I. Pastar, "Optical coherence tomography for assessment of epithelialization in a human ex vivo wound model," Wound Rep. Reg. **25**(6), 1017–1026 (2017).

Paper III

A. Bjorgan, B. S. Pukstad, and L. L. Randeberg, “Identification of wound healing in an in vitro wound model,” To be submitted.

Identification of wound healing in an in vitro wound model

Asgeir Bjorgan[1], Brita Pukstad[2,3], and Lise Lyngsnes Randeberg[1]

[1]*Department of Electronic Systems, NTNU Norwegian University of Science and Technology, Trondheim, Norway*
[2]*Department of Clinical and Molecular Medicine, NTNU Norwegian University of Science and Technology, Trondheim, Norway*
[3]*Department of Dermatology, St. Olavs Hospital, Trondheim University Hospital, Trondheim, Norway*

December 25, 2020

Abstract

It is a major clinical challenge to assess whether a wound or ulcer is healing. In vitro wound models provide controllable means for investigating wound healing in a laboratory setting. The healing process can then be assessed systematically by e.g. histology. However, histology is a destructive technique and optical techniques such as hyperspectral imaging might be a better choice as it enables non-invasive characterization of the same sample over time. The aim of this study is to identify key markers in hyperspectral reflectance- and fluorescence images, and then use these markers for auto-detection of wound healing. Factors like collagen formation and re-epithelialization are hypothesized to affect the spectral data. A reflectance clustering model is used as a baseline to analyze the wound development. This model is further expanded using supervised classification techniques. Peak shift analysis and basic modeling techniques are used to interpret the fluorescence before comparison to reflectance data. It is shown that fluorescence peak properties can be used to visualize the wound boundary. The extracted fluorescence properties are shown to be related to re-epithelialization rather than collagen formation. Re-epithelialization can also be detected from reflectance derivatives, which is shown to provide high cross-validation scores using a linear classifier needing only a few wavelengths. It is thus found that fluorescence imaging provides uncomplicated visualization of re-epithelialization, while reflectance imaging yields features well suitable for training of robust, but still simple wound classification techniques.

1 Introduction

In vitro wound models are useful for investigation of wound healing. The main goal of this study is to find histology-free, objective and automatic means for identifying and evaluating

wound healing in such models.

Previously, hyperspectral reflectance images of wound models followed over 22 days were characterized [2]. The reflectance spectra from wounds differed from re-epithelialized and intact skin in a consistent way. The changes in optical properties were attributable to an increasing thickness of the epidermal layer [2, 4]. It is therefore hypothesized that automatic classification of unhealed wound tissue is possible using hyperspectral imaging. A classification map can in turn be used to calculate the wound size over time and identify whether a wound model is healing.

Two main simultaneous processes are present during wound healing: Re-epithelialization, and collagen formation. The former is detectable using hyperspectral reflectance imaging [2]. Hyperspectral fluorescence imaging is a promising technique for detection of the latter. The aim of this study is to identify key features in the fluorescence and reflectance data, use these to characterize wound healing, and finally develop robust and automatic techniques for such characterization. Wang et al. [20] has earlier used fluorescence spectroscopy to characterize collagen and tryptophan in similar wound models at excitation/emission wavelengths 335/390 nm and 295/340 nm, respectively, to evaluate wound closure and image keratinocyte proliferation.

Details on the wound model preparation and measurement setup is given in an earlier study [2]. In short, 8 wound models were prepared: 2 without wounds, 3 with 3 mm sized wounds, 3 with 4 mm sized wounds. These wound models were measured every other day over a period of 22 days using a HySpex VNIR-1600 hyperspectral camera (Norsk Elektro Optikk, Lillestrom, Norway). The samples were illuminated in reflectance mode by two linear light sources (Model 2900 Tungsten Halogen, Illumination Technologies, New York) and then in fluorescence mode by excitation by a 355 nm light source. The excitation wavelength was chosen in order to excite collagen signatures within the wavelength range of the imaging system.

2 Background

2.1 Wound healing

Wound healing is a complex multi-step process, which involves triggers and biological mechanisms that are fully outlined in Singer et al. [16] and Arnoux et al. [1]. For brevity, only parts relevant for optical characterization are given here. Epidermal cells [16] (keratinocytes [1]) start migrating into the wound from the surrounding tissue a few hours after the injury, which after 1-2 days starts generating new epidermal cells from the edge and into the center of the wound [16]. Fibroblasts migrate into the wound after four days, and start to deposit a collagen matrix in the wound area, causing a remodeling of the extracellular matrix [16]. Collagen type III is produced, to later be replaced by collagen type I [1].

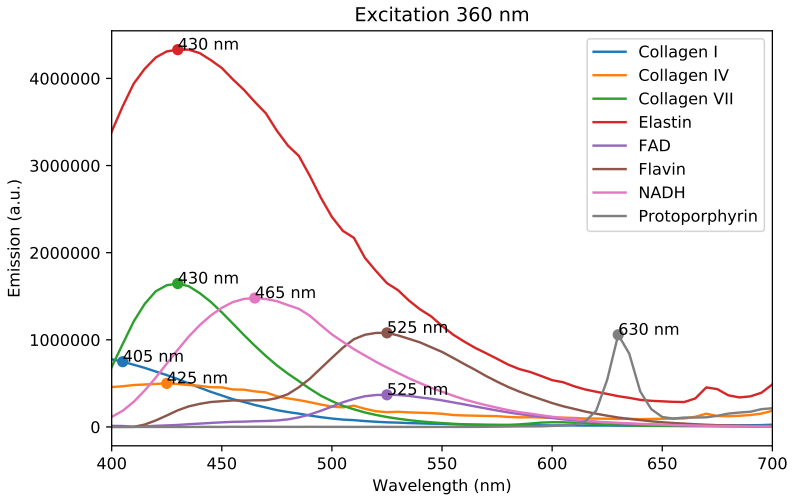

Figure 1: Fluorescence emission spectra extracted from data made available by DaCosta et al. [5].

2.2 Fluorescence emission at excitation wavelength 355 nm

Fluorophores present in human tissue that show significant fluorescence at an excitation wavelength of 355 nm are NADH, collagen, elastin, lipo-pigments and various types of flavins [10, 7, 19]. The recorded fluorescence is a combination of the emission spectra from these fluorophores.

DaCosta et al. [5] has made available full excitation-emission matrices for some endogeneous fluorophores. Emission maxima at excitation wavelength 360 nm can be found for collagen I (405 nm), IV (425 nm) and VII (430 nm), elastin (430 nm), FAD (525 nm), flavin (525 nm) and NADH (465 nm). Some of these were shifted 5-10 nm when considering excitation at 350 nm, indicating that 355 nm excitation should have similar emission spectra. Extracted spectra are shown in figure 1. Collagen and elastin maxima found in the 400-440 nm wavelength region is consistent with peaks found after excitation at nearby wavelength [19, 7, 8]. NADH emission maximum at 460 nm is also consistent with the literature [10, 14, 19, 21, 15]. Collagen as measured from whole tissue is claimed to have emission peaks around 460 nm (excitation 370 nm) [7] or 436 nm (excitation 370 nm) [17], which would be consistent with combinations of the emission spectra from the collagen and elastin components as seen above. Lipo-pigments (not plotted) has an excitation maximum close to 350-355 nm, and a corresponding emission spectrum with maximum at 550 nm [19].

Several types of collagen have been identified in human tissue, where only fluorescence from types I, IV and VII are shown above. Mainly collagen types I and III are involved in wound healing [1, 6]. The emission spectra of collagen I and III were measured by Laifer et

al. [9] at excitation 325 nm. These were shown to have similar wavelength-dependencies, with a peak maximum close to 400 nm. Fluorescence spectroscopy of collagen formation in rat wounds also shows a peak in collagen fluorescence around 405 nm when excited at 325 nm [11, 12, 13]. Swatland [18] measured collagen types I and III excited at 370 nm. Here, types I and III have the same spectral dependency, and type I matches the spectral dependency in figure 1. Therefore, collagen type I and III are expected to have more or less the same fluorescence emission spectra at excitation wavelength 355 nm.

3 Materials and methods

3.1 Fluorescence analysis techniques

The main hypothesis of the experiment was that formation of collagen could be detected using fluorescent hyperspectral imaging, and that this could be used as a marker for wound healing. Fluorescence of both type I and III start at some peak below 415 nm, having exponential-like decay until above 500 nm. A spectral shift towards shorter wavelengths is expected once collagen formation starts contributing to the fluorescence spectrum. The hypothesis was further that the collagen formation therefore could be characterized by the peak shift. Influence from the optical properties of the tissue is expected, and this is taken into consideration by photon transport simulations and inspection of corresponding reflectance spectra.

3.1.1 Peak shift analysis

Smoothing splines has been identified as a possible technique for peak position extraction in fluorescence images [3]. The method is suitable for interpolation between the discrete wavelengths imaged by the hyperspectral system. This is here used for sub-resolution peak wavelength extraction, in order to be able to better evaluate whether a given emission spectrum has a peak wavelength closer to one or the other imaged wavelengths. This method was used to estimate the peak position at all pixels within the hyperspectral image.

Essentially, smoothing splines fit natural cubic splines to a given spectrum, and restricts the coefficients according to a roughness penalty. The roughness factor is chosen by cross-validation, and in practice acts like a denoising method. The simple, polynomial-like behavior of the fluorescence spectra makes the method suitable for these data.

3.1.2 Photon transport modeling

Photon transport simulations are used to investigate the influence of the re-epithelialized layer on fluorescence originating in dermis.

Gillies et al. [7] showed that epidermis had no significant contribution to the fluorescence at excitation wavelengths above 310 nm. Fluorescence from healed and intact tissue should therefore originate in dermis.

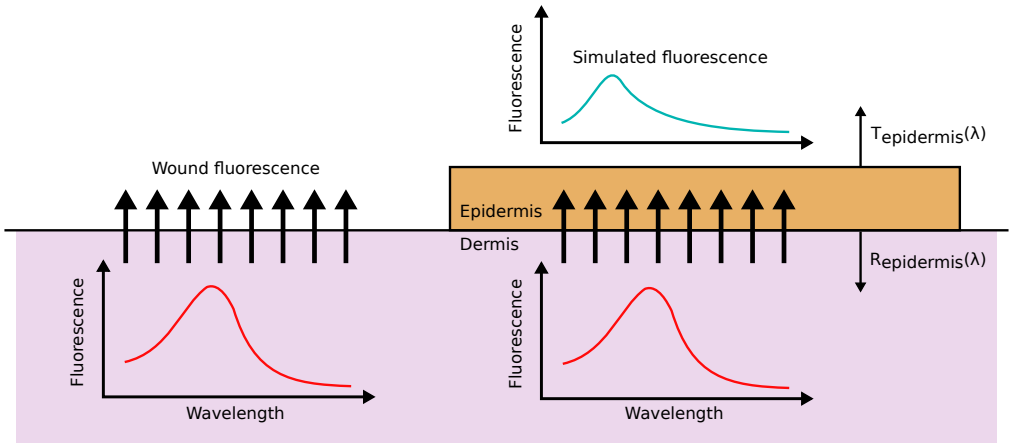

Figure 2: Simulation setup for evaluating the effect of re-epithelialization on fluorescence obtained from wound tissue.

Fluorescence originating from a wound-like dermis layer, including all influence by optical properties of this layer, is described by the fluorescence emission spectrum from the wound. Fluorescence through an epidermis is simply emulated by simulating the transmission T_{epi} of an epidermal layer, and obtaining the transmitted fluorescence as

$$F_{\text{healed}} = F_{\text{wound}} T_{\text{epi}}. \tag{1}$$

Fluorescence propagating from a dermal layer through an epidermis on top would also have contributions from light being back-scattered from the epidermis into the dermis again. This is rectified by considering the light reflected off the epidermal addition, and then reflected back from the dermal layer by

$$F_{\text{healed}} = F_{\text{wound}}(T_{\text{epi}} + R_{\text{epi}} R_{\text{wound}} T_{\text{epi}} + (R_{\text{epi}} R_{\text{wound}})^2 T_{\text{epi}} + \dots) \tag{2}$$

$$= F_{\text{wound}} T_{\text{epi}} \sum_{i=0} R_{\text{epi}}^i R_{\text{wound}}^i = F_{\text{wound}} T_{\text{epi}} \frac{1}{1 - R_{\text{epi}} R_{\text{wound}}}. \tag{3}$$

The simulated spectra in this study were rectified by this factor. The factor will be close to 1, however. Angle distributions are not considered for simplicity. The simulation setup is illustrated in figure 2.

Reflectance spectra taken from spatial positions corresponding to wound and healed tissue can be used to estimate the properties of the re-epithelialized layer [4, 2]. Monte Carlo simulations can be run in order to find the transmittance T and reflectance R used above.

3.2 Reflectance analysis techniques

The behavior of the reflectance spectra has been established in a previous study [2]. The main objective of the current paper is to compare the fluorescence results to the reflectance results, and further develop more robust wound classification techniques.

3.2.1 Clustering analysis

In a previous study, a K-Means based model was used for clustering the full bulk of hyperspectral data into two spectrally different clusters. The clusters were shown to be consistent with tissues with and without epidermis.

In short, a K-Means model with a large number of clusters was trained on all days of a given model series. These clusters were combined down to two clusters using agglomerative analysis. Finally, clusters found from a given wound model were used to classify the other wound models, and a final cluster was assigned by a majority vote.

The result is the separation of wound and intact or re-epithelialized skin across this dataset, with upper and lower boundaries on wound sizes given by the variation across the clustering models. This basic segmentation of the dataset is used to investigate healing in these wound models, and compared with the other techniques outlined in this paper.

3.2.2 Supervised classification

The development of a robust wound classification technique based on supervised classification is important for objective evaluation of healing rates. Supervised rather than unsupervised techniques are more convenient for extension to new data or new wound models. Further, such methods can yield interpretable classification rules. Two main classification techniques are used in this paper: Random forest as a general non-linear technique, and linear discriminant analysis (LDA) as a general linear technique.

Previously [2], reflectance slopes were indicated to be an important feature characterizing the missing presence of epidermis in in vitro wounds. A Savitzky-Golay filter with a window length of 21 was used to obtain derivatives. Random forest classifiers were trained and tested on reflectance and derivative spectra in order to compare classification performance. An LDA classifier was further applied to selected wavelengths of the derivative spectra in order to investigate the linearity of the classification problem.

Training data Two sets of training data are used in this study. Unsupervised clustering results were used as training labels for the first set. For the second set, smaller regions well within and well outside the wound boundary were selected across all models and days.

The latter training data set was used to evaluate the classification techniques independently from the results of the clustering, while the former training data set was used to create a harder classification problem by including re-epithelialized tissue in the training data.

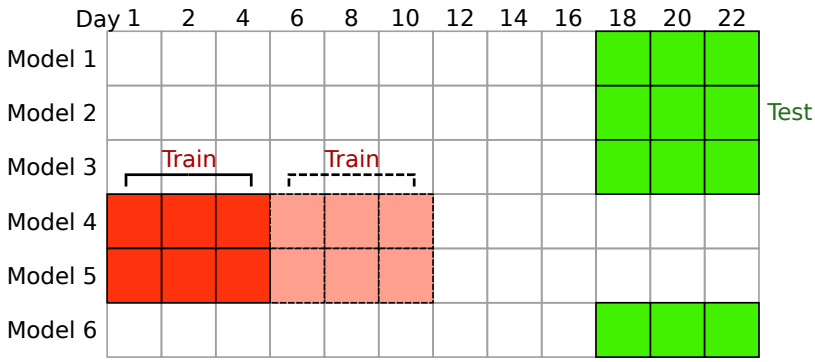

Figure 3: Basic cross-validation setup. The given classification model is trained on the first three days of the selected wound model series, and then the next three days, and tested on the last three measurements of all wound models not included in the training set. Final test scores are averaged over multiple series combinations.

Cross-validation Evaluation of model performance is challenging due to all wound models being acquired from the same donor and treated in the same way. The data is also essentially a time series. A special cross-validation scheme was therefore used.

The cross-validation scheme is illustrated in figure 3. A number of wound models from three days are used as training data. The classification models are tested on three other days and different models not included in the training set. The selected days used during training are day 1, 2 and 4, and day 6, 8 and 10. For testing, days 18, 20 and 22 are used.

Two variants of the basic scheme is used: Training on one wound model series and testing on the rest (1 vs 5), training on three wound model series and testing on the rest (3 vs 3). Finally, each scheme is run in reverse: The last 3 + 3 days are used for training, and the first three days are used for testing.

The basic configuration evaluates the model performance across a time gap, while restricting the number of wound model series the classification model is allowed to see. This is suitable for evaluating relative scores among the classification models.

4 Results and discussion

The key features of the fluorescence and reflectance images are identified and associated with physical processes in section 4.1. Reflectance and fluorescence data are then used to evaluate wound healing in section 4.2. Last, robust techniques for detecting wound healing are tested in section 4.3.

4.1 Influence of wound healing on fluorescence and reflectance spectra

The behavior of the reflectance has already been investigated in a previous study [2], and is briefly summarized here. Next, the fluorescence is investigated.

4.1.1 Summary of established reflectance behavior in the wound models

The reflectance data were characterized in a previous study [2]. The reflectance from healed and intact tissue were found to be suppressed and scewed as compared to reflectance from wound. This was found to be attributable to the addition of a diffuse, epidermis-like layer placed on top of tissues representing the optical properties of wound [2]. The modulation of the spectra over the wound boundary could be explained by a change in the thickness of the layer [4]. This is behavior consistent with the re-epithelialization process [2]. Further, a temporal development attributed to the medium was found in the reflectance spectra over the first 4-8 days [2], with the largest change from day 1 to 2. This development is summarized in figure 4 for one of the wound models.

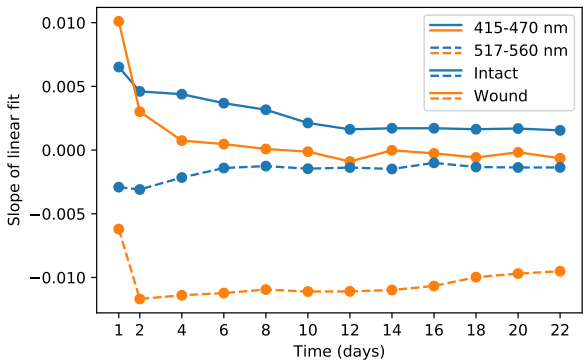

Figure 4: Temporal development in the reflectance spectra of a single wound model, charaacterized by linear fits at selected spectral regions.

4.1.2 Investigation of the fluorescence behavior

Regions corresponding to wound and intact tissue were selected from days 1, 10 and 22. Mean fluorescence spectra are plotted on figure 5. The fluorescence peaks in the wound at around 480 nm for the first day, which is shifted to 485 for the last day. Intact skin peaks at around 490 nm, which is shifted to around 495 nm for the last day. Thus, there is a peak shift from wound to intact tissue, and a peak shift over time. Peak behavior for healed tissue is similar to peak behavior for intact tissue.

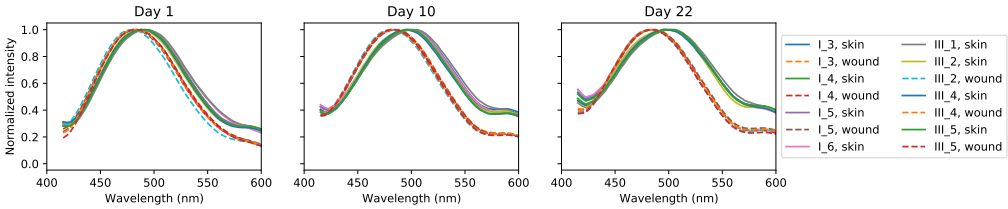

Figure 5: Normalized mean fluorescence spectra from wound and intact skin regions.

Peak shift from wound to healed tissue The reflectance spectra from healed and wound tissue were used to find the transmittance and reflectance spectra characterizing the re-epithelialized layer. These were then used to evaluate the effect of adding an epidermis-like layer on top of wound fluorescence. These fluorescence spectra are compared to measured fluorescence from the re-epithelialized region in figure 6. Losses at the excitation wavelength were not accounted for, and the spectra were therefore peak-normalized.

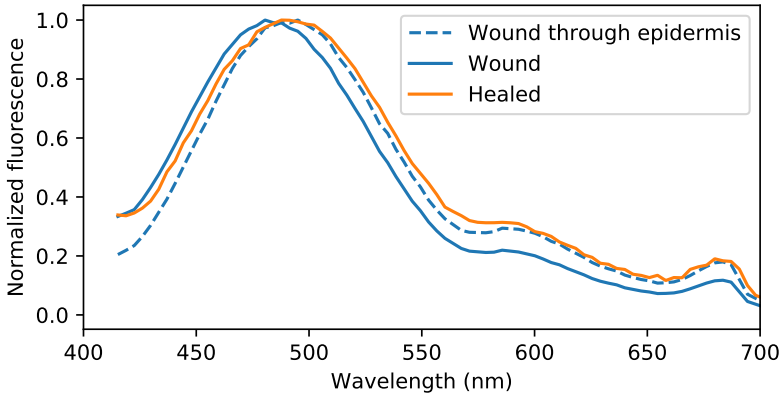

Figure 6: Demonstration of peak shift of fluorescence emission observed through an epidermis-like layer.

This result clearly shows that adding an epidermis-like layer shifts the peak wavelength of the fluorescence. The observed peak wavelength shift can therefore be attributed to the re-epithelialization. A decrease in peak value is also present (not shown), which is similarly explained by the same processes.

Temporal development in peak shift The temporal development of the peak shift is plotted in figure 7. Comparing the temporal peak shift to the temporal development of the reflectance shows that both processes converge after the same number of days.

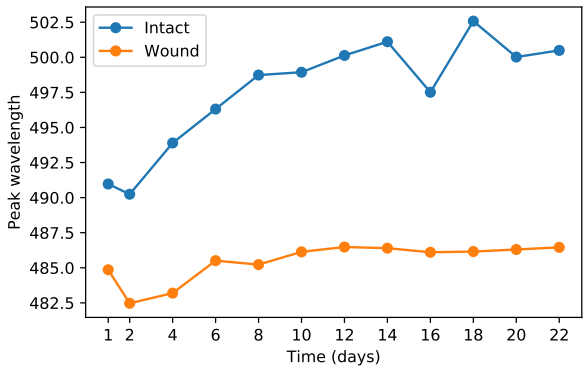

Figure 7: Temporal development in fluorescent peak shifts in the same regions displayed in figure 4.

The transition in reflectance to day 2 suggests a decrease in absorption at 415-470 nm and an increase in absorption at 517-560 nm. A decrease in the absorption here would correspondingly lead to an increase in the fluorescence, and thus explain the shift towards shorter wavelengths. After day 2, there is a decrease in the slope at 517-560 nm, which could explain the shift towards longer wavelengths. However, the behavior here is more challenging to fully explain without simulations. It is in any case clear that this behavior is not due to collagen formation. Both intact tissue and wound experience similar shifts towards longer wavelengths, and increased collagen activity is expected only within the wounded areas.

4.1.3 Concluding remarks

There is an apparent decrease in absorption at 415-470 nm over the first 8 days, which happens simultaneously with the expected increase in collagen fluorescence. Proper identification of collagen fluorescence therefore evades the peak shift analysis outlined in this paper. Its subtle influence, if present, would require full separation of the influence from optical properties, characterization by other means or changes to the experimental setup. This is therefore not a robust feature in these data.

However, another wound marker has been identified - the peak properties across the wound boundary. This does not provide more information than the reflectance, but offers up a simpler feature that could be directly related to the re-epithelialization. It also probes the re-epithelialized tissue in a different way by having the light sources effectively located within the tissue.

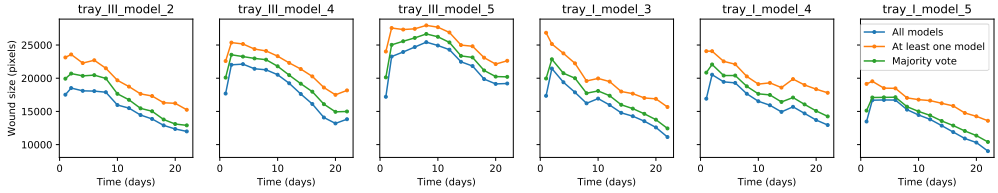

Figure 8: Wound sizes across all wound models as extracted from the reflectance clustering model.

4.2 Evaluation of wound healing using reflectance and fluorescence data

Reflectance and fluorescence data are used to evaluate healing in the presented wound models. The previously established clustering model is used to summarize the reflectance data, while the fluorescence peak features are used from the fluorescence data.

Derived wound sizes from the reflectance data, along with lower and upper bounds, are shown in figure 8. In general, the development in wound size would seem to be reasonable from day 8 and on, with a close to linear relationship between day and wound size. The increase in size from day 1 to day 2 across all wound models has been identified to be due to day 1 being a spectral outlier, and epidermal remnants [2]. Stabilization of wound size is in order for the first days [2]. All tray III models have a 8 day delay in wound healing, while model I_5 has a 5 day delay. The other tray I models apparently start healing already from day 2.

Wound boundaries derived from the cluster models and fluorescence peak position and value are shown for selected wound models in figure 9 and 10. The separation between tissue with and without epidermis is clearly characterized by the peak shift. The lowest peak wavelength is in agreement with the cluster boundary at all days for the tray III model and most of the days for the tray I model. The boundary increases in diffusiveness, consistent with the gradual increase in epidermal thickness here. Further, early healing in the shown tray I model would seem to be in order according to the peak features.

The tray III and I models were prepared with 4 mm and 3 mm size wounds, respectively. The imaged extent of the tray I model wounds with early healing is the same as the 4 mm wounds. Only the tray I model with healing delay, I_5, has a wound extent consistent with the 3 mm size. The former models have inhomogeneous shapes, while the latter is circular. One possible explanation for the early healing is tearing in the surrounding skin outside of the actual dermal cut when the wound was prepared. Such tearing would typically be shallow, and heal quickly. This is somewhat indicated by the higher peak shifts and lower peak values in these regions.

Histologies are not available for this dataset. The previous study included an example of histologies for a similar wound model [2], which indicated complete coverage by keratinocytes during the first 7 days for 4 mm wounds. The 4 mm wounds start healing detectable by

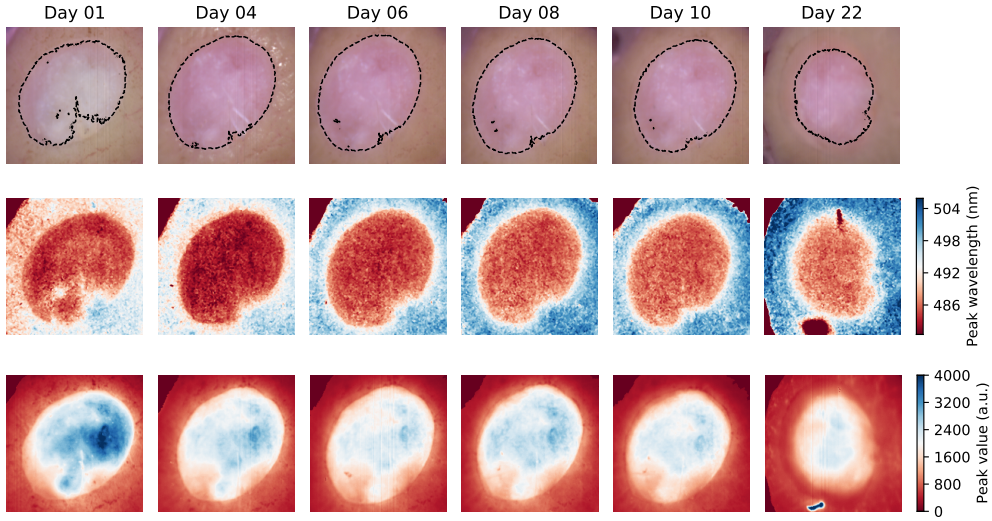

Figure 9: Temporal development in wound cluster size (top), compared to fluorescent peak shift (center) and peak value (bottom) for model III_2 (4mm wound).

hyperspectral imaging from day 8 and on. It is possible that only a mature enough re-epithelialized layer is detectable by hyperspectral imaging [2]. Such tissues would follow coverage by the keratinocyte layer, and the keratinocyte layer is thus indirectly detectable. As for the fluorescence, there is a reduction in the peak value and a shift of the peak position from the edge of the wound and in over these days that could be consistent with keratinocyte coverage.

The combination of reflectance and fluorescence images are thus valuable for evaluating wound healing. Taking these basic methods further is then the next step.

4.3 Identifying a robust technique for detection of wound healing

Both reflectance and fluorescence has been shown to be suitable for evaluating re-epithelialization. Excitation at 355 nm is invasive, however, and the fluorescence spectra are noisy and mostly feature-less. The latter makes the development of classification techniques challenging, and the reflectance data are more suitable for this.

4.3.1 Comparison of classification techniques

Cross-validation scores are shown in figure 11. Various cross-validation schemes are used in order to characterize the classification problem, and indicate what kind of technique would be necessary in order to solve the problem more generally.

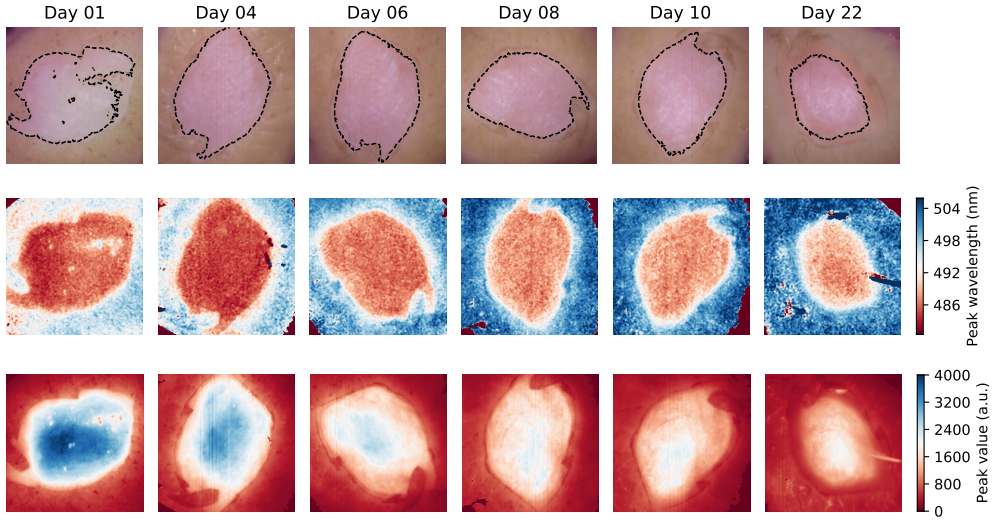

Figure 10: Temporal development in wound cluster size (top), compared to fluorescent peak shift (center) and peak value (bottom) for model I_4 (3 mm wound).

Non-linear classification The 1 vs 5 cross-validation scheme on the random forest classifier is first considered, where a single wound model series is included in the training set. Taking the derivatives enables the random forest classifier to obtain a high mean cross-validation score (0.991) across all other models despite using only a single wound model series during training. Conversely, raw reflectances yield a lower mean cross-validation score (0.952) for the same classifier.

The 3 vs 3 cross-validation scheme increases the training dataset by including three wound model series during training. This increases the cross-validation scores for raw reflectance (0.952 to 0.994) and derivatives (0.991 to 0.997). Thus, the random forest classifier trained on raw reflectance needs more training data points in order to achieve a cross-validation accuracy higher than 0.99, while applying the classifier to first derivative spectra yields a cross-validation accuracy higher than 0.99 for either cases.

The behavior between cross-validation schemes suggests nonlinear behavior in the reflectance that requires enough data to properly approximate the decision surfaces, and that the derivatives yield features that have more common behavior across all wounds.

Linear classification To test this, two wavelengths (542 and 582 nm) from the derivatives were used to train a simple linear classifier, LDA. These wavelengths can be related back to wavelength regions that in the characterization study was shown to be clearly affected by the re-epithelialization in an almost linear way, and which have the highest reflectance slopes. The highest cross-validation scores (0.995 and 0.998) are obtained using this technique.

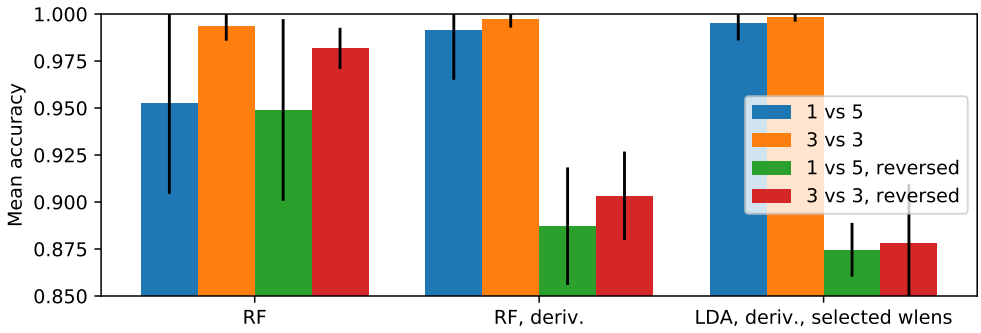

Figure 11: Comparison of mean cross-validation scores for different classification schemes: Random forest, random forest trained on derivatives and LDA trained on the derivatives at selected wavelengths (542 and 582 nm). The used classification schemes (1 vs 5, 3 vs 3) refers to the number of wound models used in training versus the number of wound models used during testing. The reversed variant swaps the days used for training and testing. Standard deviations of the scores are marked with a black line.

Further, the standard deviations are lower.

Each of these two wavelengths consists in reality of multiple wavelengths (21) due to the window length in the Savitzky-Golay filter used in obtaining the derivatives. LDA performance was evaluated as a function of window length in order to get an impression of the necessary number of wavelengths. The cluster results from earlier were used as training labels in order to make the problem harder. The results in figure 12 shows that the optimal choice of filter length is somewhere between 13 and 19 (cross-validation score 0.99). Decreasing the number of wavelengths in the filter to 5 (10 wavelengths in total) reduces the cross-validation score to around 0.97. Using the difference spectra (2 wavelengths per derivative, 4 wavelengths in total), yields a cross-validation accuracy of 0.965.

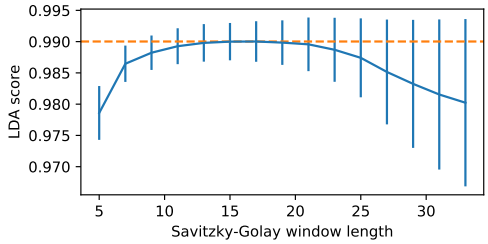

Figure 12: LDA performance as a function of the window length in the Savitzky-Golay filter used to obtain derivatives.

Reverse cross-validation splits It has been shown that the reflectance spectra of the first days are different from reflectance spectra obtained from the later days [2]. Running the cross-validation schemes in reverse, by training the classifiers on the last days and testing them on the first, shows a degraded performance especially for the derivative based classifiers, while raw reflectance still yields smilar classification performance. Good classification accuracy over the temporal developments thus needs more non-linear classifiers and knowledge of the absolute reflectance levels. The first days can be considered to be spectral outliers, however.

Concluding remarks The results serve to demonstrate the homogeneous behavior of the slope throughout most of the measurements after stabilization of optical properties, and confirms the importance of the epidermal presence in classifying wound tissue. This is thus a result founded in both the physics and the statistics of the problem. Derivatives can provide features that lead to classifiers with high cross-validation scores. Further, the linear classifier shows that in vitro wound imaging can be achieved using few wavelengths.

4.3.2 Discussion of the classification results

The methods were tested on wound and intact tissue. These regions have high separation, and therefore yield higher classification accuracies. The cluster results were used for evaluation of the Savitzky-Golay filter length, which includes re-epithelialized tissue and thus represents a harder classification problem. The reduction in classification performance is only minor, however.

It is important to be aware the use of clustering results as training labels can lead to classification rules that reproduce the clustering results rather than the rules separating wound from other tissue types. A manual and independent labeling which includes re-epithelialized tissue is challenging due to the uncertainty of the boundaries. The chosen way of obtaining training data, well within the wounds and well within intact tissue parts, therefore serves as a good middle-ground despite the high separation.

The choice of training data means that re-epithelialized tissue is implicitly detected by being similar enough to intact tissue. This is similar to the outcome of the clustering technique. This approach can be justified: The transition in reflectance from wound to intact tissue is modulated by the thickness of the epidermal layer, and turns spectra more similar to wound into spectra more similar to intact tissue. Separating re-epithelialized tissue from other types of tissue would otherwise be challenging.

This means that the wound class can include re-epithelialized tissues that do not have a large enough epidermal thickness to be spectrally similar to intact tissue. The developed technique is still suitable for detecting wound healing, and for comparing wound models, since it would be consistent in its tissue definitions and what degree of re-epithelialization is necessary for being counted as a part of healed tissue. Thus, once the healing process has reached its necessary stage, healing will be detected.

The reflectance classification approach takes a hard decision between wound and healed tissue. The spectral transition over the re-epithelialized parts of the tissue is gradual. Flu-

orescence has been shown to represent a simple visualizer of this. It thus complements a reflectance classification. Fluorescence classification would likely be more challenging and require spatial information, while reflectance classification has been shown to be possible based on spectral information alone.

The cluster model from the previous study [2] was shown to be suitable for evaluating wound healing in section 4.2. The systematic testing of more easily trainable and objective classification techniques in the current section has shown suitable classification performance, and thus represents a robust and extensible alternative.

5 Conclusion and further work

Reflectance and fluorescence data as been acquired from wound models. The hypothesis was that re-epithelialization could be detected using reflectance imaging, and collagen formation by fluorescence imaging. However, also fluorescence was found to mainly be influenced by re-epithelialization in this case. Both techniques were found to be well suitable for evaluation of wound healing in these models. Wound classification was further found to be possible using few wavelengths by exploiting the derivatives of the reflectance.

Acknowledgments

Thanks to Ingvild Haneberg and Matija Milanic for acquisition of the data.

References

[1] V. Arnoux, C. Come, D. F. Kusewitt, L. G. Hudson, and P. Savagner. Cutaneous wound reepithelialization: A partial and reversible emt. In P. Savagner, editor, *Rise and fall of epithelial phenotype: Concepts of Epithelial-Mesenchymal Transition*, chapter 8. Plenum Publishers, 2005.

[2] A. Bjorgan, B. Pukstad, and L. L. Randeberg. Hyperspectral characterization of re-epithelialization in an in vitro wound model. *J. Biophotonics*, 13(10):e202000108, 2020.

[3] A. Bjorgan and L. L. Randeberg. Application of smoothing splines for spectroscopic analysis in hyperspectral images. *Proc. SPIE*, 10873, 2019.

[4] A. Bjorgan and L. L. Randeberg. Exploiting scale-invariance: A top layer targeted inverse model for hyperspectral images of wounds. *Biomed. Opt. Express*, 11:5070–5091, 2020.

[5] R. S. DaCosta, H. Andersson, and B. C. Wilson. Molecular fluorescence excitation-emission matrices relevant to tissue spectroscopy. *Photochem. Photobiol.*, 2003.

[6] P. D. Dale, J. A. Sherratt, and P. K. Mainin. A mathematical model for collagen fibre formation during foetal and adult dermal wound healing. *Proc. Biol. Sci.*, 1996.

[7] R. Gillies, G. Zonios, R. R. Anderson, and N. Kollias. Fluorescence excitation spectroscopy provides information about human skin in vivo. *J. Invest. Dermatol.*, 115(4):704–707, 2000.

[8] A. Kuehn, A. Graf, U. Wenzel, S. Princz, H. Mantz, and M. Hessling. Development of a highly sensitive spectral camera for cartilage monitoring using fluorescence spectroscopy. *J. Sens. Sens. Syst.*, 2015.

[9] L. I. Laifer, K. M. O'Brien, M. L. Stetz, G. R. Gindi, T. J. Garrand, and L. I. Deckelbaum. Biochemical basis for the difference between normal and atherosclerotic arterial fluorescence. *Circulation*, 1989.

[10] R. Na, I.-M. Stender, L. Ma, and H. C. Wulf. Autofluorescence spectrum of skin: component bands and body site variations. *Skin Res. Technol.*, 6, 2000.

[11] V. Prabhu, E. M. Fernandes, B. S. S. Rao, and K. K. Mahato. Non-invasive, in vivo fluorescence technique as an objective tool for monitoring wound healing following low level laser therapy. *Proc. SPIE*, 8565, 2013.

[12] V. Prabhu, S. B. S. Rao, S. Chandra, P. Kumar, R. Lakshmi, V. Guddattu, K. Satyamoorthy, and K. K. Mahato. Spectroscopic and histological evaluation of wound healing progression following low level laser therapy (lllt). *J. Biophotonics*, 5, 2012.

[13] V. Prabhu, S. B. S. Rao, E. M. Fernandes, A. C. K. Rao, K. Prasad, and K. K. Mahato. Objective assessment of endogenous collagen in vivo during tissue repair by laser induced fluorescence. *PLoS One*, 9, 2014.

[14] Y. Pu, W Wang, G. Tang, and R. R. Alfano. Changes of collagen and nicotinamide adenine dinucleotide in human cancerous and normal prostate tissues studied using native fluorescence spectroscopy with selective excitation wavelength. *J Biomed Opt*, 2010.

[15] L. Shi, L. Lu, G. Harvey, T. Harvey, A. Rodriguez-Contreras, and R. R. Alfano. Label-free fluorescence spectroscopy for detecting key biomolecules in brain tissue from a mouse model of alzheimer's disease. *Sci. Rep.*, 2017.

[16] A. J. Singer and R. A. F. Clark. Cutaneous wound healing. *N. Engl. J. Med.*, 341(10):738–746, 1999.

[17] H. J. C. M. Sterenborg, M. Motamedi, R. F. Wagner, M. Duvic, S. Thomsen, and S. L. Jacques. In vivo fluorescence spectroscopy and imaging of human skin tumors. *Laser Med Sci*, 1994.

[18] H. J. Swatland. Effect of excitation wavelength on the separation of types i and iii collagen by fiber optic fluorimetry. *J. Food Sci.*, 1987.

[19] G. A. Wagnieres, W. M. Star, and B. C. Wilson. In vivo fluorescence spectroscopy and imaging for oncological applications. *Photochem. Photobiol.*, 1998.

[20] Y. Wang, E. Gutierrez-Herrera, A. Ortega-Martinez, R. R. Anderson, and W. Franco. UV fluorescence excitation imaging of healing of wounds in skin: Evaluation of wound closure in organ culture model. *Laser Surg. Med.*, 48(7):678–685, 2016.

[21] C. Zhu, G. M. Palmer, T. M. Breslin, J. Harter, and N. Ramanujam. Diagnosis of breast cancer using fluorescence and diffuse reflectance spectroscopy: a monte-carlo-model based approach. *J. Biomed. Opt.*, 2008.

Paper IV

A. Bjorgan and L. L. Randeberg, "Application of smoothing splines for spectroscopic analysis in hyperspectral images," *Proc. SPIE*, vol. 10873, 2019. DOI: https://doi.org/10.1117/12.2506618

Application of smoothing splines for spectroscopic analysis in hyperspectral images

Bjorgan, Asgeir, Randeberg, Lise

Asgeir Bjorgan, Lise L. Randeberg, "Application of smoothing splines for spectroscopic analysis in hyperspectral images," Proc. SPIE 10873, Optical Biopsy XVII: Toward Real-Time Spectroscopic Imaging and Diagnosis, 108730O (4 March 2019); doi: 10.1117/12.2506618

SPIE.

Event: SPIE BiOS, 2019, San Francisco, California, United States

Application of smoothing splines for spectroscopic analysis in hyperspectral images

Asgeir Bjorgan and Lise L. Randeberg

Department of Electronic Systems, NTNU Norwegian University of Science and Technology, Trondheim, Norway

ABSTRACT

The spectral and spatial resolution of hyperspectral imaging is useful for investigation of tissue autofluorescence. The low-light, noisy conditions in fluorescence imaging usually necessitates noise removal for extraction of precise spectral signatures and peak shifts. However, noise removal techniques like low-pass filtering or the Maximum Noise Fraction transform might discard information or distort spectral features. In this study, smoothing splines is proposed as an alternative technique to avoid spectral distortion in analysis of hyperspectral fluorescence images in the wavelength range 400-1000 nm. Continuous tuning parameters and use of natural cubic splines makes the method advantageous for unbiased peak extraction. The method was tested on ex vivo images of atherosclerosis lesions and simulations. The method was used to estimate autofluorescence peak shifts, and found to perform well in comparison with MNF.

Keywords: fluorescence imaging, subresolution peak extraction, tissue optics, noise removal, maximum noise fraction transform

1. INTRODUCTION

Hyperspectral imaging is a valuable tool for investigation of tissue autofluorescence. It has the spectral resolution required to resolve multiple fluorophores, and can yield spatial maps over the locations of spectral signatures of interest. Applications of hyperspectral fluorescence imaging include imaging of atherosclerotic plaques,[1] food quality control[2,3] and various medical applications like characterization of cancer cells.[4] In the current study, smoothing splines is explored as a tool for removing noise and characterizing autofluorescence peaks in hyperspectral fluorescence images.

Imaging spectrometers require sufficient illumination. However, the only light available in imaged fluorescence scenes is the low-intensity autofluorescence light generated in the samples. Increasing the integration time of the camera or the power of the excitation light source is normally not feasible, as long exposure to strong radiation would bleach the fluorophores. Hyperspectral fluorescence imaging therefore leads to images with a low signal-to-noise ratio (SNR), where noise removal can be necessary as a pre-processing technique.

Automated characterization is important for processing larger datasets acquired as time series and across samples. An ultimate goal is to unmix the data with respect to the various fluorophores. This is challenging in tissue due to strong scattering and absorption at both excitation and emission wavelengths. Full unmixing requires full characterization of e.g. reflectance images acquired under a visible light source to estimate scattering and absorption properties, and the appropriate pairing of optical properties and apparent emission spectra. Manual decision making might be necessary.

Emission peak characterization in terms of peak position, peak height and peak width is an alternative technique for obtaining an overview over the data. This can be used as a part of the fluorophore characterization process, and for the initial visualization of the data. Comparability is an important requirement, where fluorophores across measurements should have the same peak behavior, and not be subject to e.g. pre-processing techniques that treat the data differently.

Further author information: (Send correspondence to A.B.)
A.B.: E-mail: asgeir.bjorgan@ntnu.no

Optical Biopsy XVII: Toward Real-Time Spectroscopic Imaging and Diagnosis, edited by Robert R. Alfano, Stavros G. Demos, Angela B. Seddon, Proc. of SPIE Vol. 10873, 108730O · © 2019 SPIE · CCC code: 1605-7422/19/$18 · doi: 10.1117/12.2506618

Extracting peak positions at sub-resolution level could be useful for obtaining more accurate representations of peak shift distributions over larger regions. These are otherwise limited to counts over the two closest wavelengths due to the wavelength discretization. Sub-resolution peak shifts lead to subtle changes in the noise dynamics, which could be exploited by a suitable interpolating technique to estimate peak shifts. Thus, there are two goals in this study: To remove noise from the spectra in a comparable and objective way, and to estimate sub-resolution peak shifts, where the two problems are strongly inter-related.

MNF (Minimum noise fraction)[5] is a noise reduction technique often used for hyperspectral images, as it retains spatial and spectral resolution while yielding smooth spectra. MNF decomposes the image in terms of typically 8-10 less noisy, mixed components, with their own maxima and minima. Each pixel in the denoised hyperspectral image will be a linear combination of these. It is not guaranteed that the MNF decomposition is sensitive to small shifts in fluorescence emission peak position due to the way the images are decomposed. The MNF technique is subject to the available image statistics. Choosing the number of components has to be done based on visual inspection. MNF is not an interpolating technique, and the number of component cannot be objectively chosen by cross-validation or similar techniques, unless techniques further down the processing pipeline have properties that can be evaluated by cross-validation. In general, the subjectivity leads to images that are not necessarily comparable.

Smoothing splines[6,7] is proposed as an alternative technique for satisfying both denoising and peak detection aspects in fluorescence images. The method uses natural cubic splines to interpolate the data. Wavelength bands can be left out during fitting, to be evaluated by the fitted model at a later time. This makes the concept of independent test data well-defined. Subresolution peak positions are efficiently found using the analytical derivative. The spline coeffients are restricted according to a roughness penalty, in effect making the method a denoising method with the appropriate smoothing parameter. Smoothing splines is a linear method, and can thus be efficiently estimated on multiple spectra at the same time. Linearity also means that the leave-one-out cross-validation error is trivial to calculate without refitting the method. All spectra in the hyperspectral datacube can therefore efficiently be represented using spline coefficients, with crossvalidated tuning parameters that objectively can yield smoothed spectra that are comparable.

Smoothing splines, or variations of the technique, have been used in both hyperspectral imaging and in fluorescence spectroscopy. Marion et al.[8] uses smoothing splines as a basis for a method to recover reflectance values within major gas absorption bands in remotely sensed images. Berman[9] uses thin-plate smoothing splines to smooth the MNF transformation bands of remote sensing data. Lee et al.[10] compares various smoothing methods on autofluorescence data, including LOESS, COBS and robust smoothing splines, which uses a scale function on the mean squared error part of equation (1). Various methods are given for approximating the cross-validation error.[8–10]

The theory for the smoothing splines technique and considerations for application to hyperspectral images is outlined in section 2. The technique is then applied to images of atherosclerosis images and simulations, and compared to MNF.

2. SMOOTHING SPLINES

Given a data set with inputs $\boldsymbol{x} = [x_1, x_2, \ldots, x_K]^T$ and outputs $\boldsymbol{y} = [y_1, y_2, \ldots, y_K]^T$, the smoothing splines method estimates the function $f(x)$ which minimizes the penalized residual sum of squares (PRSS)[6]

$$\mathrm{PRSS}(f, \alpha) = \sum_{i=1}^{K} \{y_i - f(x_i)\}^2 + \alpha \int_{-\infty}^{\infty} \left\{ \frac{d^2}{dt^2} f(t) \right\}^2 dt. \tag{1}$$

The first term deals with the closeness of the function $f(x)$ to the outputs y_i, and the second term penalizes the curvature of the function.[6] Setting $\alpha = 0$ interpolates the outputs exactly (maximum curvature), while $\alpha = \infty$ yields a straight line (no curvature allowed). In practice, α controls the smoothness of the resulting function, and regularizes between under- and overfitting. An alternative, more convenient formulation is to express the PRSS as[7] $p \sum_{i=1}^{N} \{y_i - f(x_i)\}^2 + (1-p) \int_{-\infty}^{\infty} \left\{ \frac{d^2}{dt^2} f(t) \right\}^2 dt$, with $\alpha = (1-p)/p$. Here, $p = 0$ yields a straight line and $p = 1$ fits all datapoints exactly.

The parameter α is a tuning parameter which has to be estimated using independent validation data or through cross-validation. Minimization of $\mathrm{PRSS}(f, \alpha)$ would always set $\alpha = 0$, effectively overfitting the model on the data.

It can be shown that the solution $\hat{f}(x)$ is a natural cubic spline with K knots,[6] meaning that the function between the first and second datapoint and the function between datapoint $K-1$ and datapoint K are linear functions. The other line segments are cubic polynomials with continuous first and second derivatives. The linear segments reduce erratic behavior at the edges of the dataset.[6] The solution can be written as

$$\hat{f}(x) = \sum_{j=1}^{K} N_j(x)\hat{\theta}_j, \tag{2}$$

where $N_j(x)$ are the basis functions for the natural cubic splines. The coefficients $\hat{\theta}_j$ are given as[6]

$$\hat{\boldsymbol{\theta}} = [\hat{\theta}_1, \ldots, \hat{\theta}_K]^T = \underbrace{(\mathbf{N}^T\mathbf{N} + \alpha\boldsymbol{\Omega}_N)^{-1}\mathbf{N}^T}_{\stackrel{\mathrm{def}}{=}\mathbf{H}_\alpha}\boldsymbol{y} = \mathbf{H}_\alpha\boldsymbol{y}. \tag{3}$$

The matrices $\mathbf{N}$ and $\boldsymbol{\Omega}_N$ consist of the elements $\{\mathbf{N}\}_{ij} = N_j(x_i)$ and $\{\boldsymbol{\Omega}_N\}_{jk} = \int \frac{d^2}{dt^2}N_j(t)\frac{d^2}{dt^2}N_k(t)dt$, respectively.[6] These are dependent only on x_i.

Evaluating $\hat{f}(x)$ at the inputs of the training set x_i yields

$$\hat{\boldsymbol{f}} = [\hat{f}(x_1), \hat{f}(x_2), \ldots, \hat{f}(x_K)]^T \tag{4}$$

$$= \sum_{j=1}^{K}[N_j(x_1), \ldots, N_j(x_K)]^T\hat{\theta}_j = \mathbf{N}\hat{\boldsymbol{\theta}} \tag{5}$$

$$= \underbrace{\mathbf{N}(\mathbf{N}^T\mathbf{N} + \alpha\boldsymbol{\Omega}_N)^{-1}\mathbf{N}^T}_{\stackrel{\mathrm{def}}{=}\mathbf{S}_\alpha}\boldsymbol{y} = \mathbf{S}_\alpha\boldsymbol{y}. \tag{6}$$

Here, the matrix $\mathbf{S}_\alpha$ depends only on the training inputs x_i and α, and the fit $\hat{\boldsymbol{f}}$ is therefore linear in $\boldsymbol{y}$. The coefficients $\hat{\boldsymbol{\theta}}$ are also similarly linear in $\boldsymbol{y}$. Linearity has two main advantages which makes the method ideal for large datasets like hyperspectral images.

First, for a single α, it is computationally efficient to apply the method to multiple spectra. Given a hyperspectral image in matrix form, $\mathbf{B} = [\boldsymbol{y_1}, \ldots, \boldsymbol{y_N}]^T$ (N spectra $\times$ K wavelengths), the corresponding x_i are the same across all spectra. The matrices $\mathbf{N}$ and $\boldsymbol{\Omega}$ can therefore be calculated once for a specific α, and spline coefficients or function evaluations are obtained by a matrix multiplication:

$$\mathbf{B}_\alpha = \mathbf{S}_\alpha\mathbf{B} \tag{7}$$

$$\hat{\boldsymbol{\theta}}_\alpha = \mathbf{H}_\alpha\mathbf{B}. \tag{8}$$

An efficient BLAS (Basic Linear Algebra Subprograms)[11] implementation then ensures computational efficiency.

Second, linearity enables the calculation of the leave-one-out cross-validation error without refitting. Leave-one-out cross-validation estimates the test error of a given method by training on $K-1$ datapoints and testing on the remaining datapoint, and averaging over all combinations. This requires the model to be fitted K times for each parameter choice. For models that are linear in $\boldsymbol{y}$, as expressed in (6), the leave-one-out cross-validation error can be calculated directly from $\mathbf{S}_\alpha$:[6]

$$\mathrm{Err}_{\mathrm{CV}}(\hat{f}_\alpha) = \frac{1}{K}\sum_{i=1}^{K}\left(\frac{y_i - \hat{f}_\alpha(x_i)}{1 - S_\alpha(i,i)}\right)^2, \tag{9}$$

where $S_\alpha(i,i)$ are the diagonal elements of the matrix $\mathbf{S}_\alpha$. Thus, the smoothing splines for a given parameter choice α has to be fitted only once, and the full cross-validation error for this parameter choice is available using the above formula without refitting. For a given spectrum $\boldsymbol{y}$, the parameter α can objectively be found by minimizing (9). This yields the lowest cross-validation error, and provides an optimal choice between closeness and smoothness in the resulting spline.

2.1 Estimating optimal tuning parameters for all pixels

Choosing any α between 0 and ∞ yields a gradual transition from high-variance, noisy fits to smoother fits - and an optimal parameter in-between representing a denoised spectrum. This coincides with the parameter chosen through cross-validation.

The tuning parameter α is directly dependent on the signal to noise ratio in a given spectrum. An image might have the same noise variance in all pixels and bands, but the signal level varies. A constrained fit with high α would be required for low signal levels, where the noise dominates, while a less constrained fit and lower α is appropriate for high signal levels, where the relative noise contribution is low. An image containing various kinds of signals and signal amplitudes requires a different α for every single pixel.

Consider a typical bracketing routine for minimizing $\mathrm{Err}_{\mathrm{CV},\alpha}$ for a given spectrum, assuming a well-behaved error curve with a single, global minimum. All spectra would require estimation of the cross-validation error at a common set of lower and upper α. Multiple spectra would likely end up within the same parameter ranges, and go through a sequence of bracketing at the same α_i. All spectra share the same x_i, and a single $\mathbf{S}_\alpha$ can be calculated for a specific α_i. A divide-and-conquer approach may therefore be used.

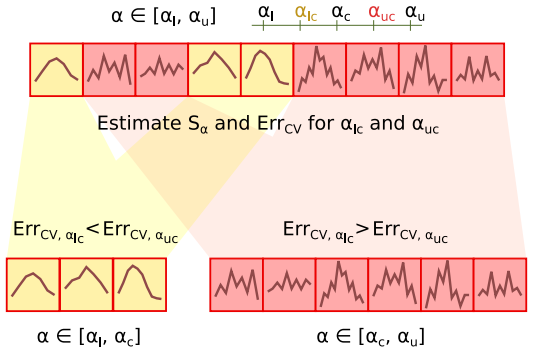

Figure 1. Split based on cross-validation error during divide-and-conquer strategy for estimating optimal α.

Assume lower and upper brackets α_l and α_u for the α providing the minimum cross-validation error for a range of pixels $\mathbf{B}$:

1. Calculate $\alpha_c = 0.5(\alpha_u + \alpha_l)$, $\alpha_{lc} = 0.5(\alpha_l + \alpha_c)$ and $\alpha_{uc} = 0.5(\alpha_u + \alpha_c)$.
2. Estimate $\mathbf{S}_\alpha$ for α_{lc} and α_{uc}.
3. Calculate the cross-validation error for all pixels for α_{uc} and α_{lc} using $\mathbf{S}_\alpha$.
4. Divide the pixel set in two subsets: Assign pixels to $[\alpha_l, \alpha_c]$ for the pixels which has the lowest cross-validation error for α_{lc}, and assign to $[\alpha_c, \alpha_u]$ for the pixels which has the lowest cross-validation error for α_{uc}.
5. Repeat the process from 1. on each of the pixel sets until convergence ($|\alpha_l - \alpha_u| < \alpha_c \cdot t$).

One iteration of the algorithm is illustrated in Fig. 1.

Thus, each pixel can have its optimal α estimated independently of each other to an arbitrary numerical precision, with full reuse of the same computations across pixels. This approach assumes that the cross-validation curve has a single minimum. This has been seen to be valid for most of the spectra encountered in this study, though there are cases where this is not valid.

Coefficients can either be kept during the cross-validation routine, or they can be obtained by reapplying the method on smoothed data using a smoothing parameter α close to 0, as illustrated in Fig. 2. The latter approach can also be applied on spectra denoised using e.g. MNF to obtain spline coefficients for peak characterization.

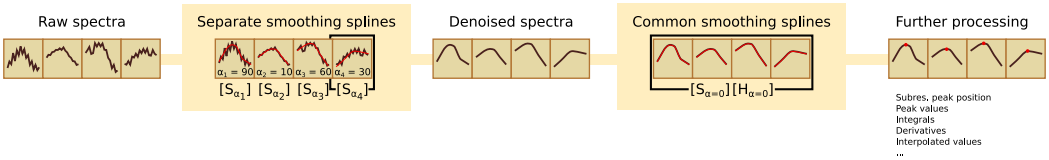

Figure 2. Flowchart for possible application of the method: Apply smoothing splines separately on each pixel and then apply a common smoothing spline matrix with low α to estimate spline coefficients for further analysis.

3. THE MINIMUM NOISE FRACTION TRANSFORM

The MNF transform $\mathbf{T}$ of an image $\mathbf{B}$ with band means $\bar{\mathbf{B}}$ can be expressed using a linear transformation matrix $\mathbf{A}$ as[5]

$$\mathbf{T} = \mathbf{A}(\mathbf{B} - \bar{\mathbf{B}}), \tag{10}$$

where the subraction of the band means $\bar{\mathbf{B}}$ are taken row-wise. The constituent vectors $\boldsymbol{a}$ of the transformation matrix $\mathbf{A} = [\boldsymbol{a_1}, \ldots, \boldsymbol{a_K}]^T$ are found by solving the eigenvalue problem[5]

$$\mathbf{\Sigma}_{\mathcal{N}}\boldsymbol{a} = \lambda\mathbf{\Sigma}\boldsymbol{a}, \tag{11}$$

where $\mathbf{\Sigma}_{\mathcal{N}}$ and $\mathbf{\Sigma}$ are the noise and image covariance matrices, respectively.

The bands in $\mathbf{T}$ are sorted in terms of decreasing SNR by sorting the eigenvalues.[5] Most of the signal is compressed in the first bands, slowly degrading into pure noise with increasing band index. Discarding the last $K - r$ bands can be used as a compression technique, and processing algorithms can be made to work on the r transformed bands instead of the full image. Using the first r components of $\mathbf{A}^{-1}$ on these r components would yield noise-reduced spectra within the original image space. If only the denoising properties of the technique are desired, this process can be expressed as

$$\mathbf{B}^* = \bar{\mathbf{B}} + \mathbf{A}^{-1}\mathbf{R}\mathbf{A}(\mathbf{B} - \bar{\mathbf{B}}) = \bar{\mathbf{B}} + \mathbf{D}(\mathbf{B} - \bar{\mathbf{B}}), \tag{12}$$

where $\mathbf{R}$ is the identity matrix with the last $K - r$ diagonal entries set to zero. All steps in the method can be implemented as matrix operations, which can make use of efficient linear algebra implementations.[12]

4. EXPERIMENTAL SETUP

The smoothing splines method was tested for its peak extraction capabilities on a fluorescence dataset. The noise removal capabilities were compared against MNF on the same dataset. Here, the ground truth is not known. Simulations were therefore also generated in order to evaluate the methods on denoising of spectra where the underlying models are known. For the simulated dataset, quantification was done using the mean squared error between the original, noise-free spectra and the denoised spectra.

4.1 Measurements

The fluorescence example dataset consists of measurements over atherosclerotic lesions from human aortic samples, previously published in Larsen et al.[13] and Randeberg et al.[14] The data were acquired using a push-broom Hyspex VNIR-1600 camera (Norsk Elektro Optikk, Lillestrom, Norway). The images were acquired in the wavelength range 400-1000 nm, with a spectral resolution of 3.7 nm. The samples were illuminated using a frequency tripled Nd:YAG-laser (Quanta Ray Lab-series L-190, Spectra Physics, Mountain View, California), providing UV-excitation at 355 nm. For more details on the experimental setup, see Larsen et al.[13]

4.2 Simulations

To emulate fluorescence spectra similar to the spectra encountered in the measurements, data were generated using the function

$$R(x) = \exp(mx \exp(-x/s + 1)/s), \tag{13}$$

with x ranging from 0 to 100 in discrete steps. Three baseline spectra were chosen using parameters $s = [10, 20, 60]$ and $m = [4.0, 3.8, 3.6]$, shown in Fig. 3.

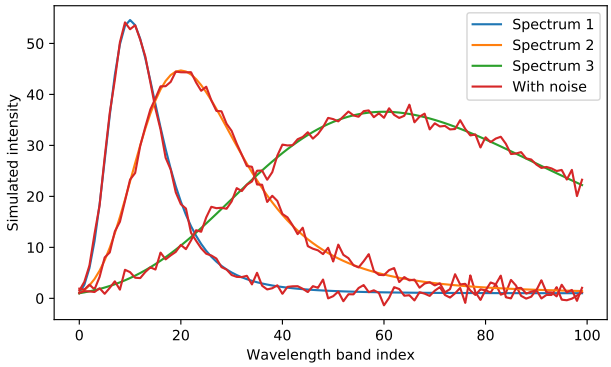

Figure 3. Three basic spectra used in the simulations.

An image with 3 rows and 500 columns was created. Each of the basic baseline spectra were assigned to a row. Each row was divided into 100 patches with 5 pixels in each patch, where parameters m and s were randomly generated from a Gaussian distribution with means corresponding to the baseline parameters and standard deviation 1, and used to yield variations of the baseline spectra. Constant variance ($\sigma = 1$) Gaussian noise was added to the spectra. The goal was to create an image with a large enough number of pixels to be able to estimate reliable image statistics, but let no specific spectrum be homogeneously overrepresented.

5. RESULTS AND DISCUSSION

The smoothing splines method is explored as a technique for noise removal and subresolution peak characterization in hyperspectral images, and compared against MNF. The method is first applied to autofluorescence measurements, and then to simulations of spectra with additive noise.

5.1 Peak position characterization in fluorescence data

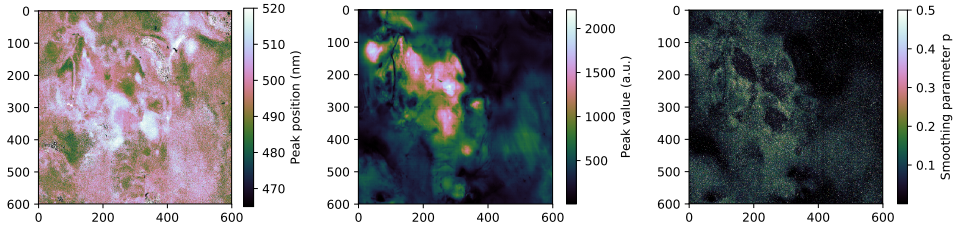

Figure 4. Peak positions (left), peak values (center) and smoothing parameters $p = \frac{1}{\alpha+1}$ as estimated using the cross-validation approach (right).

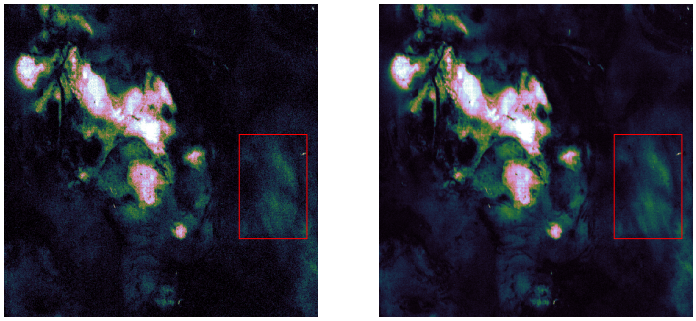

Figure 5. Comparison of the blue band before and after application of smoothing splines.

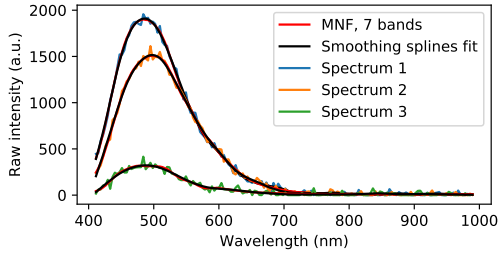

Figure 6. Raw spectra compared against smoothing splines and MNF denoised spectra.

Peak positions, peak values and the corresponding smoothing parameters for the measurements are shown in Fig. 4.

Band images before and after application of the technique for one of the noisier bands in the blue region are shown in Fig. 5. Spatial noise is reduced in these bands after application of the technique, due to the constraining effect of the splines. See for example the region marked in red, where graininess in the raw image is replaced by a smoother texture with more detail.

Raw fluorescence spectra were selected from three pixels for further comparison (positions $(x, y) = (279, 232)$, (272, 336), (598, 398) for spectrum 1, 2 and 3, respectively), and are compared against the smoothing splines fit in Fig. 6. The splines yield smooth spectra that well follow the trends in the spectrum.

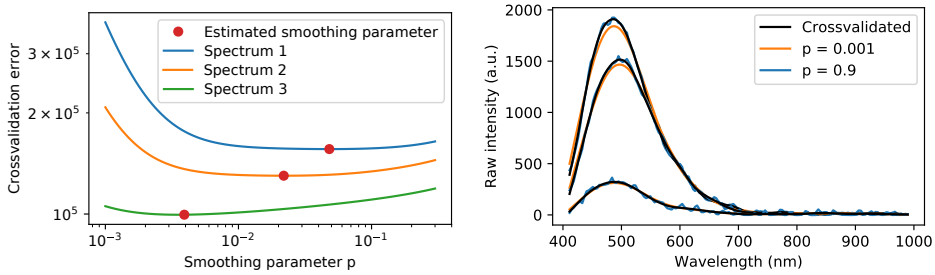

Figure 7. Cross-validation curves (left) and corresponding spectra (right) at the cross-validated smoothing parameters and parameters above and below this parameter.

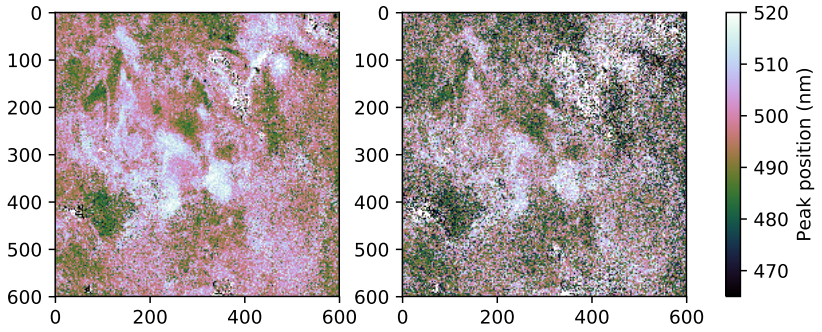

Figure 8. The rounded smoothing splines maximum estimate (left), compared to the maximum position as estimated using `max` on each raw spectrum (right).

Corresponding cross-validation error curves are shown in Fig. 7, along with examples of spectra smoothed at parameters outside the minimum. A parameter above the cross-validated parameter yields a spectrum which follows the noise. A parameter below the cross-validated parameter yields a smooth spectrum, but has bias. The smoothing parameter at the lowest cross-validation error yields a compromise between the two.

The peak position as estimated from the raw spectra by simply finding the index position for the max value throughout the noisy spectrum was compared against the rounded smoothing splines estimate in Fig. 8. Rounding the peak position as obtained from the smoothing splines method yields an index value similar to the simple max, but chooses a wavelength index closer to the sub-resolution estimate. This represents an estimate with less spatial noise. Working in the subresolution regime would especially be useful for characterization of gradual changes over time when the wavelength discretization is large. The use of cross-validation to estimate smoothness makes the results comparable across pixels and images.

5.2 Comparison between smoothing splines and MNF

The smoothing splines method was compared to MNF on the autofluorescence data and the simulations described in section 4.2.

5.2.1 Application of MNF to fluorescence data

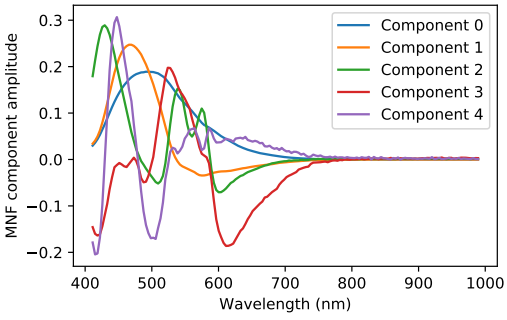

Figure 9. Components of the inverse MNF matrix.

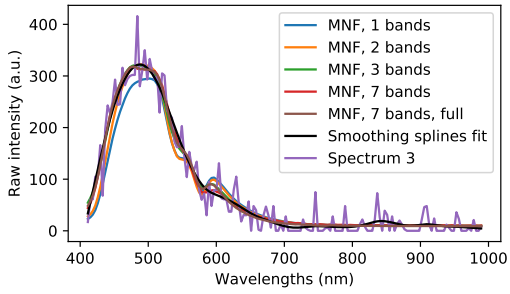

Figure 10. Inverse MNF spectra for different number of components in inverse, and statistics obtained from a larger subset of the image.

The first components in the inverse transform and the corresponding first bands in the forward transformed image are shown in Fig. 9 and 11, respectively. The inverse, denoised spectra will be a linear combination of

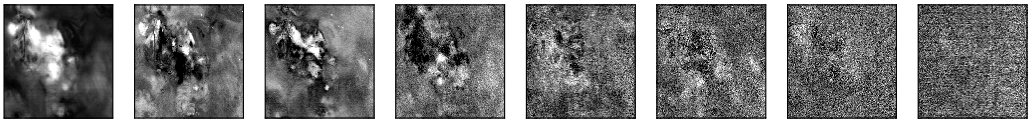

Figure 11. The first bands of the MNF transform.

the components in the inverse transform, with the pixel values in the transformed bands as the coefficients. It is seen that the components gradually contain more and more noise. Seven bands were taken to construct the inverse transform considered further on.

Example spectra are compared against corresponding splines in Fig. 6. This shows some deviations between the smoothing splines spectrum and the MNF spectrum: for spectrum 1, the denoised spectra do not overlap around 500 nm, and for spectrum 3, the MNF spectrum has oscillations not present in the smoothing splines spectrum. The true spectra are not known here, and the differences were therefore not evaluated for the measurements. Differences for simpler simulations are evaluated in section 5.2.3.

MNF has a tuning parameter similar to the smoothing parameter, the number of components to use in the inverse transform. Selecting a low number of components leads to bias in the inverse spectrum, which is demonstrated by the denoised spectra using 1 and 2 bands in the inverse in Fig. 10. Including all components in the inverse reproduces the original spectrum exactly. An intermediate value produces a smooth approximation, subject to the image statistics and the spectrum at hand.

Tuning number of components using cross-validation is not well-defined, as MNF would have to be fitted with one of the bands missing from the data. MNF does not interpolate missing bands, and calculating the prediction error on the left-out band is not well-defined. The number of components is therefore usually selected through visual inspection of the plot over the SNR as a function of the number of components, or by visual inspection of the noisiness of the transformed MNF bands or inverse spectra. In addition to subjectivity, this means that the parameter is chosen based on the bulk properties of the image. Individual spectra could require less or more components due to spatial variations in the SNR, but adjusment on pixel level is not possible due to the method not being interpolating.

MNF is expected to yield a less optimal estimate if the shape of the spectrum at hand is less represented in the statistics matrices. Essentially, pure components would be used to represent less represented spectra. Different components would be mixed where there is no mixture of such fluorescence components. Such mixture behaviour would be more prominent with less components, while more components leads to more noise, essentially being a bias-variance consideration.

5.2.2 Comparison of denoising matrices

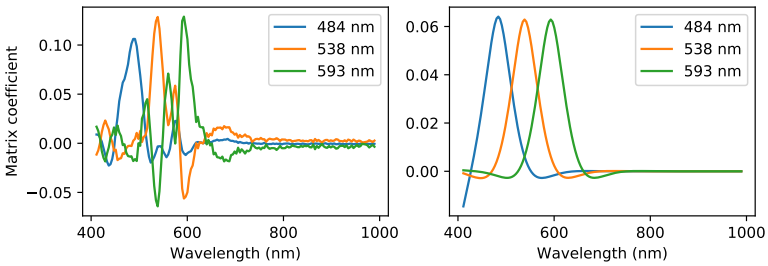

Figure 12. Components of the denoising matrices for MNF (left) and smoothing splines (right, $p = 0.001$) that yields denoised spectral values at three discrete bands.

Evaluating the smoothing splines at the training points x_i can be expressed as a matrix multiplication $\mathbf{S}_\alpha \boldsymbol{y}$, while denoising using MNF is also similarly expressed as a matrix multiplication $\mathbf{D}(\boldsymbol{y} - \bar{\mathbf{B}})$. A value at the band i is therefore calculated by linearly combining values of the raw spectrum using coefficients present along a row i of the denoising matrix. Linear combination coefficients yielding a specific band value are plotted in Fig. 12, and shows that the coefficients are similar for smoothing splines and MNF. There exists a relation between smoothing splines and ridge regression,[6] and ridge regression and PCA,[6] and MNF can be expressed as a PCA transform of the noise whitened image.[15] The similarity of the denoising matrices could indicate some relation between smoothing splines and MNF, but would have to be further investigated.

5.2.3 Application of MNF and smoothing splines to simulations

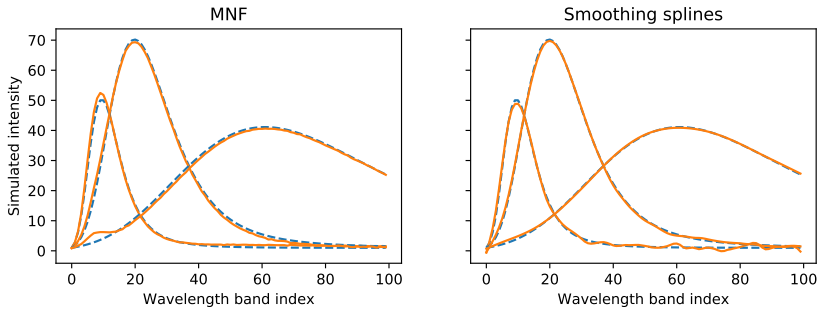

Figure 13. Comparison of MNF and smoothing splines as applied to simulated spectra.

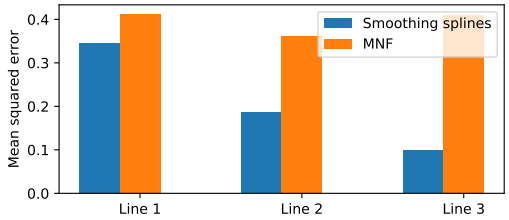

Figure 14. Mean squared error between smoothing splines and MNF for the three spectral types present in the simulated dataset.

MNF was run on the simulations with 6 components in inverse, with the seventh component consisting of pure noise. Examples of denoised spectra are shown in Fig. 13. The mean squared error between the original spectra before noise was added and the denoised spectra is shown in Fig. 13. The examples show alien spectral components in the MNF denoising of spectrum 3. This demonstrates component mixing, where components from from spectrum 1 are used to denoise spectrum 3. The spectra also show some bias. The bias is summed up as a higher bulk mean squared error as compared to the smoothing splines technique. The smoothing splines technique has lower mean squared error, and the examples show that the smoothing splines method well approximates the high-SNR parts of the original spectra. However, the smoothing splines estimate has high variance and follows the noise too closely for the low-SNR parts. The choice of α is low in order to accomodate the high-SNR parts, but results in a fit with too many degrees of freedom in the low-SNR parts. This is behavior that was also seen for the measured fluorescence spectra, especially evident in Fig. 10.

5.2.4 General discussion

Smoothing splines interpolates the trends of the noisy spectra, using an objective measure with a clear minimum to determine the amount of smoothness for each pixel. This makes the results comparable regardless of image

and noise statistic estimates, which is especially useful for characterization across images. The smoothing splines tuning parameter is continuous, allowing individual tuning down to an arbitrary numerical precision.

MNF is tuned by visual inspection of either components or SNR plots, and the results are not necessarily comparable across different images or even pixels. The MNF tuning parameter is discrete, restraining somewhat the possbility for tuning.

MNF takes image statistics from the image at large into account when smoothing the spectra, whereas smoothing splines considers only one spectrum at a time. This can have both advantages and disadvantages. It was seen in the simulations that using the full image to denoise single spectra can lead to component mixing, which can have negative ramifications for further processing. Different images would have different image statistics, and different components would be used to build the denoised spectra. Using components from the full image makes full use of the available information, however, and restrains the spectra in low-SNR parts properly, as seen in the simulations. The smoothing splines estimates of α mainly satisfies the high-SNR parts of the spectra, while the low-SNR parts will have an α which is not restrictive enough.

Thus, MNF and splines represent two extremes: MNF uses information from the image at large, but makes no individual tailoring, while smoothing splines considers each spectrum individually, but makes no use of prior information. Improvements could be made by centering and standardizing the image bands or applying weights to the method using the image covariance matrix. In addition, there exists modifications to the technique which have α dependent on x,[16–19] which would be appropriate here.

MNF would also be more adaptable for various types of noise distributions and image spectra, while the smoothing spline is more restrictive and sensitive to spectral behavior. Attempts to apply the method on reflectance data from human skin yielded unphysical results due to the high variation in noise variance as a function of wavelength, and absorption features being confused as undesired noise variance. The method was more suitable for fluorescence data, due to the simple polynomial-like behavior of these spectra. Centering and standardization of the image bands could improve applicability to reflectance data. It is expected that the method will be less suitable when the fluorescence spectra are strongly influenced by absorption features.

Inverse spectra obtained using the MNF transform can discard or mix important spectral features. Still, MNF is often the most suitable alternative, and for some data this might be a good enough approximation. The variant of MNF considered here is also the most extreme variant, in that a hard cut-off is used for the transformed bands. A more gradual variant could be to apply gradually more aggressive noise removal on the transformed bands before back-transformation, but objective evaluation of such improvements could be challenging. MNF is also valuable in dimensionality reduction.

Regardless of denoising method, the smoothing splines method is well suitable for investigating the spectra at subresolution positions and be used to estimate fluorescence emission peak positions or other properties that are easily extracted from spline coefficients. The results here also suggests that it is appropriate as a denoising method for fluorescence spectra.

6. CONCLUSION

The smoothing splines method has been adapted for use in hyperspectral images, with individual smoothing parameters that are appropriate for every single pixel in the image. The method has been applied to images of atherosclerosis plaques, and found to yield smooth spectra. The spline coefficients were used to find sub-resolution peak positions of the emission spectra. Comparison of MNF and smoothing splines on simulations showed the smoothing splines estimate to yield spectra with lower bias. While the appropriateness of MNF is subject to the availability of image statistics, smoothing splines represents a robust method with an objective choice between smoothness and closeness of the spectra, and which apparently has advantages over MNF for the type of data represented by autofluorescence images.

APPENDIX A. MANIPULATING SMOOTHING SPLINES SOFTWARE PACKAGES TO OBTAIN THE SMOOTHING MATRIX

The techniques presented in this paper assume the availability of $\mathbf{S}_\alpha$, the smoothing matrix. This is usually not made available in a given software implementation. Smoothing splines is implemented in MATLAB (version 9.2.0, The MathWorks Inc., Natick, Massachusetts, USA) through the function `csaps`, and a Python implementation can be found in the Python package `pywafo`.[20] Both implement smoothing splines according to the definitions given in de Boor,[7] which use p instead of α as the smoothing parameter.

A.1 Estimation using the identity matrix

This method requires no software modification, and obtains $\mathbf{S}_\alpha$ by manipulating the input. Given a spectrum $\boldsymbol{I_1} = [1, 0, \ldots, 0]^T$, the resulting fitted smoothing spline is

$$\hat{\boldsymbol{f}}_\alpha = \mathbf{S}_\alpha \boldsymbol{I_1} = [S_{11}, S_{12}, \ldots]^T. \tag{14}$$

Iteratively putting in columns of the identity matrix I reproduces $\mathbf{S}_\alpha$.

A.2 Estimation using intermediate results

This method requires software modification. As both MATLAB and pywafo implementations are based on de Boor,[7] a couple of intermediate results can be exploited to estimate $\mathbf{S}_\alpha$ directly. Below, this is outlined using de Boor's notation, usually translated into similar variable names in the code. de Boor's method also considers the covariance matrix of y, $\mathbf{D}$, but this is neglected below for simplicity.

The smoothing splines are here formulated in terms of their piece-wise polynomial form (ppform). One of the intermediate results is the vector $\boldsymbol{a}$, defined to be

$$f_p(x_i) = a_i, \tag{15}$$

i.e. the elements of $\boldsymbol{f_p}(\boldsymbol{x}) = \mathbf{S}_\alpha \boldsymbol{y}$. It is in the packages found from

$$\boldsymbol{a} = \boldsymbol{y} - 6(1-p)\mathbf{Q}\boldsymbol{u}. \tag{16}$$

The vector $\boldsymbol{u}$ is found by solving

$$\underbrace{(6(1-p)\mathbf{Q}^T\mathbf{Q} + p\mathbf{R})}_{\stackrel{\text{def}}{=}\mathbf{B}_p}\boldsymbol{u} = \mathbf{Q}^T\boldsymbol{y} \tag{17}$$

Both $\boldsymbol{a}$ and $\boldsymbol{u}$ are used to estimate the other parameters defining the ppform of the smoothing spline, which can then be used for interpolation. The matrices $\mathbf{Q}$ and $\mathbf{R}$ are calculated from differences between data points x_i.

Inserting (17) into (16) then yields

$$\boldsymbol{a} = \underbrace{(\mathbf{I} - 6(1-p)\mathbf{Q}\mathbf{B}_p^{-1}\mathbf{Q}^T)}_{\mathbf{S}_\alpha}\boldsymbol{y}. \tag{18}$$

Thus, $\mathbf{S}_\alpha$ is estimated from $\mathbf{Q}$ and $\mathbf{B}_p$, which are all available in a given smoothing splines implementation.

ACKNOWLEDGMENTS

Thanks to Eivind L.P. Larsen for acquisition of the data.

REFERENCES

[1] Larsen, E. L. P., Randeberg, L. L., Olstad, E., Haugen, O. A., Aksnes, A., and Svaasand, L. O., "Hyperspectral imaging of atherosclerotic plaques in vitro," *J Biomed Opt* **16**(2), 026011 (2011).

[2] Noh, H. K. and Lu, R., "Hyperspectral laser-induced fluorescence imaging for assessing apple fruit quality," *Postharvest Biol. Technol.* (2007).

[3] Gowen, A. A., O'Donnell, C. P., Cullen, P. J., Downey, G., and Frias, J. M., "Hyperspectral imaging - an emerging process analytical tool for food quality and safety control," *Trends Food Sci. Tech.* **18**(12), 590–598 (2007).

[4] Lu, G. and Fei, B., "Medical hyperspectral imaging: a review," *J. Biomed. Opt.* **19**(1), 010901 (2014).

[5] Green, A. A., Berman, M., Switzer, P., and Craig, M. D., "A transform for ordering multispectral data in terms of image quality with implications for noise removal," *IEEE Trans. Geosci. Remote Sensing* **26**(1), 65–74 (1988).

[6] Hastie, T., Tibshirani, R., and Friedman, J., [*The elements of statistical learning*], Springer, second ed. (2008).

[7] de Boor, C., [*A practical guide to splines*], Springer-Verlag (1978).

[8] Marion, R., Michel, R., and Faye, C., "Measuring trace gases in plumes from hyperspectral remotely sensed data," *IEEE Trans. Geosci. Remote Sens.* **42**, 854 – 864 (2004).

[9] Berman, M., "Automated smoothing of image and other regularly spaced data," *IEEE Trans. Pattern Anal. Mach. Intell.* **16**, 460–468 (1994).

[10] Lee, J. S. and Cox, D. D., "Robust smoothing: Smoothing parameter selection and applications to fluorescence spectroscopy," *Comput. Stat. Data Anal.* **54**, 3131–3143 (2010).

[11] Dongarra, J., "Basic linear algebra subprograms technical forum standard," *Int. J. High Perform. Comput. Appl.* **16**(2), 1–111 (2002).

[12] Bjorgan, A. and Randeberg, L. L., "Real-time noise removal for line-scanning hyperspectral devices using a minimum noise fraction-based approach," *Sensors* **15**(2) (2015).

[13] Larsen, E. L., Randeberg, L. L., Olstad, E., Haugen, O. A., Aksnes, A., and Svaasand, L. O., "Hyperspectral imaging of atherosclerotic plaques in vitro," *J. Biomed. Opt.* **16**(2) (2011).

[14] Randeberg, L. L., Larsen, E. L. P., Haugen, O. A., and Svaasand, L. O., "Hyperspectral characterization of atherosclerotic plaques," *Proc. SPIE* **7368** (2009).

[15] Lee, J., Woodyatt, A. S., and Berman, M., "Enhancement of high spectral resolution remote sensing data by a noise-adjusted principal components transform," *IEEE Trans. Geosci. Remote Sens.* **28**(3) (1990).

[16] Mackay, D. J. C. and Takeuchi, R., "Interpolation models with multiple hyperparameters," *Stat. Comput.* **8**, 15–23 (1998).

[17] Abramovich, F. and Steinberg, D. M., "Improved inference in nonparametric regression using lk-smoothing splines," *J. Stat. Plan. Inference* **49**, 327–341 (1996).

[18] Pintore, A., Speckman, P., and Holmes, C. C., "Spatially adaptive smoothing splines," *Biometrika* **93**, 113–125 (2006).

[19] Ruppert, D. and Carroll, R. J., "Theory & methods: Spatially-adaptive penalties for spline fitting," *Aust N. Z. J. Stat.* **42** (2002).

[20] "pywafo source code repository." Available online on https://github.com/wafo-project/pywafo. Visited 2019-01-23.

Paper V

A. Bjorgan and L. L. Randeberg, “A random forest-based method for selection of regions of interest in hyperspectral images of ex vivo human skin,” *Proc. SPIE*, vol. 10889, 2019. DOI: https://doi.org/10.1117/12.2506620

A random forest-based method for selection of regions of interest in hyperspectral images of ex vivo human skin

Bjorgan, Asgeir, Randeberg, Lise

Asgeir Bjorgan, Lise L. Randeberg, "A random forest-based method for selection of regions of interest in hyperspectral images of ex vivo human skin," Proc. SPIE 10889, High-Speed Biomedical Imaging and Spectroscopy IV, 108891K (4 March 2019); doi: 10.1117/12.2506620

SPIE.

Event: SPIE BiOS, 2019, San Francisco, California, United States

A random forest-based method for selection of regions of interest in hyperspectral images of ex vivo human skin

Asgeir Bjorgan and Lise L. Randeberg

Department of Electronic Systems, NTNU Norwegian University of Science and Technology, Trondheim, Norway

ABSTRACT

Hyperspectral imaging is a useful tool for characterization of human tissue. However, the vast amount of data created makes it challenging and tedious to manually select spatial regions of interest for further processing. In this study, a random forest-based method was evaluated on basis of its ability to segment human skin regions from the background. The method was compared to the performance of two alternative methods, spectral angle mapper (SAM) and a K-means clustering-based method. The methods were tested on hyperspectral images of ex vivo and in vivo human skin in the wavelength range 400-1000 nm. The random forest approach was found to be robust and perform well regardless of image type. The method is simple to train, and requires minimal parameter tuning for good skin segmentation results.

Keywords: image segmentation, machine learning, tissue imaging, binary classification, spectral angle mapper, K-means clustering

1. INTRODUCTION

Hyperspectral imaging combines high spatial and spectral resolution in one modality, giving images with high spectral resolution in every pixel. This makes it a useful tool for characterization of human tissue.[1–5] Characterization can involve investigation of larger datasets that are acquired from many individual samples, or from the same sample over time. The large amount of data makes it challenging to identify systematic variations across images without additional analytical tools. Background clutter and non-relevant spectral signatures can influence the results of statistical algorithms. Segmentation is in general needed for proper visualization of the results. Visual selection of regions of interest is subjective, and automatic selection is therefore one important cornerstone of any processing chain.

Examples of hyperspectral data include reflectance images,[3,5] transmittance images[6,7] and autofluorescence images.[8–10] Each of these imaging techniques yield different types of spectral data, and a method for selection of regions of interest should be generic and robust for all kinds of images. Hyperspectral images have large dimensionality, with a large number of spectral bands that are highly correlated. Due to the correlation, using the spectral bands as features in classification algorithms can be challenging, typically requiring dimensionality reduction or feature engineering. It is desired to avoid individual tailoring and ad-hoc adjustments, and the required parameter tuning should be minimal.

Random forest classification is a robust technique which is able to obtain high prediction accuracy with little to no parameter tuning,[11,12] and which can be applied directly to data with high dimensionality and a relatively low number of samples.[13,14] This makes it attractive as a general technique which can be adapted for various types of images. An example of a simple segmentation technique would be the application of some kind of thresholding to the image bands. A decision tree[12] takes this further by considering a chain of thresholding operations that all are dependent on the results of the previous. Tree-based methods are promising due to their ability to model highly nonlinear relations, which could be adaptable for selection of regions of interest in complicated images. The random forest technique improves the test accuracy of decision tree-based methods by averaging the results from multiple decorrelated trees. The nature of the method makes it appropriate for a highly correlated predictor space such as hyperspectral data.[13,14]

Further author information: (Send correspondence to A.B.)
A.B.: E-mail: asgeir.bjorgan@ntnu.no

High-Speed Biomedical Imaging and Spectroscopy IV, edited by Kevin K. Tsia, Keisuke Goda, Proc. of SPIE
Vol. 10889, 108891K · © 2019 SPIE · CCC code: 1605-7422/19/$18 · doi: 10.1117/12.2506620

The random forest technique can be used for both regression and classification tasks, and has earlier been used in hyperspectral imaging for classification in remote sensing[13,15] One study was also found on the application of detecting human skin in hyperspectral images.[16]

The primary aim of this study was to segment ex vivo human skin from the background, but the technique was also tested on images acquired from living humans. The technique was compared to SAM (spectral angle mapper) and a simplified K-means classifier. SAM classifies a spectrum based on the angle between the spectrum and a signature of interest. K-means classification clusters the data into K clusters based on centroid distances. The clusters can be used for classification after having training data labels assigned to them.

The techniques considered in this paper are all supervised classification methods, where a model $f(\boldsymbol{x})$ is built to predict a class label g from a spectrum $\boldsymbol{x}$. K-means clustering is an example of an unsupervised learning technique, where clusters, structures or relationships are learned from the data without having an associated response g. Associating such clusters with a response g makes the method supervised.

The theory behind the used classification methods is presented in section 2. The datasets used to evaluate the methods are presented in section 3, and the methods evaluation setup is presented in section 4. The results of the evaluation on the various datasets are presented in section 5.

2. METHODS

A general overview over the classification problem is first given, before the random forest, SAM and simplified K-means classifier methods are outlined.

2.1 Classification and target detection

The problem of segmenting human skin from background pixels is a binary classification problem, where every pixel $\boldsymbol{x}$ is assumed to belong to a class $g \in \{\text{background}, \text{skin}\}$. A pixel with K wavelengths can be considered a vector of predictors $\boldsymbol{x} = [x_1, \cdots, x_K]^T$ in a K-dimensional space. Classification effectively means that the vectors are labeled according their position in this space.[12] A classification method can be seen as a method to find region boundaries or decision surfaces for appropriate labeling,[12] or to model class probabilities and assign the class with the largest likelihood.[12]

The problem can also be considered to be similar to the target detection problem in remote sensing. Here, the task is to detect, enhance or calculate probabilities for a pixel to belong to a target of interest.[17] This problem corresponds to a binary classification problem if a hard decision is made.

The classification error can be defined as[12]

$$\text{Error} = \frac{1}{N} \sum_{\text{pixels}} (\hat{g}(i) \neq g(i)), \tag{1}$$

or the prediction accuracy as

$$\text{Accuracy} = 1 - \text{Error}. \tag{2}$$

The latter will be used to assess the performance of the algorithms investigated in this study. A prediction accuracy of 1 means that all pixels were assigned the correct class, while prediction accuracy of 0 means that none of them were. Prediction accuracy of 0.5 means that the classifier has the same performance as selecting the classes randomly.

Modified measures that weight background and target classification and misclassification differently exists, but are not considered in this study.

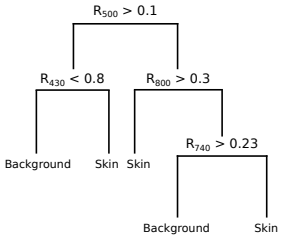

Figure 1. Example of decision tree for skin classification.

2.2 Random forest

A decision tree partitions the predictor space into rectangles, and assigns a class to each rectangle according to training data.[12] An example of a decision tree classifier for reflectance spectra is shown in Fig. 1. A class is assigned to a spectrum according to splits along reflectance values at specific wavelengths. This is effectively a series of thresholding operations on the band values of the image.

Small changes in the training data can lead to large changes in the structure of the tree due to a different series of splits being considered.[12] Several trees built based on bagged training data can be averaged to decrease this variance.[12] Such trees have identical probability distributions, and the expectation over the bagged estimate is the same as the expectation over a single tree.[12] The expected test error is therefore reduced only through reduction of the estimator variance, since the bias is constant.[12] Predictors that are strongly correlated with the response would typically always be selected during the first splits of the trees, leading to correlation between the trees.[18] This limits the variance reduction, and the potential test accuracy of the approach.[12]

The random forest technique[11] removes the correlation by always choosing m random predictors out of the total K predictors every time a new split in the tree is considered.[12] This decorrelates the trees, and improves the variance reduction and final prediction accuracy.[12]

In this study, 50 trees, also referred to as estimators, were used, unless otherwise specified. The parameter m was set to the square root of the total number of wavelengths available, following the typical recommendations for random forest classification.[12] The latter can be tuned with respect to test errors or cross-validation errors. This was not considered in this study in order to evaluate the method using only default parameters. The data were sum-normalized before application of the algorithm.

The final technique used for actual processing includes post-processing using binary hole filling, median filtering and selection of the largest contigous region. This is done in order to rectify for small misclassified regions. Post-processing was not applied to the results presented in this paper in order to properly evaluate misclassification in the various techniques. The Python method `sklearn.ensemble.RandomForestClassifier` was used as the random forest implementation. In practice, a random forest was trained and saved to file, and then applied to images in bulk in order to obtain masks for further application and processing.

2.3 SAM and simplified K-means clustering classification

The random forest algorithm was compared against two simpler methods, SAM and a K-means based method.

SAM assumes a hyperspectral pixel to be vector in a p-dimensional space. Considering two hyperspectral spectra $\boldsymbol{x}_1$ and $\boldsymbol{x}_2$ ($p \times 1$), spectral angle can be defined as[19]

$$\theta = \arccos\left(\frac{\boldsymbol{x}_1^T \cdot \boldsymbol{x}_2}{\|\boldsymbol{x}_1\|\|\boldsymbol{x}_2\|}\right). \tag{3}$$

Taking θ to be a measure of spectral similarity, all spectra in an image can be compared against a spectrum $\boldsymbol{m}$ representing e.g. human skin. Thresholding θ yields a binary classification. The angle θ effectively represents a correlation measure between the two spectra that should be theoretically insensitive to illumination conditions. In this study, $\boldsymbol{m}$ was found from the training data by averaging over the pixels representing skin, and the

threshold was chosen by calculating the threshold yielding optimal separation between skin and background in the training data.

K-means classification is an unsupervised classification technique which assumes that K classes are present in the data, and finds K centroids within the predictor space.[12] Finding K such clusters within the data, assigning class labels to each of them and predicting class labels on new data according to the distance to the centroids can be used as a classification technique, and is considered a prototype method.[12] Selecting the optimal number K is not well-defined and has to be done through visual inspection of a within-class variance plot. Using $K = 2$ is not necessarily correct, since the background and the tissue of interest can consist of multiple clusters. In this study, a simplified variation of this technique was therefore used in order to get a general impression of the behavior of a similar method. The skin and background samples were averaged to yield spectra $\boldsymbol{m}_{\text{skin}}$ and $\boldsymbol{m}_{\text{background}}$. Class labels were then assigned according to the least Euclidean distance to each class centroid. This is not strictly the K-means classification technique proper, but vaguely related.

SAM and the simplified K-means classifier used in this paper are related, and differ only by the distance metric.

3. DATASETS

A number of datasets were used to train and test the methods. All data were acquired using a push-broom Hyspex VNIR-1600 camera (Norsk Elektro Optikk, Lillestrom, Norway). The images were acquired in the wavelength range 400-1000 nm, with a spectral resolution of 3.7 nm. The datasets are listed in table 1.

Table 1. List of datasets used in this study. Acquisition setup is described in the text.

Dataset	Subject	Training image	Test image
Arm images	Ventral side of the arm of a healthy, female volunteer (Caucasian, 39 years old)	Baseline	Image acquired after 5 minutes of pressure cuff occlusion
Skin model I	In vitro skin model with wound	Image acquired at day 1	Image acquired at day 22
Skin model II	In vitro skin model without wound	Image acquired at day 1	Image acquired at day 22

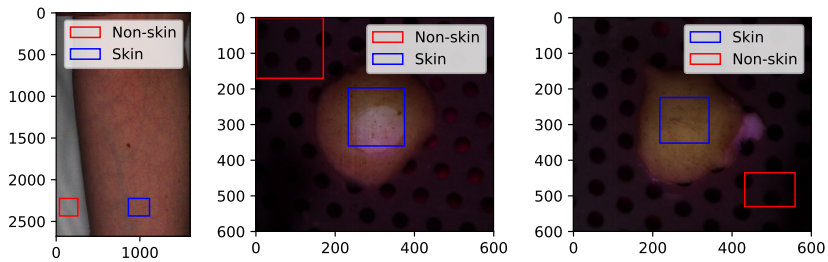

Figure 2. Training images labeled with the pixel subsets used for training: Arm, skin model I and skin model II.

The images were acquired with two linear light sources (Model 2900 Tungsten Halogen, Illumination Technologies, New York). Polarizers were mounted on the camera lens and the light sources (VLR-100 NIR, 450–1100 nm, Meadowlark Optics, Frederick, Colorado) in order to avoid specular reflection. The images were converted into reflectance and corrected for uneven illumination across the field of view using a Spectralon reflectance target (SRT-50-050 Reflectance Target, 12.7×12.7 cm, ACAL Bfi Nordic AB, Uppsala). The arm reflectance image has earlier been used in Bjorgan et al.[20] and Denstedt et al.[21] An earlier iteration of the in vitro wound model experiment has been presented in Randeberg et al.,[22] where the wound size was 5 mm. The data used in the current study had a wound size of 3 mm.[23]

4. EXPERIMENTAL EVALUATION SETUP

Various investigations were done into the accuracy and behavior of the methods.

Each method was trained on each of the training images listed in table 1 by training on the regions of interest shown in Fig. 2 and applying the methods on the corresponding test images. Test accuracies were calculated by comparing the segmentation results to a manual labeling of each pixel in the image. Training regions were selected in this way in order to emulate a typical application of the methods in a real data processing situation. Here, it is not desirable to manually label every pixel in the training image, but rather select e.g. rectangular bulk regions for each class.

In the next steps, each pixel in the training image of skin model I were manually labeled. A random subset without replacement of the training points were selected for each investigation, with equal number of data points in each class. First, the dependence on the size of the training data was found by training on a variable number of training points. Second, using a fixed number of training points, the random forest technique was tested as a function of the number of trees/estimators. Finally, to investigate the nature of the data used in this study, a PCA transform was fitted on the training data and applied on a random number of training and test data points for exploration of data clustering along the first two principal axes.

For all investigations, each method was trained on a specific training image, and tested on the corresponding test image acquired over the same object at a later day or after object manipulation, as outlined in table 1.

5. RESULTS AND DISCUSSION

The random forest method represents a tuning-free classification method which could be useful for selection of regions of interest in hyperspectral images of human tissue. The method is first compared against SAM and a simplified K-means classifier on the test datasets, and then investigated in detail in terms of its dependence on the training set and the number of estimators.

5.1 Comparison of the methods across images

Test accuracies for each of the methods are shown in Fig. 3. Corresponding visualizations of the classification results are shown in Fig. 4. The results show an overall higher test accuracy for the random forest method as compared to the other two methods in this study.

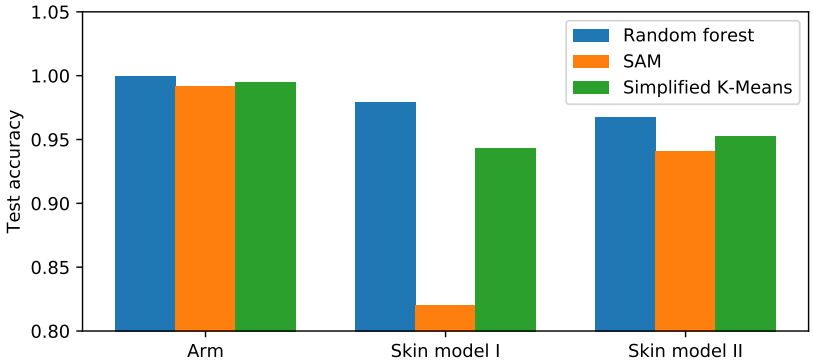

Figure 3. Test accuracy for models trained on the images shown in Fig. 2.

The accuracy is high for the arm image regardless of the classification method applied. This is due to the homogeneity of the sample. Similar behavior is seen for skin model II, which also is homogeneous over the region of interest, but has more complicated background.

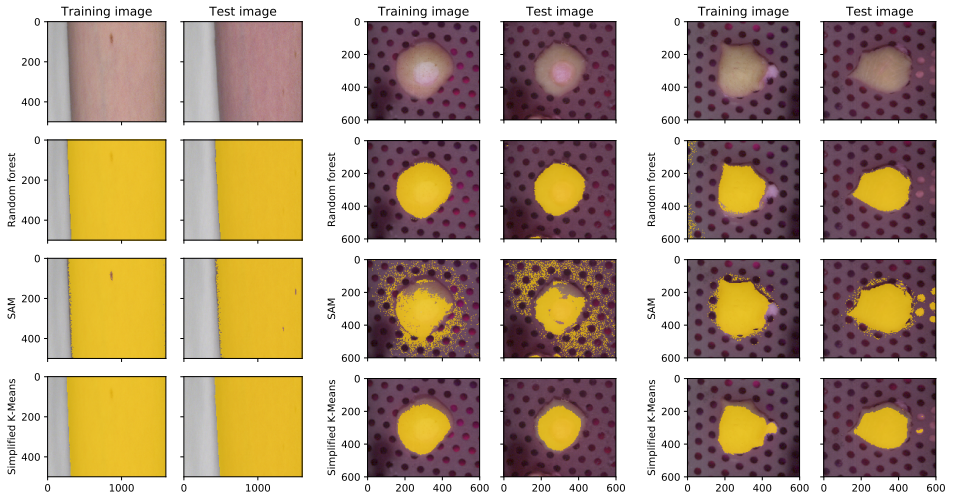

Figure 4. Segmentation results for the models trained on reflectance images: Arm (left), skin model I (center) and skin model II (right). Original images are shown on top, segmentation overlaid with original images in the following rows.

For the images of skin model I, random forest and the simplified K-means classifiers have test accuracies above 0.90, while SAM has a test accuracy below 0.85. This image has a more complicated surface than the image of skin model II due to the presence of a wound, causing the SAM spectrum to be less representative over the entire sample. The simplified K-means classifier is affected in the same way. SAM and the simplified K-means classifier are therefore susceptible to selection of training data points, while the random forest method adapts.

5.2 Application to a measurement series

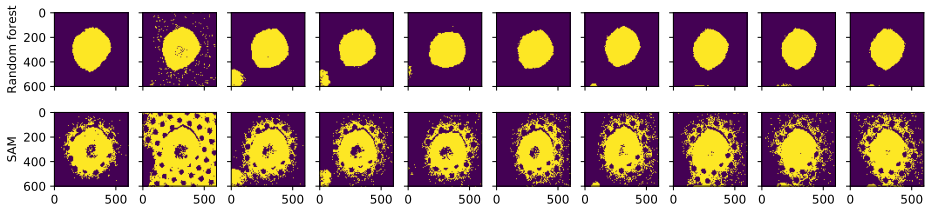

Figure 5. Application of random forest and SAM to a full reflectance image series of in vitro skin collected over several days. The methods were trained with 5000 datapoints from the first image.

The main application of this method is to segment larger series of images based on few training samples. Random forest and SAM were applied to a full measurement series in Fig. 5. SAM has higher misclassification of background, which is to be expected as the reflectance spectrum in the background is similar to the sample of interest. Background misclassification is suppressed for the random forest method. In both cases, application of proper spatial post-processing techniques would improve the results.

5.3 Dependence on the number of training points

In the initial tests, the methods were found to depend on the training samples. In order to investigate this, the test accuracy is plotted as a function of the size of the training set in Fig. 6.

The random forest method shows higher test accuracy with higher number of included points. This is to be expected for this method since random forest builds trees and generalizes based on training examples. The simplified K-means classifier and SAM, on the other hand, have no such dependence on training points. These methods work on mean spectra over the objects of interest. This leads to high test accuracy for simple situations, like the arm image, but taking the mean over more complex objects or backgrounds has low accuracy and changes with the samples included.

It would be appropriate to define multiple clusters within objects of interest and background in order to properly represent the complexity of the problem. For the simplified K-means classifier, this would be the same as using a conventional K-means classifier with some K defined. Such a method would have an increase in the test accuracy with the number of training points, but parameters like the number of clusters would have to be tuned. Random forest is already appropriate for representing such implicit multi-cluster situations without parameter tuning.

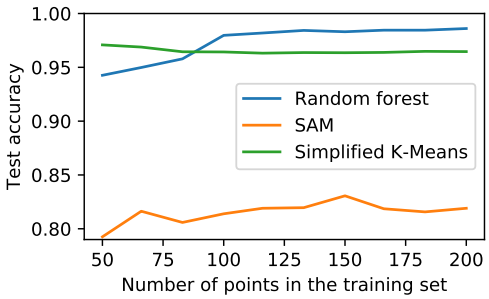

Figure 6. Test accuracy as a function of training set size for images of skin model I.

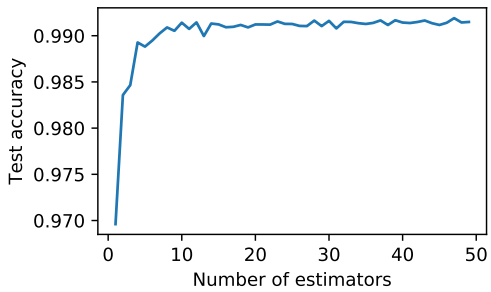

Figure 7. Test accuracy as a function of number of estimators in the random forest method for skin model I.

5.4 Feature importances and the dependence on the number of estimators

The test accuracy as a function of number of trees in the random forest method is plotted in Fig. 7. These results show that the trees converge towards a more or less constant test accuracy at around 10 trees.

Feature importances are plotted in Fig. 8, which is a measure for how many times a specific feature is used for splits in the trees. This implicitly shows which wavelenghts are important for the classification, and a method re-trained on these wavelengths would yield approximately the same test accuracy. The noisiness of the feature importances could indicate that the methods are slightly overfitted to the training data.

5.5 Investigation of the data in a lower dimensional space

Investigating the clustering behavior of the data could explain the behavior of the compared methods. A PCA transform was thus fitted to a centered and standardized reflectance image of skin model I in order to yield a rotated coordinate system along directions of the highest variance. Scores along the first two principal components are plotted in Fig. 9 for a random subset of each of the classes.

The classes consist of three clusters in the PCA space, with a gradual boundary in-between. The background and tissue would here be separable by a linear decision boundary. This explains why the simplified K-means classifier has a test accuracy comparable to the random forest classifier for the homogeneous reflectance data, as the clusters can be represented by their combined centroids. However, the elongation of the clusters also means that K-means clustering is not optimal for this kind of problem.

The data have a more or less homogeneous background and object of interest, and the simplicity of the problem is reflected with a linear decision boundary in the PCA space. More complex examples could be expected to have non-linear decision surfaces. The random forest classifier is well suitable for modeling non-linear decision

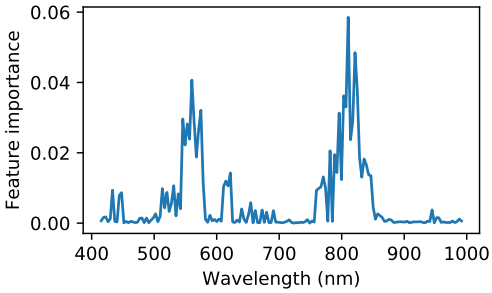

Figure 8. Feature importances in the random forest method for skin model I.

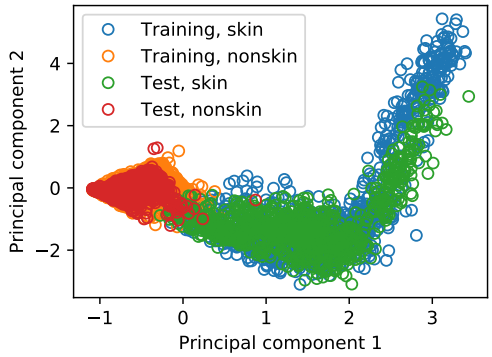

Figure 9. Data points corresponding to hyperspectral pixels along the first two components of a PCA space for reflectance images of skin model I.

surfaces, while methods like SAM or the simplified K-means classifier would have to be modified for implicit multi-class behavior.

Having more background clutter would be an example of a more complex image. This could typically be removed using pre- or post-processing, but such treatment would require manual tuning for each situation. Background clutter is not necessarily separable from the object of interest if they partially overlap. The random forest classifier automatically takes this into account. This avoids the need for manual tuning, and facilitates for automatic techniques.

5.6 General discussion

SAM and simplified K-means clustering are simple techniques that can be motivated from geometrical considerations of hyperspectral images, and which work well for simple scenes like homogeneous reflectance from a human arm. A flexible method like the random forest classifier seems to be appropriate for more complex situations wound images and complex backgrounds. The random forest technique is also appropriate for modeling of non-linear decision surfaces due to the underlying tree-based model. Having an adaptable technique with overall high classification accuracy across different types of images without parameter tuning is valuable.

However, the flexibility of the method can also make it less appropriate. The training data needs to be representative. The method can overtrain and not be able to find accurate decision surfaces. The PCA results showed that a linear decision boundary is appropriate for the examples shown in this study, meaning that restrictive methods would yield higher test accuracies. This study is not exhaustive, and linear classification techniques like LDA, QDA, logistic regression or SVM[12] could be appropriate for the examples shown. Gaussian clusters of data with equal or non-equal covariances would make methods like LDA and QDA optimal.[12] However, as seen in the reduced PCA space, each class is more likely to consist of multiple Gaussians, which makes the problem more challenging. Methods like LDA have challenges with large numbers of correlated features,[12] as is the case in hyperspectral imaging. Methods like SVM requires parameter tuning and selection of kernel functions. Other ensemble methods like boosting[12] might also be appropriate. Further work should involve testing more methods on both simpler and more complicated examples. SAM and the simplified K-means classifier are not necessarily optimal for the classification task at hand, and the random forest technique might have an unfair advantage.

Many classification techniques require preprocessing techniques like noise removal or dimensionality reduction. Dimensionality reduction would have to be fitted to the training data only, however, and could be less appropriate for the test data. Random forest is not dependent on preprocessing techniques, and is robust against the number

of features. The data were sum-normalized before application in order to make the spectra comparable and obtain some small improvements to the prediction accuracy, but no other preprocessing was applied.

Initial tests on fluorescence data (not shown here) showed that the random forest classifier had higher test accuracy than SAM and the simplified K-means classifier. The low photon count and highly correlated spectra of these data leads to a challenging classification problem, for which the random forest classifier was found to be well suitable. The classifier converged after 30-40 trees, whereas convergence was shown for 10 trees for the reflectance data used in this paper. The convergence rate thus depends on the complexity of the imaged samples. The required number of trees is expected to vary for reflectance data, and would depend on the required functional behavior of the decision surface and the behavior of the data points within the hyperspectral vector space.

Training and test images were chosen from the same data set. For both datasets, the test image was acquired over the same object as in the training data, but at a different time, and with changed spectral responses. It can be argued that these do not represent truly independent data since they are collected from the same object. They therefore do not properly measure the generalization ability of the method. However, selecting truly independent data would not necessarily yield a representative test accuracy, since the spectral responses could be too different across images. Statistical models generally do not necessarily extrapolate well outside the range of the training data.

The likely application of the method is to apply it within a specific measurement series over the same or similar objects, where it is convenient to manually label a small region in order to segment the rest of the images. Creating a truly generalizable method which can be trained once to be applied on any measurement series is outside of the scope of this study and the requirements of the method.

6. CONCLUSION

The random forest classifier has been found to be a robust technique for selection of regions of interest, and adapts well to different types of spectral data. There is no need for parameter tuning or consideration of preprocessing or modeling of implicit multi-cluster behavior in the data.

ACKNOWLEDGMENTS

Thanks to Lukasz Paluchowski for help in acquisition of the arm reflectance image. Thanks to Ingvild Haneberg and Matija Milanic for acquisition of in vitro skin model data. Thanks to Brita Pukstad for collaboration in the in vitro wound model experiment.

REFERENCES

[1] Lu, G. and Fei, B., "Medical hyperspectral imaging: a review," *J. Biomed. Opt.* **19**(1) (2014).

[2] Paluchowski, L. A., Nordgaard, H. B., Bjorgan, A., Hov, H., Berget, S. M., and Randeberg, L. L., "Can spectral–spatial image segmentation be used to discriminate experimental burn wounds?," *J. Biomed. Opt.* **21**(10) (2016).

[3] Denstedt, M., Pukstad, B. S., Paluchowski, L. A., Hernandez-Palacios, J. E., and Randeberg, L. L., "Hyperspectral imaging as a diagnostic tool for chronic skin ulcers," *Proc. SPIE* **8565** (2013).

[4] Yudovsky, D., Nouvong, A., and Pilon, L., "Hyperspectral imaging in diabetic foot wound care," *J. Diabetes Sci. Technol.* **4**(5), 1099–1113 (2010).

[5] Randeberg, L. L., Larsen, E. L. P., and Svaasand, L. O., "Characterization of vascular structures and skin bruises using hyperspectral imaging, image analysis and diffusion theory," *J. Biophotonics* **3**(1-2), 53–65 (2010).

[6] Milanic, M., Paluchowski, L. A., and Randeberg, L. L., "Hyperspectral imaging for detection of arthritis: feasibility and prospects," *J. Biomed. Opt.* **20**(9) (2015).

[7] Lu, R. and Ariana, D. P., "Detection of fruit fly infestation in pickling cucumbers using a hyperspectral reflectance/transmittance imaging system," *Postharvest Biol. Technol.* **81** (2013).

[8] Luthman, A. S., Dumitru, S., Quirós-Gonzalez, I., and Bohndiek, S. E., "Hyperspectral fluorescence imaging with multi wavelength LED excitation," *Proc. SPIE* **9711** (2016).

[9] Larsen, E. L. P., Randeberg, L. L., Olstad, E., Haugen, O. A., Aksnes, A., and Svaasand, L. O., "Hyperspectral imaging of atherosclerotic plaques in vitro," *J. Biomed. Opt.* **16**(2) (2011).

[10] Hernandez-Palacios, J., Randeberg, L. L., Baarstad, I., Loke, T., and Skauli, T., "Hyperspectral low-light camera for imaging of biological samples," *Work. Hypersp. Imag.* (2010).

[11] Breiman, L., "Random forests," *Machine Learning* **45** (2001).

[12] Hastie, T., Tibshirani, R., and Friedman, J., [*The elements of statistical learning*], Springer, second ed. (2008).

[13] Belgiu, M. and Dragut, L., "Random forest in remote sensing: A review of applications and future directions," *ISPRS J. Photogramm. Remote Sens.* (2016).

[14] Chan, J. C.-W., Bechers, P., Spanhove, T., and Borre, J. V., "An evaluation of ensemble classifiers for mapping natura 2000 heathland in belgium using spaceborne angular hyperspectral (chris/proba) imagery," *Int. J. Appl. Earth Obs.* (2012).

[15] Ham, J., Chen, Y., Crawford, M. M., and Gosh, J., "Investigation of the random forest framework for classification of hyperspectral data," *IEEE Trans. Geosci. Remote Sens.* (2005).

[16] Marques, I., Grana, M., Sanchez, S. M., Alkhatib, M. Q., and Velez-Reyes, M., "Person detection in hyperspectral images via skin segmentation using an active learning approach," *Proc. SPIE* **9472** (2015).

[17] Eismann, M. T., [*Hyperspectral remote sensing*], SPIE (2012).

[18] James, G., Witten, D., Hastie, T., and Tibshirani, R., [*An introduction to statistical learning*], Springer, first ed. (2013).

[19] Keshava, N. and Mustard, J., "Spectral unmixing," *IEEE Signal Proc. Mag.* **19**, 44 –57 (jan 2002).

[20] Bjorgan, A., Milanic, M., and Randeberg, L. L., "Estimation of skin optical parameters for real-time hyperspectral imaging applications," *J. Biomed. Opt.* **19**(6) (2014).

[21] Denstedt, M., Bjorgan, A., Milanic, M., and Randeberg, L. L., "Wavelet based feature extraction and visualization in hyperspectral tissue characterization," *Biomed. Opt. Express* **5**(12), 4260–4280 (2014).

[22] Randeberg, L. L., Hegstad, J. L., Paluchowski, L. A., and Pukstad, B. S., "Hyperspectral characterization of an in vitro wound model," *Proc. SPIE* **8926** (2014).

[23] Haneberg, I. J. A., *Hyperspectral imaging of in vitro wound models from human skin*, Master's thesis (2014).

Paper VI

A. Bjorgan and L. L. Randeberg, "Combining hyperspectral classification and heat transport modeling: An investigation of experimental burn wound heterogeneity," In submission. Submitted to Journal of Biomedical Optics.

Combining hyperspectral classification and heat transport modeling: An investigation of experimental burn wound heterogeneity

Asgeir Bjorgan[a], **Lise Lyngsnes Randeberg**[a,*]
[a]Department of Electronic Systems, NTNU Norwegian University of Science and Technology, Trondheim, Norway

Abstract.
Significance: Burns can be painful and disabling, and early evaluation of burn severity is imperative for appropriate treatment. This has resulted in several studies on optical techniques for burn assessment, including hyperspectral imaging.
Aim: The current study aims to gain better understanding of damage characterization and unexpected damage heterogeneity in a previously collected hyperspectral dataset, which used an experimental burn protocol using water bath heated metal and varying contact times.
Approach: Heat transport modeling was used to understand the temperature development in the tissue and the expected damage. Supervised classification and a photon transport model were used to investigate detectable damage and optical property changes.
Results: Collagen damage was indirectly classifiable using the hyperspectral data, but through coincident superficial perfusion changes. The burn severity was mainly related to deeper vascular damage seen in the histologies. This deep damage was not classifiable using the applied methods. By investigating changes to the boundary condition in the heat transport model, trapped steam between metal and skin was found to be a feasible explanation for the burn heterogeneity.
Conclusions: A better understanding of the burn procedure and the evaluable physical properties in the hyperspectral data has been obtained.

Keywords: burn wound classification, pig model, heat equation, tissue optics.

*Lise Lyngsnes Randeberg, lise.randeberg@ntnu.no

1 Introduction

If not treated according to the severity of the injury, burns can be both painful and disabling to the patient. Significant scientific effort has therefore been made to develop reliable, non-contact diagnostic methods for early and accurate diagnostics. In the process of developing and validating these technologies, it has been instrumental to develop reproducible methods for creating clinically relevant and controllable experimental burn wounds. This work addresses the understanding of burn dynamics by exploring supervised classification of hyperspectral burn data. In addition, it aims to assess and explain observed heterogeneity in burn severity in the employed wound model by simulations of optical and thermal propagation in skin.

Optical techniques are highly relevant for burn classification as they can be made non-invasive and non-contact. The difficulty involved in early evaluation of second degree burn wounds[1–3] has been the main motivator for the development of such techniques. Methods seen include laser doppler imaging,[4] laser speckle imaging,[4] spatial frequency domain imaging (SFDI)[1–3,5–8] and hyperspectral imaging.[9–16]

A common approach is to estimate blood perfusion parameters from optical measurements and then relate these to the vessel viability in dermis,[4] which determines whether a burn wound can heal without surgical intervention or not.[1,4] SFDI has been proved to be one of the most promising

technique in that it can separate tissue absorption from scattering, which is related to perfusion and collagen structure, respectively.[1,2] The blood perfusion parameters alone have been found to be unreliable early after injury,[1,2,17,18] while collagen destruction has been found to stabilize early enough to be used to characterize the damage.[1,2]

Hyperspectral imaging is expected to be sensitive to the same changes to absorption and scattering, and can potentially detect both types of damage. In a previous study, controlled burn wounds were created in two pigs in order to investigate the feasibility of using hyperspectral imaging in evaluation of burn wound severity.[19,20] Hyperspectral classification of burn severity turned out to be challenging, and unexpectedly, the results were difficult to interpret due to a high heterogeneity within each burn wound. In our opinion it is important to explain the heterogeneity itself in order to achieve a better understanding of the physics behind the damage mechanisms as such understanding is expected to ease hyperspectral classification.

The burn injuries in the previous study were created by heating up metal to $100\,^{\circ}\mathrm{C}$ using a water bath, and using different contact times to induce burns of varying depth and thus severity. Wound heterogeneity is commonly observed across the literature employing the same experimental burn induction procedure.[21] Gaines et al.[21] blames the adherence of vapor bubbles to the brass block during heating which makes block heating uneven and the final contact temperatures heterogeneous. Another possible explanation is that steam from left-over water on the block and water within the tissue is trapped between the block and the skin, and impedes heat transfer from the metal to the skin.

The thermal propagation in the tissue is fundamental to the injury mechanisms, and links the progression of different types of damage to the original damage method. Heat transport models are not frequently included as a part of studies on optical detection techniques, but understanding the thermal propagation can lead to better understanding of the relation between different damage mechanisms and expected optical detectability. The burn wound heterogeneity within a single burn and contact time represents a distortion with respect to the expected thermal evolution, and a heat transport model can be applied to find possible explanations. In the previous study, the heterogeneity appeared as a major artifact in the dataset, and establishing plausible explanations can help link observed spatial changes in optical properties to damage mechanisms. Better understanding of the burn heterogeneity can make it a useful asset of the dataset rather than an artifact.

Hyperspectral image data were previously gathered to explore the feasibility of this technique for burn classification. The data can be used to develop supervised classification techniques, where training data from the labeled histology locations are used to extrapolate the damage evaluation to the other parts of the images where histologies are not present. Such classification maps can be used to investigate the regional behavior of burn heterogeneity. As unsupervised classification was seen to be challenging in the previous study on the same data set,[19] further work has been invested in evaluating classification models and which types of damage it is possible to classify. In this study, the final damage evaluation is concluded based on multiple properties in the histologies, and it is explored how the relation between these individual properties can be more important than a classification based on the final burn level. Such investigation can also add to the feasibility of the technique for burn evaluation in general.

This study has been divided in three parts. The relation among the various burn damage types

obtained by histology is first investigated and systematized. Next, a heat propagation model is established and used to investigate the relation between the expected thermal evolution and resulting types of damage, and construct possible explanation models for the burn heterogeneity. Finally, the hyperspectral data is analyzed to establish a supervised classification model. Regional damage maps are obtained and discussed in terms of the expected thermal evolution. The goals of the study are two-fold, and the study seeks to understand and establish likely explanations for the burn heterogeneity and the feasibility of the hyperspectral technique.

2 Materials and methods

2.1 Experimental setup

The experimental method, details on the animal treatment and ethical considerations, and data acquisition procedure has been described in detail elsewhere.[19,20,22] The animals were treated in accordance with the "European Convention for the Protection of Vertebrate Animals used for Experimental and Other Scientific Purposes, Strasbourg, 18.III 1986" and Norwegian national regulations, and approval was given by the Norwegian Ethics Committee on animal research.

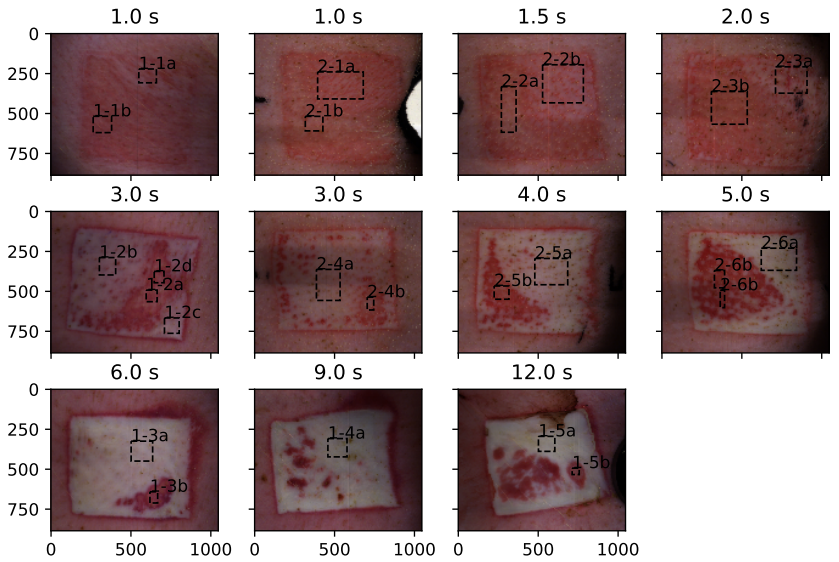

Fig 1: RGB images constructed from the 615, 564 and 459 nm wavelength bands over the hyperspectral images considered in this study, sorted by contact time. Training data locations and associated histology labels are marked with dotted boxes.

In short, a brass rod (4 x 4 x 3 cm) was heated up to $100\,^{\circ}\mathrm{C}$ in a water bath, and used to introduce burn wounds using different contact times. Hyperspectral images were regularly acquired up until 30 and 8 hours after injury for pig 1 and pig 2, respectively. Biopsies were collected after euthanasia, and analyzed by independent pathologists according to the method in Papp et al.[23] Various properties like e.g. deepest vascular damage, depth of collagen reorganization were evaluated, and final burn level was assigned according to the deepest present damage regardless of burn damage type, in anatomical levels according to epidermis (1), superficial, center or lower (2-4) dermis and subcutis (5). Level 3-4 corresponds to partial thickness wounds (second degree), while level 5 corresponds to full thickness wounds (third degree). RGB images at the last timepoint are shown in Fig. 1.

The histology properties were investigated and systematized by visual inspection of plots, and by training decision trees to predict burn level from the other properties. A decision tree is a supervised classification method which divides the input space into rectangular regions that assign the final class to the contained training data class.[24] This is well suited for categorical input data and is a reasonable and simple model for a decision process.

2.2 Heat transport theory

2.2.1 Model

The homogeneous heat equation is given as[25]

$$\frac{d^2T}{dx^2} - \frac{1}{\kappa}\frac{dT}{dt} = 0, \tag{1}$$

where the diffusivity $\kappa = \frac{K}{\rho c}$, K is the thermal conductivity, ρ the mass density and c the specific heat capacity of the medium. The Pennes bioheat equation[26] is often used to model heat transport in tissue,[27–31] which adds terms to the right hand side of (1) for metabolic heat generation and cooling by blood circulation. Metabolic heat generation is negligible compared to other heat fluxes involved from the heat source.[29] The blood perfusion will increase over time scales larger than 20 seconds when the tissue is heated,[27] but can in most cases be neglected.[32] A single-layer, semi-infinite model was assumed for simplicity. One-dimensional analysis was used under the assumption that the heat development well within the border of the metal rod is not influenced by convection against air. Assumed coefficient values were $K = 0.40\,\mathrm{W\,m^{-1}\,K^{-1}}$, $\rho = 1200\,\mathrm{kg\,m^{-3}}$ and $c = 3600\,\mathrm{J\,kg^{-1}\,K^{-1}}$, from Johnson et al.[30]

2.2.2 Boundary conditions

The temperature evolution was modeled in two phases: Heating by metal assumed to hold the temperature T_{metal} for the given contact time, and cool-down/relaxation after removal of the heat source. Normal damages are assumed to be induced by direct contact with the metal. The burn heterogeneity is assumed to be a result of either a lowering of the contact temperature, or the addition of contact surface resistance due to a steam interface. The boundary conditions are illustrated in Fig. 2.

Contact surface resistance can be expressed using linear heat transfer at the surface,

$$f = K\frac{dT}{dx}\Big|_{x=0} = H(T(x=0,t) - T_{\text{metal}}). \tag{2}$$

This expresses that there is some resistance $R = 1/H$ for the surface of the skin to attain the temperature of the metal. The solution is given in (11).

With $R \to 0$ or $H \to \infty$, the surface would instantaneously reach the metal temperature, and the boundary condition would be the same as

$$T(x=0,t) = T_{\text{metal}}. \tag{3}$$

The solution is given in (10).

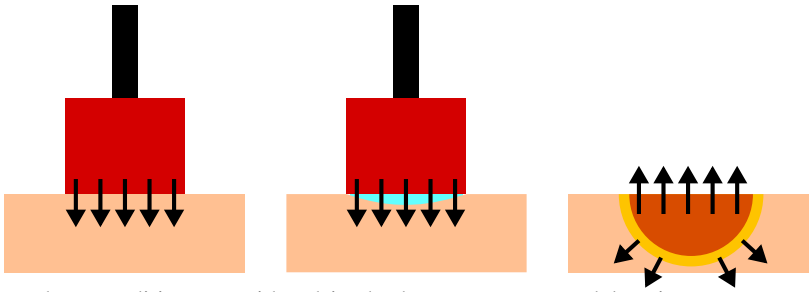

Fig 2: Boundary conditions considered in the heat transport model: Direct contact with metal (left), heat transfer being impeded by an effective heat transfer coefficient $H < \infty$ (center) and accumulated heating being propagated throughout the tissue or exchanged with air (right).

Heating by direct contact between metal and tissue Sufficiently hot water or hot metal with high heat conductivity are considered to have sufficiently large H[30,33] that (3) can be used. The temperature T_{metal} is assumed to be $100\,^{\circ}\text{C}$ by default. This contact temperature is modified to check what other temperatures could explain the heterogeneity.

Heating with steam interface between metal and tissue Assuming thickness d, conductivity $K_{\text{steam}} = 24.57\,\text{mW}\,\text{m}^{-1}\,\text{K}^{-1}$,[34] steady state ($\frac{dT}{dt} = 0$) in the interface and no additional contact resistances, the heat flux at the lower end of a steam interface is given by

$$f = \frac{K_{\text{steam}}}{d}(T_{\text{skin}} - T_{\text{metal}}). \tag{4}$$

Due to continuity of the flux, this also represents the boundary condition for the tissue. Comparison with (2) shows that they are equivalent with $H = K_{\text{steam}}/d$. The thickness of the layer is modified to check the steam interface thickness required to explain the heterogeneity.

Cool-down by air convection The heat source is removed after the contact period t_0. The boundary condition in (2) is appropriate with $H_{\text{air}} = 10\,\text{W}\,\text{m}^{-2}\,\text{K}^{-1}$[30] and $T_{\text{metal}} \to T_{\text{air}} = 25\,^\circ\text{C}$. The tissue has the initial temperature profile $T(x)$ as obtained after t_0 seconds of heating. The solution is given in (12).

2.2.3 *Arrhenius integral*

A damage integral can be used to assess tissue damage,[27,29,30,33] based on an Arrhenius rate reaction. The damage index

$$\Omega(\tau) = -\ln(C_\tau/C_0) \tag{5}$$

expresses the ratio between damaged cells C_τ and undamaged cells C_0 after heat exposure.[27] The rate is given as[35]

$$\frac{d\Omega}{dt} = P\exp(-\Delta E/RT), \tag{6}$$

where P is the pre-exponential frequency factor, ΔE the activation energy, R the molar gas constant and T the absolute temperature.[27] The value of Ω at some time t is obtained by integrating (6) from 0 to t.[27] Damage is evaluated by evaluating the integral at the basal layer, or locating the tissue depth at which $\Omega = 1$.[30] Values $P = 3.1 \times 10^{98}\ \text{s}^{-1}$ and $\Delta E = 6.28 \times 10^5\ \text{J}\,\text{mol}^{-1}$ (Henriques values[35]) are used in this study.

Another useful quantity, the critical temperature

$$T_c = \frac{\Delta E}{R\ln P}, \tag{7}$$

represents the temperature at which the damage rate $\frac{d\Omega}{dt} = 1$.[36]

2.2.4 *Damage characterization*

The thickness of dermis was assumed to be $2000\,\mu\text{m}$, from available estimates from the histologies. Histologies with increasing collagen damages had decreasing dermal thicknesses down to $1000\,\mu\text{m}$, but were assumed to be transformed by the heat.

Vascular and collagen damages were given in papillary dermis (first 4% of dermis), upper third, center third or lower third of dermis. This block division gives a lower and upper boundary for the depth of injury, respectively representing a depth at which there should be damage and a first depth where there should be no damage.

The temperature for discrete depths and times were simulated up until the contact time t_0 for all contact times using $T_m = 100\ ^\circ\text{C}$ and (10). The solution for $T(x, t = t_0)$ was then used as the initial temperature distribution $T(x)$ in (12), and further calculated at the same depths over 20 seconds. The Arrhenius integral was calculated over the temperature evolution. Assuming the most severe damages for each contact time to correspond to metal being applied directly to the tissue, the Arrhenius coefficients were adjusted to fit the observed damage depths for each injury and contact time.

Next, the temperature evolution was calculated in a similar way with contact temperatures from 50 to $100\,^\circ\text{C}$ and steam interfaces from 0 to $100\,\mu\text{m}$, and related to a depth of injury using the

adjusted Arrhenius coefficients. The steam interface thickness and contact temperature required to produce the most severe damage for each contact time where then calculated.

2.2.5 *Heat transport in metal*

Simplified heat propagation within regions of different temperature within the metal was investigated using a 1D model of finite thickness L. Boundary conditions were $T_{\text{metal, lowered}}$ initially, and T_{metal} at $x = 0$ and $x = L$. The solution is given in (16). $K_{\text{brass}} = 109\,\text{W}\,\text{m}^{-1}\,\text{K}^{-1}$,[37] $\rho_{\text{brass}} = 8500\,\text{kg}\,\text{m}^{-3}$[38] and $c_{\text{brass}} = 380\,\text{J}\,\text{kg}^{-1}\,\text{K}^{-1}$[39] were assumed.

2.3 *Hyperspectral image analysis*

2.3.1 *Classification methods*

The compared classification methods were linear discriminant analysis (LDA), quadratic discriminant analysis (QDA), support vector machine (SVM), random forest and Gaussian Naive Bayes (GNB). The input x is taken to be a hyperspectral pixel.

SVM and random forest were included due to reported good performance when applied directly to hyperspectral data,[40–44] due to the ability of the former to find appropriate decision surfaces in high-dimensional spaces, and the latter's decision tree-based flexibility combined with the random feature selection appropriate for high-dimensional features. LDA has bias due to lack of valid assumptions (Gaussian class density, common covariance), but provides planar decision surfaces with low variance that can lead to good overall performance.[24] The information required for LDA classification spans a lower-dimensional subspace, and the method can be used for class-aware dimensionality reduction. Gaussian Naive Bayes was included as a simple subsequent technique after LDA dimensionality reduction in order to relax some of the bias in LDA. QDA is similar to LDA, except that the classes are assumed to have different rather than identical covariance matrices.

2.3.2 *Training data selection*

Regions were manually labeled in the hyperspectral images according to photos over the histology locations. These regions were taken to be somewhat larger than the actual histology locations based on visual inspection of the homogeneity in the RGB images, in order to increase the number of available training data points and include both shadowed and non-shadowed regions. Training data used for training the classifiers were selected randomly from the original data, ensuring equal number of training data points per class (10 000) wherever possible.

2.3.3 *Classification method evaluation*

Each pixel was considered a sample during training of the classification method, but these are not strictly independent. The cross-validation was therefore done in such a way that each histology location, considered to be more independent, was fully contained on one side of the cross-validation split. Accuracy scores and confusion matrices were used for evaluation.

The classification method was selected based on cross-validation on pig 1 data. The images here had flat illumination, with little variation due to breathing, and contact times ranging from 1

to 12 seconds. The selected method was then evaluated by including pig 2 in the cross-validation, and classification maps were obtained for final evaluation of the damage.

2.3.4 Photon transport modeling

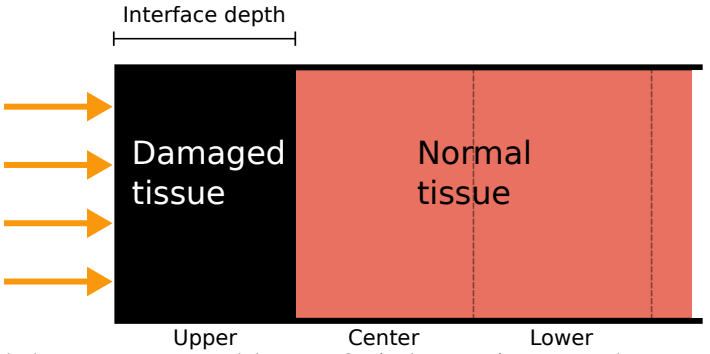

Fig 3: Forward photon transport model setup. Optical properties assumed to correspond to damaged and undamaged tissue are set in the upper and lower layer, respectively, and only the thickness of the upper layer is varied with different damage severity.

A simple two-layer model was used to explain the general behavior of the reflectance. Neglecting influences from epidermis, the full extent of the model was assumed to correspond to dermis. The absorption in normal tissue was modeled as

$$\mu_{\mathrm{a}} = \left(\mu_{\mathrm{oxy}}(\lambda)O + \mu_{\mathrm{deoxy}}(\lambda)(1-O)\right) B, \tag{8}$$

where $B = 0.01$ is the blood volume fraction, $O = 0.8$ the oxygenation, and $\mu_{\mathrm{oxy}}(\lambda)$ and $\mu_{\mathrm{deoxy}}(\lambda)$ the absorption spectra for oxygenated and deoxygenated blood, respectively. The scattering was modeled as

$$\mu_s' = \mu_{\mathrm{s},500}' \left(f_{\mathrm{Mie}}(\lambda/500)^{-b_{\mathrm{Mie}}} + (1 - f_{\mathrm{Mie}}(\lambda/500)^{-4}\right). \tag{9}$$

Coefficients $\mu_{\mathrm{s},500} = 3500\,\mathrm{m}^{-1}$, $f = 0.51$ and $b_{\mathrm{Mie}} = 0.22$ were used, based on scattering values from Bashkatov et al.[45] Damaged tissue was, for simplicity, assumed to consist of two layers: A damaged tissue layer down to the damage depth, and a normal tissue layer, as illustrated in Fig. 3. Letting only the thickness of the damage layer be the varied property between the different damage depths, the model was used to investigate what kind of changes to the skin properties would be necessary in the damage layer to explain the observed reflectance spectra. The reflectance was modeled using the diffusion model solution in Svaasand et al.[46]

3 Results and discussion

Histology property relations are first established in Sec. 3.1. The heat transport model is established in 3.2 and used to characterize the damages and estimate necessary changes to the boundary

conditions to explain the burn wound heterogeneity. Hyperspectral classification is investigated and used to discuss the heterogeneity in Sec. 3.3.

3.1 Histology analysis

The relation between the evaluated histology properties is investigated in order to systematize the damage. Collagen and vascular damage are especially interesting due to the expected influence on the optical properties.

Evaluation of deepest vascular damage, collagen reorganization and final assigned burn level for each histology sample are plotted as a function of contact time in Fig. 4.

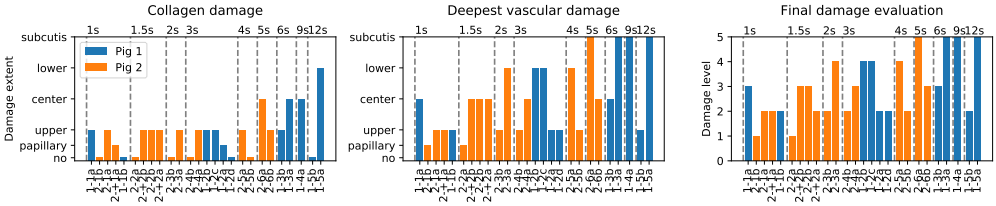

Fig 4: Evaluated damage for all available histology samples. The samples are grouped with respect to the contact time, labeled on top.

Longer contact times generally result in more severe damage. A high heterogeneity is observed: Within one contact time, the damage ranges from relatively low severity to relatively high severity, e.g. damage down to both subcutis and the upper part of dermis at 12 s contact time. The vessel damages are consistently located deeper than the collagen damages. The final assigned burn level follows the same functional behavior as the vessel damage.

The damage evaluations are plotted as a function of burn level in Fig. 5. The final assigned burn level is correlated with the evaluated vessel damage, showing that vessel damage mostly is the deepest type of injury in these cases. The collagen damage has a weak correlation with the final burn level.

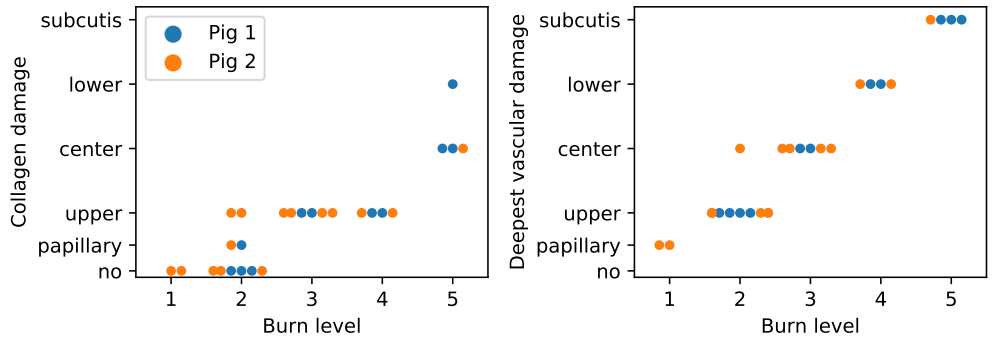

Fig 5: Relation between burn level, and collagen damage (left) and vascular damage (right).

The correlation was investigated further using decision trees. Decision trees were trained to predict assigned burn level from collagen and vessel damages. Leave-one-out cross-validation was used to evaluate the model. Decision trees trained on vessel damages yielded a cross-validation score of 1.00, while decision trees trained on collagen damages yielded a cross-validation score of 0.70: 0.81 for pig 1 and 0.58 for pig 2. The burn levels can be determined entirely from the evaluated vessel damage, and from the collagen damages for pig 1 to some point.

3.2 Heat transport modeling

A heat transport model was set up in order to understand the thermal development in the tissue after application of the heat source.

A temperature profile is built up after t_0 seconds of heating, before the accumulated heat propagates further into the tissue or air, as shown in Fig. 6. A given temperature development can be related to a depth of injury using the Arrhenius integral. The damage was found to be severe enough during the initial 15 seconds to neglect the effects of blood circulation, which was also found by Ng et al.[32]

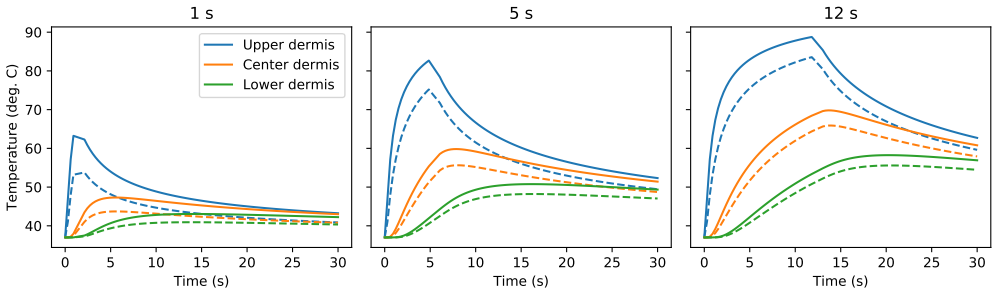

Fig 6: Temperature development at the center depth in the upper, center and lower thirds of dermis, corresponding to depths $333\,\mu m$, $1333\,\mu m$ and $1667\,\mu m$, for different contact times. The dotted lines are simulations with a $10\,\mu m$ steam interface.

The histology overview in the previous section shows that a contact time has both superficial and deep damages present. It is likely that this is due to a change in the boundary conditions, which will be investigated here.

3.2.1 Establishing Arrhenius damage coefficients from the most severe damages

The heat transport model was used to characterize the damages in order to better understand the damage mechanisms under normal circumstances.

It is assumed that the most severe damages for each contact time had direct contact with metal at $100\,°C$. Vascular and collagen damages have different depths of injury, and are therefore expected to have different damage mechanisms. Arrhenius coefficients for different types of injuries are available,[36] but were found to vary much and not necessarily be suitable due to different injury requirements. Optimally, they should be fitted to the available damage data. A lower and upper

depth between which Ω should be 1 is available for each contact time, but fitting the cofficients under these constraints was found to be unstable with multiple possible solutions. Actual contact time, dermal thickness before heat exposure and whether the direct contact assumption is correct is not known, and damages should not be fit exactly.

Only the damage threshold was fitted to the data, which has the same effect as modifying A to yield $\Omega = 1$ at different depths. This represents a simpler injury model where both types of injury are more directly comparable, and explains only the general damage trend. The requirement of $\Omega = 1$ is somewhat arbitrary, representing 63% cell destruction. Injury is expected to pass this point.

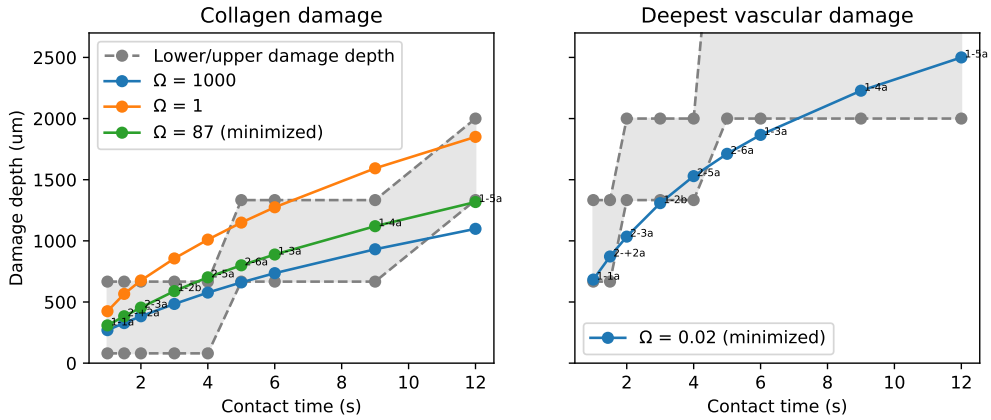

Fig 7: Assumed depth of injuries for the most severe experimental damages as compared to predicted depth of injury by Arrhenius integrals. Corresponding histology sample names are marked along the minimized damage curve.

The modeled depth of injury as compared to the experimental depth of injuries is shown in Fig. 7. The threshold that best explains the collagen damage data is $\Omega = 87$, while the threshold that best explains the vascular damage data is $\Omega = 0.02$. Equivalent A and critical temperature for these damages are $A = 3.5810^{96}$, $T_{\text{crit}} = 66.6\,^{\circ}\text{C}$ and $A = 1.9710^{100}$, $T_{\text{crit}} = 54.0\,^{\circ}\text{C}$ for collagen and vascular damages, respectively.

The collagen damages are generally more superficial. Modeling by Arrhenius damage integrals shows that a higher temperature or longer duration is required for collagen damage to occur than vascular damage.

Comparison with literature Thomson and Pearce[36] compiled damage coefficients and associated T_{crit} from various studies, with 68-80 °C for collagen damage, 80-84 °C for blood cell damage and 55-65 °C for general skin damage. Literature on treatment of port wine stains generally assume blood vessel coagulation above 70 °C,[47–49] 60-70 °C[50,51] or 75 °C.[52,53] Changes to the optical properties of blood have been reported above 65 °C,[54] and destruction above 70 °C.[55] Blood vessel

damage has been reported above 77 °C[56] and shrinking above 70-75 °C.[57] Collagen is reported to denaturate above 60-70 °C,[51] 62-67 °C[58] or above 65 °C.[59] Some studies have found vessel destruction thresholds to coincide with collagen damage thresholds,[58] which could be attributed to collagen being a major component of the vessel wall.[57] Thus, the damage threshold for vessel damage or blood coagulation should be higher than or coincide with the damage thresholds for collagen damage. Vessel damage depths should be more superficial than or equal to the collagen damage depths.

The opposite behavior was found in the experimental data, however. This has lead to vascular damage thresholds far lower than the thresholds found in the literature. It can be speculated that the deepest vascular damage has different damage requirements, and correspond to some damage, any damage to the vessels at this depth, and not complete destruction to the vessels throughout the full depth. The existence of patent vessels at more superficial depths corroborates to this (table 1). The progression of depth for the highest patent vessel coincides somewhat with the collagen damage depth. This indicates extensive vessel destruction that has the same progression as the collagen damage and is more consistent with the damage thresholds found in the literature.

The damage thresholds will be discussed in relation with the found spectral results in Sec. 3.3.2, but the vascular damage thresholds are for now used for characterization of the least severe damages since the damage thresholds should be internally consistent within the same dataset.

3.2.2 Using Arrhenius coefficients to characterize the least severe damages

The heat transport model and associated damage thresholds found above was used to investigate plausible explanations for the heterogeneity of the burn wounds using different boundary conditions to the problem.

Mappings can be found between a change to the boundary condition of the heat transport problem and the resulting depth of injury, which can be used to relate the most superficial damages to a required change in the boundary condition.

Simulating the temperature development for for contact temperatures ranging from 50 to 100 °C and assuming the empirical damage thresholds above yields the mapping in Fig. 8. To e.g. reduce a collagen damage from predicted center-lower dermis to no damage at contact time 12 seconds, a reduction in contact temperature to below 70 °C would be necessary. Estimated contact temperatures for all superficial damage samples are shown in Fig. 9. A range is shown for each injury, where the low and high temperatures corresponds to no damage and damage throughout the entire block, respectively. Contact temperatures estimated for the collagen damages and the vascular damages overlap. Required contact temperature vary somewhat between the damages, however. At worst, a contact temperature below 60 °C is needed to explain the damage for a contact time of 12 seconds.

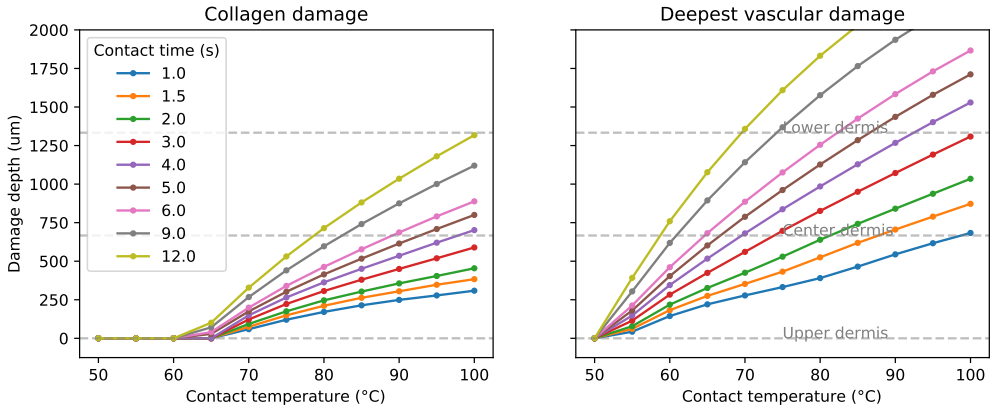

Fig 8: Mapping between contact temperature and predicted depth of injury, collagen damages (left) and vessel damages (right).

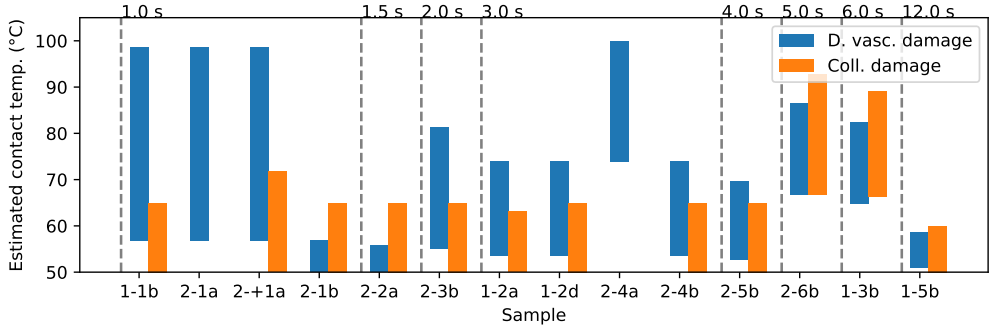

Fig 9: Estimated contact temperature ranges required to explain the least severe damages for each contact time.

Similar to the contact temperature characterization, the relation between a steam interface thickness and the corresponding damage depth is plotted in Fig. 10, and the estimated steam interface thicknesses are plotted in Fig. 11.

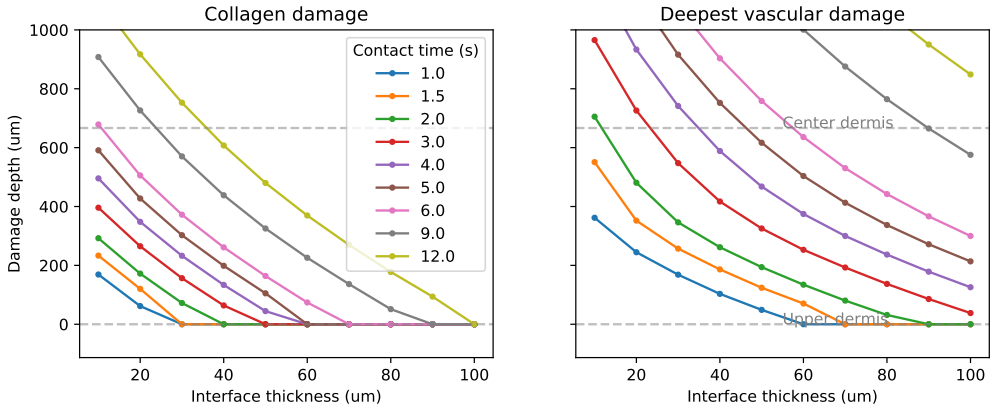

Fig 10: Mapping between steam interface thickness and the predicted depth of injury, for collagen damages (left) and vessel damages (right). The functional behavior close to damage depth 0 is not strictly correct for some of the contact times, in particular 1 and 4 s contact times, due to the limited resolution in the interface thickness.

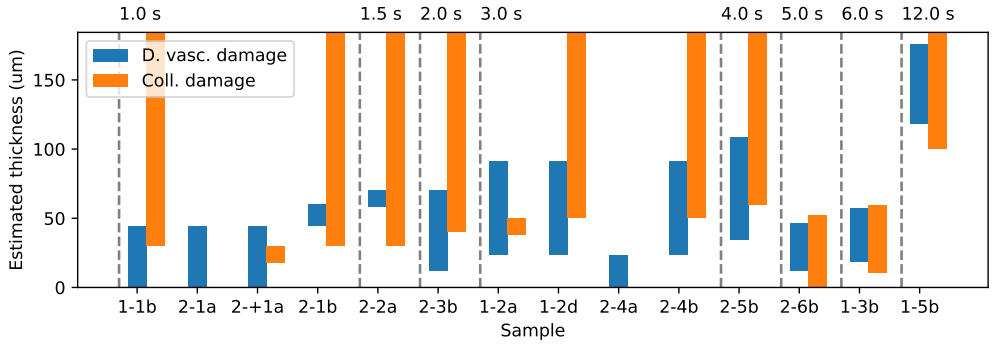

Fig 11: Estimated interface thickness ranges required to explain the least severe damages for each contact time.

The burn wounds had locations with no damage to the collagen structure. The mapping in Fig. 10 shows that there is no damage to the collagen structure when the interface thickness is larger than a threshold. The thickness for these samples was therefore assumed to be any thickness larger than this threshold. Interfaces estimated from collagen and vessel damages overlap, and are self-consistent. At worst, an interface with thickness above $130\,\mu\mathrm{m}$ is needed, but generally the required thickness is somewhere around 30 to $70\,\mu\mathrm{m}$.

3.2.3 *Heat transport in metal*

The explanation model where the contact temperature is lowered requires that the metal has cold spots where the temperature is lowered compared to the rest of the metal. The heat exchange dynamics in such a situation was investigated using the 1D model in Sec. 2.2.5 with temperature $70\,^{\circ}\mathrm{C}$ and the ends $x = 0$ and $x = L$ maintained at temperature $100\,^{\circ}\mathrm{C}$. Figure 12 shows the time for the minimum temperature in this model to reach above $90\,^{\circ}\mathrm{C}$ for different regions. The time is below 1 seconds for a region with thickness 1 cm, and below 7 seconds for 4 cm regions.

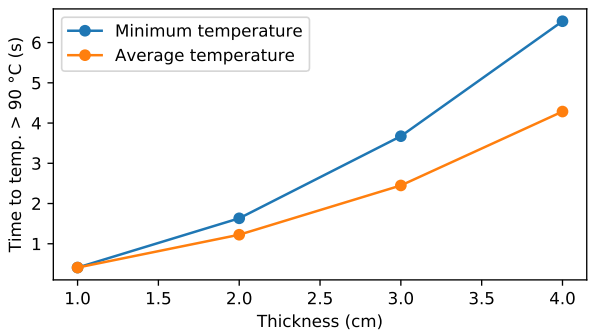

Fig 12: Time until a cold spot of temperature $70\,^{\circ}\mathrm{C}$ within a $100\,^{\circ}\mathrm{C}$ region reaches above $90\,^{\circ}\mathrm{C}$.

3.3 *Hyperspectral characterization*

A hyperspectral classification model for detectable damage is established statistically, and then investigated in terms of changes in optical properties and classification map behavior in order to understand which changes have been detected and whether the premise can be expected to generalize. The classification model is used to investigate the spatial extent of the burn wound heterogeneity and related back to the findings in Sec. 3.2.

3.3.1 *Model selection*

Preprocessing treatment and classification model is first selected based on cross-validation on pig 1, in order to obtain a basic classification method for further investigation in the later sections.

The method selection was run on collagen classification only. Initial classification of burn level was found to be challenging, and misclassification of samples with different burn level could be traced to the samples having the same collagen damage depth. Histologies 1-2a and 1-3b were left out due to the final collagen damage decision not being clear.

Methods and preprocessing treatments are compared using cross-validation on pig 1 in Fig. 13. LDA was found to have the best performance with respect to the accuracy score, with a minor improvement when followed by Gaussian Naive Bayes. Similar performance was also found using LDA followed by SVM-RBF (not shown). LDA+Naive Bayes was chosen for further testing due to inconvenient parameter tuning requirements in SVM. No more methods were compared here due to an apparent upper limit in the classification accuracy. The upper limit could be attributed

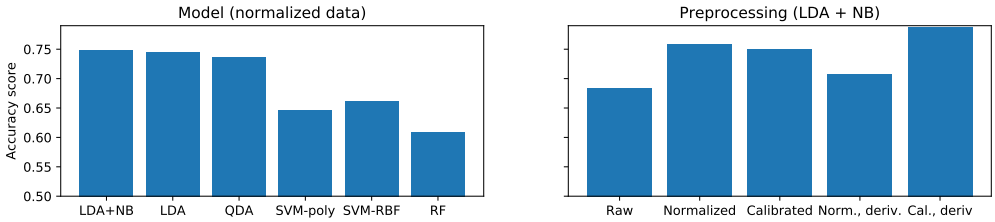

Fig 13: Comparison of cross-validation accuracy scores over classification methods and preprocessing treatments for collagen classification of pig 1. SVM-poly and SVM-RBF were tuned, using $C = 20$ and $d = 7$ for SVM-poly, and $C = 70$ and $\gamma = 0.1$ for SVM-RBF.

to disagreement among the pathologists, and mislabeling of individual training data pixels that would otherwise be difficult to rectify for without relying on a prior classification. The accuracy is apparently low, but accuracy is a harsh metric in the multi-label case since it does not evaluate whether a label is close to the correct label, only that the predicted labels do not match exactly. The score should still be appropriate for relative evaluation of the various techniques.

Normalized spectra were used during model selection, and other preprocessing treatments were compared in the same figure. First derivatives of calibrated spectra had the highest cross-validation accuracy. Normalization was still chosen as the main preprocessing method due to expected difficulties with shadow artifacts in the rest of the data, and a concern that calibration treatments rather than real spectral differences could end up being classified.

3.3.2 Classifiability of the damage properties

Evaluation of the classification model is extended by including pig 2 in the cross-validation setup, and classification of burn level, vascular damage and collagen damage are compared and related to likely changes in optical properties.

Classification accuracy for different types of damage Final score after model selection on pig 1 is not representative, and pig 2 is included in order to evaluate the performance further. Understanding the difficulties in detecting burn level in the previous study is important for understanding the feasibility of the technique, and classification of different histology properties is compared.

Confusion matrices for classification of burn level and collagen reorganization are shown in Fig. 14 when trained on both pigs. Overall accuracy scores for burn level, deepest vascular damage and collagen damage were 61%, 61% and 82%, respectively. Accuracy scores for burn level and collagen damage were 77% and 79% for pig 1, and 47% and 85% for pig 2, respectively. It was seen in Sec. 3.1 that the burn level could be determined entirely from the deepest vascular damage, and the results for burn level determination are therefore also assumed to be valid for determination of deepest vascular damage. Classification of burn level has lower classification accuracy, but less so for pig 1 than for pig 2. It was shown in Sec. 3.1 that the final burn level was more correlated with the collagen level for pig 1 than for pig 2, which could attribute for this difference. Collagen damage level thus seems to be the main detectable property by hyperspectral

imaging, while deepest vascular damage, and hence burn level by the results in 3.1, is difficult to classify.

The applied method was selected specifically for collagen damage classification, and burn level classification using the same method has a disadvantage. However, burn level classification was found to be challenging no matter the classification method or preprocessing treatment.

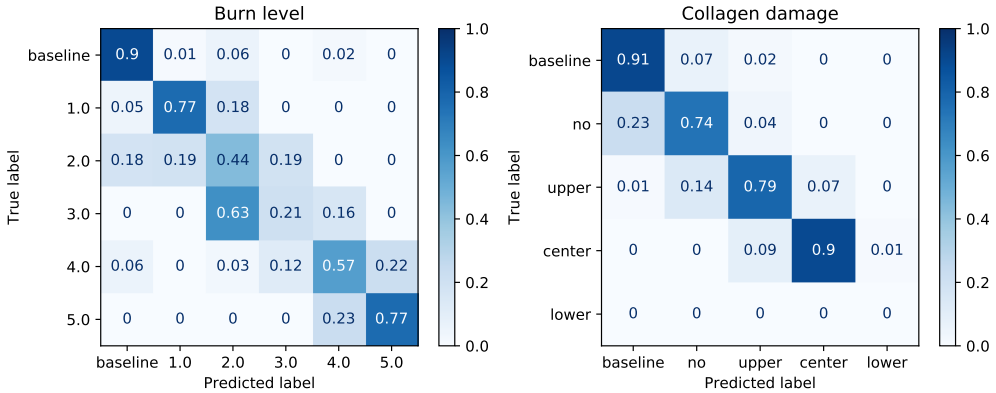

Fig 14: Confusion matrices for LDA + GNB trained to predict burn level (left) and collagen reorganization (right) from normalized spectra, obtained from cross-validation including both pigs.

Reflectance spectra Understanding the relation between the classifiable spectral differences and the underlying physical behavior is important for understanding the limits of the technique and explaining the results above.

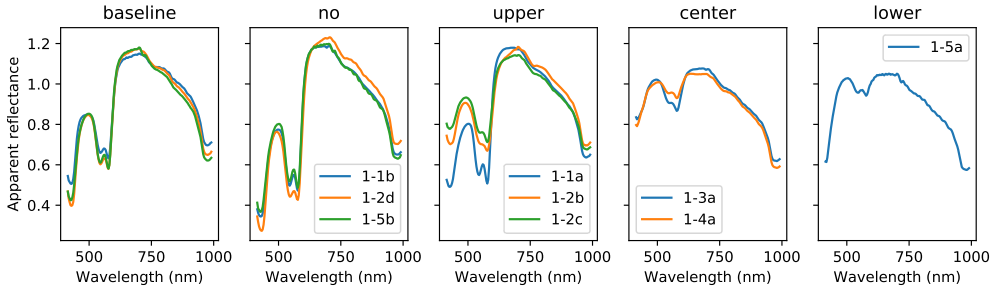

Fig 15: Apparent reflectance spectra for pig 1, grouped by collagen damage. The raw spectra and reflectance standard spectra were both normalized before reflectance calibration.

Apparent reflectance spectra are first investigated. These are plotted in Fig. 15. These were normalized and then calibrated by normalized reflectance standards due to changes in reflectance standard height. Aside from level changes, the main observed spectral feature is a reduction in the

dynamic behavior ("crunching") from 500 to 700 nm and a scewing of the spectra with damages down to upper and center dermis. Damage down to lower and center dermis are apparently separable through differences below 500 nm, but is more likely to be due to light source calibration differences since the absolute damage depth is the same in these two cases.

Techniques like LDA likely have high classification accuracy due to each collagen damage corresponding to a major change in the reflectance that varies around a mean value. The higher performance of the spectral derivatives of the reflectance in the last section can be attributed the derivatives providing better features for the observed crunching effect.

Forward modeling The forward model outlined in Sec. 2.3.4 was used to understand the spectral behavior. Changes to the scattering only in the damage layer did not give the required differences between the damage depths, and it was necessary to reduce the blood volume of the damage layer. Modeled spectra are shown in Fig. 16. The scattering of the damage layer was set to 70% of the normal scattering level per SFDI studies of full thickness burn wounds.[1,2] Adjusting the scattering parameters had some influence on the level and sloping, but the main attribute seemed to be the reduction in blood volume. The expected reduction in scattering levels has a relatively small influence on the reflectance as compared to the blood volume effect.

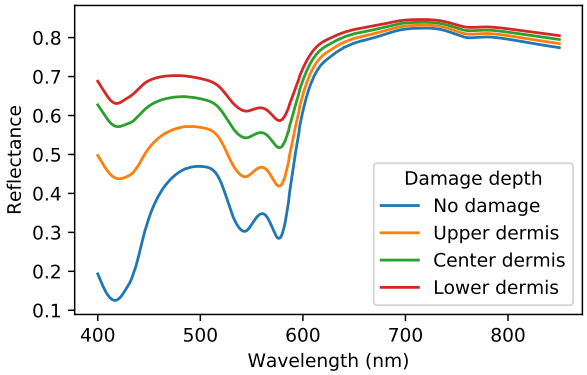

Fig 16: Simple two-layer burn model with layer interface placed at upper, lower or center dermis: The effect of decreasing the blood volume fraction in the damaged layer from 1% to 0.01%. The scattering in the damage layer was set to 70% of the normal scattering levels.

Progression of damage depth is expected from SFDI studies to lead to an early reduction in scattering levels due to collagen damage, and later reduction in blood content and oxygenation due to vascular destruction.[1,2] Hyperspectral and reflectance spectroscopy studies have found similar reductions in the scattering level[16] and oxygenation and blood volume.[9–11,14,16]

The spectral changes associated with collagen damage in the current study mainly seems to be attributable to blood volume reductions rather than a scattering reduction. The detected changes are therefore more related to vascular damage and lowering of perfusion rather than the structural changes expected from collagen damage alone. The blood volume changes have a progression

in depth similar to the progression in collagen damage depth. This is in line with earlier optical studies, but a discrepancy with respect to the histologies of the current study, as the deepest vascular damage had only a weak correlation with the collagen damage.

However, as shown in Sec. 3.2.1, the deepest vascular damage had unexpectedly low temperature damage thresholds, and might not represent full vascular damage throughout the entire depth. The collagen damage could coincide with complete destruction to the vasculature, which would then have damage thresholds more consistent with the literature presented in 3.2.1, and could explain the coincident reductions in blood volume. This would also be more in line with the studies reporting coincident vascular and collagen destruction.

That superficial perfusion changes is the main detectable feature further explains the difficulty in classifying on the deepest vascular damage. Deeper, but not complete vascular damage would lead to subtle perfusion-related changes which are challenging to separate from the strong, superficial perfusion changes resulting from the more complete vascular destruction higher up in the tissue.

The expected differences due to collagen damage alone have only a small and subtle effect on the reflectance. It is unlikely that this can be completely separated from the perfusion effects, which would be a prerequisite for enabling early detection in a similar way as SFDI.

Summarized, the hyperspectral data can discriminate between collagen damage depth to some point, but indirectly through a coincident change to the perfusion. Only the last measurement timepoint can be properly classified.

3.3.3 Classification maps

A classification model for collagen damage has been established. This model is applied to the rest of the images, and discussed in terms of the burn heterogeneity explanation models.

The collagen damage classification was applied to the last measurement only. Classification maps are shown in Fig. 17.

Discussion of the classification maps The classification maps are first discussed in order to evaluate correctness and investigate some of the spatial features.

The presence of a higher severity collagen damage classification and the development in class size demonstrates a systematic increase in collagen damage with respect to contact time. The classification maps provide the full spatial extent of the burn heterogeneity, showing regions with damage of lower severity embedded within high severity damage regions.

The full rectangular damage region is surrounded by a thin border of low severity damage, which can be attributed to heat escaping from the high severity damage regions into the surrounding tissue. The thickness corresponds to some heat diffusion length. Longer contact times have a similar envelope surrounding the low severity damage regions.

Collagen damage at contact time 12 seconds is mostly classified as damage down to center dermis rather than lower dermis. Only a small region is classified with damage down to lower dermis. This is likely enforced by minor spectral differences in the training data, since the results of the previous section showed that the only available lower dermis damage sample is similar to damages down to center dermis.

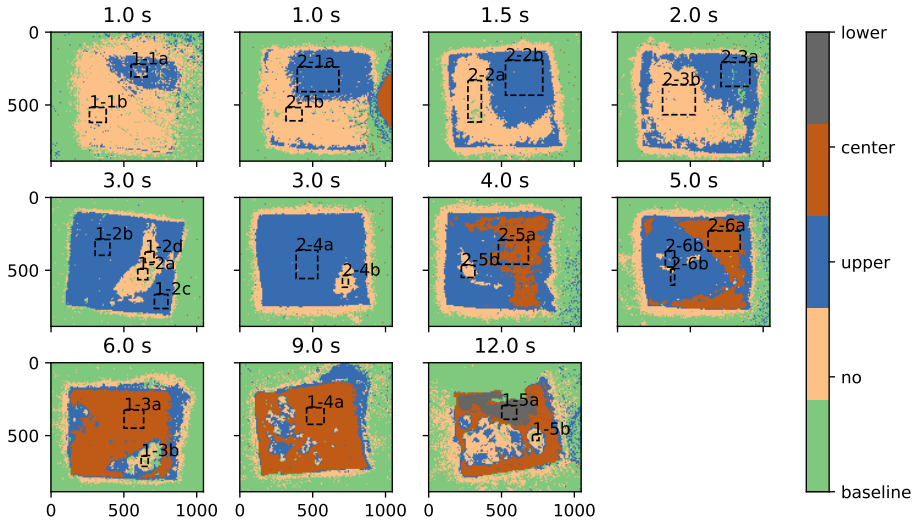

Fig 17: Classification maps for collagen damage classification on both pigs, grouped by contact time.

The classified low severity damage region at contact times 3 and 4 seconds does not seem to match the full extent of the low severity damage region indicated by red regions in the RGB images in Fig. 1. This might be attributed to the low severity damage regions transitioning into upper dermis at the same time as the high severity damage regions are transitioning from upper to center dermis, leading to a similar damage classification on both sides of the boundary.

Discussion of burn wound heterogeneity Explanation models for the burn heterogeneity have been proposed in this study: Lowered contact temperature, and the addition of a contact surface resistance by a steam interface. The feasibility of the explanation models are subject to the physical behavior shown by the classification maps.

At contact times 1.5s and 2.0s, regions of width 1.3-2 cm are present, and a region of width around 1.3 cm at contact time 12 seconds. The latter is especially interesting, as a low severity damage region is maintained throughout the full exposure of 12 seconds. Given the contact temperature change explanation, average contact temperature needs to be below $70\,^{\circ}\mathrm{C}$ within this region. The metal heat transport simulations in Sec. 2.2.5 shows that it should not be possible to retain such regions throughout the full exposure. Another possible explanation is the presence of a cold spot which increase in temperature over time to create similarly low severity damages. The start

temperature needs to be yet lower, however. The formation of vapor bubbles during heating that blocks the heat transfer to the metal has previously been blamed for the heterogeneity.[21] However, the time scales for the heat transport in the metal show that they should be quickly homogenized during heating and during application to the pig. Cold spots for slightly lower temperatures than the intended $100\,^{\circ}\mathrm{C}$ can exist due to such an effect, but not for the contact temperatures required to reproduce the damages.

The steam interface explanation allows for arbitrary steam interfaces to build up over time, and can be maintained throughout the full exposure. Water was observed to be adhered to the metal. The temperature of the water is assumed to hold temperatures close to $100\,^{\circ}\mathrm{C}$, and with the metal holding the boiling point temperature it can be assumed that the existence of spontaneous steam should be feasible. It is possible that it can be a combination of the two effects, however. Water was also investigated for whether it can provide similar contact resistances, but has higher conductivity requiring thicker interfaces to reproduce the required heat transfer coefficient. There is a limit to the water interface thickness that could be maintained due to water being squeezed out from underneath the metal, but water vapor could exhibit some pressure and maintain a distance/steam thickness between the skin and the metal.

Solutions for reducing the burn heterogeneity exists, including using a PEG-H2O solution to raise the boiling point when heating up the metal,[21] and using dry heating.[6] Interestingly, both approaches would also reduce the possibility for spontaneous steam creation.

Hyperspectral classification and heat transport modeling have thus been used to better understand the burn wound heterogeneity. The least severe damages for each contact time do not develop much in severity over various contact times, and lacks the systematics present in the burn wounds representing unchanged boundary conditions. Classification maps are still somewhat challenging to interpret, but have been reduced to more basic principles and by classifying on properties that can be reasonably sure to be detectable. The results of this study adds to better understanding of the underlying mechanisms and the resulting optical property variation.

4 Conclusion

A heat transport model has been established and used to characterize collagen and vascular damage. Collagen damage requires higher temperatures or durations than vascular damage, and are therefore generally more superficial. A burn heterogeneity is observed, and two possible explanation models have been established using the same heat transport model: a contact temperature reduction, or surface contact resistance resistance through the creation of a steam interface. Hyperspectral classification of the damages show that contact temperature reduction alone is unlikely since a low temperature region would have to be maintained in high-conducting metal over longer durations.

The final evaluated burn level was found to be mainly related to deep vascular damage properties. These were difficult to classify using the hyperspectral technique, and mainly collagen damage levels could be classified. The collagen damage seems to coincide with a reduction of the perfusion properties down to the same depths as the collagen damage.

A better understanding of the burn wound data used in this study has been obtained through a use of heat transport modeling, photon transport modeling and hyperspectral classification techniques.

Appendix A: Histology

Table 1: Histology table with relevant fields. The abbreviated column headers correspond to "Sample", "Contact time", "Deepest vascular damage", "Highest patent vessel" and "Collagen damage", respectively.

Samp.	C. time	D. vasc. damage	High. pat. vess.	Coll. damage	Level
1-1a	1.0	center	upper	upper	3
1-1b	1.0	upper	upper	no	2
1-2a	3.0	upper	upper	papillary	2
1-2b	3.0	lower	upper	upper	4
1-2c	3.0	lower	upper	upper	4
1-2d	3.0	upper	upper	no	2
1-3a	6.0	subcutis	upper/center	center	5
1-3b	6.0	center	upper	upper	3
1-4a	9.0	subcutis	upper/center	center	5
1-5a	12.0	subcutis	lower	lower	5
1-5b	12.0	upper	upper	no	2
2-1a	1.0	upper	upper	upper	2
2-+1a	1.0	upper	upper	papillary	2
2-1b	1.0	papillary	upper	no	1
2-2a	1.5	papillary	upper	no	1
2-+2a	1.5	center	upper	upper	2
2-2b	1.5	center	upper	upper	3
2-+2b	1.5	center	upper	upper	3
2-3a	2.0	lower	upper	upper	4
2-3b	2.0	upper	upper	no	2
2-4a	3.0	center	upper	upper	3
2-4b	3.0	upper	upper	no	2
2-5a	4.0	lower	upper	upper	4
2-5b	4.0	upper	upper	no	2
2-6a	5.0	subcutis	center	center	5
2-6b	5.0	center	upper	upper	3

Appendix B: Heat transport solutions

Tissue models The solution to (1) with (3) is

$$T(x,t) = (T_{\text{metal}} - T_0)\text{erfc}\left(\frac{x}{2\sqrt{\kappa t}}\right) + T_0. \tag{10}$$

Including a heat transfer coefficient $H < \infty$ in (2) has the solution[25]

$$T(x,t) = \left[\text{erfc}\left(\frac{x}{2\sqrt{\kappa t}}\right) - \exp(hx + h^2\kappa t)\text{erfc}\left(\frac{x}{2\sqrt{\kappa t}} + h\sqrt{\kappa t}\right)\right](T_e - T_0) + T_0, \quad (11)$$

where $h = H/K$. Initial temperature profile $T(x)$ at $t = 0$ and linear heat transfer at the surface has the solution[25]

$$T(x,t) = \int_0^\infty u(x',x,t)T(x')dx' + \kappa h \int_0^t u(x'=0,x,t-\tau)T_0 d\tau, \quad (12)$$

with

$$u(x',x,t) = \frac{1}{2\sqrt{\pi\kappa t}}\left\{\exp(-(x-x')^2/4\kappa t) + \exp(-(x+x')^2/4\kappa t)\right\} - \ldots \quad (13)$$

$$h\exp(\kappa t h^2 + h(x+x'))\text{erfc}\left\{\frac{x+x'}{2\sqrt{\kappa t}} + h\sqrt{\kappa t}\right\}. \quad (14)$$

The last solution was evaluated by numerical integration.

Metal model Assuming $v(x=0) = 0$, $v(x=L) = 1$ and $v(x,0) = 0$, the solution is[25]

$$v(x,L) = \sum_0^\infty \left[\text{erfc}\left(\frac{(2n+1)l - x}{2\sqrt{\kappa t}}\right) - \text{erfc}\left(\frac{(2n+1)l + x}{2\sqrt{\kappa t}}\right)\right]. \quad (15)$$

With $T(x,0) = T_{\text{initial}}$ and $T(x=0,t) = T(x=L,t) = T_{\text{maintained}}$,

$$T(x,t) = (T_{\text{maintained}} - T_{\text{initial}})\left(v(x,t) + v(L-x,t)\right) + T_{\text{initial}}. \quad (16)$$

Disclosures

The authors have no conflicts of interest to disclose.

Acknowledgments

Thanks to Lukasz Paluchowski for acquisition of the hyperspectral data, to Håvard B. Nordgaard and Lukasz Paluchowski for planning and performing the animal experiment, and to Håkon Hov and Sissel M. Berget for evaluation of the biopsy material.

Code, Data, and Materials Availability

Code and data used to produce the results and figures of this paper can be made available from the corresponding author upon reasonable request.

References

1 A. Ponticorvo, D. M. Burmeister, B. Yang, *et al.*, "Quantitative assessment of graded burn wounds in a porcine model using spatial frequency domain imaging (sfdi) and laser speckle imaging (lsi)," *Biomed. Opt. Express* **5**(10), 3467–3481 (2014).

2 A. Mazhar, S. Saggese, A. C. Pollins, *et al.*, "Noncontact imaging of burn depth and extent in a porcine model using spatial frequency domain imaging," *J. Biomed. Opt.* **19**(8), 086019 (2014).

3 D. M. Burmeister, A. Ponticorvo, B. Yang, *et al.*, "Utility of spatial frequency domain imaging (sfdi) and laser speckle imaging (lsi) to non-invasively diagnose burn depth in a porcine model," *Burns* **41**(6), 1242–1252 (2015).

4 M. Kaiser, A. Yafi, M. Cinat, *et al.*, "Noninvasive assessment of burn wound severity using optical technology: A review of current and future modalities," *Burns* **37**(3), 377–386 (2011).

5 A. Ponticorvo, D. M. Burmeister, R. Rowland, *et al.*, "Quantitative long-term measurements of burns in a rat model using spatial frequency domain imaging (sfdi) and laser speckle imaging (lsi)," *Lasers Surg. Med.* **49**(9), 293–304 (2017).

6 A. Ponticorvo, R. Rowland, M. Baldado, *et al.*, "Evaluating clinical observation versus spatial frequency domain imaging (sfdi), laser speckle imaging (lsi) and thermal imaging for the assessment of burn depth," *Burns* **45**(2), 450–460 (2019).

7 R. Rowland, A. Ponticorvo, M. Baldado, *et al.*, "Burn wound classification model using spatial frequency-domain imaging and machine learning," *J. Biomed. Opt.* **24**(5), 056007 (2019).

8 A. Ponticorvo, R. Rowland, M. Baldado, *et al.*, "Spatial frequency domain imaging (sfdi) of clinical burns: A case report," *Burns Open* **4**(2), 67–71 (2020).

9 K. M. Cross, M. A. Hastings, J. R. Payette, *et al.*, "Near infrared point and imaging spectroscopy for burn depth assessment," *International congress series* **1281**, 137–142 (2005).

10 M. Levasseur, L. Leonardi, J. Payette, *et al.*, "Near infrared hyperspectral imaging: The road traveled to a clinical burn application," *Proc. SPIE* **5969**, 59691O (2005).

11 M. S. Chin, O. Babchenko, J. Lujan-Hernandez, *et al.*, "Hyperspectral imaging for burn depth assessment in an animal model," *Plast Reconstr Surg Glob Open* **3**(12), e591 (2015).

12 M. A. Calin, S. V. Parasca, R. Savastru, *et al.*, "Characterization of burns using hyperspectral imaging technique – a preliminary study," *Burns* **41**(1), 118–124 (2015).

13 M. A. Calin, S. Parasca, and D. Manea, "Comparison of spectral angle mapper and support vector machine classification methods for mapping skin burn using hyperspectral imaging," *Proc. SPIE* **10677**, 106773P (2018).

14 H. Ding and R. C. Chang, "Hyperspectral imaging with burn contour extraction for burn wound depth assessment," *ASME J. Eng. Sci. Med. Diagn. Ther.* **1**(4), 041002 (2018).

15 S. V. Parasca, M. A. Calin, D. Manea, *et al.*, "Hyperspectral index-based metric for burn depth assessment," *Biomed. Opt. Express* **9**(11), 5778–5791 (2018).

16 P. Wang, Y. Cao, M. Yin, *et al.*, "Full-field burn depth detection based on near-infrared hyperspectral imaging and ensemble regression," *Rev. Sci. Instrum.* **90**(6), 064103 (2019).

17 H. Hoeksema, K. Van de Sijpe, T. Tondu, *et al.*, "Accuracy of early burn depth assessment by laser doppler imaging on different days post burn," *Burns* **35**(1), 36–45 (2009).

18 A. D. Jaskille, J. C. Ramella-Roman, J. W. Shupp, *et al.*, "Critical review of burn depth assessment techniques: Part ii. review of laser doppler technology," *J. Burn Care Res.* **31**(1) (2010).

19 L. A. Paluchowski, H. B. Nordgaard, A. Bjorgan, *et al.*, "Can spectral-spatial image segmentation be used to discriminate burn wounds?," *J. Biomed Opt.* **21**(10), 101413 (2016).

20 L. A. Paluchowski, A. Bjorgan, H. B. Nordgaard, *et al.*, "Spectral-spatial classification combined with diffusion theory based inverse modeling of hyperspectral images," *Proc. SPIE* **9689** (2016).

21 C. Gaines, D. Poranki, R. A. F. Clark, *et al.*, "Development of a porcine deep partial thickness burn model," *Burns* **39**(2), 311–319 (2013).

22 L. A. Paluchowski, *Characterization of biological tissue using statistical and physics-based hyperspectral image processing methods*. PhD thesis, NTNU (2018).

23 A. Papp, K. Kiraly, M. Harma, *et al.*, "The progression of burn depth in experimental burns: a histological and methodological study," *Burns* **30**(7), 684–690 (2004).

24 T. Hastie, R. Tibshirani, and J. Friedman, *The elements of statistical learning*, Springer, 2nd edition ed. (2009).

25 H. S. Carslaw and J. C. Jaeger, *Conduction of heat in solids*, Oxford science publications, 2nd edition ed. (1959).

26 H. H. Pennes, "Analysis of tissue and arterial blood temperature in the resting human forearm," *J. Appl. Physiol.* **1**(2), 93–122 (1948).

27 T. Log, "Modeling skin injury from hot spills on clothing," *Int. J. Environ. Res. Public Health* **14**(11), 1374 (2017).

28 E. Y.-K. Ng and L. T. Chua, "Prediction of skin burn injury. part 1: numerical modelling," *Proc. Inst. Mech. Eng. H.* **216**(3), 157–170 (2002).

29 K. R. Diller and L. J. Hayes, "A finite element model of burn injury in blood-perfused skin," *J. Biomed. Eng.* **105**(5), 300–307 (1983).

30 N. N. Johnson, J. P. Abraham, Z. I. Helgeson, *et al.*, "An archive of skin-layer thicknesses and properties and calculations of scald burns with comparisons to experimental observations," *J. Thermal Sci. Eng. Appl* **3**(1), 011003 (2011).

31 M. Fu, W. Weng, and H. Yuan, "Numerical simulation of the effects of blood perfusion, water diffusion, and vaporization on the skin temperature and burn injuries," *Numer. Heat Tr. A-Appl.* **65**(12), 1187–1203 (2014).

32 E. Y.-K. Ng and L. T. Chua, "Prediction of skin burn injury. part 2: parametric and sensitivity analysis," *Proc. Inst. Mech. Eng. H.* **216**(3), 171–183 (2002).

33 K. Buettner, "Effects of extreme heat and cold on human skin. i. analysis of temperature changes caused by different kinds of heat application," *J. Appl. Physiol.* **3**(12), 691–702 (1951).

34 "https://www.engineeringtoolbox.com/water-liquid-gas-thermal-conductivit
2012.html, visited 2020-09-25."

35 F. C. Henriques and A. R. Moritz, "Studies of thermal injury v: The predictability and the significance of thermal induced rate processes leading to irreversible epidermal injury," *Arch. Pathol.* **43**(5), 489–502 (1947).

36 S. Thomsen and J. A. Pearce, "Thermal damage and rate processes in biologic tissues," in *Optical-Thermal Response of Laser-Irradiated Tissue*, A. J. Welch and M. J. C. van Gemert, Eds., ch. 13, Springer, 2nd edition ed. (2011).

37 "http://hyperphysics.phy-astr.gsu.edu/hbase/Tables/thrcn.html, visited 2020-09-25."

38 "https://www.engineeringtoolbox.com/metal-alloys-densities-d_50.html, visited 2020-09-25."

39 "http://www2.ucdsb.on.ca/tiss/stretton/database/Specific_Heat_Capacity_Table.html, visited 2020-09-25."

40 F. Melgani and L. Bruzzone, "Classification of hyperspectral remote sensing images with support vector machines," *IEEE Trans. Geosci. Remote Sens.* **42**(8), 1778–1790 (2004).

41 Y. Tarabalka, M. Fauvel, J. Chanussot, *et al.*, "Svm- and mrf-based method for accurate classification of hyperspectral images," *IEEE Geosci. Remote. Sens. Lett.* **7**(4), 736–740 (2010).

42 G. Camps-Valls and L. Bruzzone, "Kernel-based methods for hyperspectral image classification," *IEEE Trans. Geosci. Remote Sens.* **43**(6), 1351–1362 (2005).

43 M. Belgiu and L. Dragut, "Random forest in remote sensing: A review of applications and future directions," *ISPRS J. Photogramm. Remote Sens.* **114**, 24–31 (2016).

44 J. C.-W. Chan, P. Bechers, T. Spanhove, *et al.*, "An evaluation of ensemble classifiers for mapping natura 2000 heathland in belgium using spaceborne angular hyperspectral (chris/proba) imagery," *Int. J. Appl. Earth Obs.* **18**, 13–22 (2012).

45 A. N. Bashkatov, E. A. Genina, and V. V. Tuchin, "Optical properties of skin, subcutaneous, and muscle tissues: A review," *J. Innov. Opt. Health Sci.* **4**(1), 9–38 (2011).

46 L. Svaasand, L. Norvang, E. Fiskerstrand, *et al.*, "Tissue parameters determining the visual appearance of normal skin and port-wine stains," *Laser Med. Sci.* **10**(1), 55–65 (1995).

47 M. J. C. van Gemert, W. J. A. de Kleijn, and J. P. H. Henning, "Temperature behavior of a model port-wine stain during argon laser coagulation," *Phys. Med. Biol.* **27**(9), 1089–1104 (1982).

48 R. R. Anderson and J. A. Parrish, "Microvasculature can be selectively damaged using dye lasers: A basic theory and experimental evidence in human skin," *Lasers Surg. Med.* **1**, 261–276 (1981).

49 J. de Boer, G. W. Lucassen, W. Verkruysse, *et al.*, "Thermolysis of port-wine-stain blood vessels: Diameter of a damaged blood vessel depends on the laser pulse length," *Lasers Med. Sci.* **11**, 177–180 (1996).

50 L. O. Svaasand, E. J. Fiskerstrand, L. T. Norvang, *et al.*, "On the damage to microvessels during pulsed laser treatment of port-wine stains," *Proc. SPIE* **2624** (1996).

51 R. R. Anderson and J. A. Parrish, "Selective photothermolysis: precise microsurgery by selective absorption of pulsed radiation," *Science* **220**(4596), 524–527 (1983).

52 A. E. Pushkareva and I. Ponomarev, “Comparative numerical analysis and optimization of blood vessels heated using various lasers,” *Laser Phys.* **28**(9), 096003 (2018).
53 I. V. Ponomarev, S. B. Topchiy, M. A. Kazaryan, *et al.*, “Numerical simulation optimization of selective heating of blood vessels in "port-wine stains" under laser irradiation in various modes,” *Bull. Lebedev Phys. Inst.* **45**(7), 17–23 (2018).
54 L. L. Randeberg, A. J. H. Hagen, and L. O. Svaasand, “Optical properties of human blood as a function of temperature,” *Proc SPIE* **4609** (2002).
55 J. Fildes, S. Fisher, C. M. Sheaff, *et al.*, “Effects of short heat exposure on human red and white blood cells,” *J. Trauma* **45**(3), 479–484 (1998).
56 V. L. Martinot, S. R. Mordon, V. A. Mitchell, *et al.*, “Determination of efficient parameters for argon laser-assisted anastomoses in rats: Macroscopic, thermal and histological evaluation,” *Lasers Surg. Med.* **15**(2), 168–175 (1994).
57 W. Gorisch and K.-P. Boergen, “Heat-induced contraction of blood vessels,” *Laser Surg. Med.* **2**(1), 1–13 (1982).
58 R. Agah, J. A. Pearce, A. J. Welch, *et al.*, “Rate process model for arterial tissue thermal damage: implications on vessel photocoagulation,” *Lasers Surg. Med.* **15**(2), 176–184 (1994).
59 L. Bozec and M. Odlyha, “Thermal denaturation studies of collagen by microthermal analysis and atomic force microscopy,” *Biophys. J.* **101**(1), 228–236 (2011).

Biographies of the authors were not available.

ISBN 978-82-326-5461-1 (printed ver.)
ISBN 978-82-326-6491-7 (electronic ver.)
ISSN 1503-8181 (printed ver.)
ISSN 2703-8084 (online ver.)

NTNU

Norwegian University of
Science and Technology